ULTRACOLD QUANTUM GASES IN TIME-AVERAGED ADIABATIC POTENTIALS

Benjamin Sherlock

A thesis submitted in partial fulfilment of the requirements for the degree of Doctor of Philosophy at the University of Oxford



Merton College

University of Oxford

Trinity Term 2011

Abstract

Ultracold Quantum Gases in Time-Averaged Adiabatic Potentials

Benjamin Sherlock, Merton College, Oxford
D.Phil thesis, Trinity 2011

This thesis describes the experimental realisation and characterisation of three non-trivial trapping geometries for ultracold atoms. The double-well, ring and to some degree shell trap are examples of a highly versatile class of traps called time-averaged adiabatic potentials (TAAPs). In this experiment the TAAPs arise from the combination of three independent magnetic fields; a static quadrupole field dressed by a uniform radio-frequency field is time-averaged by a bias field oscillating at in the kHz regime. The result is a very smooth potential, within which ultracold atoms can be evaporatively cooled to quantum degeneracy, and subsequently manipulated into new geometries without destroying the quantum coherence.

The vertically offset double-well potential provided the first example of ultracold atoms confined in a TAAP. The same potential is used to demonstrate efficient evaporative cooling across the Bose-Einstein condensate (BEC) phase transition using only the Landau-Zener loss mechanism. Switching off the time-averaging fields loads atoms from the double-well TAAP into the rf-dressed shell trap. A characterisation of this potential measured low heating rates and lifetimes of up to 58 s. With efforts ongoing to increase the trap anisotropy, this potential shows promise for research into the static and rapidly rotating 2D systems. In the presence of a single time-averaging field, the shell geometry is transformed into a ring-shaped trap with an adjustable radius. The ring trap can be controllably tilted and progress towards multiply connected condensates is being made. A rotation scheme to spin up atoms in the ring trap has been demonstrated, presenting the opportunity to investigate the dynamics of superflow in degenerate quantum gases.

This thesis is dedicated
in loving memory to
Christopher Dearden Cobbett
and
Hazel Scott Aiton.

Acknowledgments

The completion of this work owes everything to a cast of hundreds that have lent their help and support to me over the years. The limitations of time and space mean that in this section I am only able to explicitly thank a small fraction of you. To those omitted below, I am indebted to you for all that you have done for me.

First and foremost I must thank my supervisor Prof. Chris Foot for giving me the opportunity to come and study atomic physics here in Oxford. His knowledge, imagination and sheer enthusiasm for science proved an inspiration throughout my DPhil. I've been fortunate enough to work alongside some highly talented students whilst undertaking my research, none more so than Marcus Gildemeister. Marcus and I worked together for the majority of our time as DPhil students and I simply could not have asked for a better partner with whom to share the journey. Together we plumbed the very depths of experimental despair and also breathed the rarefied air at the height of a breakthrough. It has been my professional privilege to have him as a colleague and a personal one to call him a friend - From one flying full back to another, thanks mate. Without the calm and methodical approach of Ben Sheard, the problem solving tenacity of Eileen Nugent or the experience and technical know-how of David Crosby the project to build and optimise a new BEC machine would have been nearly insurmountable, and so to you I am particularly thankful.

My time in the Clarendon has been a stimulating, fruitful and overall enjoyable one, and much of the thanks for this go to my fellow lab (and office) mates Sarah Al-Assam, Felix Binder, Hebert Crepaz, Duncan England, Marcin Kubasik, Dave McCabe, Edward Owen, Dimitri Trypogeorgos and Ross Williams. I'd also like to thank the Clarendon technical staff for their never ending patience and creativity in helping to solve the large number of practical problems that arose during the building stage of the project.

They say you never forget a good teacher and during my time as a student of physics I have been fortunate enough to have a number of highly talented and committed mentors, that taught me how to think like a scientist. To Dr. Ifan Hughes and Prof. Charles Adams of the AtMol research group at the University of Durham, and to Mr Alan Rees, Mr Tony Gregory and a number of other similarly outstanding teachers at Queen Elizabeth

Cambria comprehensive school I am hugely grateful for your help.

Outside of physics I have been lucky enough to meet a wonderful group of friends in Oxford that have not only been willing to listen to latest disaster/breakthrough that happened in my research, but to furnish me with a beer whilst doing so. In this I must principally thank Svet Bajlekov, for a better friend, house mate or fellow adventurer I could not have asked for - Thanks for everything mate. I would also like to say thanks to the Austrian pairing of David Loew and Martin Mikalski for their not inconsiderable contribution to the craic, to my other house mates David Lloyd and Patricia Dijkman for their continued commitment to host the best house parties in Jericho, and to all the friends who refused to adhere to the belief that living in Oxford was all about work. From Oxford I would finally like to thank Max Burton and all the lads from Mansfield Road FC who have so graciously accepted my inability to celebrate scoring a goal with anything approaching humility.

I owe an immeasurable debt of gratitude also to my friends from outside of Oxford who have kept me sane and happy during weekend breaks, long holidays and a number of reunions, parties, bar crawls and celebrations that must stretch into the hundreds. Big thanks thus to the London dwelling Hatfielders (Matt, Emma, Sy, Henry, Lucy, Costers, Sam, Si, Cat, Katy, Baz, Rach, Bob and Laura), the Llanllwni Barmy Army (Sian, Tam, George and Rob to name a few) and the bois from Cambria (Jimbo, Lopez, Dyfs, Larry *et al*).

Finally I'd like to thank my family for their steadfast love and support these past 27 years.

Contents

1 Introduction **1**
1.1 Quantum simulators 1

2 Aspects of BEC theory **4**
2.1 Bose-Einstein condensation 4
2.1.1 The non-interacting free Bose gas 5
2.1.2 The non-interacting harmonic oscillator 7
2.1.3 The Gross-Pitaevskii equation 7
2.1.4 The Thomas-Fermi approximation 8
2.2 Superfluidity 9
2.3 Phase transitions in 2D systems 10
2.4 Quantum simulation of fractional quantum Hall states 12

3 Cooling and trapping neutral atoms **16**
3.1 Atom-photon interactions 16
3.2 Radiative forces 17
3.3 Doppler cooling 18
3.4 Sub-Doppler cooling 19
3.5 The magneto-optical trap 21
3.6 Magnetic trapping 25
3.6.1 The quadrupole trap 26
3.6.2 The TOP trap 27
3.7 Evaporative cooling 29
3.7.1 Radio-frequency evaporation 31
3.7.2 TOP trap evaporation 32

4 Atoms in time-dependent magnetic fields **33**
4.1 Time-averaging . . . 33
4.2 Radio-frequency dressing . . . 33
4.2.1 Classical magnetic dipole . . . 34
4.2.2 Semi-classical approximation . . . 35
4.2.3 The perpendicular component . . . 42
4.2.4 Magnetic rf polarisation . . . 45
4.2.5 Linear polarisation . . . 45
4.2.6 Elliptical polarisation . . . 46
4.3 The dressed states . . . 46
4.3.1 The bare states . . . 47
4.3.2 Atom-photon coupling . . . 48
4.3.3 Transitions between rf-dressed states . . . 54
4.4 Time-averaged adiabatic potentials . . . 56

5 The experimental apparatus **58**
5.0.1 Overview . . . 58
5.1 The vacuum system . . . 60
5.2 The laser system . . . 62
5.2.1 The cooling light . . . 62
5.2.2 The repumping laser . . . 66
5.2.3 The tapered amplifier . . . 66
5.2.4 The probe beam . . . 68
5.3 The magneto-optical trap . . . 68
5.4 The magnetic trap . . . 70
5.4.1 The DC coils . . . 72
5.4.2 The AC coils . . . 74
5.5 The imaging system . . . 80
5.6 Computer control . . . 82

6 BEC production **83**
6.0.1 MOT loading and optimisation . . . 83
6.0.2 Magnetic trap loading . . . 84
6.1 Hybrid magnetic transport sequence . . . 86
6.2 Evaporative cooling in the quadrupole trap . . . 89

6.3 Loading the TOP trap . . . 89
6.4 Evaporation in the TOP trap . . . 90
6.5 Imaging the atoms . . . 92
6.6 Observing the BEC phase transition . . . 93

7 The double-well TAAP trap **95**
7.0.1 Thesis nomenclature . . . 96
7.1 Overview . . . 96
7.1.1 Loading the TAAP trap . . . 96
7.1.2 Characterisation . . . 98
7.2 Natural evaporation in the TAAP trap . . . 99
7.3 The horizontal double-well potential . . . 102
7.4 Conclusion . . . 105

8 The rf-dressed shell trap **107**
8.1 Two dimensional systems . . . 108
8.2 Characterising the potential . . . 108
8.2.1 The lifetime of atoms in the shell trap . . . 109
8.2.2 Heating rate . . . 112
8.2.3 Tilting the shell trap . . . 113
8.2.4 RF evaporation in the shell trap . . . 115
8.2.5 Shell trap frequencies . . . 115
8.3 Increasing the shell trap anisotropy . . . 116
8.3.1 The zTOP modified shell trap . . . 118
8.3.2 Increasing the dressing frequency . . . 120
8.3.3 Time-averaging the rf polarisation . . . 120
8.4 Conclusion . . . 121

9 The TAAP ring trap **126**
9.1 Introduction . . . 126
9.2 The ring radius . . . 128
9.3 Ring trap frequencies . . . 130
9.4 Lifetime in the ring trap . . . 130
9.5 Tilting in the ring trap . . . 132
9.6 Rotation in the ring trap . . . 133

9.7 Conclusion 135

10 Conclusions and outlook **139**

10.1 Conclusion 139

10.2 Outlook 140

A Calibration **142**

A.1 The TOP field 142

A.2 The quadrupole gradient 143

A.3 The rf-dressing coils 143

B Evaporation in the shell and TAAP traps **146**

List of Figures

3.1 Light shifts for the magnetic sublevels in the $5^2S_{1/2} \rightarrow 5^2P_{3/2}$ transition in ^{87}Rb for σ^+ and σ_- polarised light, detuned below resonance. 20
3.2 The Sisyphus cooling mechanism. 22
3.3 The principle of operation for a magneto-optical trap in 1D. 24
3.4 Conventional and pyramidal MOT schematics. 25
3.5 Single wire approximations of the magnetic field pattern along the separation axis of a concentric coil pair operating in anti-Helmholtz configuration 27
3.6 Magnetic fields and the origin of the TOP trap. 28
3.7 Magnetic fields in the TOP trap. 29
3.8 The effect of gravity on the TOP trap frequencies. 30

4.1 Classical dipole in the presence of a magnetic field. 35
4.2 The ellipsoidal potential surface resulting from the rf-dressing of a quadrupole magnetic field, around which the resonance condition is satisfied. 41
4.3 Angles within the spherical polar coordinate system defined relative to the Cartesian axes. 43
4.4 The variation of the coupling strength around a cross-section of the resonant ellipsoid for linear polarisation taken in the $y = 0$ plane. 45
4.5 The variation of the coupling strength around a cross-section of the resonant ellipsoid for circular polarisation taken in the $y = 0$ plane. 47
4.6 Bare energy levels for the $F = 1$ hyperfine manifold in a quadrupole magnetic field dressed by a rf field at a frequency ω_{rf}. 48
4.7 Atomic energy level behaviour in the region where the resonance condition is satisfied. 50
4.8 The normalised contributions by the different magnetic substates to the $|+\rangle$ dressed state plotted as a function of the detuning δ. 51

4.9 Energy levels for σ^- (left) and σ^+ (right) polarised rf. 53
4.10 Linearly polarised dressing radiation produces avoided crossings at symmetrical positions in a quadrupole field. 54
4.11 Energy levels in a three state rf-dressed quadrupole field. 55

5.1 Overview of the experimental apparatus 59
5.2 Simplified diagram of the laser system. 60
5.3 Labelled CAD drawing of the vacuum system. 61
5.4 A diode laser aligned on a diffraction grating in Littrow configuration. . . 63
5.5 The hyperfine structure of the D2 line ^{87}Rb 65
5.6 A schematic representation of the optical layout. 67
5.7 A photograph looking down on the fully assembled pyramid mirror, located *in situ* in the MOT chamber. 70
5.8 Schematic diagram of the MOT optics. 71
5.9 Schematic cross section of the DC coil layout around the science cell. . . 73
5.10 Water cooled DC coils in their custom cut Tufnel 10G/40 mounts. 75
5.11 The MOSFET bank circuit diagram. 76
5.12 3D diagram of the science cell and coils involved in generating the TAAP trap. 77
5.13 The main AC coil array. 79
5.14 The horizontal and vertical imaging systems. 81

6.1 The 'quick start' circuit for rapidly changing the current in the *Transport* coils. 85
6.2 View from above of the pyramid mirror located inside the MOT chamber. 87
6.3 Magnetic transfer current ramps in the DC magnet coils. 88
6.4 Changes to the quadrupole gradient and TOP field during the TOP trap evaporation sequence. 91
6.5 Evaporation frequency and TOP trap bottom changes during the TOP trap evaporation sequence. 91
6.6 Images of a cloud of atoms cooled across the BEC phase transition. . . . 94
6.7 Images of the anisotropic expansion of a BEC released from the TOP trap as it falls under time of flight. 94

7.1 The vertically offset double-well TAAP trap. 95

7.2 Energy levels in the TOP trap in the absence and presence of a rf-dressing field. 97
7.3 The TAAP-trap loading scheme. 99
7.4 Changes in phase space density with atom number during natural and rf forced evaporation in the TAAP trap. 101
7.5 Atom number changes over the course of natural and rf evaporation. . . . 101
7.6 Phase space density changes over the course of natural and rf evaporation. 102
7.7 The location of the minimum trapping position in the double well TAAP trap. 103
7.8 Simulated changes to the radial trapping frequency at the position of the lower well in the double-well TAAP trap during natural evaporation. . . 103
7.9 Simulated changes to the axial trapping frequency at the position of the lower well in the double-well TAAP during natural evaporation. 104
7.10 The horizontal double-well TAAP trap. 104
7.11 A BEC being split in the horizontal double-well potential. 105
7.12 Images of a BEC in a tilted horizontal double-well. 106

8.1 Thermal atoms in the rf-dressed shell trap. 107
8.2 Simulations of the shell potential in the $y = 0$ plane. 110
8.3 Comparison between the coupling strength and gravitational potential energy at the South pole of the shell potential. 111
8.4 Lifetime of atoms trapped at the bottom of a shell trap. 111
8.5 Evidence for natural cooling in the shell potential. 113
8.6 Tilting the shell potential using an axial dressing field. 114
8.7 Radial and axial shell trap frequencies at the bottom of the shell trap. . . 117
8.8 Energy scales in the shell trap. 118
8.9 Trap frequency measurements in the modified shell TAAP trap. 119
8.10 Axial and radial trap frequencies at the bottom of the shell trap. 121
8.11 Simulations of z_{rf} time-averaging in the shell potential in the $y = 0$ plane. 122
8.12 Proposed time-averaged dipole potential to increase radial frequencies in the shell trap. 124

9.1 Absorption image of atoms confined in the TAAP ring trap. 126
9.2 Simulations showing the formation of the ring potential in the $y = 0$ plane. 129
9.3 Variation of the ring radius r_0 with the quadrupole gradient B'_{q}. 130

9.4 Ring trap frequency measurements as a function of the modulation depth γ. 131
9.5 Ring trap lifetime for increasing values of the quadrupole field gradient B'_{q}. 132
9.6 Ring trap lifetimes for increasing value of the modulation depth γ. 133
9.7 Images of a BEC in a tilted ring trap. 134
9.8 The ring trap rotation scheme in the $z = 0$ plane. 135
9.9 Evidence for rotation in the ring potential. 136
9.10 The persistence of rotation in the ring trap. 137

A.1 TOP field calibration data 143
A.2 Radio-frequency dressing coil calibration data. 145

B.1 Spatial variation of the atom's quantisation axis around the resonant ellipsoid in the $y = 0$ plane. 147
B.2 Evaporation in the shell and vertical double-well TAAP traps. 148

Chapter 1

Introduction

In his Nobel lecture of 1913, the grandfather of low temperature physics Heike Kamerlingh Onnes spoke of his continued desire to work [1]

> *"...towards lifting the veil which thermal motion at normal temperatures spreads over the inner world of atoms and electrons."*

Almost a century after the recognition of his pioneering work with liquid helium, the Nobel committee has seen fit to award (either fully or partially) a further 10 prizes to experimental and theoretical investigations of phenomena arising from or relating to aspects of low temperature physics.[1] The proposals for laser cooling of trapped gases [2, 3] heralded a new era of ultra-low temperature physics where atomic physicists exploited the suppressed thermal effects to study their systems with unprecedented precision. Early optical cooling techniques gave the first glimpses of matter cooled to the μK regime [4]. The nK temperatures brought about by evaporative cooling in conservative potentials gave systems which were dominated by quantum statistics rather than thermal effects [5]. The latest cooling techniques published this year [6] have achieved temperatures in the pK range where it is anticipated that exotic states of matter such as correlated magnetic quantum phases will exist for atoms in optical lattices. The journey towards ever lower temperatures is punctuated by seminal advances in experimental and theoretical physics. In this field of vanishingly low temperatures it still appears true that less is more.

1.1 Quantum simulators

Much of the work presented in this thesis involves the realisation and characterisation of non-trivial trapping geometries for ultracold atoms. It is far from an unreasonable

[1] 1962, 1972, 1975, 1978, 1987, 1996, 1997, 1998, 2001 and 2003.

question to ask in general why this is important. The principle argument presented here begins with the idea that simulating large quantum systems using classical systems is an exponentially difficult thing to do. These sentiments are encapsulated in the following quote from the visionary physicist Richard Feynman [7],

> *"...nature isn't classical, dammit, and if you want to make a simulation of nature, you'd better make it quantum mechanical, and by golly it's a wonderful problem, because it doesn't look so easy."*

Feynman's argument is that the best tool to simulate a quantum system of interest is another quantum system. This concept was extended by David Deutsch who showed that in principle a single quantum system could be used to simulate all others. Deutsch named this single system a 'universal quantum computer'. Despite considerable efforts being made with a number of promising technologies, the technical advances needed for the realisation of a scalable quantum computer remain beyond current experimental reach. A less general but also less demanding form of quantum simulation is the engineering of bespoke Hamiltonians to allow a simple, well understood quantum system to emulate the behaviour of a more complex one.

The tuneability of both the interaction strength (via a Feshbach resonance [8]) and the confinement of ultracold quantum gases makes them attractive candidates for building quantum simulators. The atoms in such gases are typically weakly interacting and are generally well described by a mean-field approximation, however under particular circumstances the atoms can be placed in strongly correlated states. A striking example is given by a harmonically trapped Bose-Einstein condensate loaded into an optical lattice to realise the Bose-Hubbard model for bosonic particles moving in a periodic crystal lattice structure. By increasing the lattice depth, number fluctuations at each lattice site are suppressed as the gas undergoes the celebrated superfluid to Mott-insulator quantum phase transition [9]. Despite the charge neutrality of ultracold atoms, they can also be used to simulate the behaviour of charged particles in magnetic fields by using for example rotation [10] or a spatially dependent Raman coupling scheme [11].

The structure of this thesis is as follows. A brief discussion on some of the theoretical concepts that underlie this experiment and its research goals is presented in chapter 2. In chapter 3 a review of the processes that facilitate the cooling and trapping of neutral atoms is given. Much of the success of this experiment hinges on the understanding of how atoms interact with time-dependent magnetic fields, and so the theory associated with the key processes of time-averaging and rf-dressing is recounted in chapter 4. The following two chapters describe the experimental apparatus and how it is used to produce and image Bose-Einstein condensates of ^{87}Rb in a time-averaged orbiting potential (TOP) trap. Chapter 7 describes some new experimental results from the double-well time-averaged adiabatic potential (TAAP) trap, the explanation for which is qualitatively supported by a simple numerical analysis. Chapters 8 and 9 describe the characterisation of the rf-dressed shell and TAAP ring traps respectively. Each experimental chapter concludes with a discussion of future goals for each trap. The final

chapter of this thesis briefly summarises the experimental work performed to date and outlines some possible avenues for future investigation.

Chapter 2

Aspects of BEC theory

2.1 Bose-Einstein condensation

Quantum mechanics stipulates that all particles of the same species are indistinguishable [12]. Of all the maxims of quantum mechanics, the seemingly intuitive indistinguishable nature of particles would appear to be a harmless symptom of the quantum condition. However, it was to have far reaching consequences.

In the formalism of quantum mechanics, particle indistinguishability requires that all physical observables must be invariant under the exchange of particle labels. Thus for two identical particles at positions r_1 and r_2 with spin states α and β the total wavefunction of the system must satisfy the following equality,

$$|\Psi(\boldsymbol{r}_1, \alpha, \boldsymbol{r}_2, \beta)|^2 = |\Psi(\boldsymbol{r}_2, \beta, \boldsymbol{r}_1, \alpha)|^2 \tag{2.1}$$

and so,

$$\Psi(\boldsymbol{r}_1, \alpha, \boldsymbol{r}_2, \beta) = \pm\Psi(\boldsymbol{r}_2, \beta, \boldsymbol{r}_1, \alpha). \tag{2.2}$$

This implies that particle wavefunctions can be categorised into forms that are either symmetric, or antisymmetric with respect to label exchange. Particles with symmetric wavefunctions are known as bosons. Bosons have integer-spin, common examples of true bosons are photons and phonons. Their counting statistics give bosons a gregarious nature that results in the probability of finding a boson in a state containing N bosons being enhanced by a factor $(1+N)$. Fermions, such as nucleons and electrons have anti-symmetric wavefunctions and half integer spin. The fermionic attitude to association with other fermions differs markedly from their neighbourly integer-spin cousins. The anti-symmetric nature of the fermionic wavefunction causes it to vanish at the point where two identical fermions coincide. This is a statement of the famous Pauli exclusion principle that provided a physical justification for much of the early quantum theory of

atomic structure.

In a room temperature atomic ensemble, the typical inter-particle separation is significantly larger than the extent of a particle wavefunction (parameterised by the thermal de Broglie wavelength λ_{dB}). In this regime the indistinguishability of particles is not important since the mean occupation of each quantum state is $\ll 1$. The behaviour of a room temperature ensemble is thus well described by classical Boltzmann statistics that do not require particle indistinguishability. At very low temperatures, the inter-particle separation and λ_{dB} become comparable, allowing significant wavefunction overlap between neighbouring particles giving rise to non-classical phenomena that are require a quantum mechanical explanation. As the mean occupation of a quantum state approaches unity, effects of indistinguishabilty cause the behaviour of an atomic ensemble to diverge from the predictions of Boltzmann statistics. For fermions, the Fermi-Dirac distribution describes the unity filling of energy levels up to the vicinity of the Fermi energy. In bosonic systems, the Bose-Einstein distribution quantifies the increase in probability of finding more than one particle in a given quantum state.

2.1.1 The non-interacting free Bose gas

The total energy for an ensemble of particles obeying Bose-Einstein statistics can, for sufficiently low temperature, have a minimum when the majority of the atomic population exists in the ground state. With vanishingly small populations in the quantised excited states, the system undergoes a phase transition to become a Bose-Einstein condensate (BEC). This phase transition is unique as it does not require interactions between the particles, the quantum statistics of the system will mediate the phase change. The condition that must be satisfied for condensation to occur is that the mean number of particles within the same unit volume of phase space (i.e. the phase space density) must be of order 1. More strictly,

$$n\lambda_{\mathrm{dB}}^3 \geq 2.612 \tag{2.3}$$

where n is the number density of particles per unit volume. To see how this process comes about, consider a large volume V filled with N non-interacting, identical bosons of mass m. The Bose-Einstein distribution quantifies the mean occupation of the single particle state with eigenenergy E_i, for a system in thermal equilibrium at a temperature T

$$n_i(E_i, T) = \frac{1}{e^{(E_i-\mu)/k_{\mathrm{B}}T} - 1}. \tag{2.4}$$

Here μ, the chemical potential is determined by the requirement that the sum of all the occupancies in the system equal the total particle number,

$$\sum_i n_i = N. \tag{2.5}$$

To evaluate this sum we must know the number of states in a given energy interval, and then count all the particles in the all states as $E \to \infty$. Provided N is sufficiently large, energy can be considered as a continuous variable [13] which gives the density of states for an unconfined gas as [14]

$$g(E) = \frac{Vm^{3/2}}{2^{1/2}\pi^2\hbar^3}E^{1/2}. \tag{2.6}$$

The sum in eqn. 2.5 can now be replaced by the integral

$$\begin{aligned} N &= \int_0^\infty n(E,T)g(E)dE & (2.7)\\ &= N_0 + \int_0^\infty \frac{g(E)}{e^{(E_i-\mu)/k_\mathrm{B}T}-1}dE & (2.8)\\ &= N_0 + N_\mathrm{ex} & (2.9) \end{aligned}$$

where N_0 is the population of the ground state which must be explicitly included since this method does not count these atoms correctly (c.f. eqn. 2.6 when $E = 0$). The integral in eqn. 2.8 therefore represents the total population of all the excited states of the system. By evaluating this integral at a sufficiently low temperature such that $\mu = 0$, and setting $N_0 = 0$ the lowest temperature at which all atoms can exist outside of the ground state of the system can be found

$$\begin{aligned} N &= \int_0^\infty \frac{g(E)}{e^{E/(k_\mathrm{B}T_\mathrm{c})}}dE & (2.10)\\ N &= \frac{V}{4\pi^2}\frac{2mk_\mathrm{B}T}{\hbar}^{3/2}\Gamma\left(\frac{3}{2}\right)\zeta\left(\frac{3}{2}\right) & (2.11)\\ T_\mathrm{c} &= \frac{2\pi\hbar^2}{mk_\mathrm{B}}\left(\frac{N}{2.612V}\right)^{2/3}. & (2.12) \end{aligned}$$

At temperatures below this, the atomic population rapidly congregates in the ground state, forming a macroscopic occupation of a single quantum state, i.e. a BEC. T_c is therefore known as the critical temperature for Bose-Einstein condensation.[1]

The condensate fraction is the proportion of atoms in the condensed state N_0, compared to those in the excited states N_ex. This can be conveniently written by substituting

[1] In arriving at this expression for the critical temperature, the standard result for the integral

$$\int_0^\infty \frac{x^{1/2}}{e^x-1}dx = \Gamma\left(\frac{3}{2}\right)\zeta\left(\frac{3}{2}\right) = \sqrt{\frac{\pi}{4}}(2.612)$$

is quoted [15].

the expression for the critical temperature back into eqn. 2.8 and rearranging to give,

$$\frac{N_0}{N_{\rm ex}} = 1 - \left(\frac{T}{T_{\rm c}}\right)^{3/2}. \tag{2.13}$$

2.1.2 The non-interacting harmonic oscillator

The formation of a condensate in a dilute atomic vapour requires a confining potential to create suitable conditions and time for the cooling processes to work. The presence of an external potential affects the distribution of quantised energy states and thus the density of states. Consider a general 3D harmonic trapping potential, with independent trap frequencies $\omega_x, \omega_y, \omega_z$

$$V(\boldsymbol{r}) = \frac{1}{2}m\left(\omega_x x^2 + \omega_y y^2 + \omega_z z^2\right). \tag{2.14}$$

For such a potential, the density of states becomes

$$g(E) = \frac{E^2}{2\left(\hbar\bar{\omega}\right)^3}, \tag{2.15}$$

where $\bar{\omega} = \sqrt[3]{\omega_x\omega_y\omega_z}$ is the geometric mean of the trap frequencies. Following a similar analysis to the previous section the critical temperature and the condensate fraction can be written as,

$$T_{\rm c} = 0.941\frac{\hbar\bar{\omega}N^{1/3}}{k_{\rm B}}, \tag{2.16}$$

$$\frac{N_0}{N} = 1 - \left(\frac{T}{T_{\rm c}}\right)^3. \tag{2.17}$$

In the experiments presented in this thesis, typical ^{87}Rb number densities of $10^{14}\,\mathrm{cm}^{-3}$ give critical temperatures of $\sim 100\,\mathrm{nK}$.

2.1.3 The Gross-Pitaevskii equation

The energy scales of the ultracold collisions are sufficiently low that the generally complicated dependence on interparticle separation may be replaced with an effective mean field interaction that is characterised by a single parameter $a_{\rm s}$, the s-wave scattering length. The interaction between two atoms is therefore approximated by a contact potential $V(\boldsymbol{r}_i - \boldsymbol{r}_j) = g\delta(\boldsymbol{r}_i - \boldsymbol{r}_j)$, where the coupling constant $g = 4\pi\hbar^2 a_{\rm s}/m$. Including

this term in the total Hamiltonian for the system gives,

$$H = \sum_{i=1}^{N} \left(\frac{p_i^2}{2m} + V(\boldsymbol{r}_i) \right) + g \sum_{i<j} \delta(\boldsymbol{r}_i - \boldsymbol{r}_j). \tag{2.18}$$

In the limit of weak interactions, the wavefunction of the N-body system Ψ_N is just the product of N single particle wavefunctions $\phi_a(\boldsymbol{r}_i)$. Following this approach, the wavefunction for a fully condensed bosonic system is,

$$\Psi_N(\boldsymbol{r}_1, \boldsymbol{r}_2, ...\boldsymbol{r}_N) = \prod_{i=1}^{N} \phi_0(\boldsymbol{r}_i) \tag{2.19}$$

where $\phi_0(\boldsymbol{r}_i)$ is the normalised, macroscopically occupied single particle state. At this juncture it is useful to introduce the concept of a condensate wavefunction $\psi(r)$ that describes the global condensed state

$$\psi(\boldsymbol{r}) = \sqrt{N}\phi(\boldsymbol{r}), \tag{2.20}$$

with number density $n(\boldsymbol{r}) = |\psi(\boldsymbol{r})|^2$. By operating on $\psi(\boldsymbol{r})$ using the Hamiltonian from eqn. 2.18 and minimising the total energy, one arrives at the time-independent Gross-Pitaevskii equation (GPE) for the ground state of a trapped condensate

$$-\frac{\hbar^2}{2m}\nabla^2\psi(\boldsymbol{r}) + V(\boldsymbol{r})\psi(\boldsymbol{r}) + g|\psi(\boldsymbol{r})|^2\psi(\boldsymbol{r}) = \mu\psi(\boldsymbol{r}). \tag{2.21}$$

In the absence of interactions the GPE reduces to the single particle Hamiltonian for harmonic confinement. For a 3D isotropic potential with trap frequency $\bar{\omega}$ the ground state solutions to this equation are Gaussian wavefunctions characterised by the harmonic oscillator length $a_{\text{ho}} = \sqrt{\hbar/(m\bar{\omega})}$. The effect on these solutions of including repulsive interactions is to increase the radius and lower the central value of the wavefunction [16].

2.1.4 The Thomas-Fermi approximation

The contribution to the ground state energy term as a result of interactions depends linearly on N. When N is sufficiently large or similarly temperatures are sufficiently low, the interaction energy of the atoms dominates the kinetic energy term, which under the Thomas-Fermi approximation may be neglected. Removing the kinetic energy term from eqn. 2.21 gives

$$\left[V(\boldsymbol{r}) + gn(\boldsymbol{r})\right]\psi(\boldsymbol{r}) = \mu\psi(\boldsymbol{r}). \tag{2.22}$$

Rearranging this equation for the condensate density, it is apparent that the condensate maps the shape of the trapping potential up to an energy equal to the chemical potential

$$n(\boldsymbol{r}) = \frac{\mu - V(\boldsymbol{r})}{g}. \tag{2.23}$$

Thus for harmonic confinement, the condensate density distribution takes on the shape of an inverted parabola

$$n(\boldsymbol{r}) = n(0)\left(1 - \frac{x^2}{R_x^2} - \frac{y^2}{R_y^2} - \frac{z^2}{R_z^2}\right), \tag{2.24}$$

where $n(0) = N\mu/g$ is the central density. The characteristic lengths $R_{x,y,z}$ are defined by the chemical potential,

$$\frac{1}{2}m\omega_{x,y,z}^2 R_{x,y,z}^2 = \mu \tag{2.25}$$

Finally, in this regime the chemical potential may be found from the normalisation of the condensate wavefunction [17] which ultimately gives

$$\mu = \frac{\hbar\bar{\omega}}{2}\left(\frac{15Na_\mathrm{s}}{a_\mathrm{ho}}\right)^{2/5}. \tag{2.26}$$

2.2 Superfluidity

The term superfluidity refers to a complex of phenomena that were first observed in liquid helium cooled below a critical temperature of 2.18 mK.[2] The unusual transport properties of this liquid gives rise to the dramatic signatures of superfluidity such as frictionless flow through narrow channels [18], infinite thermal conductivity [19], the nucleation of quantised vortices under rotation [20] and the metastability of ring currents [21]. More subtle effects such as a non-classical moment of inertia (the Hess-Fairbank effect) [22] have also been observed.

The first theoretical explanation for superfluidity to receive widespread support invoked a phenomenological, hydrodynamic approach. The two-fluid model developed by Tisza [23] and Landau [24] used the assumption that liquid helium consists of two miscible components, a quantum[3] superfluid part that carries no entropy and has an irrotational velocity field, and a normal liquid phase. The contemporary view on superfluidity associates the quantum liquid with a form of BEC and the normal phase with a series of elementary excitations [25].[4]

[2] This phase of helium is commonly referred to as He II.

[3] A quantum liquid has a mean interparticle separation that is less than the de Broglie wavelength λ_dB.

[4] The link between superfluidity and BEC was first proposed by London in 1938 [26], however the connection is a complex one and so the development of a comprehensive, microscopic theory took time.

A full discussion of the theoretical concepts mentioned above is beyond the scope of this thesis, however the following simple analysis is used to demonstrate the origin of the irrotational flow pattern which underlies many of the observed superfluid phenomena. Echoing the approach to modelling a BEC, the superfluid is assigned a macroscopic wavefunction[5]

$$\psi_0(\boldsymbol{r}) = \sqrt{n(\boldsymbol{r})}e^{i\theta(\boldsymbol{r})}, \tag{2.27}$$

where $n(\boldsymbol{r})$ is the condensate number density. From the continuity equation this wavefunction has a current density j_s of,

$$\boldsymbol{j}_\mathrm{s} = \frac{\hbar}{m} n \nabla\theta$$

which implies the superfluid velocity is proportional to the gradient of the phase,

$$\boldsymbol{v}_\mathrm{s} = \frac{\hbar}{m}\nabla\theta. \tag{2.28}$$

By taking the curl of this quantity it is apparent that superflow is irrotational,

$$\nabla \times \boldsymbol{v}_\mathrm{s} = 0. \tag{2.29}$$

The requirement for the wavefunction to be single valued means that around a closed loop the superfluid phase must change by an integer multiple of 2π. Thus the circulation around a closed path is given by,

$$\oint \boldsymbol{v}_\mathrm{s} \cdot d\boldsymbol{l} = \frac{\hbar}{m} 2\pi l = \frac{h}{m} l \tag{2.30}$$

which implies the circulation of a superfluid is quantised by the integer l in units of h/m. The flow pattern for $l \neq 0$ is that of a vortex line, where the condensate density tends to zero at the centre of the vortex. Quantised vortices [27] are just one of the hallmarks of superfluidity that have been observed in dilute atomic vapours BECs [28, 29, 30].

2.3 Phase transitions in 2D systems

The order that characterises all states of matter is profoundly related to the dimensionality of the system under consideration [31]. Theoretical investigations in the 1960's suggested the absence of magnetic ordering in uniform two-dimensional (2D) systems at finite temperatures [32]. This work was extended to imply that any long-range order in these systems would be destroyed at non-zero temperature by thermal fluctuations

[5]For dilute atomic gases this is straightforward, however for liquid helium the strong interactions between particles cause significant quantum depletion from the single particle ground state. Nevertheless this approach produces some qualitatively useful results.

[33]. There is however a phase transition in uniform 2D systems that leads to quasi-long-range order via a novel mechanism. The theoretical basis underlying the 2D phase transition was published by Berezinskii [34], and Kosterlitz and Thouless [35], and in recognition of this it is commonly referred to as the BKT phase transition. The BKT mechanism involves the establishing of a topological order via the pairing of vortices with opposite circulation. Vortices are topological defects that act as a source of phase fluctuations that destroy the coherence of the system. Below a critical temperature transition temperature T_{BKT}, the vortices and anti-vortices form bound pairs, with zero net circulation. As the temperature of the system increases so does the pair size until at the transition temperature the pairs unbind and create a plasma of free vortices that destroys the quasi-long-range order of the system.

In pure 2D systems the BKT phase transition occurs suddenly, precisely coinciding with the onset of superfluidity in these systems. BKT type transitions have been observed in the macroscopic properties of a diverse range of 2D systems from superfluidity in cryogenically cooled thin films of liquid helium [36] to superconductivity in arrays of Josephson junctions [37]. However, in these systems no measurements could be made of the vortex pairing mechanism that expedites formation of topological order.

Trapped ultracold gases present a promising opportunity to investigate the microscopic process behind the BKT mechanism. The temperature, density and dimensionality of ultracold samples can be finely controlled and the presence of phase defects such as vortices can be measured directly. In dilute vapour atomic gases, a quantum degenerate system is considered 2D if the confinement along one axis is sufficiently tight to make the healing length shorter than the Thomas-Fermi radius in this direction. As a result this gas is kinematically two dimensional, with excitation in the tight direction being energetically 'frozen out'. This regime is reached when the 3D chemical potential $\mu < \hbar\omega_z$ where ω_z represents trap frequency in the tight trapping direction.

The behaviour of 2D ultracold gases is enriched by the presence of interactions and also the trapping potential. Bagnato and Kleppner [38] noted that the effect of harmonic confinement on the density of states was to allow for the presence of a BEC in a 2D trapped system. The finite nature of trapped atomic gases blunts the sharpness of the BKT phase transition, introducing an intermediate phase of matter that precipitates full Bose-Einstein condensation where the sample in neither thermal nor fully phase coherent [39]. The so called quasicondensate state is characterised by a phase coherence length that is longer than the healing length but shorter than the dimensions of the system. A quasicondensate can be visualised as consisting of pockets of phase coherence where a true condensate exists, but with no phase correlation between neighbouring pockets [40]. During the quasicondensate phase, the superfluid fraction is predicted to grow gradually, with the transition being observed first at the trap centre where the density is highest [41].

The role of vortex pairing in the BKT phase transition was investigated in a beautiful experiment performed in Paris where matter-wave heterodyning was used to infer the presence of a free vortex [42]. An experiment performed in NIST [43] claimed to have

observed a weakly interacting 2D gas phase that they called a 'non-superfluid quasi-condensate'. By cooling the sample further a sharp transition to a superfluid state was observed. However, the time of flight detection scheme employed in this work has failed to convince the wider community that definitive evidence has been found. In JILA, a BEC divided into a 2D array of Josephson junctions was used to look at vortex proliferation in the regime of the BKT transition. This experiment was able to make some quantitative measurements of vortex anti-vortex pair size as the temperature of the gas was changed [44]. The same group performed another experiment in 2010 which used measurements of the compressibility of a 2D gas above T_{BKT} as evidence for non-mean field physics occurring before the transition to a superfluid [45].

2.4 Quantum simulation of fractional quantum Hall states

The quantum Hall effect is a widely studied process in the field of condensed matter physics. A complete discussion of the theoretical background to this phenomena is beyond the scope of this work, however in order to motivate some of the long term goals of this experiment a brief overview is presented (for a more complete review of the topic with specific reference to the relevance for ultracold matter systems see [46, 47]).

The Hall resistance R_{H} of a 2D electron gas in a magnetic field is quantised in units of h/e^2. This effect was first observed by Klaus von Klitzing in 1980 [48] by placing an electron gas confined in the inversion layer of a metal-oxide-semiconductor field-effect transistor (MOSFET) in a strong magnetic field of order 15 T. In this experiment the measured R_{H} changed in a stepwise fashion with increasing magnetic field strength, with its value at each plateau equalling an integer multiple of h/e^2. By using higher mobility samples, Tsui and Störmer observed fractional quantisation of the Hall resistance [49]. Both of these landmark observations were recognised with the Nobel prize in physics (in 1985 and 1998 respectively).

The integer quantum Hall effect is explained in terms of single particle effects driven by the Pauli exclusion principle. The exactness of the quantisation (a few parts in a billion) has led to this method being adopted to define the global resistance standard. The fractional quantum Hall effect (FQHE) is an example of an emergent phenomenon where the behaviour of the system diverges from the mean-field approximation and instead must be described as a collective effect arising from the strong correlations between the constituent particles. Both integer and fractional quantum Hall states can be characterised by the filling factor ν which equals the ratio of the number of particles to the number of vortices. In the integer effect this number takes integer values, whereas FQH states are labelled with fractional values of ν. The explanation for the FQHE provided by Laughlin [50] opened a new paradigm in condensed matter physics and

earned its creator a share of the 1998 Nobel prize. Laughlin's famous wavefunction,

$$\Psi_{\mathrm{m}}(\boldsymbol{z}_1,\ldots,\boldsymbol{z}_N)=\prod_{j\langle k\rangle}^{N}(\boldsymbol{z}_j-\boldsymbol{z}_k)^m\exp\left[-\frac{1}{4l^2}\sum_{j}^{N}|\boldsymbol{z}_j|^2\right] \tag{2.31}$$

accurately described the ground state for the first experimentally achieved quantum Hall system where $\nu = 1/3$ (i.e. when $m = 3$ in the above equation). More generally, this wavefunction can be used to describe FQH states occurring in fermionic (where m is an odd integer) and bosonic systems (where m is an even integer). Whilst a full discussion of this wavefunction is not presented here, it is worth noting that Ψ_{m} quickly vanishes when any two particles closely approach one another (i.e. when $\boldsymbol{z}_j \to \boldsymbol{z}_k$). This implies a strong anti-correlation between particles in FQH systems. This property will form a key diagnostic for future experiments using ultracold atoms to simulate these systems.

The interest surrounding the FQHE can be understood in terms of the properties of the quasiparticles that are invoked by Laughlin to describe these systems. Adopting this approach, there now follows a heuristic description of the origin and properties of these quasiparticles. The vortices that form under the application of a strong perpendicular magnetic field to a 2D electron gas attach to the electrons creating new composite particles. The vortices can be naively thought of as concentrated regions of the absence of electric charge. As they attach to individual electrons, the vortices act to screen the bare electrons from their neighbours, lowering the Coulombic repulsion energy of the system. This shielding effect actually results in the composite particles having only weak interactions, transforming the system from a complex many-body problem of simple particles, into a single particle problem of complex composite particles [51]. The shielding is also responsible for the remarkable property of quasiparticles with fractional charges. In a $\nu = 1/3$ system, when the magnetic field is slightly increased, the few additional vortices that are created cannot attach to the any of the electrons as this would break the symmetry of the system. These vortices represent holes in the composite particle background, and so act like quasiparticles possessing fractional (in this case $e/3$) electronic charge [52].[6] Certain non-Abelian FQH states possess an intrinsic robustness against decoherence and yet via a process called 'braiding' (dragging quasiparticles around each other) allow unitary operations to be performed with arbitrary accuracy [56]. Because of these highly attractive properties, the quasiparticles arising from the FQHE are proposed as a candidate for the realisation of a topological quantum computer [57, 58].

The connection between the FQHE in 2D electron gases placed in intense magnetic fields and systems of rapidly rotating ultracold atoms was first published in 1998 [59]. The basis for this link is the mathematical similarity between the Lorentz force on a moving electron in a magnetic field ($-e\boldsymbol{v}\times\boldsymbol{B}$) and the Coriolis force in a rotating frame ($-2m\boldsymbol{\Omega}_{\mathrm{rot}}\times\boldsymbol{v}$). The single particle Hamiltonian for a neutral atom of mass m in a

[6] The revolutionary idea of dividing up the fundamental unit of electronic charge was confirmed by three experiments performed in the mid 90's [53, 54, 55].

harmonic potential is modified in a frame rotating at angular velocity $\mathbf{\Omega}_{\rm rot}$,

$$\begin{aligned} H_{\rm rot} &= H_0 - \mathbf{\Omega}_{\rm rot} \cdot \boldsymbol{L} \\ &= \frac{1}{2m}\left(\boldsymbol{p} - m\mathbf{\Omega}_{\rm rot} \times \boldsymbol{r}\right)^2 + \frac{1}{2}m\left(\omega_r^2 - \mathbf{\Omega}_{\rm rot}^2\right)\left(x^2 + y^2\right) + \frac{1}{2}m\omega_z^2 z^2 \end{aligned}$$

where ω_r and ω_z are the angular oscillation frequencies of the atoms in the radial and axial directions respectively. The centrifugal force works against the trapping in the plane of rotation, such that as $|\mathbf{\Omega}_{\rm rot}|$ approaches ω_r, the confinement in the radial plane tends to zero, causing the condensate to expand and become essentially 2D.[7] In this instance the Hamiltonian takes on the form of an electron in a magnetic field [60],

$$H = \frac{1}{2m}\left(\boldsymbol{p} + \frac{e}{2}\boldsymbol{B} \times \boldsymbol{r}\right)^2. \tag{2.32}$$

where the applied rotation rate simulates the action of a the magnetic field on a charged particle

$$eB = 2m\Omega_{\rm rot}. \tag{2.33}$$

This 2D system can now be understood in terms of Landau levels which originally were used to describe the quantised orbits of charged particles in magnetic fields. The Landau levels in the case of rotating atoms are discrete angular momentum states. An applied rotation breaks the symmetry between angular momentum states with opposite handedness, reducing (increasing) the energy of the co-rotating (counter-rotating) states. As $|\mathbf{\Omega}_{\rm rot}| \to \omega_r$ the states form highly degenerate Landau levels where the separation between levels equals $2\hbar\omega_r$ [61]. Atoms are confined to the lowest Landau level (LLL) when the chemical potential μ of the condensate falls below the separation between Landau levels. Very close to the brink of instability the system departs from the mean-field LLL regime and enters a strongly correlated state where bosonic versions of the Laughlin wavefunction are predicted to appear [62]. This transition is predicted to occur when the number of vortices becomes similar to the atom number, a regime which can be written as

$$\frac{\omega_r - \Omega_{\rm rot}}{\omega_r} < \frac{8a}{Nl_z}, \tag{2.34}$$

where a is the s-wave scattering length, N is the number of atoms in the system, and l_z is the harmonic oscillator length in the frozen-out axial direction [63]. The exacting nature of this condition can be seen by entering some experimental values attained with the current apparatus. For the maximum axial trapping frequency measured on this experiment $\omega_z = 2\pi \times 350\,\text{Hz}$ (see section 8.3.3), even with only 70 atoms in the

[7] Of course in the limiting case where $\Omega_{\rm rot} = \omega_r$ in a purely harmonic trap, the atoms would rapidly leave the trap. In a trap with additional higher order confinement, such as the quartic confinement of the shell trap the atoms can still be trapped at the regions where the higher order confinement dominates the harmonic component.

cloud, the cloud rotation would still have to be within 0.1 % of the radial frequency.[8] In standard magnetic traps the best experiments have fallen several orders of magnitude short of satisfying the criterion in relation 2.34. Researchers in JILA led by Eric Cornell pioneered evaporative spin-up techniques [64] to push a cloud of 5×10^4 atoms in a weak TOP trap up to $\Omega_{\text{rot}} = 0.993\omega_r$ and so into the LLL [65]. Due to the 'large' number of atoms necessary for reliable imaging in their system, the lowest filling factor achieved was $\nu \geq 500$. For a number of years this set of experiments represented the closest attempt at reaching the FQH regime.

In 2010 new results were circulated in a pre-print from an experiment in Stanford performed by Gemelke and Chu [66]. This experiment used a 3D optical lattice where the phases of the lattice beams were modulated in such a way as to rotate the individual lattice sites. The experiment thus consisted of a large number of independent, rotating few-body systems. The combination of extremely tight confinement ($\omega_r = 2\pi \times 2.1\,\text{kHz}$, $\omega_z = 2\pi \times 28\,\text{kHz}$) and the small number of atoms at each lattice site allowed the researchers to observe a dip in the rate of atom loss via photoassociation as the system was brought into the FQH regime. This dip was used to infer the anti-correlations between atoms at each lattice site.[9]

It is also worth noting that rotation is not the only way to simulate the action of a magnetic field. In 2010 a synthetic magnetic field for ultracold atoms was created using light-induced gauge potentials [11]. This approach uses optical coupling between internal states of the atoms to realise a Hamiltonian with a spatially dependent vector potential.[10] The great advantage of this technique is that it can simulate large magnetic fields whilst avoiding the technical difficulties inherent in rapidly rotating systems. The addition of a 1D lattice to this experiment is expected to give an opportunity to access the FQH regime.

[8] Precisely controlling the rotation rate is not the only formidable technical challenge. The trap used for these experiments must also be highly symmetric in the plane of rotation to avoid the rotation rate exceeding the trap frequency along a single axis.

[9] Despite these intriguing results, to date the paper remains to be published.

[10] By changing the configuration of the experiment to give a spatial uniform, time-dependent vector potential a synthetic electric field was realised [67].

Chapter 3

Cooling and trapping neutral atoms

3.1 Atom-photon interactions

Electromagnetic fields may be used to control both internal (e.g. electronic configuration, spin polarisation) and external (e.g. position, momentum) degrees of freedom in an atom. A photon with an energy comparable to the interval between atomic energy levels may be absorbed by an atom causing it to enter an energetically excited state. The process of stimulated emission occurs when an atom emits a photon into a mode determined by the surrounding light field. The atom may also spontaneously emit a photon in a random direction by coupling to fluctuations in the vacuum field.

Despite this phenomenological description of atomic population dynamics in terms of photons, much of the underlying physics of atom-photon interactions may be elucidated by using a semi-classical approximation. In this approach the atom is modelled as a quantised two-level system interacting with a classical time-dependent perturbation. The dynamics of the system are found by studying the evolution of the Schrödinger equation,

$$i\hbar\frac{\partial\Psi}{\partial t} = H\Psi. \tag{3.1}$$

where H the Hamiltonian is decomposed into a time-independent part H_0 and a time-dependent perturbation H'.

The interaction between the oscillating electric field and the induced dipole moment of the atom, gives a perturbation

$$H' = -e\mathbf{r}\cdot\mathbf{E}_0\cos(\omega t), \tag{3.2}$$

where e is the electron charge, $\mathbf{r}$ is the displacement of the electron from the atom's centre of mass and $\mathbf{E}_0$ is the amplitude of the electric field oscillating at a frequency ω.

The dipole interaction couples the energy levels and (in the absence of any spontaneous processes) causes the energy level populations to oscillate at the Rabi frequency, defined as [68]

$$\Omega = \frac{\langle g|e\mathbf{r}\cdot\mathbf{E}_0|e\rangle}{\hbar}. \tag{3.3}$$

The frequency of Rabi oscillations therefore depend on the intensity (since $I \propto \mathbf{E}^2$) of the incident light field.[1]

Spontaneous emission, which occurs at a rate independent of the driving radiation, interrupts cycles of Rabi oscillations causing the atom to return to its ground state after a time τ known as the natural lifetime of the excited state. Hence at low incident intensities spontaneous emission determines the time-averaged population of the excited state. At high intensities, stimulated processes dominate. The saturation intensity,

$$I_{\text{sat}} = \frac{\pi}{3}\frac{hc}{\lambda^3\tau} \tag{3.4}$$

marks the crossover between these two regimes where $\Omega \sim 1/\tau$.

3.2 Radiative forces

The mechanical effects of light were invoked by Johannes Kepler in his treatise *De Cometis* (1619) as an explanation for the orientation of comet tails with respect to the sun. Such effects were quantified by James Clerk Maxwell in his celebrated treatise on electromagnetism and observed in the laboratory by pioneering experiments at the turn of the twentieth century [69, 70, 71].

Radiative forces can be broadly categorised into two types; dissipative and dispersive forces. Dispersive forces arise because population transfer is not the only result of the interaction between electric field and the induced dipole moment. Light shift is the name given to the effect of the apparent energy of each quantised level being shifted as a result of this interaction. The energy change of the levels is given by

$$\Delta_{\text{light}} = \frac{\hbar\Omega^2}{4\delta}, \tag{3.5}$$

where $\delta = (\omega - \omega_0)$ is the angular frequency detuning of the light from the atomic resonance ω_0. Here it is assumed that $|\delta| \gg \Gamma$, where Γ is the radiative linewidth of the excited state.[2] Thus the magnitude of the light shift is proportional to the square of the electric field, causing the spatial intensity profile of the incident radiation to be mapped

[1] A common approximation for transitions in the optical (and lower frequency) range is used here. The dipole approximation takes the electric field amplitude to be constant across the atom. This can be safely assumed if the dimensions of the atom are significantly smaller than the wavelength of the incident radiation. For optical transitions this is typically well satisfied.

[2] $\Gamma = \frac{1}{\tau}$.

onto the shift in atomic energy levels. The gradient of the light shift is the source of the dipole force which is widely used to trap laser cooled atoms in a dilute atomic vapour [72]. The detuning δ of the light field determines the sign of the light shift and thus whether atoms are attracted towards an intensity minima ($\delta > 0$) or maxima ($\delta < 0$). The topic of light shifts and the resulting dipole forces experienced by the atoms will be re-visited in the following section in order to explain some of the more subtle processes of laser cooling.

Dissipative forces are associated with the exchange of linear momentum between atoms and photons in resonant scattering processes. When an atom absorbs a photon, momentum conservation requires it receive a kick of magnitude $\hbar k$ in the direction of travel of the incident photon. Following absorption, the atom may be stimulated to emit a photon back into the incident beam resulting in no net momentum change, or spontaneously emit a photon in a random direction. Over many cycles the momentum change due to spontaneous emission averages to zero and thus the atom experiences a force, known as the scattering force in the direction of the beam. The size of the scattering force is determined by the photon momentum and the atomic scattering rate,

$$F_{\mathrm{s}} = \hbar k \times \frac{\Gamma}{2} \frac{I/I_{\mathrm{sat}}}{1 + I/I_{\mathrm{sat}} + 4\delta^2/\Gamma^2}. \tag{3.6}$$

The time-averaged maximum value of this force can easily evaluated under the limit of high intensity (i.e. $I \to \infty$) resonant light. Thus,

$$F_{\mathrm{s}}^{\mathrm{max}} \sim \hbar k \times \frac{\Gamma}{2}, \tag{3.7}$$

which for the D2 transition in ^{87}Rb gives accelerations of the order of $10^3\times$ g.

3.3 Doppler cooling

The cooling of atoms by a beam of photons is a prominent demonstration of the mechanical effects of light. In 1975 Hänsch and Schawlow published a proposal to use the force arising from cycles of resonant absorption and spontaneous emission of narrow band laser light to cool atoms [2]. Four years later this proposal was successfully implemented using trapped ions [3] and the field of laser cooling was born.

The proposal of Hänsch and Schawlow suggested using a controlled imbalance in the scattering force to dissipate an atom's kinetic energy into the spontaneously emitted light field. Simplifying to the 1D case, the proposal involved illuminating an atom with two counterpropagting beams of equal intensity, detuned below an atomic resonance. A stationary atom experiences no net momentum change as the scattering forces of each beam balance. The symmetry is broken for an atom moving with non-zero velocity $\mathbf{v}$, where the Doppler effect shifts the apparent frequency of each beam as seen by the atom. The red detuning ensures the atom preferentially scatters light from the

counterpropagating beam. The resulting imbalance in the scattering force,

$$\begin{aligned} \boldsymbol{F}_{\mathrm{D}} &= \boldsymbol{F}_{\mathrm{s}}^{\rightarrow} + \boldsymbol{F}_{\mathrm{s}}^{\leftarrow} && (3.8) \\ &= (\hbar\boldsymbol{k})\,\frac{\Gamma}{2}\left[\frac{I/I_{\mathrm{sat}}}{1+I/I_{\mathrm{sat}}+4(\delta-\boldsymbol{k}\cdot\boldsymbol{v})^2/\Gamma^2}\right] \\ &- (\hbar\boldsymbol{k})\,\frac{\Gamma}{2}\left[\frac{I/I_{\mathrm{sat}}}{1+I/I_{\mathrm{sat}}+4(\delta+\boldsymbol{k}\cdot\boldsymbol{v})^2/\Gamma^2}\right] && (3.9) \end{aligned}$$

takes the form of a dissipative force $\boldsymbol{F}_{\mathrm{D}} = -\alpha\boldsymbol{v}$ in the limit of low velocity (i.e. $|\boldsymbol{k}\cdot\boldsymbol{v}| \ll \Gamma$).

For three orthogonal pairs of laser beams, the motion of an atomic ensemble is damped in every direction. The analogy of this mechanism with that of a moving object in a viscous medium led to the cooling technique being referred to as 'optical molasses'. Cooling was first observed in this configuration by Chu *et al.* in 1985 [73].

The temperature limits of Doppler cooling are set by the intrinsic heating associated with the stochastic nature of spontaneous scattering events, which cause the atom to undergo a random walk in momentum space. Competition between the processes of cooling and heating is parameterised by the detuning, which gives a minimum in the achievable temperature at a value of $\delta = \Gamma/2$ [17]. This temperature is referred to as the Doppler temperature T_D, where

$$k_{\mathrm{B}}T_{\mathrm{D}} = \frac{\hbar\Gamma}{2}. \tag{3.10}$$

This limit for rubidium is $T_{\mathrm{D}} = 146\,\mu\mathrm{K}$, however as is discussed in the following section optical cooling techniques can operate well below the Doppler limit.

3.4 Sub-Doppler cooling

Early temperature measurements showed atoms in optical molasses could be cooled significantly below the Doppler limit [4]. This could not be explained within the theoretical framework of laser cooling which had been rigorously derived for a two-level system. The sub-Doppler cooling mechanisms proposed independently by Dalibard and Cohen-Tannoudji [74], and Chu [75] that solved this problem required a multi-level solution that allowed for optical pumping between ground states and took account of polarisation gradients in the overlapping beams.

For a static atomic ensemble, optical pumping ensures the orientation of the ground state population distribution reflects the local light field polarisation. In a moving ensemble, the atoms sample a changing polarisation. In the limit of weak pumping, the ground state population distribution cannot follow this change quickly enough to remain adiabatic and so lags behind the local light field polarisation. This non-adiabatic following is the critical requirement for the operation of sub-Doppler cooling processes

since it sets up non-equilibrium situations, where the excess energy can be dissipated by spontaneous emission.

The following paragraphs present a discussion of the origin of the sub-Doppler cooling process known as Sisyphus cooling. However, when the polarisation of the light field is arranged such that the counterpropagating beams have circular polarisations of the same helicity (the $\sigma^+ - \sigma^-$ configuration), the Sisyphus cooling mechanism does not occur. In its stead an entirely independent sub-Doppler cooling mechanism operates. Motion induced orientation cooling relies on population imbalances between the magnetic substates to achieve unbalanced radiative forces [74].[3]

A description of the Sisyphus effect begins with a pair of counterpropagating laser beams with orthogonal linear polarisations (lin⊥lin). The polarisation of the standing wave changes along the propagation axis, from σ^+ to linear to σ^-.[4] Such a light field will produce state selective, spatially varying light shifts that split the degeneracy of the ground state Zeeman sublevels.

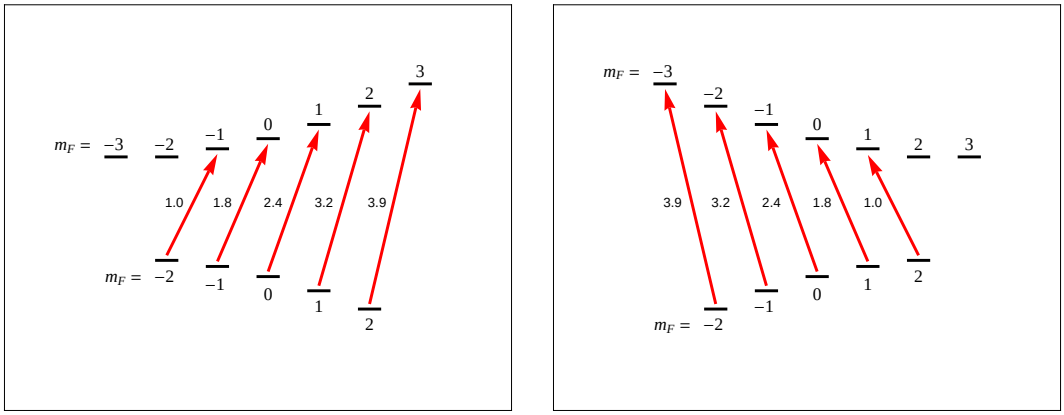


Figure 3.1: Light shifts for the magnetic sublevels in the $5^2S_{1/2} \rightarrow 5^2P_{3/2}$ transition in ^{87}Rb for σ^+ (left) and σ^- (right) polarised light, detuned below resonance. In the steady state all the atomic population will reside in the state with the largest light shift. Transition strengths are quoted relative to the weakest allowed transition strength. All data obtained from [76].

As is shown in fig. 3.1 the light shift of a given energy level is related to the coupling strength between the two levels involved in an optical transition. An atom in the region

[3] In most conventional six beam magneto-optical traps, motion induced cooling is used to cool the atoms below the Doppler limit. However, as is elaborated in chapter 5 no sub-Doppler cooling is possible in this experiment. Hence the discussion of sub-Doppler cooling mechanisms are presented here simply for completeness.

[4] Technically σ^+ and σ^- refer to transitions in the atom that result in a change of atomic angular momentum. With reference to laser beam polarisations, they represent circularly polarised light that is able to excite these transitions.

of σ^+ polarisation will be optically pumped into the maximally stretched state. As this atom moves relative to the standing wave configuration, it exchanges kinetic for the potential energy gained by moving into a region where the light shift of its m_F state is less. An atom entering a region where the polarisation tends towards σ^- will be optically pumped into the stretched state of the opposite polarity. As this state is now the one that is most strongly light shifted (downward), the potential energy of the atom is dissipated into the spontaneously scattered light field.

Over each optical pumping cycle the atom loses an amount of kinetic energy approximately equal to the maximum light shift between the Zeeman sublevels. Sisyphus cooling[5] will work until the atom's kinetic energy drops below this value. Conventional sub-Doppler cooling techniques perform best when the residual magnetic field experienced by the atoms is a minimum [77]. For field strengths between 0.1 G and 1.0 G the Zeeman shifts of the magnetic substates are approximately equal to lights shifts, reducing the efficiency of sub-Doppler cooling processes.[6] The coldest temperatures measured for a sample of atoms cooled by sub-Doppler processes is 2.5 μK for cesium atoms [79]. The recoil energy $E_\mathrm{r} = (\hbar k)^2/2M(\hbar k)^2$ represents the ultimate limit for sub-Doppler cooling techniques. Raman cooling [80] or velocity selective coherent population trapping [81] are examples of techniques that have been developed that can cool below the recoil limit.

3.5 The magneto-optical trap

The velocity dependence of the force in optical molasses facilitates cooling but not trapping of atoms. The low atomic velocities following Doppler cooling, result in atoms diffusing out of the system over a few 100 ms. The magneto-optical trap (MOT) proposed by Jean Dalibard provides significantly longer trapping times by generating a spatial dependence for the scattering force. In such a trap, an atom experiences a net force until it has come to rest *at a single point in space*, i.e. the trap centre. The magneto-optical trap was first demonstrated in 1987 [82] and has gone on to become an integral component in many ultracold atom experiments.

A MOT is formed by overlapping the centers of 3D optical molasses in $\sigma^+ - \sigma^-$ configuration with a cylindrical quadrupole magnetic field of the form

$$\boldsymbol{B}(\mathbf{r}) = B'_\mathrm{q}\left(x\hat{\mathbf{e}}_{\boldsymbol{x}} + y\hat{\mathbf{e}}_{\boldsymbol{y}} - 2z\hat{\mathbf{e}}_{\boldsymbol{z}}\right). \tag{3.11}$$

[5]So named due to the motion of the atom in continuously climbing the light shifted potentials resembling the mythical punishment bestowed upon Sisyphus, a king of ancient Greece. For his trickery, Zeus punished Sisyphus to an eternity of rolling a heavy boulder to the top of a hill. No matter how hard Sisyphus tried, just before the boulder reached the hilltop, it would roll back down to the bottom, and Sisyphus would have to start again.

[6]Techniques were subsequently developed to cool atoms below the Doppler limit in a presence of a strong magnetic field. In this instance the atom's are cooled towards a finite (non-zero) velocity [78].

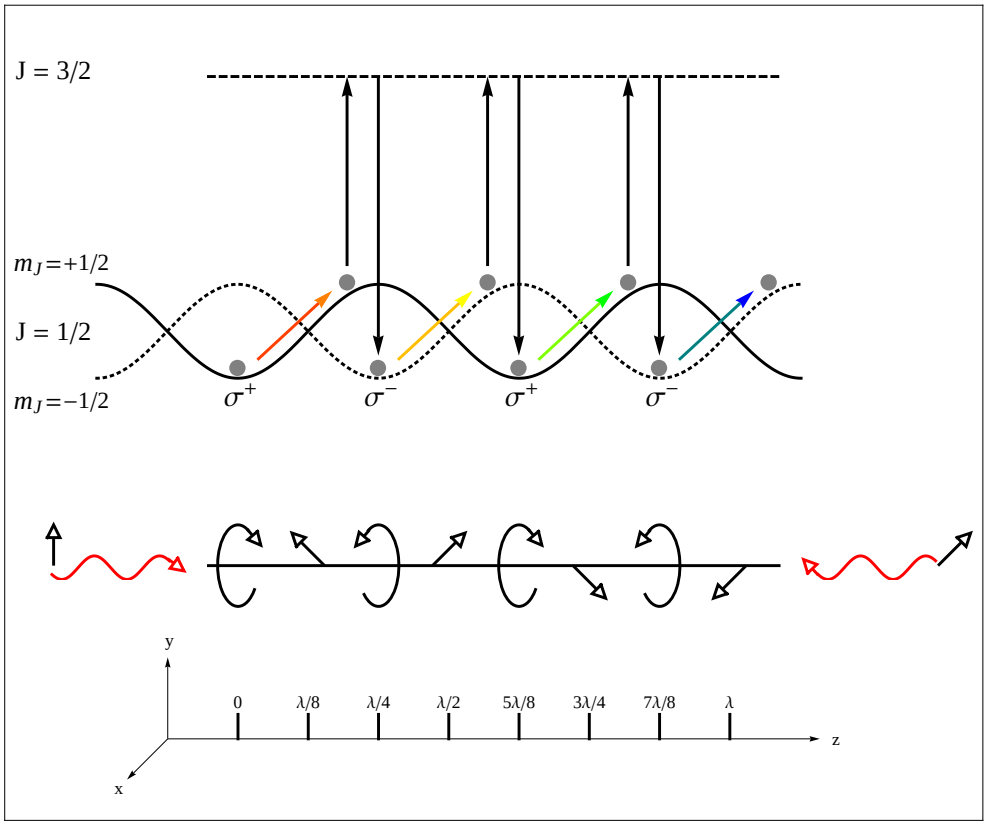


Figure 3.2: The Sisyphus sub-Doppler cooling mechanism. The lower part of the figure shows the spatially dependent light field polarisation resulting from the superposition of two counterpropagating beams with orthogonal linear polarisations. The upper part of the figure shows the corresponding light shifts of the Zeeman sublevels. The coloured arrows represents the motion of the atom as it climbs out of the local minimum to the region where it is undergoes a transition to an excited state. Note how under spontaneous emission the atom always falls back to the ground state with a lower potential energy.

Such a field is generated by circulating a current in opposite directions through a concentric coil pair. This configuration of coils and currents will hereafter be referred to as the *anti-Helmholtz* configuration. It should be noted the gradient of the field B'_{q} only remains linear over distances from the field zero that are smaller than the radius of the coils. The magnetic field gives rise to spatially dependent Zeeman shifts in the magnetic substates of an atom. In the $\sigma^+ - \sigma^-$ configuration, the selection rules dictate that these energy shifts will result in an imbalance in the scattering force that is proportional to the position of the atom relative to the quadrupole centre.

To discuss the implementation of these ideas in the MOT, consider an atom with ground state angular momentum $J = 0$ and a (degenerate in the absence of a magnetic field) excited state with $J = 1$. The quadrupole magnetic field splits the single excited state into three energy levels, where the energy separation between them varies linearly with distance from the field zero. In the 1D case, a pair of red-detuned, counterpropagating beams in $\sigma^+ - \sigma^-$ configuration is incident upon the atoms, which are located in the vicinity of the zero of the quadrupole field. An atom in its ground state, at a position $z > 0$ in this system will have the transition to the $m_J = -1$ substate Zeeman shifted towards resonance, and so will preferentially scatter atoms from the σ^- beam. The intrinsic symmetry of the system requires an atom at a position $z < 0$ to have the transition to the $m_J = +1$ level brought towards resonance and so scatter more photons from the σ^+ beam. In both cases an atom experiences a force directed toward, and proportional to the distance from the trap centre. This restoring force operates alongside the frictional force of optical molasses, allowing the MOT to provide both cooling and trapping for atoms.

Early iterations of the MOT trapped $\sim 10^7$ atoms that had to be pre-cooled by other optical methods such as chirped cooling [83] or Zeeman slowing of an atomic beam [84]. Pre-cooling processes act to increase the number of atoms within a Maxwell-Boltzmann distribution with a velocity below a critical value. The capture velocity v_{c} of a MOT is the maximum initial velocity of an atom that is just brought to rest after traversing the full MOT diameter. This quantity neatly parameterises the collection efficiency of a MOT since only those atoms with $v < v_c$ may be captured. An upper estimate for v_c is given by assuming large intensities for the MOT beams (i.e. $I/I_{\mathrm{sat}} \to \infty$) where the scattering rate saturates to $\Gamma/2$ and scattering force is a maximum as quoted in eqn. 3.7. Simple kinematics estimates that capture velocity for a MOT of diameter d varies as[7]

$$v_{\mathrm{c}} = \sqrt{\frac{\hbar k \Gamma d}{m}}, \tag{3.12}$$

and so significant improvements to MOT performance may be achieved by using beams of a larger diameter [85]. The rapid improvements in magneto-optical trapping allowed

[7]In reality the average scattering rate across a full transit of the MOT is somewhat lower than this limiting value as the decreasing Doppler shift experienced by a decelerating atom causes it to move away from resonance with the cooling light at some position in the MOT.

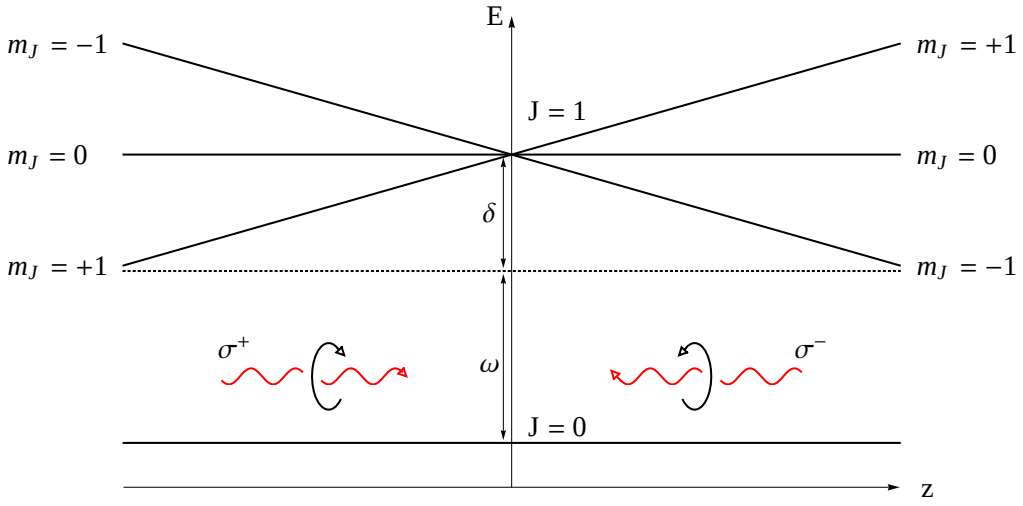


Figure 3.3: The principle of operation for a magneto-optical trap in 1D. The Zeeman sublevels of the $J = 1$ excited state are split by the presence of an inhomogeneous quadrupole magnetic field (not shown) centered about $z = 0$. Note, in this figure the direction of the magnetic field and the polarisation of the incident light has been determined relative to a quantisation axis directed along $+z$.

the research group in Boulder, Colorado to demonstrate efficient loading of caesium atoms from a room temperature vapour in 1990 [86]. Present day experiments using rubidium, caesium or sodium frequently neglect the pre-cooling stage before MOT loading is initiated. However, other elements that are less well suited to optical cooling methods such as calcium or strontium, retain this stage to ensure a sufficient atom number is loaded into the MOT. Continued development in this field led to the realisation of the first pyramidal MOT in 1996 [87]. Under this scheme, the six counter-propagating beams (with correct polarisations) were generated by reflections of single incident beam off a hollow, four sided pyramidal mirror located inside the vacuum system (see fig. 3.4). The advantage of this scheme is the robustness of the optical alignment over more conventional schemes.

The hyperfine splitting of the ground state requires two frequencies to be used in the realisation of a rubidium MOT. Cooling light is used to drive excitations on the cycling $|F = 2, m_F\rangle \rightarrow |F' = 3, m'_F = m_F + 1\rangle$ transition of the D2 line in ^{87}Rb . However, off-resonant excitations also occur on the $|F = 2, m_F\rangle \rightarrow |F' = 2, m'_F = m_F + 1\rangle$ transition, from where atoms may spontaneously decay to either the $F = 1$ or $F = 2$ ground states. The 6.8 GHz ground state hyperfine splitting in ^{87}Rb effectively renders the $F = 1$ state dark with respect to the cooling light. Thus a second laser, resonant with the $|F = 1, m_F\rangle \rightarrow |F' = 2, m'_F = m_F + 1\rangle$ transition is employed to repump the atoms into the cooling cycle.

Magneto-optical traps have not been able to deliver suitably low temperatures and

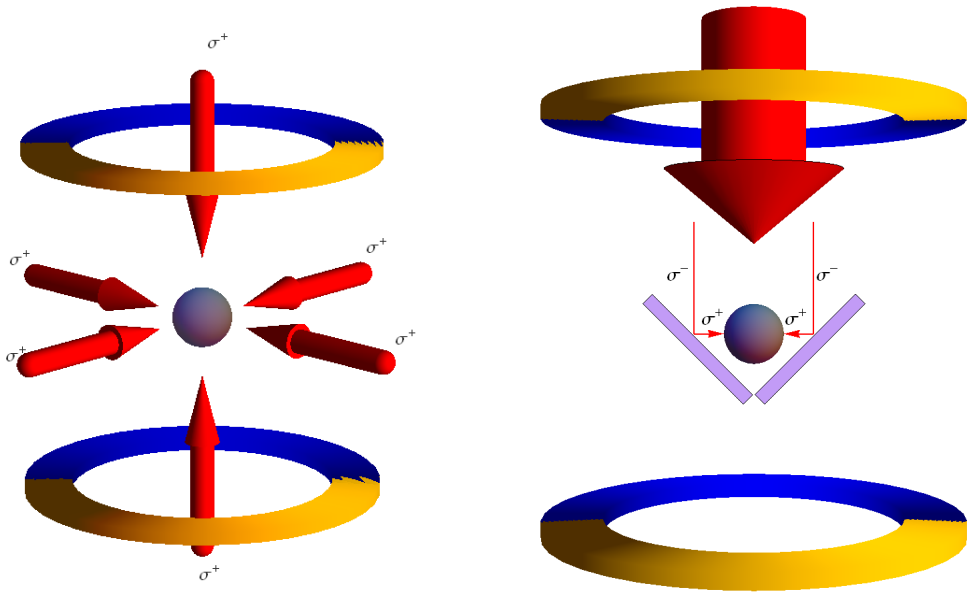


Figure 3.4: (Left) Configuration for conventional 6-beam cross MOT with σ^+ polarised, red detuned light. (Right) Pyramidal MOT schematic. Single incident beam is σ^- polarised, but after reflection reverses its handedness to become σ^+ polarised [88]. In this figure, the atoms and anti-Helmholtz field producing coils are schematically represented. Note all polarisations have been defined relative to the local magnetic field.

high densities to achieve quantum degeneracy. The density within a MOT is complicated function of many variables, including the number of atoms trapped in the MOT itself. For a cloud of $N \approx 10^9$, typical values for temperature and density in a MOT are $T \approx T_\mathrm{D}$ and $n \approx 10^{10}\,\mathrm{cm}^{-3}$. The cloud density can be increased by using techniques such as the dark spontaneous-force optical trap (dark SPOT) where the intensity of the central portion of the repumping laser beam is dramatically reduced, so that atoms at the centre of the trap to spend $\sim 99\,\%$ of their time in the lower hyperfine ground state, where the scattering rate is significantly reduced [89].

3.6 Magnetic trapping

The use of magnetic fields to confine and manipulate large numbers of laser cooled, neutral atoms has proved to be a versatile technique since it was first experimentally realised in 1985 [90]. An atom with a non-zero magnetic moment possesses quantum states where the Zeeman energy changes with the magnitude of the local magnetic field. When Zeeman energy increases with the strength of the applied magnetic field the atom

experiences a potential minimum where the **B** field vanishes. Such states of an atom are known as *low-field seekers* and under the correct conditions can be used to localise a large number of atoms at a single point in space.[8] The concomitant high-field seeking states are not employed in conventional magnetic trapping since it is not possible for a DC magnetic field to have a local maximum in free space [91].

The interaction between a neutral atom and a magnetostatic field $\mathbf{B}(\boldsymbol{r})$ is proportional to the atomic dipole moment $\boldsymbol{\mu}$. The energy of this interaction in the weak-field regime can be written as

$$U_{\text{mag}} = -\boldsymbol{\mu} \cdot \mathbf{B}(\boldsymbol{r}) = m_F g_F \mu_{\text{B}} |\mathbf{B}(\boldsymbol{r})|, \tag{3.13}$$

where g_F is the Landé g-factor and μ_{B} is the Bohr magneton.

There are two principle requirements that must be fulfilled to ensure stable magnetic confinement of an atom. The first is that an atom's thermal energy should be considerably less than the change in the Zeeman energy from the trap centre to trap edge (i.e. the trap depth). The second is that the atom's motion is adiabatic with respect to the spatially inhomogeneous field, such that the projection of the atomic dipole along the local field direction is preserved.[9] This is equivalent to requiring that the rate of change of the field does not approach the Larmor precession frequency $\omega_{\text{lam}} = \frac{m_F g_F \mu_{\text{B}}}{\hbar} |\mathbf{B}(\boldsymbol{r})|$.

3.6.1 The quadrupole trap

The first magnetic trap for laser cooled atoms was formed using a cylindrically symmetric quadrupole field identical in form to that employed in the MOT (see eqn 3.11), but with a gradient B'_{q} that is an order of magnitude larger to account for the absence of optical confinement. The quadrupole trap has a single minimum where the field vanishes at the trap centre and a linear field dependence with position that begins to roll-off at a distance approximately equal to the radius of the coils.

The researchers at NIST were able to observe ^{23}Na atoms trapped with a lifetime of 0.83 s that was limited by collisions with background atoms. The trap depth in the first instance was 17 mK indicating the necessity of employing laser cooling techniques to prepare the atoms prior to loading into a magnetic trap.

The quadrupole trap violates the requirement for adiabaticity at the trap centre where $|\mathbf{B}(\boldsymbol{r})| = 0$. In this region atoms undergo Majorana spin flip transitions to other m_F states where there is a high probability that they are lost from the trap. Under conditions of UHV ($\leq 10^{-9}$ mbar) spin flips at the field zero represent the dominant loss channel for laser cooled atoms in the quadrupole trap. The loss rate increases for colder, denser clouds, thus the path to BEC in the quadrupole trap is significantly hampered by increasingly short trap lifetimes as the degenerate regime approaches.

[8] In the $F = 1$ hyperfine ground state manifold of ^{87}Rb , $g_F = -1/2$ hence only the $|F = 1, m_F = -1\rangle$ state is trapped.

[9] This is the justification for the interaction energy in eqn. 3.13 only depending on magnitude of the field, since as the field changes direction, the dipole follows it adiabatically.

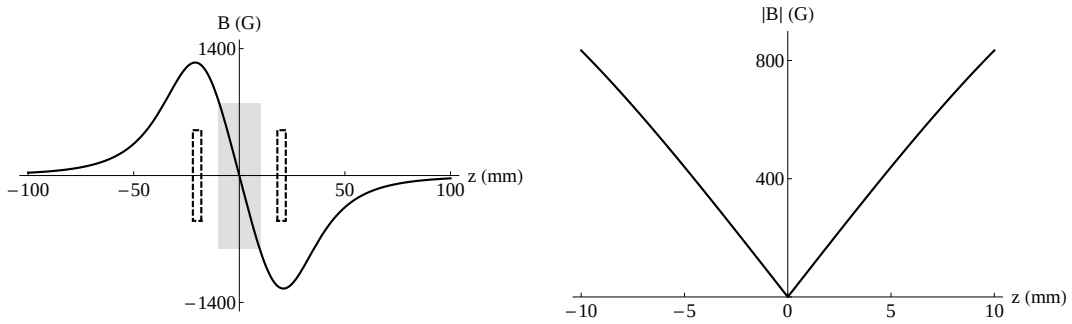


Figure 3.5: (Left) Single wire approximations of the magnetic field pattern along the separation axis of a concentric coil pair operating in anti-Helmholtz configuration. The coil separation (37.2 mm) and radii (26.95 mm) correspond to the values for the *Quad* coil pair used in the magnetic trap for the experiments reported in chapters 7, 8, 9. The plot was made using 330×20 Ampere-turns which equals the maximum output of the available high current supply multiplied by the number of turns in each *Quad* coil respectively. The positions of the coils are represented by the dashed rectangles. (Right) The modulus of the field within the grey shaded rectangle of the neighbouring figure.

To circumvent this issue, new traps were designed which either modified the standard quadrupole trap, or provided a finite static magnetic field at the trap centre. The traps falling into the latter category are all broadly based on a proposal for a Ioffe type trap by David Pritchard [92] and have been widely used to create and manipulate BEC's [93, 94, 95, 96, 97]. The former class of traps include two examples that expedited the earliest atomic vapor BEC's, the optically plugged quadrupole trap [98] and the time-averaged orbiting potential (TOP) trap [5].

3.6.2 The TOP trap

The time-averaged orbiting potential (TOP) trap employs a bias field rotating at a frequency ω_{T} to modulate the static quadrupole potential in such a way as to remove the field zero from the trap centre. It was first proposed and demonstrated in JILA [99]. Characteristics of the TOP trap are a background limited lifetime (usually at bias fields > 1 G) and a cylindrically symmetric geometry that readily lends itself to rotation experiments [100, 101, 102].

In a radially symmetric configuration the bias field is,

$$\mathbf{B}_{\mathrm{T}}(t) = \mathrm{B}_{\mathrm{T}}[\cos(\omega_{\mathrm{T}} t)\ \hat{\mathbf{e}}_x + \sin(\omega_{\mathrm{T}} t)\ \hat{\mathbf{e}}_y]. \tag{3.14}$$

The effect of such a field on the quadrupole is to change the locus of the field zero from a point to a circle of radius $r_0 = \mathrm{B}_{\mathrm{T}}/B'_{\mathrm{q}}$. The rotation frequency of the bias

field $\omega_{\rm T}$ is selected such that it lies in the interval between the harmonic trap frequency $\omega_{\rm r}$ and the Larmor frequency $\omega_{\rm lam}$, i.e. $\omega_{\rm r} < \omega_{\rm T} < \omega_{\rm lam}$. The upper bound to this inequality ensures the rotating bias field does not perturb the projection of the dipole along the instantaneous magnetic field (and so cause transitions to untrapped m_F states). The lower bound causes the atoms to experience a time-averaged potential as they cannot motionally follow the periodic changes in the trapping fields. In the following experiments $\omega_{\rm r}$ was of the order of 100 Hz, whereas the Larmor frequency in a 1 G field is 1.4 MHz. To satisfy both requirements the bias field frequency $\omega_{\rm T} = 7$ kHz.

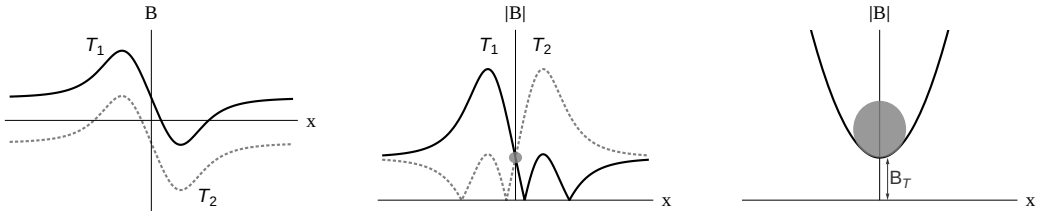


Figure 3.6: (Left) The instantaneous magnetic field resulting from the superposition of quadrupole and time-dependent magnetic bias fields directed along the x axis. The fields are illustrated at two instants T_1 and T_2 that are separated by a half period of oscillation. (Centre) Modulus of the total field, with trapping position of the atoms shown. (Right) The time-averaged magnetic field in the regions close to the origin. The atoms experience harmonic confinement with a finite minimum that equals the magnitude of the bias field $\rm B_T$.

To calculate the resulting trap geometry, the instantaneous magnetic field

$$\mathbf{B}_{\rm TOP}(\boldsymbol{r},t) = [B'_{\rm q}x + {\rm B_T}\cos(\omega_{\rm T}t)]\ \hat{\mathbf{e}}_x + [B'_{\rm q}y + {\rm B_T}\sin(\omega_{\rm T}t)]\ \hat{\mathbf{e}}_y - 2B'_{\rm q}z\ \hat{\mathbf{e}}_z \qquad (3.15)$$

is integrated over one period of the oscillating field to give the time-averaged potential

$$\begin{aligned} U_{\rm TOP}(\boldsymbol{r}) &= \frac{\omega_T}{2\pi}\int_0^{\frac{2\pi}{\omega_T}} m_F g_F \mu_{\rm B} |\mathbf{B}_{\rm TOP}(\boldsymbol{r},t)| dt & (3.16)\\ &\approx m_F g_F \mu_{\rm B}[{\rm B_T} + \frac{B'^2_q}{4{\rm B_T}}(x^2+y^2+8z^2)], & (3.17)\end{aligned}$$

where only up to quadratic terms have been retained. Thus the TOP trap provides radially symmetric harmonic confinement for $|\mathbf{r}| = \sqrt{x^2+y^2+z^2} \lesssim r_0$ with a non-zero value of the potential at the trap centre. The harmonic trap frequencies in the radial ω_r

and axial ω_z directions can be deduced from the eqn. 3.17 as

$$\omega_r = \sqrt{\frac{m_F g_F \mu_B B_q'^2}{8m\mathrm{B_T}}} \tag{3.18}$$

$$\omega_z = \sqrt{\frac{m_F g_F \mu_B B_q'^2}{m\mathrm{B_T}}} \tag{3.19}$$

$$\omega_z = \sqrt{8}\omega_r.$$

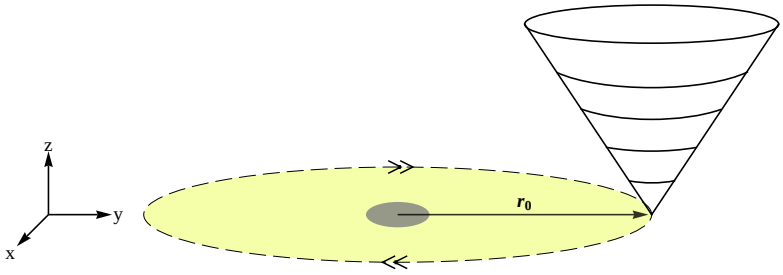


Figure 3.7: Magnetic fields in the TOP trap. The radial rotating bias field causes the zero of the quadrupole field to orbit in the xy plane at a constant distance r_0 from the atoms. Inside this region the atoms experience harmonic confinement.

The effect of gravity

When the potential of the TOP trap is reformulated to include the force of gravity [103], the equilibrium position of the cloud moves downwards from the origin to the position $(0, 0, \tilde{z})$ where $\tilde{z} = r_0\beta/(1-\beta^2)^{1/2}$. For typical values employed in this experiment, $B'_\mathrm{q} = 100\,\mathrm{G/cm}$ and $\mathrm{B_T} = 1\,\mathrm{G}$ the gravitational sag $\tilde{z} = 32\,\mu\mathrm{m}$. The trap frequencies are also affected so that

$$\omega'_r = (1-\beta^2)^{1/4}(1+\beta^2)^{1/2}\omega_r \tag{3.20}$$

$$\omega'_z = (1-\beta^2)^{3/4}\omega_z, \tag{3.21}$$

where $\beta = mg/(m_F g_F \mu_\mathrm{B} B'_\mathrm{q})$ is the ratio of an atom's weight to the magnetic trapping force it experiences in the vertical direction.

3.7 Evaporative cooling

The attainment of phase space densities of order unity in dilute atomic gases typically requires temperatures in the 100 nK range, and densities of order $10^{13}\,\mathrm{cm}^{-3}$. Optical

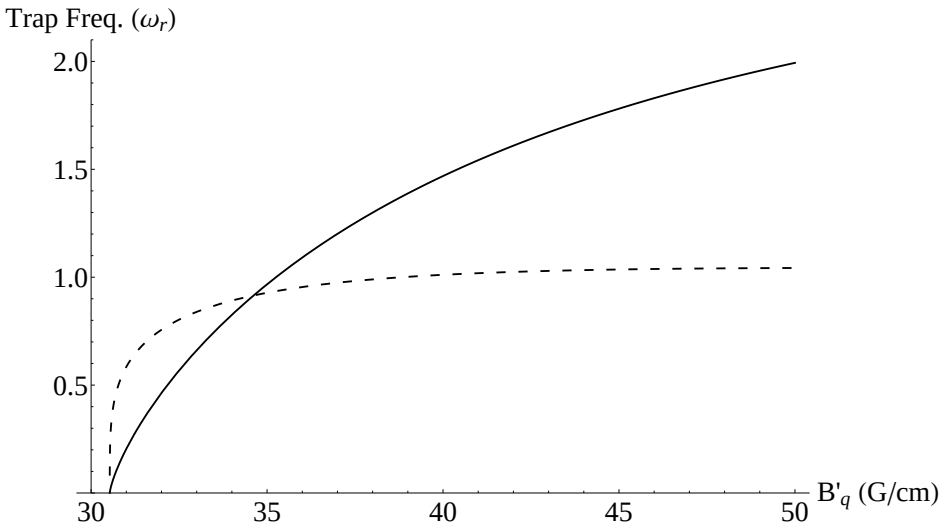


Figure 3.8: The effect of gravity on the TOP trap frequencies ω_r' (solid) and ω_z' (dashed) plotted in units of ω_r as a function of quadrupole gradient $B_{\rm q}'$. As trap stiffness decreases the impact of gravity on the TOP trap becomes more significant. The axial direction is more strongly affected, causing the trap aspect ratio to pass through unity when $B_{\rm q}' = 34.6\,{\rm G/cm}$. Atoms are no longer supported against gravity when $B_{\rm q}' = 30.5\,{\rm G/cm}$ (corresponding to $\beta = 1$).

cooling methods are limited by the phase-space densities that they can achieve due to effects such as radiation pressure[10] or excited state collisions.[11]

Evaporative cooling, the same process by which a hot liquid cools down to the ambient temperature, is an alternative cooling concept first demonstrated in spin-polarised hydrogen systems [104] where energy is carried away from the atomic ensemble not by photons, but by the atoms themselves. Evaporative cooling does not suffer from the same limitations as optical cooling techniques and its application to magnetically trapped atomic vapours proved to be a decisive breakthrough in the realisation of BEC in these systems in the mid 90's.

The goal with evaporative cooling is to achieve the largest increase in phase space density of the sample, for the smallest decrease in atom number. Evaporative cooling is driven by elastic collisions that ensure the thermal equilibrium of a gas of atoms. Provided the rate of elastic collisions significantly exceed the rate of inelastic collisions then the mechanisms of evaporative cooling can effect efficient cooling of a sample. The elastic collision rate is linearly related to the in-trap mean atomic density, and thus can be

[10]When the density of an atomic sample becomes too high, the probability increases that a photon scattered by one atom will be re-absorbed by another before it can leave the system. This results in a net repulsion between the two atoms, and the global effect is a form of outward radiation pressure that prevents the density from increasing further.

[11]There collisions are generally inelastic and lead to atom loss from the trap.

adjusted to the requisite level by using tightly confining[12] potentials. Inelastic collisions with background atoms are minimised by using a vacuum system with a residual pressure of order 10^{-11} mBar. On the practical side, for efficient evaporative cooling a pathway must exist whereby atoms of above average kinetic energy are able to exit the system. There also must be sufficient time for the sample to rethermalise following the loss of atoms, allowing the process to proceed towards ever lower temperatures.

In a system obeying Maxwell-Boltzmann statistics, following the truncation of the distribution by an evaporative 'cut', the high energy tail is repopulated by repeated elastic collisions between atoms. The elastic collision rate is therefore the critical parameter when attempting to evaporatively cool a sample of atoms. Generally, the rethermalisation time must be short in comparison to the lifetime of the sample, which is typically limited by inelastic collisions, either with background atoms when the density is low, or as 3-body losses when the density gets above $10^{14}\,\mathrm{cm}^{-3}$ [105]. The overall efficiency of evaporation can therefore be characterised by the ratio of elastic to inelastic collisions. To achieve the large increases in phase-space density required for BEC it is beneficial to enter the regime of 'runaway evaporation' where the elastic collision rate increases as evaporation proceeds, positively reinforcing the efficiency of the process. Where trap losses are low, runaway evaporation precipitates the occurrence of BEC.[13]

The following sections present a discussion on several specific implementations of evaporative cooling that are relevant to the experiments reported in subsequent chapters. Note that the process of natural evaporation in the double-well TAAP trap is not included here, but is discussed in detail in chapter 7. A common theme amongst all methods is the rate of evaporative cooling is controlled by the adjusting the form of the confining potential. In contrast to the more familiar *spontaneous* evaporation, the system is effectively *forced* towards lower temperatures hence the name for this process of forced evaporative cooling. For a comprehensive review of both theory and practice of evaporative cooling see [106].

3.7.1 Radio-frequency evaporation

As will be discussed in more detail in subsequent chapters the spatially inhomogeneous magnetic fields used to confine laser cooled atoms result in similarly non-uniform Zeeman shifts between magnetic substates in the same hyperfine ground state. A uniform radio-frequency (rf) magnetic field can be used to drive the magnetic dipole transitions between Zeeman substates at positions where the radio-frequency equals the frequency splitting of the states. For atoms in a quadrupole trap, this resonance condition is fulfilled on an oblate spheroid centered on $\mathbf{B}(\boldsymbol{r}) = 0$.

[12] In very tight traps, as a thermal cloud is cooled towards higher and higher densities, the 3-body collisions must be taken into consideration, however for the trap frequencies and atom numbers in this experiment, this inelastic mechanism has not been observed to cause detrimental effects.

[13] Although it is not optimal, quantum degeneracy can still be reached if the collision rate remains constant throughout the final stages of evaporation.

For a dilute gas in a harmonic potential, the period of oscillation is typically less than the mean time between atom collisions. This allows the atoms with above average thermal energy to oscillate further from the trap centre, into regions of larger Zeeman shift. By starting with a high frequency evaporative field, only the most energetic atoms sample the region of rf resonance, resulting in them making transitions to untrapped states and thus leaving the system. By ramping down the evaporative field frequency, atoms with increasingly lower energy are selectively removed from the sample. This frequency ramp should be slow compared to the rethermalisation time so the sample is driven towards lower temperatures and higher phase-space densities.

3.7.2 TOP trap evaporation

In the TOP trap, although the region where $\mathbf{B}(\boldsymbol{r}) = 0$ has been displaced away from the atoms, it can still cause non-adiabatic transitions to untrapped states. However, unlike the bare quadrupole, the TOP trap affords control over the degree to which this process occurs and a selectivity regarding which atoms are removed from the system. The rotating field zero orbits exterior to the atoms at a distance (r_0) proportional to the magnitude of the TOP field. As B_T is reduced, atoms which intersect this circular path as they oscillate in the trap have a high probability of being removed from the system via a spin-flip. Since the extremities of a trapped cloud are predominantly populated by atoms with above average thermal energy, these are the ones that are preferentially removed via this mechanism and so the cloud is evaporatively cooled by an amount which is determined by the magnitude of B_T [107]. This evaporative scheme has the added advantage of increasing the stiffness of the trap (see eqns. 3.18 and 3.19) and hence the elastic collision rate as it proceeds.

Chapter 4

Atoms in time-dependent magnetic fields

4.1 Time-averaging

Time-averaging of potentials is a versatile trapping technique that has been successfully employed with electric, optical and magnetic fields [108, 109, 99]. The process exploits the difference in the timescales that govern an atom's ability to change its motional state, limited by the trapping frequency ω_r, and its internal state, closely related to the Larmor frequency $\omega_{\rm lam}$. Thus by introducing a periodic time dependence to a potential with a frequency $\omega_{\rm T}$ with $\omega_r \ll \omega_{\rm T} < \omega_{\rm lam}$ an atom experiences a modified potential without changing its m_F state.

Time-averaging underlies the TOP trap detailed in the previous chapter, and in the following sections it will be demonstrated how time-averaging can be used in harmony with the process of rf-dressing to enrich the spectrum of accessible trap geometries.

4.2 Radio-frequency dressing

Magnetic resonance is the name given to the process whereby transitions are driven between Zeeman sublevels by a coupling of the atomic magnetic dipole moment to an oscillating magnetic field. The technique of rf-dressing, first proposed in [110] employs the principal of magnetic resonance to trap ultracold atoms at the positions in a magnetostatic potential where the applied radiation is resonant with the transition between two Zeeman sublevels in the same hyperfine level. The effect of the rf is to place the atoms in a coherent superposition of internal states, the composition of which is a function of the position of the atom in the trap. These superpositions are the dressed states

that are the eigenstates of the global system. An important milestone in the practical development of rf-dressed traps for ultracold atoms was achieved by researchers in Paris who demonstrated this superposition of internal states is stable against collisional decay processes [111].

The spatial variation of the eigenenergies of this system give rise to adiabatic potentials (APs) that present attractive arenas for performing cold atom experiments. Adiabatic potentials can trap atoms in a range of non-trivial geometries with tunable parameters. A variable spacing double-well [112], ring [113, 114] and anisotropic shell [115] potential have already been realised and proposals exist for more complex toroidal [116] and lattice [117] potentials. Only electronic ground states are involved so spontaneous emission is negligible allowing the atoms to be trapped at the resonant positions where the modification is most significant.[1] The dressing fields result from the far-field radiation pattern of a set of custom magnet coils and so are smooth and corrugation free on the scale of the trapped cloud.[2] The vectorial nature of the coupling between the atom and dressing radiation provides an extra degree of control over the confinement experienced by the atoms. Adiabatic potentials have been shown to be a simple, robust realisation of a coherent beam splitter for a BEC [112, 120], allowing matter-wave interferometry experiments in an adjustable double well. Evaporative cooling using an additional, weak rf field has been employed since 2005 [118] to produce BEC in adiabatic potentials. Work presented in this thesis demonstrates the feasibility of using the intrinsic Landau-Zener loss mechanism to evaporate a cloud through the BEC phase transition.

4.2.1 Classical magnetic dipole

A classical magnetic dipole in an applied magnetic field provides a useful introduction to the nature of the interaction between atoms that possess a permanent magnetic dipole and magnetic fields. In the presence of a static, external magnetic field directed along a single axis, a classical magnetic dipole experiences a torque which acts to align it with the field. If the dipole is unable to dissipate energy it precesses around the axis of the field at a rate known as the Larmor frequency ω_{lam}. During this process, both the magnitude of the dipole moment and the angle between it and the applied field remain constant.

The addition of an oscillating component with a frequency of order the Larmor

[1] This is in contrast to optical dipole traps which couple ground and excited states and so must be operated far from atomic resonance to suppress spontaneous emission, necessitating considerable power in the dipole trapping beams.

[2] Such is the smoothness afforded by rf-dressing, this technique is used to smooth out rough magnetostatic potentials such as those found on atom chip experiments [118]. Here the microscopic imperfections in the current carrying wires are manifest in the magnetic fields they produce. The close vicinity of the atoms to the wires gives no distance for these imperfections to be damped out, resulting in heating and fragmentation of the cloud [119]. The addition of a rf field allows the atoms to be confined further from the wires without compromising the trap stiffness or depth.

precession frequency to the static magnetic field causes a change in axis of precession. The oscillating field also exerts a torque on the magnetic dipole, causing it to oscillate about an effective magnetic field that lies in the plane of the static and oscillatory fields. For a static field $\mathrm{B}\hat{\mathbf{e}}_z$ and a field B_{rf} oscillating at a frequency ω_{rf} along $\hat{\mathbf{e}}_x$, transforming into a frame rotating at ω_{rf} gives an effective magnetic field of,

$$\mathbf{B}_{\mathrm{eff}} = \mathrm{B}_{\mathrm{rf}}\hat{\mathbf{e}}_x + \left(\mathrm{B} - \frac{g_F \mu_{\mathrm{B}} \omega_{\mathrm{rf}}}{\hbar}\right)\hat{\mathbf{e}}_z. \tag{4.1}$$

The result is that the magnitude of the magnetic dipole projection along the static field is no longer preserved and oscillates at a characteristic frequency Ω called the Rabi frequency.

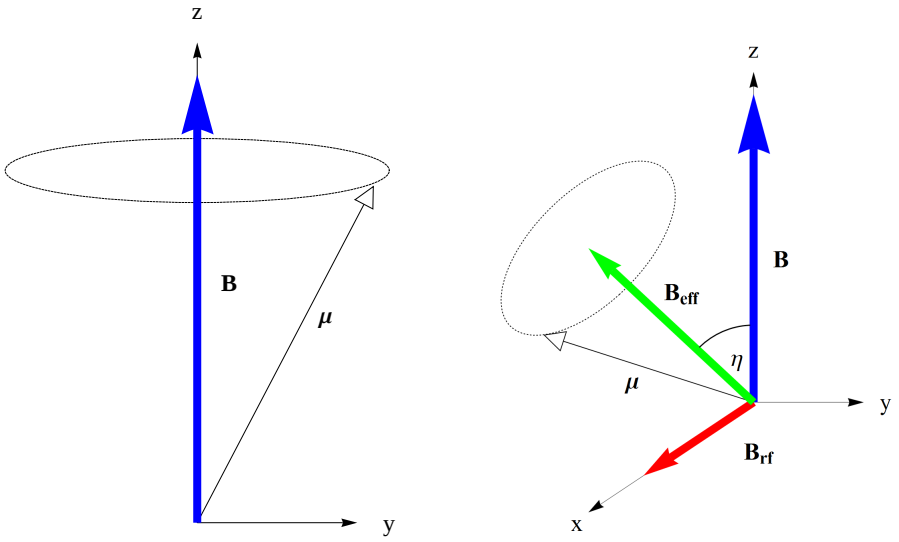


Figure 4.1: Classical dipole in the presence of a magnetic field. Where the field is static (left), the dipole rotates about the field at the Larmor frequency. In the rotating frame, the addition of a non-collinear, oscillating field (right) causes the dipole to precess about an axis defined by an effective magnetic field. The angle η subtended by the effective magnetic field depends on the magnitude and frequency of the applied field.

4.2.2 Semi-classical approximation

The following analysis adopts a perturbative approach to determine the Hamiltonian that describes an atom with hyperfine structure interacting with a classical magnetic field. The interaction between the atom and field is mediated by the atomic dipole moment $\boldsymbol{\mu} = \frac{g_F \mu_{\mathrm{B}}}{\hbar}\boldsymbol{F}$, where $\boldsymbol{F}$ is the total atomic angular momentum operator [121]. All fields are assumed sufficiently small that the quantum number F and its projections

along the quantisation axis m_F remain 'good' quantum numbers throughout.[3] The time-dependent Schrödinger equation for this system is

$$i\hbar\frac{d|\Psi\rangle}{dt} = H|\Psi\rangle. \tag{4.2}$$

Following [122] the atomic dynamics are governed by the Hamiltonian

$$H = \frac{g_F\mu_\mathrm{B}}{\hbar}\mathbf{B}_\mathrm{tot}\cdot\boldsymbol{F}. \tag{4.3}$$

The magnetic field is separated into spatially dependent, static and oscillating terms

$$\mathbf{B}_\mathrm{tot}(\boldsymbol{r},t) = \mathbf{B}_0(\boldsymbol{r}) + \mathbf{B}(\boldsymbol{r},t). \tag{4.4}$$

The time-dependent term can be written out explicitly as

$$\mathbf{B}(\boldsymbol{r},t) = \mathrm{B}_x\cos(\omega_\mathrm{rf}t)\hat{\mathbf{e}}_x + \mathrm{B}_y\cos(\omega_\mathrm{rf}t+a)\hat{\mathbf{e}}_y + \mathrm{B}_z\cos(\omega_\mathrm{rf}t+b)\hat{\mathbf{e}}_z \tag{4.5}$$

where the terms a and b represent the phase with respect to B_x of the components oscillating along the y and z axes respectively. The Hamiltonian H is now written in terms of time-dependent and time-independent parts

$$H = H_0 + H' \tag{4.6}$$

$$H = \frac{g_F\mu_\mathrm{B}}{\hbar}\left[\mathbf{B}_0(\boldsymbol{r})\cdot\boldsymbol{F} + \mathbf{B}(\boldsymbol{r},t)\cdot\boldsymbol{F}\right]. \tag{4.7}$$

In order to simplify the process of solving the Schrödinger equation for the above Hamiltonian, two frame transformations are performed. Under the first, the coordinate system is rotated through a fixed angle to align the z axis with the static field. The new coordinate system is labelled with a tilde, thus $\boldsymbol{r}\rightarrow\tilde{\boldsymbol{r}}$. In this new frame, the interaction between the static field $\mathbf{B}_0(\tilde{\boldsymbol{r}},t)$ and $\boldsymbol{\mu}$ can be written as

$$H_0 = \frac{g_F\mu_\mathrm{B}}{\hbar}\mathbf{B}_0(\tilde{\boldsymbol{r}})\cdot\boldsymbol{F} = \frac{g_F\mu_\mathrm{B}}{\hbar}\mathrm{B}_0F_{\tilde{z}}, \tag{4.8}$$

where $F_{\tilde{z}}$ is the projection of angular momentum operator on the $\tilde{z}$ axis and $\mathrm{B}_0 = |\mathbf{B}(\tilde{\boldsymbol{r}})|$.

In the $|F,m_F\rangle$ basis, $F_{\tilde{z}}$ is given by a diagonal matrix, where the elements of the main diagonal represent the quantum numbers used to label the magnetic sublevels. The experiments reported in this thesis were all performed in the $F=1$ ground state hyperfine manifold of ^{87}Rb , and therefore this analysis is presented with specific reference to this three state system, where the energy spacing between each state is equal. For the sake of clarity,

[3] For rubidium, this assumption is valid for fields up to several thousand gauss [8].

$$F_{\tilde{z}} = \hbar \begin{pmatrix} -1 & 0 & 0 \\ 0 & 0 & 0 \\ 0 & 0 & 1 \end{pmatrix}.$$

Adopting a new coordinate system requires reformulating $\mathbf{B}(\boldsymbol{r}, t)$ in terms of its components with respect to the new axes $\{\hat{\mathbf{e}}_{\tilde{x}}, \hat{\mathbf{e}}_{\tilde{y}}, \hat{\mathbf{e}}_{\tilde{z}}\}$,

$$\mathbf{B}(\boldsymbol{r}, t) \rightarrow \mathbf{B}(\tilde{\boldsymbol{r}}, t) = \mathrm{B}_{\tilde{x}} \cos(\omega_{\mathrm{rf}} t + \alpha)\hat{\mathbf{e}}_{\tilde{x}} + \mathrm{B}_{\tilde{y}} \cos(\omega_{\mathrm{rf}} t + \beta)\hat{\mathbf{e}}_{\tilde{y}} + \mathrm{B}_{\tilde{z}} \cos(\omega_{\mathrm{rf}} t + \gamma)\hat{\mathbf{e}}_{\tilde{z}}. \quad (4.9)$$

The second frame transformation involves transforming into a rotating frame which, by a judicious choice of rotation axis, removes the time dependence of interaction from the Schrödinger equation. In quantum mechanics, rotations within a Hilbert space are effected by unitary operators. In this instance, the operator

$$U = e^{-(iF_{\tilde{z}}\omega_{\mathrm{rf}} t/\hbar)} \quad (4.10)$$

transforms the coordinate system into a frame rotating around the z axis at a frequency ω_{rf} equal to the time-dependent magnetic field. The handedness of the rotation is selected to be the same as the Larmor precession in the system of interest. In matrix representation U is written as[4]

$$U = \begin{pmatrix} e^{-i\omega_{\mathrm{rf}} t} & 0 & 0 \\ 0 & 1 & 0 \\ 0 & 0 & e^{i\omega_{\mathrm{rf}} t} \end{pmatrix}.$$

In the rotating coordinate system the wavefunction of the system is $|\Psi\rangle^{\mathrm{R}} = U|\Psi\rangle$ and so the Schrödinger equation becomes

$$\begin{aligned} i\hbar \frac{d|\Psi\rangle^{\mathrm{R}}}{dt} &= \left(UHU^{\dagger} - i\hbar U \frac{dU^{\dagger}}{dt} \right) |\Psi\rangle^{\mathrm{R}}, & (4.11) \\ &= \left(UH_0U^{\dagger} + UH'U^{\dagger} - i\hbar U \frac{dU^{\dagger}}{dt} \right) |\Psi\rangle^{\mathrm{R}}, & (4.12) \\ &= H^{\mathrm{R}}|\Psi\rangle^{\mathrm{R}}. & (4.13) \end{aligned}$$

The terms within the brackets represent the effective Hamiltonian for the system in the rotating basis which will now be evaluated. Note that by selecting the z axis about which to rotate the coordinate system, the interaction with any components of the magnetic field that lie along this axis is identical to that in the non-rotating basis.[5]

[4] In the case of a diagonal matrix, the matrix exponential is obtained by exponentiating each element on the main diagonal [123].

[5] This can be seen by inspection if one acknowledges that U and $U^{\dagger}$ commute with $F_{\tilde{z}}$.

This is the case for the interaction of the atomic dipole with the static field where

$$UH_0U^\dagger = \frac{g_F\mu_\mathrm{B}}{\hbar}U\mathrm{B}_0F_{\tilde{z}}U^\dagger = \frac{g_F\mu_\mathrm{B}}{\hbar}\mathrm{B}_0F_{\tilde{z}}. \tag{4.14}$$

The final term in the brackets in eqn 4.12 is straight forward to evaluate since

$$\frac{dU^\dagger}{dt} = i\omega_\mathrm{rf}U^\dagger, \tag{4.15}$$

and so

$$i\hbar U\frac{dU^\dagger}{dt} = -\hbar\omega_\mathrm{rf}F_{\tilde{z}}. \tag{4.16}$$

The last term from eqn 4.12 to be evaluated is the interaction between the oscillating magnetic field and the atomic magnetic dipole moment. Following [124] the interaction with fields oscillating parallel to the static field can be neglected if $|\frac{g_F\mu_\mathrm{B}}{\hbar}\mathbf{B}_{\tilde{z}}(\boldsymbol{r},t)| \ll \omega_\mathrm{rf}$. This leaves the only unevaluated term in eqn 4.12 being the interaction between the atomic dipole moment and the oscillating field that lies *perpendicular* to the local static field,

$$\frac{g_F\mu_\mathrm{B}}{\hbar}U\mathbf{B}^\perp_\mathrm{rf}(\tilde{\boldsymbol{r}},t)\cdot\boldsymbol{F}U^\dagger = \frac{g_F\mu_\mathrm{B}}{\hbar}U\left[\mathrm{B}_{\tilde{x}}\cos(\omega_\mathrm{rf}t+\alpha)F_{\tilde{x}} + \mathrm{B}_{\tilde{y}}\cos(\omega_\mathrm{rf}t+\beta)F_{\tilde{y}}\right]U^\dagger. \tag{4.17}$$

At this juncture it is convenient to define a new pair of operators that are linear combinations of the $F_{\tilde{x}}$ and $F_{\tilde{y}}$

$$F_+ = \frac{1}{2}(F_{\tilde{x}} + iF_{\tilde{y}}) \qquad F_- = \frac{1}{2i}(F_{\tilde{x}} - iF_{\tilde{y}}). \tag{4.18}$$

These ladder operators act to create (F_+) or destroy (F_-) quanta of atomic angular momentum [125] e.g. for states within the $F = 1$ manifold

$$F_+|1,m_F\rangle = \sqrt{2}\hbar|1,m_F+1\rangle, \tag{4.19}$$
$$F_-|1,m_F\rangle = \sqrt{2}\hbar|1,m_F-1\rangle. \tag{4.20}$$

The ladder operators in the $F = 1$ manifold can be represented in matrix form,

$$F_+ = \sqrt{2}\hbar\begin{pmatrix}0&0&0\\1&0&0\\0&1&0\end{pmatrix} \qquad F_- = \sqrt{2}\hbar\begin{pmatrix}0&1&0\\0&0&1\\0&0&0\end{pmatrix}.$$

The RHS of eqn 4.17 can now be written in terms of ladder operators

$$\frac{g_F\mu_\mathrm{B}}{\hbar}U\left[\frac{\mathrm{B}_{\tilde{x}}}{2}\cos(\omega_\mathrm{rf}t+\alpha)(F_+ + F_-) + \frac{\mathrm{B}_{\tilde{y}}}{2i}\cos\left(\omega_\mathrm{rf}t+\beta\right)(F_+ - F_-)\right]U^\dagger.$$

The interaction of a single component in full matrix representation is written as,

$$\frac{g_F\mu_B}{2\hbar}U\mathrm{B}_{\tilde{x}}\cos(\omega_{\mathrm{rf}}t+\alpha)(F_+ + F_-)U^\dagger = \frac{g_F\mu_B\sqrt{2}}{2}\mathrm{B}_{\tilde{x}}\times$$
$$\begin{pmatrix} e^{i\omega_{\mathrm{rf}}t} & 0 & 0 \\ 0 & 1 & 0 \\ 0 & 0 & e^{-i\omega_{\mathrm{rf}}t} \end{pmatrix}\begin{pmatrix} 0 & \cos(\omega_{\mathrm{rf}}t+\alpha) & 0 \\ \cos(\omega_{\mathrm{rf}}t+\alpha) & 0 & \cos(\omega_{\mathrm{rf}}t+\alpha) \\ 0 & \cos(\omega_{\mathrm{rf}}t+\alpha) & 0 \end{pmatrix}\begin{pmatrix} e^{-i\omega_{\mathrm{rf}}t} & 0 & 0 \\ 0 & 1 & 0 \\ 0 & 0 & e^{i\omega_{\mathrm{rf}}t} \end{pmatrix}.$$

Performing the matrix multiplications and writing the cosine in terms of complex exponentials gives

$$\frac{g_F\mu_B\sqrt{2}}{4}\mathrm{B}_{\tilde{x}}\begin{pmatrix} 0 & (e^{2i\omega_{\mathrm{rf}}t}e^{i\alpha}+e^{-i\alpha}) & 0 \\ (e^{i\alpha}+e^{-2i\omega_{\mathrm{rf}}t}e^{-i\alpha}) & 0 & (e^{2i\omega_{\mathrm{rf}}t}e^{i\alpha}+e^{-i\alpha}) \\ 0 & (e^{i\alpha}+e^{-2i\omega_{\mathrm{rf}}t}e^{-i\alpha}) & 0 \end{pmatrix}.$$

Under the assumption that the oscillating field is close to resonance[6] and the frequency of Rabi oscillations $\Omega \ll \omega_{\mathrm{rf}}$ is much less than the frequency of the driving field[7] [126], the rotating wave approximation (RWA) may be made. The approximation allows the terms rotating in the opposite sense to coordinate system (i.e. those with a factor of $2\omega_{\mathrm{rf}}$ in the exponent) to be disregarded from the expression on the grounds that their rapid oscillations will average to zero on the timescales relevant to the physics of interest.[8] Therefore making the RWA gives,

$$\frac{g_F\mu_B}{2\hbar}U\mathrm{B}_{\tilde{x}}\cos(\omega_{\mathrm{rf}}t)(F_+ + F_-)U^\dagger = \frac{g_F\mu_B\sqrt{2}}{4}\mathrm{B}_{\tilde{x}}\begin{pmatrix} 0 & e^{-i\alpha} & 0 \\ e^{i\alpha} & 0 & e^{-i\alpha} \\ 0 & e^{i\alpha} & 0 \end{pmatrix}.$$

A similar analysis for the y component gives,

$$\frac{g_F\mu_B}{2\hbar}U\mathrm{B}_{\tilde{y}}\cos(\omega_{\mathrm{rf}}t+\beta)(F_+ - F_-)U^\dagger = \frac{g_F\mu_B\sqrt{2}}{4i}\mathrm{B}_{\tilde{y}}\begin{pmatrix} 0 & -e^{-i\beta} & 0 \\ e^{i\beta} & 0 & -e^{-i\beta} \\ 0 & e^{i\beta} & 0 \end{pmatrix}.$$

Combining the above two expressions to satisfy eqn 4.17 gives the interaction of atomic magnetic dipole moment with the magnetic field oscillating perpendicular to the

[6] In an inhomogeneous magnetic field the Larmor frequency varies spatially and this assumption only valid at certain locations in 3D space. However, in the rf-dressed potentials discussed here these locations match the trapping positions of the atoms, justifying the use of this assumption.

[7] In the experiments reported in the final three chapters of this thesis, the Rabi frequency is typically $\Omega = 2\pi \times 300\,\mathrm{kHz}$ whereas $\omega_{\mathrm{rf}} = 2\pi \times 1.4\,\mathrm{MHz}$.

[8] The inclusion of the counter-rotating terms results (to leading order) in small change in the Larmor frequency known as a *Bloch-Siegert* shift[127].

static field as,

$$\frac{g_F\mu_\mathrm{B}}{\hbar}U\mathbf{B}^\perp(\tilde{\boldsymbol{r}},t)\cdot\boldsymbol{F}U^\dagger=\frac{g_F\mu_\mathrm{B}\sqrt{2}}{4}\begin{pmatrix}0 & \mathrm{B}_{\tilde{x}}e^{-i\alpha}+i\mathrm{B}_{\tilde{y}}e^{-i\beta} & 0\\ \mathrm{B}_{\tilde{x}}e^{i\alpha}-i\mathrm{B}_{\tilde{y}}e^{i\beta} & 0 & \mathrm{B}_{\tilde{x}}e^{-i\alpha}+i\mathrm{B}_{\tilde{y}}e^{-i\beta}\\ 0 & \mathrm{B}_{\tilde{x}}e^{i\alpha}-i\mathrm{B}_{\tilde{y}}e^{i\beta} & 0\end{pmatrix}.$$

Thus the full, now time-independent Hamiltonian in the rotating frame can be written explicitly in matrix representation as

$$H^R=\hbar\begin{pmatrix}-\left[\omega_\mathrm{rf}-\frac{g_F\mu_\mathrm{B}\mathrm{B}_0}{\hbar}\right] & \frac{g_F\mu_\mathrm{B}\sqrt{2}}{4\hbar}\left[\mathrm{B}_{\tilde{x}}e^{-i\alpha}+i\mathrm{B}_{\tilde{y}}e^{-i\beta}\right] & 0\\ \frac{g_F\mu_\mathrm{B}\sqrt{2}}{4\hbar}\left[\mathrm{B}_{\tilde{x}}e^{i\alpha}-i\mathrm{B}_{\tilde{y}}e^{i\beta}\right] & 0 & \frac{g_F\mu_\mathrm{B}\sqrt{2}}{4\hbar}\left[\mathrm{B}_{\tilde{x}}e^{-i\alpha}+i\mathrm{B}_{\tilde{y}}e^{-i\beta}\right]\\ 0 & \frac{g_F\mu_\mathrm{B}\sqrt{2}}{4\hbar}\left[\mathrm{B}_{\tilde{x}}e^{i\alpha}-i\mathrm{B}_{\tilde{y}}e^{i\beta}\right] & \left[\omega_\mathrm{rf}-\frac{g_F\mu_\mathrm{B}\mathrm{B}_0}{\hbar}\right]\end{pmatrix}.$$

Solving for the eigenvalues of this Hamiltonian in the standard way gives the following results,

$$E_{m_F}=\begin{cases}0 & \text{for } m_F=0.\\ \pm\hbar\sqrt{\left(\omega_\mathrm{rf}-\frac{g_F\mu_\mathrm{B}\mathrm{B}_0(\boldsymbol{r})}{\hbar}\right)^2+\left[\frac{g_F\mu_\mathrm{B}}{2\hbar}\right]^2\left(\mathrm{B}_{\tilde{x}}^2+\mathrm{B}_{\tilde{y}}^2+2\mathrm{B}_{\tilde{x}}\mathrm{B}_{\tilde{y}}\sin\left[\alpha-\beta\right]\right)} & \text{for } m_F=\pm1.\end{cases}\tag{4.21}$$

In eqn. 4.21 first term under the square root is interpreted as the angular frequency detuning of the oscillating magnetic field from the atomic resonance frequency at which $\Delta m_F=\pm1$ transitions occur,

$$\delta(\boldsymbol{r})=\omega_\mathrm{rf}-\frac{g_F\mu_\mathrm{B}\mathrm{B}_0(\boldsymbol{r})}{\hbar}.\tag{4.22}$$

At $\delta(\boldsymbol{r})=0$ the resonance condition $|g_F\mu_\mathrm{B}\mathrm{B}_0(\boldsymbol{r})/\hbar|=\omega_\mathrm{rf}$ is satisfied. Neglecting the coupling term, it is apparent that the locus of minimum energy lies on a 3D isosurface of constant $|\mathbf{B}(\boldsymbol{r})|$ defined by the resonance condition. The shape of this surface is determined by the spatial variation of the underlying static field from which the spatially dependent Zeeman shifts derive. In all the experiments presented in this thesis, the static field is a cylindrically symmetric quadrupole field that has its symmetry axis (approximately, see Chapter 7) aligned with gravity. The resulting traps take on elliptical (or more accurately oblate spheroidal) geometries (see fig. 4.2) where r_e the semi-major axis of the ellipsoid is given by

$$r_e=\frac{\hbar\omega_\mathrm{rf}}{g_F\mu_\mathrm{B}B'_\mathrm{q}}.\tag{4.23}$$

The second term in eqn. 4.21 under the square root represents the frequency of Rabi

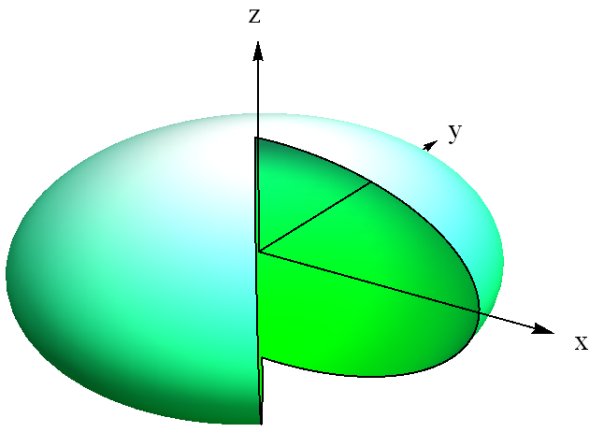


Figure 4.2: The ellipsoidal potential surface resulting from the rf-dressing of a quadrupole magnetic field, around which the resonance condition is satisfied. The potential provides tight confinement in the direction perpendicular to the ellipsoidal surface. The color scheme is representative of the variation in the coupling strength around the ellipsoidal surface when using xy circularly polarised dressing radiation (Green for maximum coupling, Blue/White for zero coupling).

oscillations between the different magnetic sub-levels

$$\Omega(\boldsymbol{r}) = \frac{g_F \mu_{\mathrm{B}}}{2\hbar} \sqrt{\mathrm{B}_{\tilde{x}}^2 + B_{\tilde{y}}^2 + 2\mathrm{B}_{\tilde{x}}\mathrm{B}_{\tilde{y}} \sin\left[\alpha - \beta\right]}, \tag{4.24}$$

$$= \frac{g_F \mu_{\mathrm{B}}}{2\hbar} B_{\mathrm{rf}}^{\perp}(\boldsymbol{r}). \tag{4.25}$$

This term quantifies the degree to which the oscillating magnetic field interacts with the atomic dipole, and for this reason is commonly referred to as the *coupling strength*. Using more concise notation eqn. 4.21 can be written as

$$E_{m_F}(\boldsymbol{r}) = m_F \hbar \sqrt{\delta^2(\boldsymbol{r}) + \Omega^2(\boldsymbol{r})}. \tag{4.26}$$

The eigenstates that correspond to these eigenenergies remain as spin states, however they are tilted away from the original quantisation axis by the angle η (c.f. fig. 4.1) where $\cos\eta = \frac{\delta}{\sqrt{\delta^2+\Omega^2}}$. In the section 4.3, the full quantum mechanical analysis of the problem will demonstrate directly how these states are coherent superpositions of the different Zeeman substates, known as dressed states. Note that in the above expressions, only the components of the oscillating field that are perpendicular to the static field make contributions to the energy of the eigenstates. Therefore the polarisation of the incident

magnetic radiation relative to the local static magnetic field determines the nature of its interaction with the atom.

4.2.3 The perpendicular component

In these experiments the static field is a cylindrically symmetric 3D quadrupole field. The spatial inhomogeneity of this field means that there will always be at least one region in space where the local field and the rf polarisation vector are collinear, resulting in a coupling strength of zero. It will be shown that in such regions, the atoms are lost from trap very quickly via spin-flip transitions. However, a careful choice of rf polarisation which takes into account the symmetry breaking effects of gravity can result in trap lifetimes of order 1 minute. To know how to choose this polarisation vector it is necessary to determine the size of the component of a general oscillating field that is perpendicular to a static quadrupole field.

The goal here is to construct a basis where one of the unit vectors points in the direction of the quadrupole field in all 3D space. Following this, the properties of the vector cross-product may be used to find the concomitant orthonormal vectors that form a complete, right handed basis set. In Cartesian coordinates, the quadrupole field unit vector has the form

$$\hat{\mathbf{e}}_{\tilde{\boldsymbol{z}}} = \frac{1}{\sqrt{x^2+y^2+4z^2}} \left(x\hat{\mathbf{e}}_{\boldsymbol{x}} + y\hat{\mathbf{e}}_{\boldsymbol{y}} - 2z\hat{\mathbf{e}}_{\boldsymbol{z}}\right). \tag{4.27}$$

It is now generally considered useful to employ spherical polar coordinates in order to simplify the problem by exploiting the inherent symmetry of the quadrupole field.

The unit vector that is parallel with the quadrupole field in spherical polar coordinates is

$$\hat{\mathbf{e}}_{\tilde{\boldsymbol{z}}} = \begin{pmatrix} \sin\theta\cos\phi \\ \sin\theta\sin\phi \\ -\cos\theta \end{pmatrix}, \tag{4.28}$$

where the angles θ and ϕ are defined in Cartesian coordinates as,

$$\sin\phi = \frac{y}{\sqrt{x^2+y^2}}, \cos\phi = \frac{x}{\sqrt{x^2+y^2}}, \sin\theta = \frac{\sqrt{x^2+y^2}}{\sqrt{x^2+y^2+4z^2}}, \cos\theta = \frac{-2z}{\sqrt{x^2+y^2+4z^2}}.$$

By taking the normalised cross product with any other vector (not collinear with $\hat{\mathbf{e}}_{\tilde{z}}$) one finds a new unit vector that is perpendicular to $\hat{\mathbf{e}}_{\tilde{\boldsymbol{z}}}$. For convenience the vector $\hat{\mathbf{e}}_{\boldsymbol{z}}$ in spherical polar coordinates is used,

$$\hat{\mathbf{e}}_{\tilde{\boldsymbol{y}}} = \frac{\hat{\mathbf{e}}_{\tilde{\boldsymbol{z}}} \times \hat{\mathbf{e}}_{\boldsymbol{z}}}{|\hat{\mathbf{e}}_{\tilde{\boldsymbol{z}}} \times \hat{\mathbf{e}}_{\boldsymbol{z}}|} = \begin{pmatrix} \sin\phi \\ -\cos\phi \\ 0 \end{pmatrix}. \tag{4.29}$$

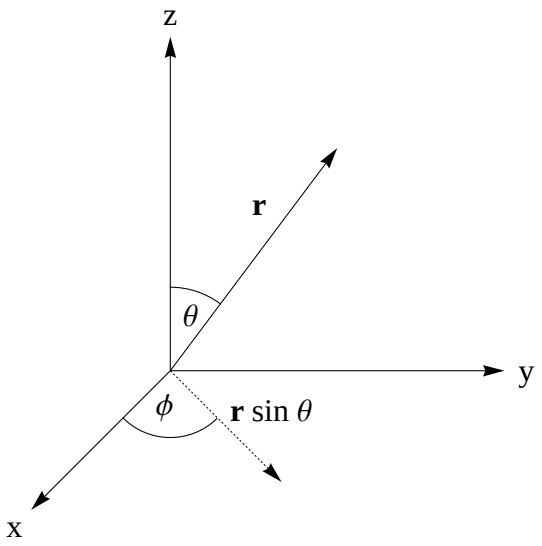


Figure 4.3: Angles within the spherical polar coordinate system defined relative to the Cartesian axes.

A final cross product completes the orthonormal basis set

$$\hat{\mathbf{e}}_{\tilde{\boldsymbol{x}}} = \frac{\hat{\mathbf{e}}_{\tilde{\boldsymbol{y}}} \times \hat{\mathbf{e}}_{\tilde{\boldsymbol{z}}}}{|\hat{\mathbf{e}}_{\tilde{\boldsymbol{y}}} \times \hat{\mathbf{e}}_{\tilde{\boldsymbol{z}}}|} = \begin{pmatrix} \cos\theta\cos\phi \\ \sin\phi\cos\theta \\ \sin\theta \end{pmatrix}. \tag{4.30}$$

The unit vectors can be combined in a single matrix R that represents the transformation from the lab frame into the quadrupole frame

$$\{\hat{\mathbf{e}}_{\tilde{\boldsymbol{x}}}, \hat{\mathbf{e}}_{\tilde{\boldsymbol{y}}}, \hat{\mathbf{e}}_{\tilde{\boldsymbol{z}}}\} = R\,\{\hat{\mathbf{e}}_{\boldsymbol{x}}, \hat{\mathbf{e}}_{\boldsymbol{y}}, \hat{\mathbf{e}}_{\boldsymbol{z}}\}, \tag{4.31}$$

where the orthogonal matrix whose columns are the complete set of orthonormal basis vectors is

$$R = \begin{pmatrix} \cos\theta\cos\phi & \sin\phi & \sin\theta \\ \cos\theta\sin\phi & -\cos\phi & \sin\theta\sin\phi \\ \sin\theta & 0 & -\cos\theta \end{pmatrix}. \tag{4.32}$$

A property of all orthogonal matrices is that the matrix inverse equals the transpose, therefore $R^{-1} = R^{\mathrm{T}}$. The matrix R performs the transformation from laboratory to quadrupole frame, however in the case of the oscillating magnetic radiation, the reverse transformation is required to elucidate the form in the lab frame of the terms $\mathrm{B}_{\tilde{x}}, \mathrm{B}_{\tilde{y}}, \mathrm{B}_{\tilde{z}}$.

So, using the properties of orthogonal matrices,

$$R^{-1} = R^{\mathrm{T}} = \begin{pmatrix} \cos\theta\cos\phi & \cos\theta\sin\phi & \sin\theta \\ \sin\phi & -\cos\phi & 0 \\ \sin\theta\cos\phi & \sin\theta\sin\phi & -\cos\theta \end{pmatrix} \tag{4.33}$$

and the column vector form of eqn 4.5 gives,

$$\mathbf{B}(\tilde{\boldsymbol{r}}, t) = R^{\mathrm{T}}\mathbf{B}(\boldsymbol{r}, t) = \begin{pmatrix} \cos\theta\cos\phi & \cos\theta\sin\phi & \sin\theta \\ \sin\phi & -\cos\phi & 0 \\ \sin\theta\cos\phi & \sin\theta\sin\phi & -\cos\theta \end{pmatrix} \begin{pmatrix} \mathrm{B}_x\cos\omega_{\mathrm{rf}} \\ \mathrm{B}_y\cos(\omega_{\mathrm{rf}}+a) \\ \mathrm{B}_z\cos(\omega_{\mathrm{rf}}+b) \end{pmatrix}$$

$$= \begin{pmatrix} \mathrm{B}_x\cos\omega t\cos\theta\cos\phi + \mathrm{B}_y\cos(\omega_{\mathrm{rf}}t+a)\cos\theta\sin\phi + \mathrm{B}_z\cos(\omega_{\mathrm{rf}}t+b)\sin\theta \\ \mathrm{B}_x\cos(\omega_{\mathrm{rf}}t)\sin\phi - \mathrm{B}_y\cos(\omega_{\mathrm{rf}}t+a)\cos\phi \\ \mathrm{B}_x\cos(\omega_{\mathrm{rf}}t+b)\sin\theta\cos\phi + \mathrm{B}_y\cos(\omega_{\mathrm{rf}}t+a)\sin\theta\sin\phi - \mathrm{B}_z\cos(\omega_{\mathrm{rf}}t+b)\cos\theta \end{pmatrix}.$$

From eqn 4.21 it is apparent that only the $\mathrm{B}_{\tilde{x}}(t)$ and $\mathrm{B}_{\tilde{y}}(t)$ components of the above vector are required to specify Ω. Writing eqn 4.9 in column vector form

$$\mathbf{B}(\tilde{\boldsymbol{r}}, t) = \begin{pmatrix} \mathrm{B}_{\tilde{x}}\cos(\omega_{\mathrm{rf}}t+\alpha) \\ \mathrm{B}_{\tilde{y}}\cos(\omega_{\mathrm{rf}}t+\beta) \\ \mathrm{B}_{\tilde{z}}\cos(\omega_{\mathrm{rf}}t+\gamma) \end{pmatrix} \tag{4.34}$$

and comparing coefficients between the last two vectors gives the following expressions that can be substituted into eqn 4.21

$$\mathrm{B}_{\tilde{x}}\cos\alpha = \mathrm{B}_x\cos\theta\cos\phi + \mathrm{B}_y\cos a\cos\theta\cos\phi + \mathrm{B}_z\cos b\sin\theta, \tag{4.35}$$

$$\mathrm{B}_{\tilde{x}}\sin\alpha = \mathrm{B}_y\sin a\cos\theta\sin\phi + \mathrm{B}_z\sin b\sin\theta, \tag{4.36}$$

$$\mathrm{B}_{\tilde{y}}\cos\beta = \mathrm{B}_x\sin\phi - \mathrm{B}_y\cos a\cos\phi, \tag{4.37}$$

$$\mathrm{B}_{\tilde{y}}\sin\beta = \mathrm{B}_y\sin a\cos\phi. \tag{4.38}$$

For the benefits of the courageous reader, this unwieldy expression is written out explicitly below,

$$\begin{aligned} (B_{\mathrm{rf}}^{\perp})^2 = {} & B_x^2\cos^2\theta\cos^2\phi + \mathrm{B}_x^2\sin^2\phi + \mathrm{B}_y^2\cos^2\phi \\ & + B_y^2\cos^2\theta\sin^2\phi + B_z^2\sin^2\theta + 2\mathrm{B}_x\mathrm{B}_y\cos^2\theta\cos a\sin\phi \\ & + 2\mathrm{B}_y\mathrm{B}_z\cos\theta\sin\phi\sin\theta\cos(a-b) + 2\mathrm{B}_x\mathrm{B}_z\cos\theta\cos\phi\sin\theta\cos b \\ & - 2\mathrm{B}_x\mathrm{B}_y\sin\phi\cos\phi\cos a + 2\mathrm{B}_x\mathrm{B}_y\sin^2\phi\sin a\cos\theta \\ & + 2\mathrm{B}_y\mathrm{B}_z\sin\theta\cos\phi\sin(a-b) + 2\mathrm{B}_x\mathrm{B}_y\sin a\cos\theta\cos^2\phi \\ & + 2\mathrm{B}_x\mathrm{B}_z\sin\phi\sin b\sin\theta. \end{aligned} \tag{4.39}$$

4.2.4 Magnetic rf polarisation

The previous section concluded with an expression detailing how the amplitudes and phases of magnetic radiation specified in the lab frame, influence the strength with which that radiation couples to the magnetic dipole moment of an atom in the quadrupole magnetic field. The following section aims to provide more insight into two specific cases where the magnetic radiation is polarised in such a way as to drastically simplify eqn 4.39. Note that contrary to the conventional definition of polarisation being the plane in which the electric field oscillates, any reference to the polarisation of the dressing radiation in this thesis refers to the plane of oscillation of the magnetic field. This convention is adopted since the magnetic field component makes the dominant contribution to the potential landscape experienced by the atom.

4.2.5 Linear polarisation

Much of the initial work in the double-well TAAP trap was performed by using linearly polarised magnetic radiation directed parallel with gravity, which corresponds to the z axis in the lab frame. Linearly polarised radiation along z is achieved when $\mathrm{B}_x = \mathrm{B}_y = 0$ and $\mathrm{B}_z = \mathrm{B}$, where presence of a only a single non-zero component does not require the phases to be specified. Therefore, the coupling strength can be written as

$$\begin{aligned} \Omega_z^2 &= \left(\frac{g_F \mu_\mathrm{B} \mathrm{B}_\mathrm{rf}}{2\hbar}\right)^2 \sin^2\theta \\ &= \left(\frac{g_F \mu_\mathrm{B} \mathrm{B}_\mathrm{rf}}{2\hbar}\right)^2 \left(\frac{x^2+y^2}{x^2+y^2+4z^2}\right). \end{aligned} \tag{4.40}$$

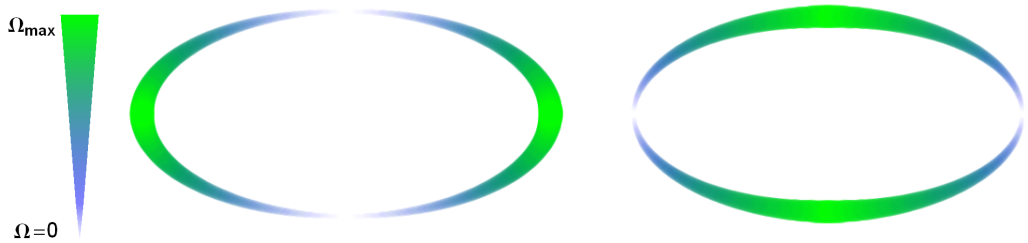


Figure 4.4: Illustration of the variation of the coupling strength around a cross-section of the resonant ellipsoid taken in the $y = 0$ plane. In both cases linearly polarised rf is used, directed along the z axis (left) and x axis (right). From the colour scheme it is apparent that with linear polarisation there are always two regions around the ellipsoid where the coupling strength is zero.

The $x^2 + y^2$ term in the numerator of the spatial term suggests that for this polarisation the coupling strength has a radial symmetry and that it vanishes where $x = y = 0$.

This behaviour is consistent with the result that only the perpendicular component of the magnetic radiation interacts with the atomic dipole. The rf field will always be collinear with the cylindrically symmetric quadrupole on the axis along which it is applied. Where this axis intersects the resonant ellipsoid, a 'hole' in the rf dressed potential results, where atoms do not experience the dressing radiation and are lost by a spin flip transition. Such holes are schematically shown in fig. 4.4.

Naturally accompanying the zero's of the coupling strength are the maxima, which are found in the regions where the quadrupole field and the rf polarisation vector are perpendicular. In the case of linear polarisation, the maxima manifest as bands that form Riemannian circles around the resonant ellipsoid, in the plane perpendicular to the polarisation vector.

4.2.6 Elliptical polarisation

The majority of the experiments reported in this thesis use not linear, but some form of elliptical, or approximately circular polarisation for the magnetic radiation. In the circular case, only a single zero forms on the resonant ellipsoid which lies on the polarisation axis, with its position being determined by the handedness of the rf. Of all the possible options for elliptically polarised rf, the most commonly used is circularly polarised rf in the xy plane. In this instance $\mathrm{B}_x = \mathrm{B}_y = \mathrm{B}$ and $a = \pm\pi/2$, thus the expression in eqn. 4.39 for the coupling strength reduces to,

$$\Omega^2_{\pm xy} = \left(\frac{g_F \mu_\mathrm{B} \mathrm{B}_\mathrm{rf}}{2\hbar}\right)^2 \left(1 \pm \frac{4z}{\sqrt{x^2+y^2+4z^2}} + \frac{4z^2}{x^2+y^2+4z^2}\right). \tag{4.41}$$

This expression gives a single zero and concomitant maxima on the resonant ellipsoid where $x = y = 0$ (i.e. on the z axis). As shown in fig. 4.5 the handedness of the radiation determines whether the minimum is located at the North or South pole of the ellipsoid. In practice, the value $a = +\pi/2$ is overwhelmingly used, as this places the zero of the coupling at the North pole of the ellipsoid, where gravity inhibits most atoms from sampling this region.[9]

4.3 The dressed states

In the following discussion, the dressed states will be presented as the eigenstates for the global Hamiltonian of an atom in the $F = 1$ hyperfine ground state, being interrogated by a quantised radio-frequency field. The bare states of the system that exist in the absence of interactions between the atom and the rf will be introduced, and then the effect of polarisation on the nature of the atom-photon coupling will be discussed for two specific

[9] As is discussed in chapter 8, this configuration gives long trap lifetimes.



Figure 4.5: The variation of the coupling strength around a cross-section of the resonant ellipsoid taken in the $y = 0$ plane. In both cases rf circularly polarised in the xy plane is used. The handedness of the radiation, i.e. $a = \pi/2$ (left) or $a = -\pi/2$ (right) determines the relative location of the coupling strength zero.

polarisations. The full quantum analysis allows a more intuitive understanding of some of the effects that are not predicted under the RWA, but are reported in appendix B.

In contrast with the classical rf field of the perturbative analysis, in this approach the monochromatic field is quantised into discrete energy levels containing N photons. The overall field is best represented by a coherent state $|\alpha\rangle$ that is a superposition of Fock states with a Poissonian distribution around the mean photon number $\langle N\rangle$ that has a width $\Delta N = \sqrt{\langle N\rangle}$ [128]. The extremely large number of photons in the rf field validates the approximation $\sqrt{N+1} \approx \sqrt{N}$ and also justifies the similarities between the results of this analysis and the semi-classical one.

4.3.1 The bare states

In the absence of an interaction between an applied electromagnetic field and an atom in a static magnetic field, the Hamiltonian of this system is simply the sum of the two operators,

$$H_0 = H_A + H_R. \tag{4.42}$$

The atomic Hamiltonian in the presence of a static magnetic field B_0 along $\hat{\mathbf{e}}_z$ can be written in terms of the resonant transition frequency ω_0 between adjacent m_F states as

$$\begin{aligned} H_A &= -\boldsymbol{\mu}\cdot\mathbf{B}, \\ &= \hbar\omega_0 F_z. \end{aligned} \tag{4.43}$$

The Hamiltonian H_R of a single mode of the rf field, where the zero-point energy has been neglected is given by,

$$H_R = \hbar\omega_{\mathrm{rf}} a^\dagger a. \tag{4.44}$$

The eigenstates for H_0 consist of the tensor product of the eigenstates of F_z and $a^\dagger a$. In the $(F = 1)$ three level system of interest, the projection of the atomic angular momentum has three eigenvectors corresponding to the eigenvalues $m_F = 0, \pm 1$. By

considering for the moment only a single mode of the field (containing N photons) the eigenstates of H_0 are written as $|m_F, N\rangle$, with eigenvalues,

$$\begin{aligned} H_0|m_F, N\rangle &= E_{m_F,N}|m_F, N\rangle, \\ E_{m_F,N} &= m_F\hbar\omega_0 + N\hbar\omega_{\rm rf}. \end{aligned} \tag{4.45}$$

If we consider all the relevant energy levels of the rf field, then it is apparent that the bare energy levels form a ladder of states, with each rung being separated at zero field by the photon energy $\hbar\omega_{\rm rf}$. At the positions in space where the resonance condition is fulfilled, states from three neighbouring rungs are degenerate (see fig. 4.6).

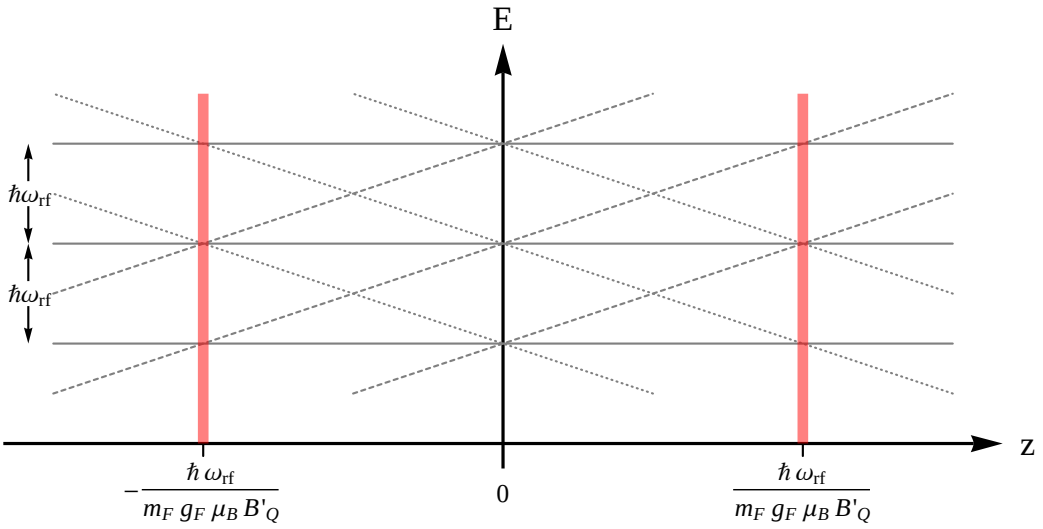


Figure 4.6: Bare energy levels for the $F = 1$ hyperfine manifold in a quadrupole magnetic field dressed by a rf field at a frequency $\omega_{\rm rf}$. In this figure, the quadrupole centre is located at $z = 0$ and all states are defined relative to a quantisation axis directed along the $+z$ direction. The $|m_F = -1\rangle$, $|m_F = 0\rangle$ and $|m_F = 1\rangle$ states are represented by dashed, solid and dotted lines respectively. The red lines mark the two positions (in 1D) relative to the quadrupole centre where the resonance condition is satisfied.

4.3.2 Atom-photon coupling

The global Hamiltonian for this system must include the interactions between the rf and the atom. The use of only electronic ground states means that coupling to empty modes of the field may be neglected. Following [129] the interaction term for radiation with

polarisation vector $\boldsymbol{\epsilon}$ can be written as,[10]

$$H_I = \lambda \left[(\boldsymbol{\epsilon} \cdot \boldsymbol{F}) a + (\boldsymbol{\epsilon}^* \cdot \boldsymbol{F}) a^\dagger \right]. \tag{4.46}$$

where λ is a coupling constant that can be determined from some of the properties of coherent states.

In quantum optics the states $\langle\alpha|$ and $|\alpha\rangle$ are eigenstates of the operators $a^\dagger$ and a respectively. Since the number of photons in a coherent state is not well defined, it follows that operating with the number operator gives,

$$\langle\alpha|a^\dagger a|\alpha\rangle = \alpha^2 = \langle N\rangle \tag{4.47}$$

where α is real. The coherent state is a close description of a classical radiation field, and so the matrix elements when operating with the full quantised interaction Hamiltonian will be the same as those in the classical case [130],

$$\begin{aligned} \lambda\langle\alpha|(a + a^\dagger)|\alpha\rangle &= \frac{g_F \mu_\mathrm{B}}{\hbar} \mathrm{B}_\mathrm{rf}^\perp, \\ \lambda\alpha &= \frac{g_F \mu_\mathrm{B}}{\hbar} \mathrm{B}_\mathrm{rf}^\perp, \\ \lambda &= \frac{g_F \mu_\mathrm{B}}{\sqrt{\langle N\rangle}\hbar} \mathrm{B}_\mathrm{rf}^\perp. \end{aligned} \tag{4.48}$$

Therefore the global Hamiltonian for this system can be written as,

$$H_\mathrm{tot} = m_F g_F \mu_\mathrm{B} |\mathbf{B}(\mathbf{r})| + \hbar\omega_\mathrm{rf} a^\dagger a + \frac{g_F \mu_\mathrm{B}}{\sqrt{\langle N\rangle}\hbar} \mathrm{B}_\mathrm{rf}^\perp \left[(\boldsymbol{\epsilon} \cdot \boldsymbol{F}) a + (\boldsymbol{\epsilon}^* \cdot \boldsymbol{F}) a^\dagger \right]. \tag{4.49}$$

The coupling gives rise to the dressed states which are superpositions of the bare states and the true eigenstates of the global Hamiltonian. As shown in fig. 4.7 in the regions where the resonance condition is satisfied and the bare states are degenerate, the coupling drives the dressed states apart forming an avoided crossing.

As shown in fig. 4.8 the bare state composition of the dressed state changes smoothly with position relative to the centre of the avoided crossing. On resonance, the dressed state is a symmetric superposition of the three bare states, but at large positive or negative detuning, it is dominated by a single bare state.

The bare states are conveniently grouped into manifolds where the angular momentum of each state within the manifold is equal. Still using the $|m_F, N\rangle$ basis each manifold consists of a set of three bare states $\{|m_F, \kappa - \mathrm{sgn}(g_F) m_F\rangle\}$.[11]

Considering only a single manifold (this is equivalent to making the RWA) the matrix

[10] Note the dipole approximation, commonly employed in the optical domain is tacitly assumed here. The macroscopic wavelength of the dressing radiation ($\sim 200\,\mathrm{m}$) acts to strengthen the validity of this approximation.

[11] κ is an integer quantised in units of angular momentum $\hbar$. The product $\kappa\hbar$ represents the total angular momentum of the system of an atom in the $F = 1$ manifold and N photons.

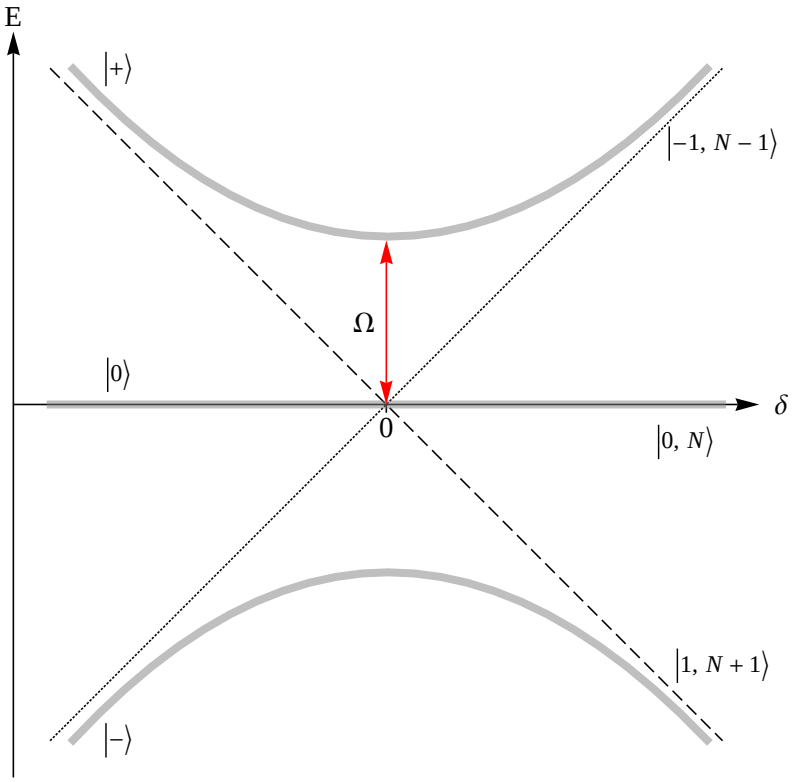


Figure 4.7: Atomic energy level behaviour in the region where the resonance condition is satisfied. The uncoupled bare states from fig. 4.6 are labelled on the right hand side of the figure. The dressed states (thick, grey lines), labelled on the left hand side of the figure always have a finite separation in energy and are said to undergo an avoided crossing where $\delta \to 0$. The separation is equal to the coupling strength and thus proportional to the magnitude of the perpendicular component of the dressing radiation. At large detunings the dressed states tend asymptotically towards one of the bare states.

form of the global Hamiltonian for the $F = 1$ state can be written as

$$\{\langle m_F, \kappa - \mathrm{sgn}(g_F)m_F|\} H_{tot} \{|m_F, \kappa - \mathrm{sgn}(g_F)m_F\rangle\} = \hbar \begin{pmatrix} \kappa\omega_{\mathrm{rf}} + \delta & \frac{\Omega^*}{\sqrt{2}} & 0 \\ \frac{\Omega}{\sqrt{2}} & \kappa\omega_{\mathrm{rf}} & \frac{\Omega^*}{\sqrt{2}} \\ 0 & \frac{\Omega}{\sqrt{2}} & \kappa\omega_{\mathrm{rf}} - \delta \end{pmatrix}. \tag{4.50}$$

The eigenvectors of this matrix are conveniently written in the $|F, m_F\rangle$ basis in terms of the mixing angle η (c.f. fig. 4.1) where $\sin\eta = \frac{\Omega}{\sqrt{\delta^2+\Omega^2}}$ and $\cos\eta = \frac{\delta}{\sqrt{\delta^2+\Omega^2}}$ as,

$$|+\rangle = \frac{1}{2}\left[(1+\cos\eta)|1,1\rangle + \sqrt{2}\sin\eta|1,0\rangle + \frac{\sin^2\eta}{1+\cos\eta}|1,-1\rangle\right], \tag{4.51}$$

$$|0\rangle = \frac{1}{2}\left[-\sqrt{2}\sin\eta|1,1\rangle + 2\cos\eta|1,0\rangle + \sqrt{2}\sin\eta|1,-1\rangle\right], \tag{4.52}$$

$$|-\rangle = \frac{1}{2}\left[(1-\cos\eta)|1,1\rangle - \sqrt{2}\sin\eta|1,0\rangle + \frac{\sin^2\eta}{1-\cos\eta}|1,-1\rangle\right]. \tag{4.53}$$

The dressed state in which atoms are trapped and manipulated in this experiment is the $|+\rangle$ state that pertains to the eigenvalue that is a minimum where $\delta = 0$.

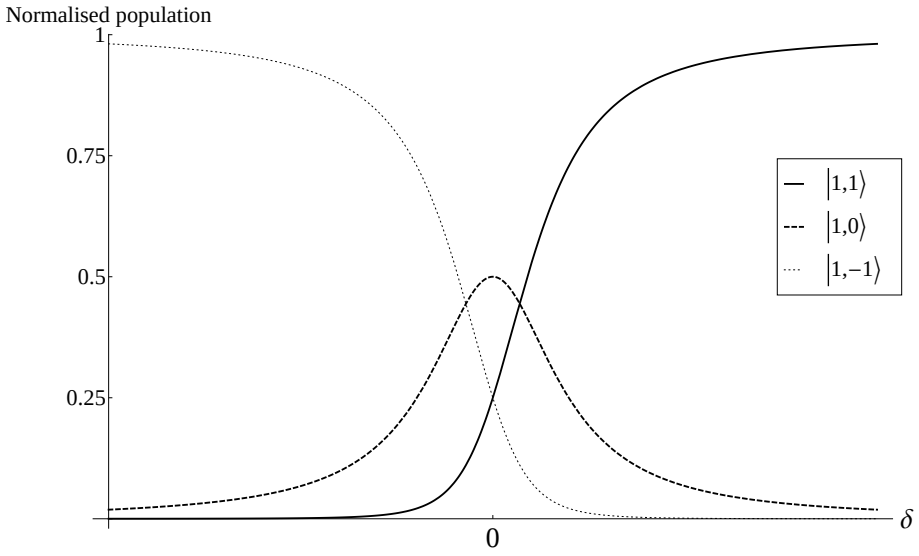


Figure 4.8: The normalised contributions by the different magnetic substates to the $|+\rangle$ dressed state plotted as a function of the detuning δ. Exactly on the resonance, the bare states provide a symmetric distribution to the composition of the dressed state, i.e. $|m_F = 1\rangle$ and $|m_F = -1\rangle$ contribute 0.25, and $|m_F = 0\rangle$ contributes 0.5 to the relative population.

Under the RWA dressed states only contain contributions from a single κ manifold, however as is discussed in the following section and experimentally demonstrated in appendix B, the RWA fails to predict certain spectroscopic results which suggest that higher-order coupling to other manifolds also occurs. In some ways this is not surprising as the RWA assumes that $\omega_{\rm rf} \gg \Omega$, however it can be the case that only a factor of 2 separates these quantities. The coupling between bare states (within and beyond the RWA) is also responsible for radiative shifts in the position of the avoided crossing relative to the bare state level crossing. The size of these shifts also scales with coupling strength (and detuning) however they do not significantly alter the behaviour of the trap [131] and have not been investigated experimentally.

Circular polarisation

The general expression in eqn. 4.46 is simplified significantly by considering only circularly polarised rf. The polarisation vector for circularly polarised rf along the z axis is $\boldsymbol{\epsilon}_{\pm} = \frac{1}{\sqrt{2}}\left(\hat{\mathbf{e}}_x \pm i\hat{\mathbf{e}}_y\right)$ thus H_I takes the form,

$$H_I^{\sigma^+} = \frac{g_F \mu_{\rm B} {\rm B}_{\rm rf}}{2\hbar\sqrt{\langle N\rangle}}\left[aF_+ + a^\dagger F_-\right] \tag{4.54}$$

or

$$H_I^{\sigma^-} = \frac{g_F \mu_{\rm B} {\rm B}_{\rm rf}}{2\hbar\sqrt{\langle N\rangle}}\left[aF_- + a^\dagger F_+\right]. \tag{4.55}$$

The interaction term couples together bare states of H_0 where the total angular momentum is conserved. For the case of $H_{I\sigma^+}$, by definition the σ^+ photons carry $+\hbar$ of angular momentum along the $+z$ axis. Therefore the total angular momentum of this system equals $(\mathrm{sgn}(g_F)m_F + N)$, and only states such as $|m_F, N-1\rangle$ and $|m_F+1, N\rangle$ are coupled together by the σ^+ photons. Similarly for σ^- photons carrying $-\hbar$ angular momentum, the total angular momentum is $(\mathrm{sgn}(g_F)m_F - N)$ and for any interaction this quantity is conserved. The matrix elements are thus,

$$\langle m_F, N|H_I^{\sigma^+}|m'_F, N'\rangle = \frac{g_F\mu_{\rm B}{\rm B}_{\rm rf}}{2\hbar\sqrt{\langle N\rangle}}\left(\sqrt{2}\hbar\sqrt{N}\delta_{m_F,m_F+1}\delta_{N,N-1} + \sqrt{2}\hbar\sqrt{N+1}\delta_{m_F,m_F-1}\delta_{N,N+1}\right) \tag{4.56}$$

where if the approximations for the large number of photons in each field mode are made, the results from the semi-classical analysis are reproduced (i.e. eqn. 4.41). Circularly polarised radiation of a given handedness produces a single avoided crossing between the dressed states at the resonant frequency. No further coupling between bare states occurs at higher frequencies since this would violate the conservation of angular momentum.[12]

[12]Note that this is also apparent in the semi-classical analysis where, when considering only circularly polarised photons, the rotating wave approximation is exact.

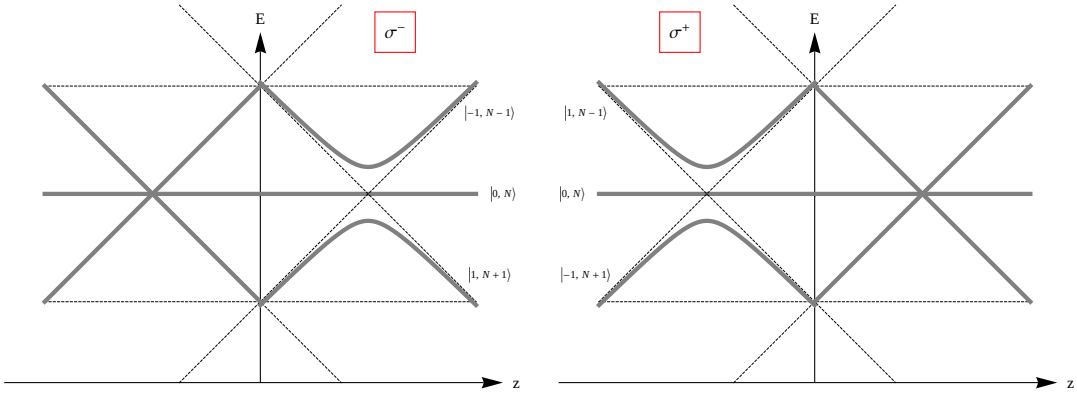


Figure 4.9: Energy levels for σ^- (left) and σ^+ (right) polarised rf. The energy of the bare (dotted) and dressed states (solid) as a function of position in a static quadrupole field is plotted. Note some energy levels have been omitted in the interests of clarity. The quantisation axis is taken to be along $+z$. The bare states that are coupled together by the dressing radiation are labelled.

Linear polarisation

For linearly polarised rf where $\boldsymbol{\epsilon} = \hat{\mathbf{e}}_x$, the expression for H_I becomes,

$$H_I^{\pi} = \frac{g_F \mu_B B_{rf}^x}{2\hbar\sqrt{\langle N\rangle}} \left[(F_+ + F_-)(a + a^\dagger)\right]. \tag{4.57}$$

Any linearly polarised photon can be decomposed into a coherent superposition of two circularly polarised photons of opposite handedness. Thus the interaction Hamiltonian can be written as

$$\begin{aligned} H_I^{\pi} &= \frac{g_F \mu_B B_{rf}^x}{2\hbar\sqrt{\langle N\rangle}} \left[aF_+ + a^\dagger F_- + a^\dagger F_+ + aF_-\right], \\ &= \frac{g_F \mu_B B_{rf}^x}{2\hbar\sqrt{\langle N\rangle}} \left[H_I^{\sigma^+} + H_I^{\sigma^-}\right]. \end{aligned} \tag{4.58}$$

In this case avoided crossings are induced to leading order at $z = \pm\frac{\hbar\omega_{rf}}{g_F\mu_B B_q'}$ (see fig. 4.10). However, unlike the circularly polarised case where only the effects predicted by the RWA in the semi-classical analysis are observed, the situation is far richer for linear polarisation. The crossing of the $H_I^{\sigma^+}$ and $H_I^{\sigma^-}$ terms allows higher order transitions to occur, producing many more avoided crossings. The composition of the dressed states in this instance involves bare states from a number of different manifolds, that are coupled together by higher order multiphoton processes where the conservation of energy and angular momentum is ensured by consecutive interactions with σ^+ and σ^- photons.

The graphs shown in figs. 4.9 and 4.10 provide a more intuitive understanding of

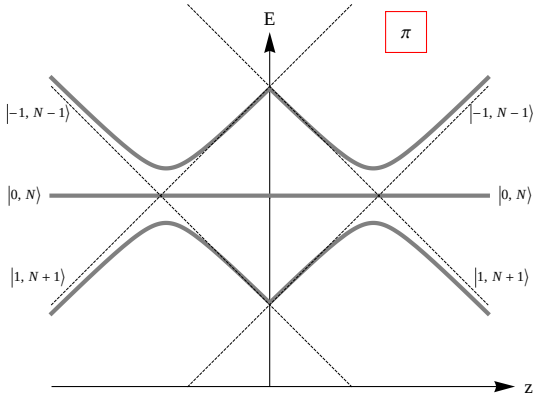


Figure 4.10: Linearly polarised dressing radiation produces avoided crossings at symmetrical positions in a quadrupole field. A nominal radiative shift in the resonance position is included.

the variation of the coupling strength around the resonant ellipsoid. The symmetry in the coupling strength that is manifest with linear polarisation results from dressing by a superposition of circularly polarised photons with opposite handedness. Whereas the purely circular case has a single zero in the coupling strength.

4.3.3 Transitions between rf-dressed states

Rf forced transitions

A second rf field with an amplitude significantly smaller than that of the dressing radiation (so as to not noticeably perturb the energy landscape of the dressed states) can drive transitions between dressed states. In general a transition between dressed states can be excited if there exists at some point in frequency space an avoided crossing between the dressed states. Where circularly polarised rf is applied, the rotating wave approximation is exact and so only three allowed transitions are predicted [132]. When dressing with linearly polarised radiation, transitions between dressed states of different manifolds are allowed via multiphoton processes. A chain of allowed transitions occur at frequencies $\nu_{spec} = p\left(\frac{\omega_{\mathrm{rf}}}{2\pi}\right) \pm \Omega$ where p is a positive integer [133]. An experimental demonstration of these predictions is the subject of appendix B.

Landau-Zener transitions

The finite energy gap between dressed states means transitions between states can occur even in the absence of an additional rf field. The Landau-Zener model [134] estimates the probability of non-adiabatic transitions occurring naturally between eigenstates of a given system. In this analysis the probability is related to the energy separation of the states and the rate at which the bare states approach each other.

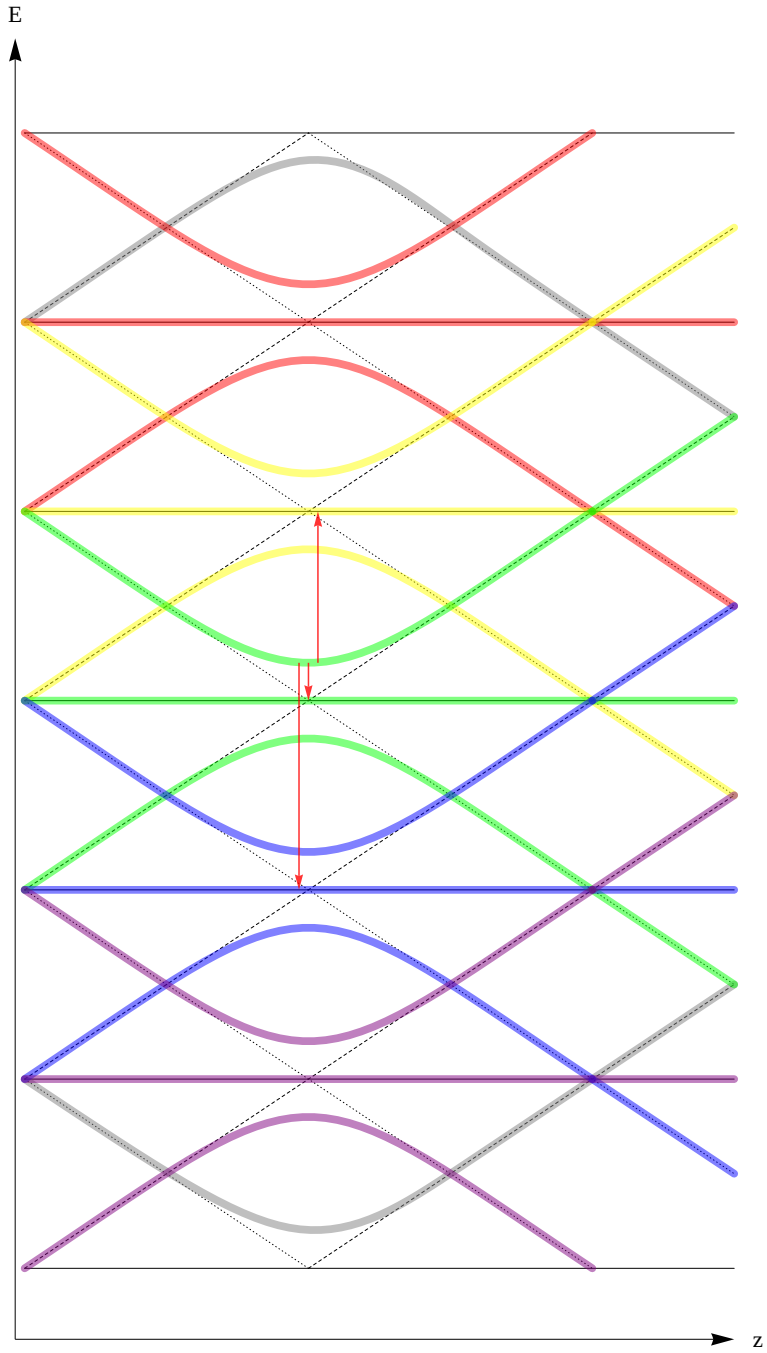


Figure 4.11: Energy levels in a three state rf-dressed quadrupole field. The left hand edge of the figure represents the region in space where the quadrupole field is zero. The Zeeman states $m_F = -1$ (dashed), $m_F = 0$ (solid) and $m_F = 1$ (dotted) for increasing N are illustrated. The corresponding dressed states grouped into 5 manifolds are included in colour (dressed states not belonging to these manifolds are coloured grey). Transitions between the dressed states allowed within the RWA are indicated from a single manifold.

In the case of atoms moving in dressed potentials, the energy separation is equal to the difference in the spatially dependent eigenvalues of each state, which takes its minimum value of Ω at the centre of the avoided crossing. The rate at which the bare states approach each other can be considered equal to the rate at which an atom traverses the avoided crossing and hence equals the rate of change of the detuning, i.e. $\frac{d\delta}{dt}$.

The original work performed independently by Landau and Zener considered non-adiabatic transitions in 2 state systems, however it has subsequently been expanded on to include 3 state [135] and then N state [136] systems. In the $F = 1$, 3 state system where the spatial gradient of the detuning is parameterised by the quadrupole gradient B'_{q}, the probability of an atom making a non-adiabatic transition is

$$P_{\mathrm{LZ}} = 1 - \left(1 - e^{-\frac{\pi\hbar\Omega^2(\mathbf{r})}{2g_F\mu_{\mathrm{B}}B'_q v}}\right)^2, \tag{4.59}$$

where v is the velocity of the atom through the avoided crossing. For rf-dressed traps that confine atoms at the avoided crossing, Landau-Zener transitions to untrapped dressed states are often the limiting factor for the trap lifetimes and thus there must be a finite coupling strength at all points where atoms are trapped. The spatial dependence of the coupling strength in a dressed quadrupole means that there will always regions where $\Omega \to 0$, and thus the lifetime of an atom trapped in this region is vanishingly short. By engineering a potential that allows only the most energetic atoms to sample such regions, evaporative cooling via Landau-Zener losses is possible. Some cooling via this method was achieved by researchers in Paris [113]. In chapter 7 evidence for controlled, efficient evaporation across the BEC phase transition using Landau-Zener transitions is presented.

4.4 Time-averaged adiabatic potentials

The development of increasingly sophisticated trapping potentials for ultracold atoms has catalysed research in the field of quantum degenerate gases. Optical lattices, double well potentials and systems of reduced dimensionality are examples where new physics has been elucidated by putting cold atoms into new types of potential landscapes. Initially large efforts were made to improve the magnetostatic traps that provided the conservative potentials within which the first BEC's were created. Subsequently, much of the focus shifted to optical dipole traps as they were perceived to offer tighter confinement and superior flexibility to their magnetic counter-parts, whilst remaining relatively simple to implement.[13]

The time-averaged adiabatic potential (TAAP) represents the state of the art in versatile magnetic potentials for ultracold atoms. A TAAP is formed by the superposition

[13]It should be noted that a large number of hybrid magnetic and optical traps that employ weak magnetic confinement along a one or two axes to generate a high degree of trap anisotropy also exist [137, 138, 114].

of three independent magnetic fields; the adiabatic potential that results from a magnetostatic trap dressed with a rf field, is time-averaged by a kHz frequency magnetic field. By carefully controlling the relative influence of each field on the atom, TAAPs can be used to realise a broad palette of trap geometries where often simple, adiabatic routes to load and dynamically adjust the traps exist.

The concept for a TAAP was first proposed by Lesanovsky and von Klitzing in 2007 [139], and first realised in Oxford in 2010 [140, 141]. A double-well, ring and modified shell geometry have so far been observed in the laboratory, however numerous alternative options were discussed in the original proposal, including multiple traps that repeated at regular intervals.

Each magnetic field contribution to a TAAP can be generated by centimetre scale magnet coils located macroscopic distances from the atoms. This property affords TAAPs the advantage that the fields that interact with the atoms are smooth, have low heating rates and allow simple alignment that does not require repeated adjustment.

In a TAAP trap the time-averaging field is used to essentially limit the regions of the rf-dressed potential that the atoms can sample. In the absence of all other fields, in an rf-dressed potential the competition between gravity and the variation in the coupling strength will determine where the atoms sit around the resonant ellipsoid, however in the TAAP double well configuration, a radial time-averaging field creates two symmetrical minima at specific points on the resonant ellipsoid. In the ring geometry, the single axial time-averaging field causes atoms to confined at the equatorial regions of the ellipsoid.

Chapter 5

The experimental apparatus

5.0.1 Overview

The apparatus for this experiment was designed, built and optimised for the purpose of making and probing the properties of quantum degenerate gases of dilute ^{87}Rb vapour when loaded into non-trivial trapping geometries. In this chapter a full description of the major systems (magnetic trapping coils and circuitry, lasers, vacuum system, and computer control) is given, with the following chapter describing how they operate in concert in a typical experimental sequence.

The MOT chamber and science cell are the two regions of the vacuum system where active cooling of the atoms takes place (Doppler cooling in a pyramidal MOT in the MOT chamber, and evaporative cooling in a magnetic trap in the cell). The regions are separated for reasons of vacuum pressure (see section 5.1) and to improve the optical access for probing the gas when cooled to the quantum degenerate regime. The atoms move between the two regions whilst confined in a quadrupole magnetic trap in a two-stage process where, first the coils generating the magnetic trapping field are translated along optical bench using a motorised translation stage. For this reason they are referred to as the *Transport* coils.[1] When the *Transport* coils come to rest, the atoms complete the journey to the site of condensate production via series of current ramps in static overlapping coil pairs (a technique pioneered by researchers in Munich [142]) in a process referred to as magnetic transfer (see section 6.1). The current ramps are empirically optimised to smoothly shift the centre of the quadrupole trap along the x axis of the vacuum system. Once in their final position in the centre of the science cell, the atoms are evaporatively cooled via rf spin-flip transitions down to BEC. The technique of magnetic

[1]The *Transport* coils are used to generate the MOT field during the optical cooling stage of the experiment, then as is expanded on in section 6.0.2 the current in the coils is jumped rapidly after the MOT light is switched off to establish a stiff quadrupole potential to trap the atoms in.

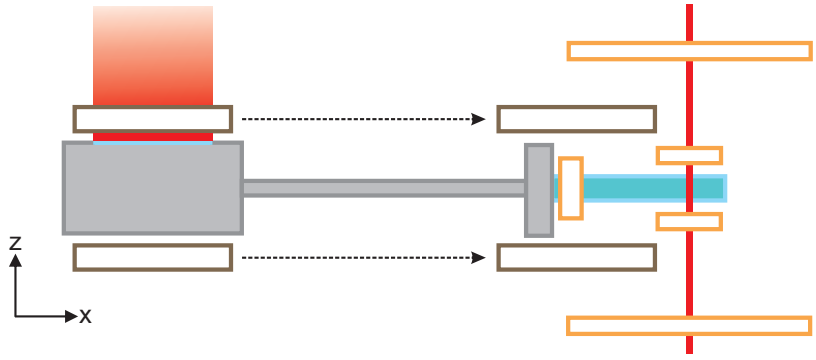


Figure 5.1: Overview of the experimental apparatus (not to scale). The vacuum system (MOT chamber on the left is separated from the science cell on the right by a 10 mm diameter differential pumping tube) is shown in cross-section in xz plane. The dark, hollow rectangles represent the *Transport* coils that provide the quadrupole field for the MOT operation and the magnetic trap in which the atoms are transported (by translating the coil positions) out of the MOT chamber and along the vacuum system. The lighter, hollow rectangles represent the static magnetic coils that facilitate the magnetic transfer process under which the atoms are moved to their final position at the centre of the glass cell. The single incident MOT beam and vertical imaging probe beam are also shown.

transport by translating the field generating coils was selected for this experiment due its simplicity to implement and control. A discussion of the relative merits of other possible techniques for moving cold atoms from one region of a vacuum system to another is presented in [143].

The light required to cool the atoms in the pyramid MOT, and probe them in the glass science cell derives from a system of diode lasers which are frequency stabilised to particular atomic transitions in ^{87}Rb. In fig. 5.2 a simplified picture of the laser system in use for this experiment is shown. The 'master' laser is frequency stabilised to the cyclical cooling transition $5^2S_{1/2} \rightarrow 5^2P_{3/2}$ in ^{87}Rb . The frequency detuning (below the atomic resonance) that increases the efficiency of cooling in MOT necessitates the use of acousto-optic modulators to controllably shift the frequency of the light from 'master' laser (which by the process of injection locking determines the frequency of the 'slave' laser). The repumping laser is used to depopulate the $F = 1$ hyperfine manifold in which atoms will not scatter light from the 'master' laser. This is relevant both in the pyramid MOT where off resonant excitation can cause atoms to fall out of the cooling cycle and in the glass cell since atoms are magnetically trapped in the $|F = 1, m_F = -1\rangle$ Zeeman state and so need to be repumped into the $F = 2$ manifold prior to imaging by the probe beam.

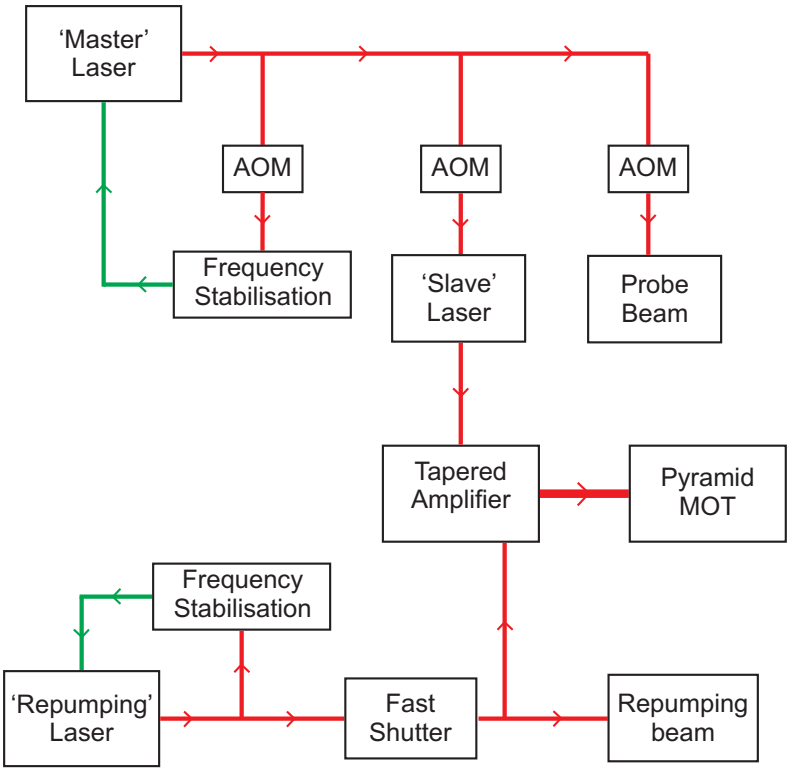


Figure 5.2: Simplified diagram of the laser system. The red lines show the paths of the laser light and the green lines represent electrical feedback signals that are used to stabilise the frequency of each laser.

5.1 The vacuum system

The vacuum system within which all the experiments were conducted is a combination of custom built and off-the-shelf components. The vacuum system can essentially be divided into two chambers, separated by a differential pumping tube. Due to the requirement for the system to maintain ultra-high vacuum (UHV) conditions, CF vacuum flanges are used exclusively to connect and seal the system.

The MOT chamber is a large (O.D. 203 mm) cylindrical chamber that houses the pyramid MOT mirrors and the rubidium dispensers. This custom designed chamber was manufactured from 316L stainless steel in the Clarendon laboratory workshop. The chamber is sealed by a custom made, non-magnetic viewport manufactured by UKAEA.[2] The MOT chamber is pumped by a $40\,ls^{-1}$ ion pump (Varian, Vacion Plus 40 Starcell).

[2]In fact the MOT chamber was designed such that it would be sealed with a standard DN160CF viewport, however the number of bolts holes had to be reduced from 20 to 18 in order to prevent the bolts impinging on the transport path of the atoms.

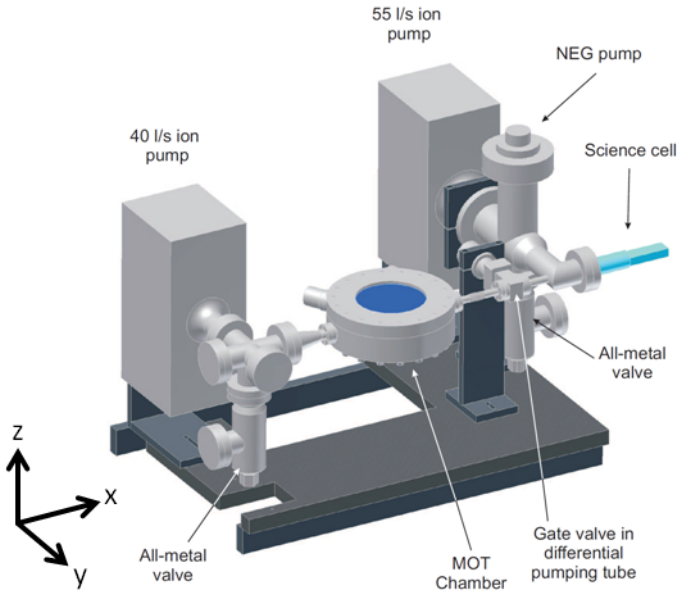


Figure 5.3: Labelled CAD drawing of the vacuum system reproduced from [143]. A Cartesian coordinate system is used to label the principal axes of the experiment, i.e. magnetic transport direction (x), horizontal imaging direction (y), anti-parallel local gravity direction (z).

This chamber was designed to have a large internal diameter to house the pyramidal MOT mirrors, but a small vertical height, i.e. of the order of the outer diameter of a standard DN40CF flange (70 mm) to avoid increasing the separation of the *Transport* coils (that locate above and below the chamber, providing both the quadrupole field for MOT operation and magnetic transport out of the chamber). The final chamber height was fixed at 74 mm.

The science cell is the moniker given to the glass chamber where the atoms are cooled to quantum degeneracy and all subsequent experiments take place. The cell is constructed from 2 mm thick quartz, has external measurements of 14 mm vertically and 20 mm horizontally[3] and is 70 mm in length. The cell is evacuated by a $55\,\mathrm{ls}^{-1}$ ion pump (Varian, Vacion Plus 55 Starcell) and a non-evaporable getter (NEG) pump (SAES, CapaciTorr-CF35, with C-400-2 DSK-St172 cartridge) which was activated before completion of the bakeout process.

The continuous emission of rubidium by the dispensers in the MOT chamber ensures a good vapour pressure for MOT loading however it causes the vacuum pressure to be limited to the order of 10^{-9} mBar. The lifetime of magnetically trapped atoms in

[3]This rectangular cross section was chosen to allow the vertically offset *Quad* coils that generate the quadrupole potential that underlies all trapping geometries in the glass cell to be positioned closer together to increase the maximum achievable field gradients.

this chamber was measured at 1.68 s, a value wholly unsuitable for efficient evaporative cooling in magnetic traps. A pressure gradient is thus required to allow the pressure to be significantly lower in the science cell. This is principally achieved by a 10 mm diameter, differential pumping tube that has a conductance of $\sim 1\,\mathrm{ls}^{-1}$ for a room temperature gas in the molecular flow regime. This tube, in parallel with the higher pumping speeds for gases such as hydrogen, allows the pressure in the glass cell to be approximately a factor of 100 lower, leading to lifetimes of 109 s for atoms in the TOP trap. A gate valve (Caburn, 302011) is located at the centre of the differential pumping tube that isolates each side of the vacuum system when fully closed, preserving the vacuum in one chamber if the other is controllably vented.[4]

5.2 The laser system

The development of the diode laser as a tool for atomic physics [144, 145] has greatly simplified the process of producing frequency stabilised, narrowband light that can saturate atomic hyperfine transitions. Diode lasers offer an inexpensive, compact and low maintenance method of generating coherent light, and where the correct wavelengths can be obtained, they are the leading choice for laser cooling type applications.

The relatively flat gain profile of diode lasers means that some considerable effort must be made to narrow the free running linewidth (several nm) to something below the natural linewidth of an electronic excited state transition (a few MHz in ^{87}Rb). The laser diode is housed in a custom built laser head which is temperature stabilised by a thermoelectric peltier cooler. The collimated diode is incident upon a diffraction grating mounted in Littrow configuration in order to direct the first diffraction order back into the laser, forming an external cavity.[5] If this setup, collectively known as an external cavity diode laser (ECDL) is properly aligned then linewidths of a few hundred kHz can be simply achieved [146, 147]. A slit in the grating mount allows the use of piezoelectric stack mounted on the end of micrometer screw to be used to change the external cavity length and thus scan the frequency of the laser.

5.2.1 The cooling light

Cooling light is the name given to the light field red-detuned from the cycling transition $|F = 2\rangle \rightarrow |F' = 3\rangle$ on the D2 line of ^{87}Rb . The light derives from two ECDLs arranged in 'master' and 'slave' configuration. The master laser consists of a laser diode (Eagleyard, EYP-RWE-0790-04000-0750-SOT01-0000) housed in a commercial laser head

[4]The integrity of the gate valve was tested when the glass science cell that originally formed part of the vacuum system was replaced. No increase in the pressure of the MOT chamber was observed during the two weeks that the valve was closed whilst the replacement cell was fitted.

[5]Diodes without anti-reflection (AR) coating on the front facet contain an internal resonator with a mode structure that competes with the external cavity to determine the laser frequency. An AR coated diode is used in the 'master' laser.

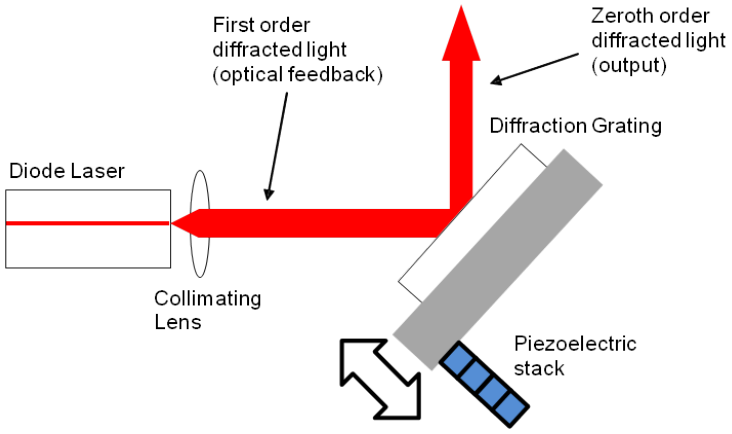


Figure 5.4: A diode laser aligned on a diffraction grating in Littrow configuration. The first order light from the grating is coupled back into the laser to form an external cavity, the length of which can be adjusted by the piezoelectric device.

(Toptica DL 100). Toptica modules are used to control the diode current (DCC 110) and laser head temperature (DTC 110). The master is frequency stabilised (or locked) to a reference frequency using a technique called modulation transfer spectroscopy. The slave laser is formed by a diode (Sanyo DL-7140-201) in an in-house built laser head, where the current and temperature is controlled by Clarendon built units (EW1291 and EW1251 respectively). The slave laser is injection locked [148] by the master and will follow frequency changes of this laser for several hundred MHz

Frequency stabilisation

The technique of modulation transfer spectroscopy (MTS) [149, 150] was first employed to lock a diode laser to an atomic reference frequency in cesium [151] however the particular method followed in this experiment was also demonstrated for rubidium [152]. Modulation transfer spectroscopy employs the familiar process of saturated absorption spectroscopy where a single incident beam is split into two parts (a stronger 'pump' and weaker 'probe' beam) which counter propagate through a room temperature rubidium vapour cell. The probe beam[6] is then incident upon a fast photodiode (Thorlabs PDA36A). Prior to entering the cell the pump beam passes through an electro-optical modulator (EOM) (Photonics Technology EOM01100013) that modulates the laser frequency at a frequency $\omega_m = 10.15\,\mathrm{MHz}$. The pump beam can be considered to have gained two weak, symmetric side bands located $\pm\omega_m$ from its strong carrier frequency. Where the beams overlap inside the vapour a strong non-linear process results in the pump modulation being mapped on to the probe beam. At the heart of modulation

[6]Note the term 'probe beam' also refers to the imaging beam that is used to analyse the atoms in the science cell.

transfer is a four-wave mixing process that combines the two frequencies of the pump beam with the single frequency of the probe beam to form a sideband for the probe. The four-wave mixing criteria is only satisfied near an atomic resonance and is strongest on the closed transition where atoms cannot relax out of the process.

To generate the error signal that will act as a frequency discriminator for the feedback electronics, the beat pattern between the probe and its sidebands is detected on the photodiode. This signal is then amplified (Minicircuits ZFL-500HLN) before being mixed with the EOM driving signal (10.15 MHz) in a phase sensitive demodulation process by a mixer (Minicircuits ZRPD-1). A phase shifter (Minicircuits JSPHS-12) is used to adjust the phase of the photodiode signal prior to the mixer in order to maximise the peak-to-peak amplitude and gradient of the error signal. The high frequency output of the mixer is blocked by a low pass filter (cutoff frequency 1.9 MHz), leaving only the DC error signal which is fed into a PID controller (Toptica PID 110). The output of the PID controller is sent to the piezoelectric device which adjusts the length of the cavity in order to correct for unwanted drifts in the centre frequency of the laser.

MTS operates on similar principles to the widely used Pound-Drever-Hall technique [153] for stabilising the frequency of a laser. The main difference between the two locking techniques is that under MTS the modulation is only present on one of the beams. The principal advantage of locking by MTS is that sidebands are not present on the light forming the cooling or imaging beams, thus avoiding any potential problems when detuning each beam by more than a few MHz. The modulation transfer process requires the sub-Doppler resonance condition to be fulfilled, therefore a clean, zero background error signal is produced. As mentioned MTS is most efficient on a closed transition, thus the strongest error signal is produced on the cooling transition, allowing the laser to be actively stabilised to this resonance.

Frequency shifting

Cooling light must be red-detuned with respect to an atomic transition in order for conventional laser cooling schemes to function. In this experiment, laser light is frequency shifted using acousto-optic modulators (AOM) aligned in double-pass configuration. The master AOM (Crystal Technology, 3110-140) frequency shifts light from the master laser before the MTS setup by 220 ± 20 MHz below the closed transition.[7] The cooling light must be closer to resonance than this and so a second AOM is employed to shift the frequency back. The slave AOM (Crystal Technology, 3080-122) is used to shift light from the master diode back towards resonance[8] before it is coupled into the slave laser. The slave AOM allows the cooling light to be detuned by up to 80 MHz from resonance.

[7] Thus, although the laser is locked to the cooling transition, its actually frequency is 220 MHz from this resonance.

[8] The master and slave AOMs are aligned to transmit opposite first diffraction orders, causing them to shift the frequency in opposing directions.

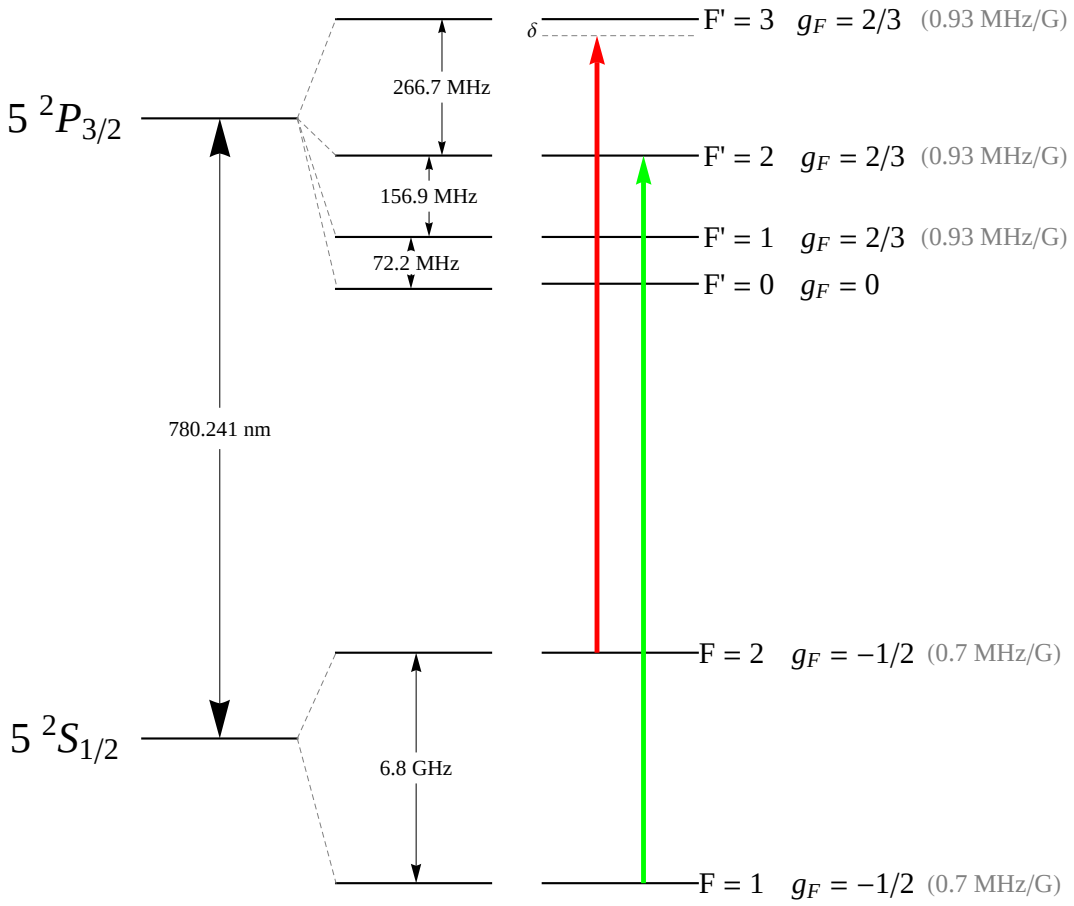


Figure 5.5: The hyperfine structure of the D2 line ^{87}Rb . The cooling (red arrow) and repumping (green arrow) transitions are indicated.

5.2.2 The repumping laser

As discussed in chapter 3, although the cooling light is detuned close to the closed transition of the D2 line in ^{87}Rb , off-resonant excitation to the $F' = 2$ state can occur during the MOT stage, necessitating the need for a second laser to depopulate the $F = 1$ hyperfine ground state and return atoms to the cooling cycle. The repumping laser, often just called the 'repumper' is fully independent of the master-slave setup and will be described here. The 'repumper' diode (Sanyo DL-7140-201) is located in a commercial laser head (Toptica DL100) forming an ECDL.[9] The repumper is not subject to controlled frequency shifts by AOM's or other such devices and so sidebands may be applied to the laser by directly modulating the diode current. The repumper is locked via this technique (known as frequency modulation or fm locking) to the $|F = 1\rangle \rightarrow |F' = 2\rangle$ transition which, other than how the sidebands are applied to the laser works on the same principals that underlie the MTS scheme.

A Pound-Drever-Hall module (Toptica PDD 110) is used to modulate the 'repumper' diode current at a frequency of 20 MHz. The laser is incident on a rubidium vapour cell in a traditional saturated absorption spectroscopy scheme [154] where the process of absorption converts the frequency modulations in the light into amplitude modulations, the beat signal of which is detected on a fast photodiode. This signal is amplified (Minicircuits ZFL - 500HLN) before being returned to the Pound-Drever-Hall module which generates the error signal by heterodyning the beat signal with the internal 20 MHz oscillator. The error signal is sent to the PID controller (Toptica PID 110) which adjusts the piezo position to stabilise the frequency to the repumping transition.

The majority of the repumper light ends up in the pyramid MOT beam, however a small fraction (~ 3 mW) is fiber coupled to the science cell. The collimated output of this fiber is reflected by a mirror along the long axis of the glass cell where it acts to optically pump atoms into $|F = 2\rangle$ hyperfine level in preparation for the imaging light.

5.2.3 The tapered amplifier

The large size of the beams in the pyramid MOT require several hundred milliwatts of cooling light to saturate the cyclical transition ($I_{\text{sat}} = 1.6\,\text{mW/cm}^2$). Even using the master-slave configuration,[10] these powers are beyond standard laser diodes. The solution employed in this experiment is to use a tapered amplifier (TA). This chip (Eagleyard, TPA-0780-01000-3006-CMT03-0000) is a tapered section of semi-conductor diode gain material that is anti-reflection coated on both the input and output facets.

[9]The piezoelectric actuator in this laser is not the one supplied by Toptica (which broke), but a replacement from Thorlabs (AE0203D04F).

[10]The output of the 'master' laser is split and used for frequency stabilisation (via MTS), frequency shifting (using AOMs) and to form the beams that probe the state of the atoms in the science cell. In combination with the use of single mode polarisation maintain optical fibers there is not sufficient optical power remaining to optimally seed the TA. Hence the master-slave configuration is used, with the injection locked output of the slave being exclusively used to seed the TA.

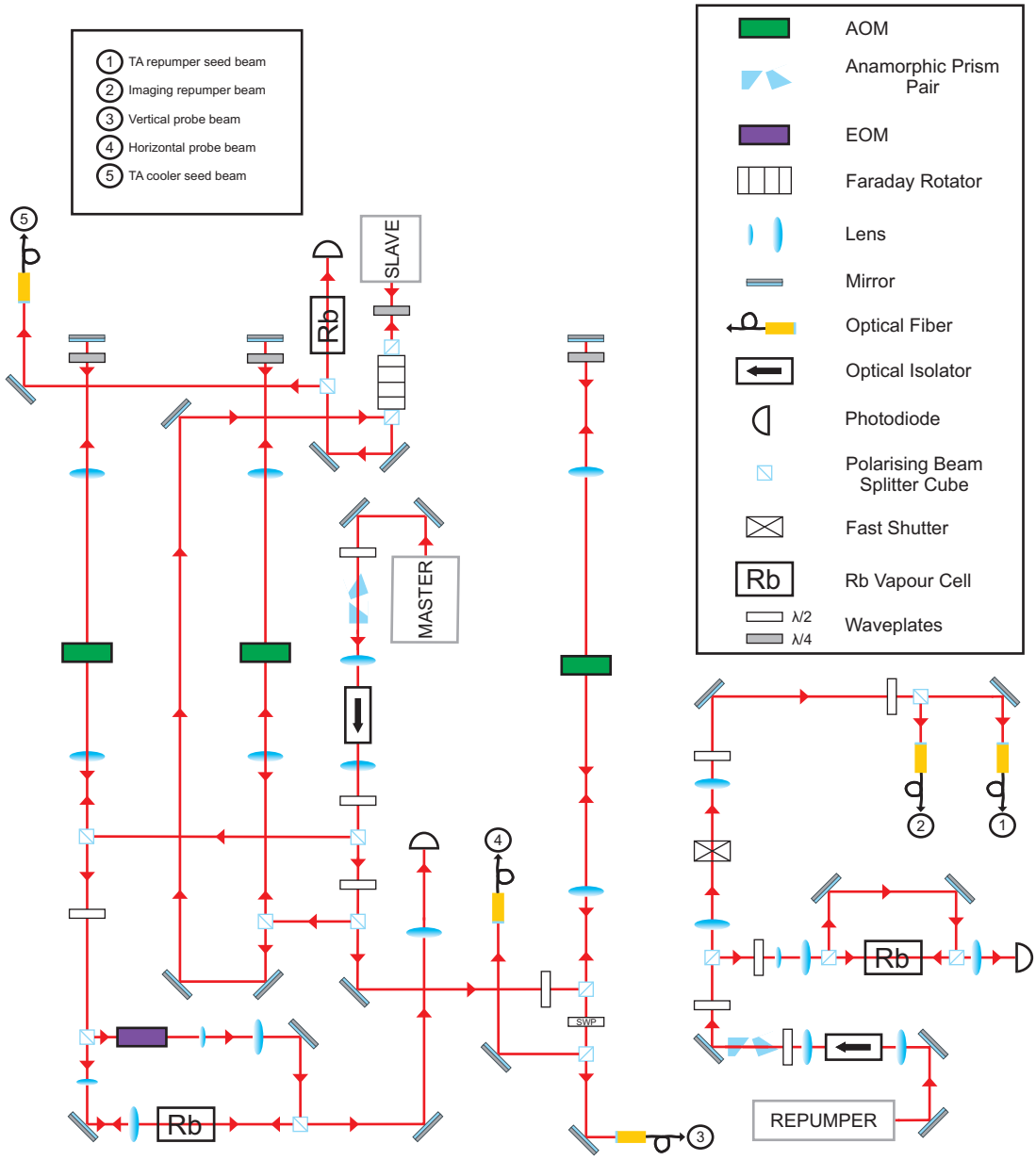


Figure 5.6: A schematic representation of the optical layout.

The TA has a custom designed mount that is temperature stabilised by a Peltier cooler (regulated by a Newport 350 temperature controller) to prevent it overheating under normal operation. The TA current is regulated by a current controller (Newport 560). The diode is specified for 13 dB of optical gain and a maximum output power of 1 W under optimal alignment.

In this experiment the TA is seeded with 15 mW of cooling light and 1 mW of repumper light, and produces strong amplification of both beams. The TA output is strongly astigmatic and divergent. A pair of cylindrical lenses limits the divergence of the beam in the horizontal direction. Following a -60 dB optical isolator a total power of ~ 700 mW is measured in front of the MOT fiber.[11] The TA light is poorly matched with the mode of the optical fiber meaning coupling efficiencies of $\sim 40\,\%$ are difficult to exceed.

5.2.4 The probe beam

The light used for imaging atoms in the glass cell (hereafter referred to as the probe beam) derives from the master laser. The probe beam has a dedicated AOM that is used to control the probe beam detuning and create short pulses (durations between $15 - 50\,\mu$s) required in particular for absorption imaging. The probe beam is coupled along one of two optical fibers to the science cell, where the choice of fiber is determined by which axis (i.e. horizontal or vertical) the atoms are to be imaged along. The switching between fibers is facilitated by an in-house built switchable waveplate. This consists of a $\lambda/2$ waveplate attached to a small relay. The relay is switched on or off by a TTL signal sent to a driver box. When the relay is on, the waveplate intercepts the beam, rotating the polarisation axis such that the beam is fully reflected by a polarising beam splitter cube and coupled down the horizontal imaging fiber. When the relay is off, the waveplate does not intercept the beam, which is fully transmitted by the cube whereafter it is coupled down the vertical imaging fiber. The switching time of the relay is of the order of 100 ms, however since the cloud is imaged destructively only a single imaging direction may be used during each experimental run. This direction is set during the MOT loading stage of each experimental sequence ($\sim$ 20 s) providing the switchable wave plate with plenty of time to complete its operation.

5.3 The magneto-optical trap

The pyramidal magneto-optical trap exemplifies the principals of simplicity and functionality upon which much of the design and construction of this experiment is based. The pyramid MOT, which routinely traps $3 - 3.5 \times 10^9$ atoms at around the Doppler

[11] The principal reason for the coupling of the output of the TA down an optical fiber is the physical separation of the TA and the vacuum system (the TA is mounted on a breadboard located off the main optical table).

limit for ^{87}Rb (146 μK), is straightforward to align, requires minimal maintenance and is relatively robust to changes in the incident beam intensities. The main disadvantages to this trap involve how it is not well suited to allow sub-Doppler cooling[12] or optical pumping[13] at the end of the compressed MOT stage.

The MOT beams derive from a single incident beam that is reflected to form 6 counter-propagating beams by an inverted pyramidal mirror. The mirror is formed from 4 triangular pieces of BK7 glass coated with 21 alternating layers of SiO_2 and TiO_2 to give the desired 180° phase shift for light upon reflection.[14] The *Transport* coils, located above and below the MOT chamber are operated in anti-Helmholtz configuration in order to give the requisite quadrupole magnetic field.

A pair of dispensers (SAES, Rb/NF/3.4/12 FT10+10) wired in series to a single UHV electrical feedthrough provide all the ^{87}Rb for the experiment.[15] A steady current of 2.95 A is passed through the dispensers during the running of the experiment. The dispensers emit rubidium at a rate which is sufficient to generate a vapour pressure of rubidium gas that allows for healthy MOT loading times, but without exhausting their limited supply too quickly.

An important difference between this and many other pyramid MOTs is that it is the only stage of laser cooling present in the experiment. Following Doppler cooling in the pyramid MOT, atoms are directly loaded into a magnetic trap whereupon they are transported to the science cell. During magnetic transport, the atoms exit the MOT region through a slot cut in two of the MOT mirror pieces. The rectangular slot measures 10 mm wide by 25 mm long and is aligned to provide a clear, free aperture along the transport axis of the vacuum system (see fig. 5.7).

The beam diameter is an important factor in determining the number of atoms that can be trapped in a MOT. In the setup of this experiment, the $1/e^2$ diameter of the single beam that is incident on the pyramid mirrors was set to 80 mm. This equals the size of the internal diameter of the *Transport* coils which sets the limit for optical access to the MOT. During the period of MOT optimisation, the MOT optics (see fig. 5.8) were used to adjust the size of the beam to maximise the number of trapped atoms. The

[12]Small imbalances in beam powers result in very short diffusion times for atoms in optical molasses. In a pyramid MOT the relative intensities of the beams are fixed by the reflectivity of the mirrors and so no individual adjustments can be made.

[13]The geometry of the pyramid mirror will cause any optical pumping beam that is sent down the same fiber as the MOT cooling and repumping light to be reflected so as to generate counter-propagating beams that will pump atoms into opposing m_F states. A possible scheme that has been discussed is to direct an optical pumping beam along the transport axis of the vacuum system (entering through the glass cell and impinging on the atoms through the slot in the pyramid mirrors), where it will be incident upon the atoms and then be reflected out of the MOT chamber. This has however yet to be implemented.

[14]Following the application of this coating by the Oxford physics thin films facility, the anomalous phase shift of each mirror piece was determined to be $< 5.4°$.

[15]Another pair of the identical dispensers was wired and mounted in place to a separate feedthrough such that the experiment can continue to operate without the need to break the vacuum when the rubidium of the first pair is fully depleted.

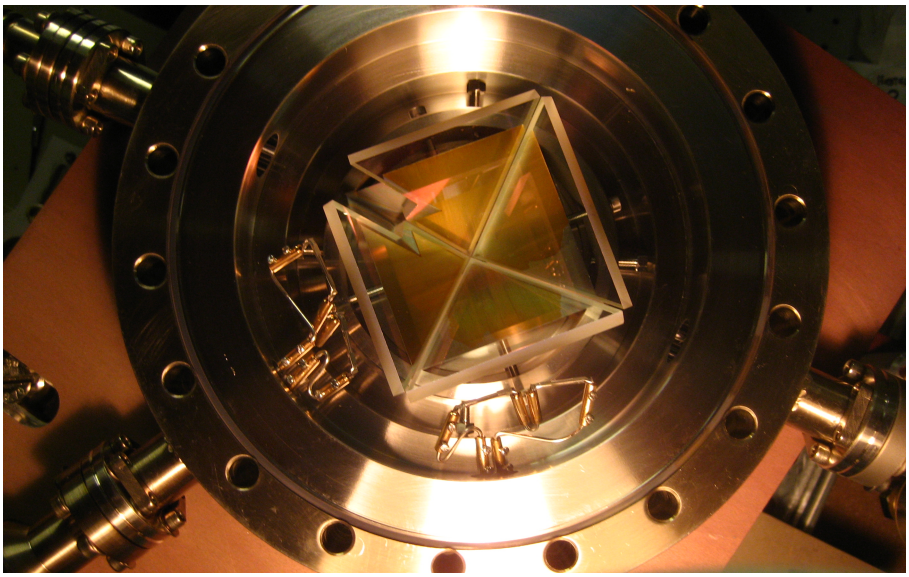


Figure 5.7: A photograph looking down on the fully assembled pyramid mirror, located *in situ* in the MOT chamber. The alignment between the hole in the mirrors and the aperture of the differential pumping tube is visible. Close to the lower edges of the pyramid mirror, the rubidium dispensers complete with UHV compatible screw down connectors are visible. This photograph was taken at 11.47pm, just before the MOT chamber was sealed and pumped down to UHV pressure for the final time.

MOT optics are held in a cage system that is mounted on a 1 m long piece of extruded aluminium that stands perpendicular to the surface of the table. To aid the process of optimising the MOT, the extruded aluminium is mounted on an xy translation stage that allows the centre of the incident beam to be adjusted with respect to the pyramid mirrors.

5.4 The magnetic trap

During the design stage, the custom configuration of coils, mounts, power supplies and associated circuitry that forms the magnetic trap for this experiment went through numerous iterations. A strong desire not to compromise on the quality of the confinement, or adversely affect other areas of the experiment drove the evolution[16] of the magnetic trap to its present, fully operational configuration.

[16]Evolution is an appropriate term to use here as it is anticipated that in the future, as new experimental goals are sighted, changes are likely to be required of the magnetic trap. The modular design of the trap encourages such changes.

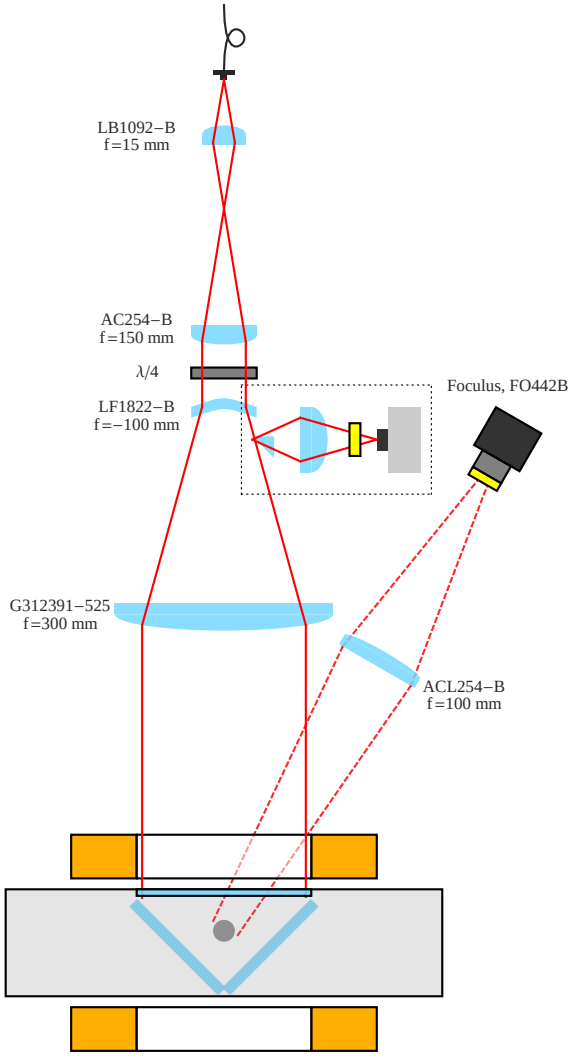


Figure 5.8: Schematic diagram of the MOT optics (not to scale). The *Transport* coils (orange rectangles located above and below the pyramid mirrors) are illustrated in the position where they produce the quadrupole field for the MOT operation. The optical elements within the dotted rectangle are responsible for real time monitoring of the incident beam power. A prism picks off a small part of the beam, which is focussed by a lens (ACL2520-B) through a 780 nm interference filter and on a photodiode (PDA36A-EC). The voltage from the photodiode is printed to a screen via an analogue input module. The approximate number of atoms in the MOT is inferred using the fluorescence focussed on to a CCD camera.

5.4.1 The DC coils

At *all* times during the running of the experiment a magneto-static potential produced by two of more of the DC current carrying coils is enabling the operation of the experiment. The DC coils and some specifications are listed in table 5.1.

Coil Name	Function	Turns	Wire type	$B_{\mathrm{q}}^{\prime(\mathrm{max})}$
Transport	MOT + Transport	15×8	Solid 1.85×3.6 mm^2	76 (G/cm)
Lateral steering	Transport	3×3	Solid 1.85×3.6 mm^2	-
Push	Transfer	3×3	Tube 3.3×3.3 mm^2	-
Auxiliary	Transfer	9×4	Tube 4.0×4.0 mm^2	55 (G/cm)
Helmholtz	Transfer	3×2	Tube 3.3×3.3 mm^2	-
Quad	Trapping	5×4	Tube 3.3×3.3 mm^2	399 (G/cm)

Table 5.1: Details of the DC magnetic trap coils. The 'tube' wire type refers to square profile, Kapton insulated Copper pipe with a central aperture through which cooling water is passed. The maximum field gradient values derive from calculations based on single wire approximations for each coil pair at its actual separation.

Magnetic transport coils

The *Transport* and *Lateral steering* coils are mounted on posts that are fixed to the motorised translation stage (Parker 404XR). Following the MOT stage (where the *Lateral steering* coil is switched off) both coils combine to trap the laser cooled atoms on the axis of the differential pumping tube as they transit from the MOT chamber to the glass cell. The *Transport* coil provides the quadrupole field to trap the atoms and the *Lateral steering* coil is used to adjust the position of the trap centre to minimise the atom loss during magnetic transport.[17] Each coil is driven by a dedicated power supply, run in voltage programming mode and controlled by a single analogue output from the computer control system. The *Lateral steering* coil is directly wired to a HP 6260B current supply, the *Transport* coil pair use another current supply (Xantrex XFR 20V-60A), however these coils are also connected in parallel with the so called 'quick start' circuit which employs a large capacitor to rapidly establish a current in the *Transport* coils (see section 6.0.2).

Magnetic transfer and trapping coils

The presence of an imaging objective lens underneath the glass cell prevents the technique of magnetic transport from being used to deliver the atoms to the site of con-

[17] This coil was not part of the original design for the experiment. Only when a manufacturing error that resulted in a kink in the differential pumping tube which caused intolerable atom loss during magnetic transport did the need for such a coil become apparent.

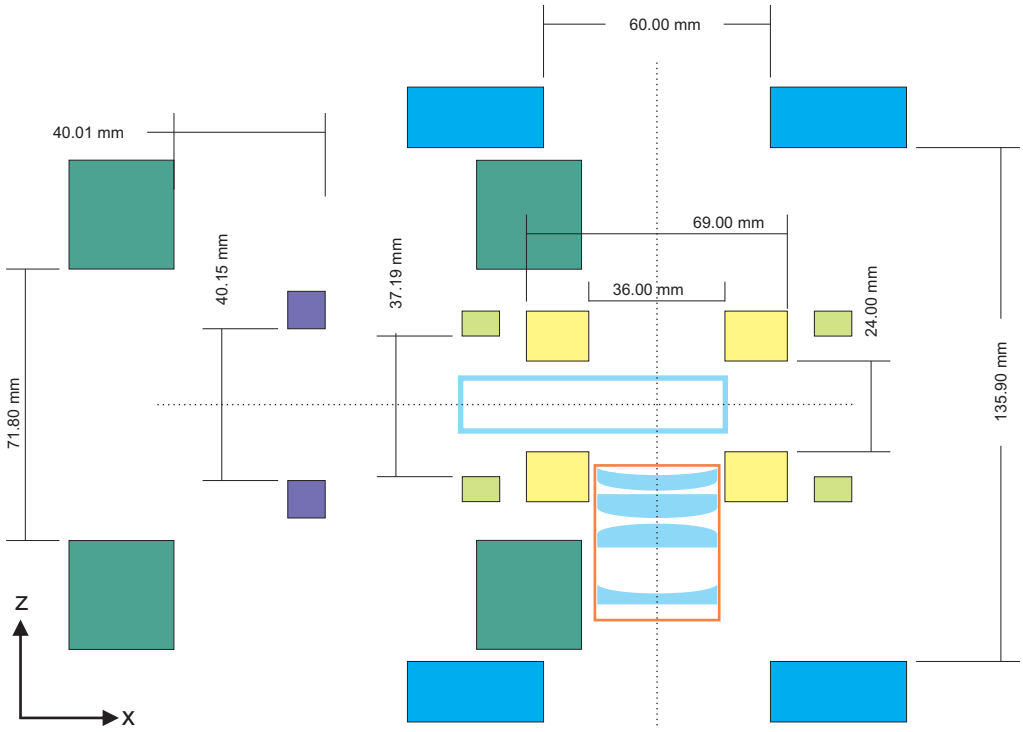


Figure 5.9: Schematic cross section of the DC coil layout around the science cell (blue outline). The *Quad* coils (yellow) are mounted coaxial with the *Helmholtz* (light green) and *Auxiliary* (blue) coil pairs. The *Transport* coils (dark green) are shown at the end of the magnetic transport sequence (see section 6.1). The cross section is taken in the xz plane, all coils have their symmetry axis located along the vertical z axis, except for the *Push* coil (purple) which lies along the x axis. The *Lateral steering* coil which is mounted in between the *Transport* coils with its symmetry axis directed along the y axis is not shown here in the interests of clarity.

densate production. The final 90 mm of the journey from MOT chamber to glass cell are achieved via a process of ramping currents in neighbouring, static coils, that in this experiment is called magnetic transfer. The *Transport*, *Push* and *Auxiliary* coils are those principally involved with the process of magnetic transfer (see fig. 5.9 for details of their alignment).[18]

The *Quad* coils provide the magnetostatic potential that underlies all magnetic trapping processes that follow the atom's arrival in the glass cell. The coils are separated by 30 mm allowing them to achieve high field gradients that are useful for present and future experiments. The *Helmholtz* coils were designed to generate a uniform bias field that allows the vertical position of the final magnetic trap to be adjusted. This is particularly useful when imaging with high numerical aperture (NA) lenses that often have working distances of only a few millimeters, requiring the atoms to be trapped very close to the cell edge.

The *Push*, *Helmholtz*, *Auxiliary* and *Quad* coils are all wired in series with a 16.6 kW power supply (Magna-Power Electronics, SQA50-330) that is capable of driving a maximum current of 330 A through the circuit. The high current power supply is operated in current control mode in which the output of the supply is stabilised to within 0.04 %, thus minimising any noise that can lead to heating in the potential. The Joule heating that results from such high currents, even for coils with a resistance of only a few hundred milliohms necessitates the use water cooling to maintain the temperature of these coils below a maximum value of 50° C under steady-state conditions.

Although the water cooled coils are all wired in series with one another, the current flowing in each coil can be adjusted independently of the others by using a system of bypasses and servo control circuitry. The high current control system (see fig. 5.11) was designed and assembled by Gehard Zürn [155]. A pair of MOSFET banks for each coil pair determine how much of the current from the SQA power supply passes through the coils and how much is diverted through a bypass branch, wired in parallel with the coils. The current in each coil pair is controlled by a single analogue output from the computer control system that fixes the gate voltage for the coil MOSFET banks. An inverted version of this signal is sent to the MOSFET banks on the bypass branch which ensures that there is always a low impedance path for the current to follow. As can be seen in fig. 5.11 the *Auxilliary* coil has an extra pair of the MOSFET banks. This part of the circuit is wired in a H-bridge formation and allows the configuration of the *Auxilliary* coil to be switched from anti-Helmholtz (required for magnetic transfer) to Helmholtz (potentially useful for vertical biasing the final trap position).

5.4.2 The AC coils

The use of time-dependent magnetic fields to control the potential experienced by ultracold atoms is a cornerstone of this experiment. In chapters 7, 8, 9 data is presented from ultracold atoms trapped in different geometries that result from either manipulating the

[18] Details of the current ramps can be found in section 6.1.

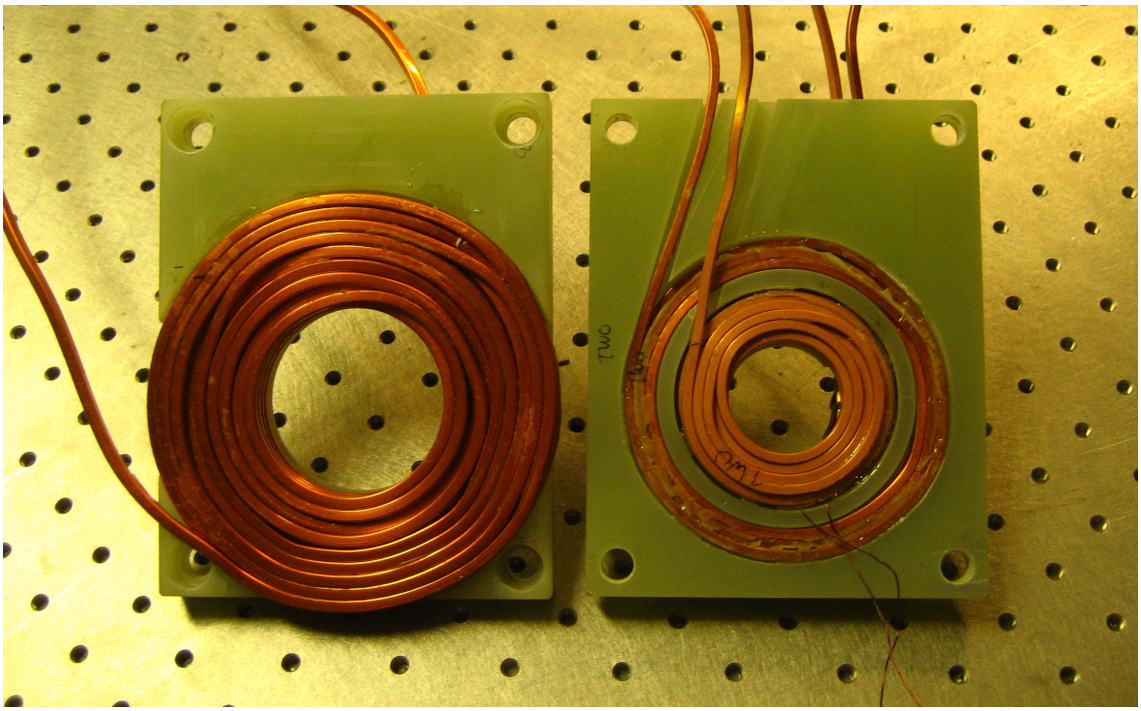


Figure 5.10: Water cooled DC coils in their custom cut Tufnel 10G/40 mounts, before being assembled in the final magnetic trap. The large *Auxiliary* coil (left) requires its own mount, however the *Helmholtz* (outer right) and *Quad* (inner right) neatly fit into the same mount. The narrow gauge wire at the bottom right of the picture is the coil leads for the *z rf* coils which are wound around (and thus concentric with) the *Quad* coils.

time-averaging field, or the rf-dressing field, or both. Thus it is the ability to accurately control the degree to which the time-averaging and rf-dressing fields interact with the atoms that underpins the versatility of the experiment. As these fields are delivered by coil pairs it is therefore important that the part of the magnetic trap responsible for producing them operate in a reliable and predictable way. Most of the coils that generate these fields are arranged in a compact array (see fig. 5.12) that locates them within a few millimeters of the glass cell, increasing the size of the field that can be achieved and preventing the DC coils from having to be spaced further apart. All AC coils form pairs that are symmetrically located about the centre of the glass cell along one of the three principal axes of the experiment. The AC coils and some specifications are listed in table 5.2.

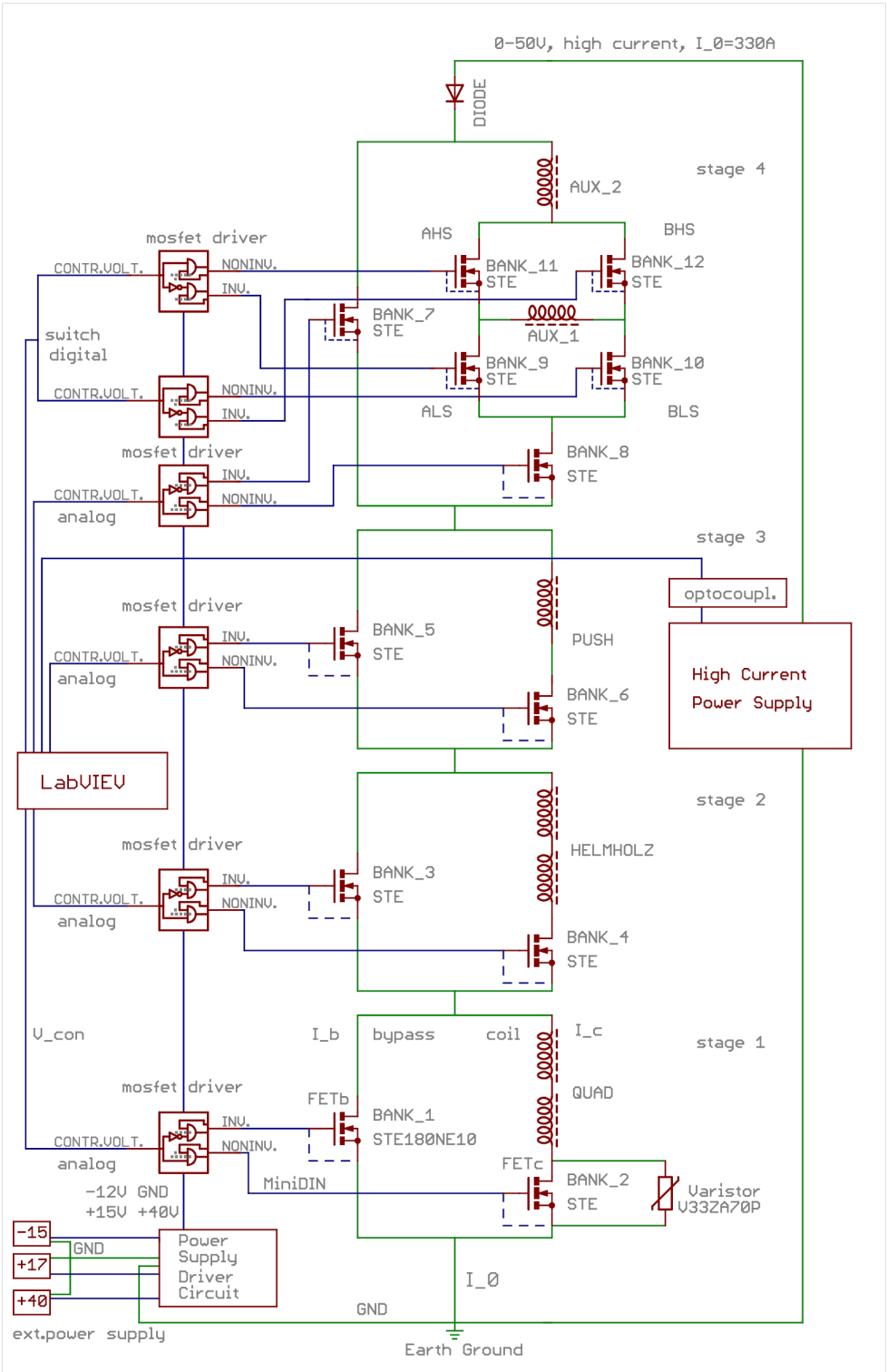


Figure 5.11: The MOSFET bank circuit diagram.

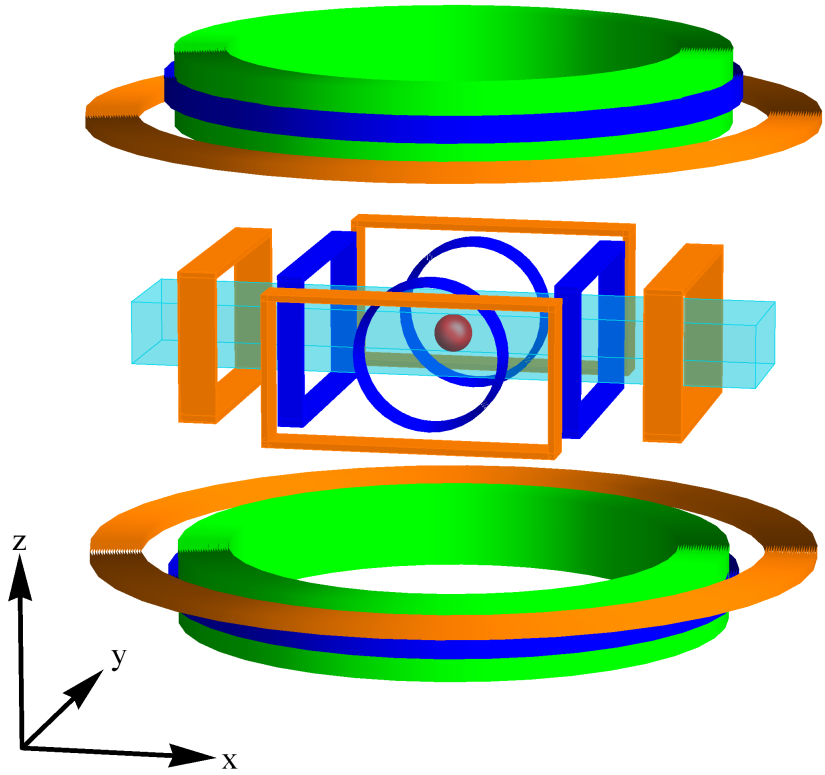


Figure 5.12: 3D diagram of the science cell and coils involved in generating the TAAP trap. Note the coil dimensions are drawn to scale, however the separations of the coil pairs has been increased in the interests of clarity. The static quadrupole field is formed by the green coil pair separated along the z axis. The time-averaging (orange coils) and rf-dressing (blue coils) fields are delivered along three perpendicular axes by dedicated coil pairs wired in approximate Helmholtz configuration.

The TOP coils

A pair of TOP coils, wired in Helmholtz configuration lie along three (approximately) orthogonal axes. Two identical coil pairs, the *xTOP* and *yTOP* coils lie in the horizontal plane and produce the time-averaging magnetic field that gives rise to the conventional TOP trap. These coils are mounted in the main AC coil array (see fig. 5.13), which is held between the *Quad* coil pair. The *zTOP* coils deliver a time-averaging field along the vertical axis and are mainly used for achieving the TAAP ring and horizontal double-well. The *zTOP* coils are wound in a flat spiral configuration and mounted on top of the *Helmholtz* coils. All three coil pairs are constructed from 1.5 mm diameter enamelled copper wire.

The *xTOP* and *yTOP* coils are driven with a 7 kHz sinusoidal signal that originates

Coil Name	Function	Turns	Geometry	Gauss per amp (G/A)
xTOP	Radial TOP field	1×7	Rectangular	0.86
yTOP	Radial TOP field	1×7	Rectangular	0.86
zTOP	Axial TOP field	1×5	Flat spiral	1.3
x rf	RF dressing	3×9	Rectangular	5.2
y rf	RF dressing	3×9	Circular	3.2
z rf	RF dressing	2×5	Circular	2.4
Evap rf	Evaporative cooling	1×2	Circular	0.45

Table 5.2: Details of the AC magnetic trap coils. The value of G/A for the *TOP* and *zTOP* coils was extracted from trap frequency measurements in the TOP trap. In the case of the rf dressing coils, the value was measured using a DC current and a gaussmeter prior to the coils being mounted on the experiment (see appendix A). The G/A value for the evaporative coils is not considered a critical experimental parameter and hence has not been accurately measured, the value quoted here being the result of a simple single wire approximation.

from a single Agilent 33220A function generator operated in 'burst' mode.[19] To achieve a circularly rotating bias field, the signal is split into two channels, with one of them being phase shifted by 90° with respect to the other. Two voltage controlled amplifiers (VCA) allow the amplitudes of each channel to be adjusted independently using analogue outputs from the computer control system. Large rotating bias fields $\sim 30\,\mathrm{G}$ increase the efficiency of the TOP loading process, hence a power amplifier (Crown XLS 5000) is used to provide large increase in the amplitude of the TOP signal. Driving the TOP coils at 7 kHz means they present a small, poorly matched load ($0.42\,\Omega$) to the audio amplifier. In order to improve impedance matching a step down transformer (turns ratio of 3.1:1) for each channel is used, allowing a maximum current of $100\,\mathrm{A_{p-p}}$, corresponding to a maximum TOP field amplitude of 43 G to be generated by the coils.

The *zTOP* coils are driven by the in-quadrature part of the radial TOP field signal. Following a VCA, the signal is amplified by a Soundmaster VF250 audio amplifier, before being passed through a LCR circuit ($L = 17.6\,\mu\mathrm{H}$, $C = 29.2\,\mu\mathrm{F}$, $R = 0.5\,\Omega$) with a resonant frequency in the region of 7 kHz. This approach was determined to give the largest value for the maximum current ($13\,\mathrm{A_{p-p}}$) that could be driven through the *zTOP* coils before reflections began to distort the signal.

The rf coils

In order to provide full control over the polarisation of the rf dressing radiation, three coil pairs wired in Helmholtz configuration, that lie along the same three axes as the TOP

[19] 'Burst' mode causes the signal generator to give an output signal that has an adjustable and deterministic phase. The output is gated by a TTL pulse from the computer control system.

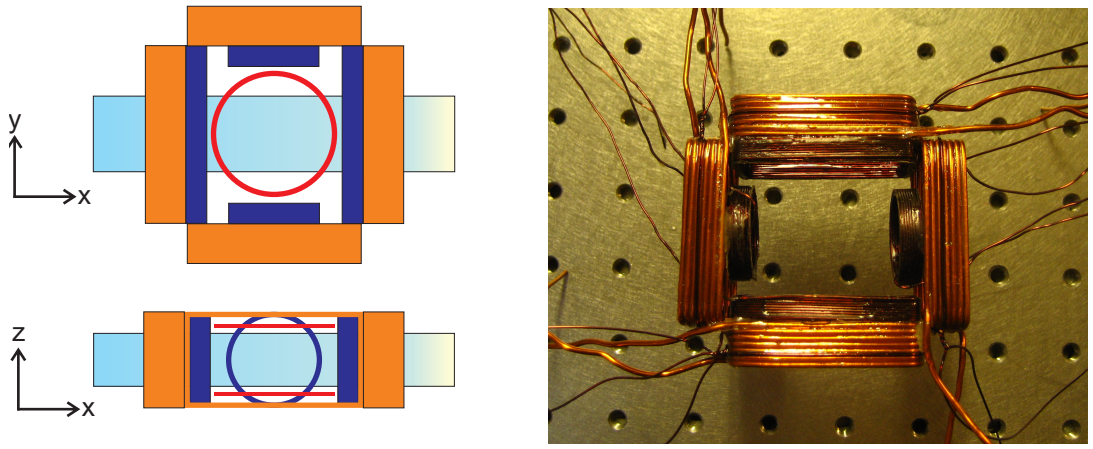


Figure 5.13: The main AC coil array. In the schematic diagram (left) the *TOP* (Orange), *x rf* and *y rf* (Blue) and *Evap rf* (Red) coils are viewed along with the glass cell (light blue) along the z (upper) and x (lower) axes . The photograph (right) shows the coil array before the *Evap rf* coils were added.

coils are used to deliver the MHz frequency magnetic fields. The rf trapping coils are all wound using 0.5 mm enamelled copper wire. The *x rf* and *y rf* coils are wound with circular and rectangular geometries to remove any physical overlap between the coils and therefore limit the degree of capacitive coupling between channels which complicates the process of setting the rf polarisation. The *z rf* coils do not form part of the main coil array due to spatial constraints but instead they are wound on top of the *Quad* coils (see fig. 5.10).

The sinusoidal 1.4 MHz dressing signal is produced by a custom-designed direct digital synthesis (DDS) frequency source. Each coil pair has its own dedicated channel on the DDS system, allowing full control over the amplitude and relative phase of the dressing fields. The DDS is not designed to give a large output (maximum of $0.4\,V_{p-p}$) so to ensure sufficient power, the rf signal is amplified first by a low noise amplifier (Minicircuits ZFL-500HLN), then by a 1W Minicircuits ZHL-32A amplifier. At 1.4 MHz the rf coils present a significant inductive load to the amplifiers.[20] In order to increase the current in the coils, this reactance is approximately cancelled using matching capacitors ($C_{y\ rf} = 333\,pF$, $C_{x\ rf} = 148\,pF$, $C_{z\ rf} = 940\,pF$) that cause the circuit to resonate close to the driving frequency.

The *Evap rf* coils are a 2 turn pair of 32 mm diameter coils, wound from 0.5 mm diameter enamelled copper wire. The coils are mounted in the main AC coil array with their symmetry axis parallel with the z axis and are driven by a dedicated channel of

[20]The coil pairs have inductances of $L_{y\ rf} = 39.1\,\mu H$, $L_{x\ rf} = 82.2\,\mu H$ and $L_{z\ rf} = 24.1\,\mu H$.

the DDS frequency source. The evaporative ramps used to cool the atoms via selective spin-flip transitions stretch over 100 MHz and so, in contrast to the other fixed radio-frequency coil circuits, a flat frequency response desired in this circuit. The *Evap rf* coils were therefore intentionally wound to have a low inductance ($\sim 4\,\mu$H) and no matching capacitor is present in the circuit. The signal from the DDS module is amplified by an amplifier (Minicircuits ZHL-1-2W) before being sent directly to the coils.

5.5 The imaging system

At the time of writing, all information about the ultracold atomic cloud is gathered via the absorption imaging technique. In principle the imaging system requires no hardware changes (small adjustments must be made to the control sequence) to perform fluorescence imaging of ultracold samples. This was demonstrated during the early stages of the experiment, however the signal to noise ratio (SNR) of the images proved inferior to the absorption technique for the number of atoms ($> 10^4$) typically being imaged. The concluding chapter of this thesis contains a proposal for the development of a fluorescence imaging technique that employs a deep, far-detuned optical lattice to catch and hold atoms whilst they fluoresce, allowing high resolution imaging of small (i.e. < 100) numbers of atoms.

Two complimentary absorption imaging paths operate in this experiment. The horizontal imaging system probes atoms along the horizontal direction (denoted as the y axis in the lab frame). Horizontal imaging was the first to be brought online in the construction of the experiment, and was used extensively to optimise the hybrid magnetic transport and evaporative cooling processes. This system has a $1\times$ magnification which gives a field of view of $8.7 \times 6.6\,\text{mm}^2$, allowing imaging of both 'hot' thermal clouds and quantum degenerate gases. The probe beam here has a $1/e^2$ diameter of 6.3 mm and a power ~ 2 mW. The rotating TOP field is synchronised in time to be collinear with the probe beam direction at the instant of the probe pulse, thereby providing a quantisation axis for the cooling light. The σ^+ light drives atoms onto the closed $|F = 2, m_F\rangle \rightarrow |F' = 3, m_F + 1\rangle$ transition which has the largest Clebsch-Gordon coefficient and thus gives the strongest absorption signal. The horizontal imaging is still used on a daily basis to check the experiment is running in a stable and repeatable fashion, and to take certain measurements (c.f. vertical trap frequency measurements).

The vertical imaging system was introduced in order to image the cloud along its symmetry axis, at a resolution that structures within the cloud such as quantised vortices could be resolved. The diffraction limited resolution for the horizontal imaging system is $7.9\,\mu$m,[21] however the 4-lens objective used for vertical imaging achieves a diffraction limited resolution of $1.8\,\mu$m (more information on the characterisation of the lens can be found in [156]). Imaging of structures within the cloud is also assisted by the $10.5\times$

[21] Note however that no rigorous test of the performance of this system has been performed, so actual resolution is most likely to be abberation limited at a higher value.

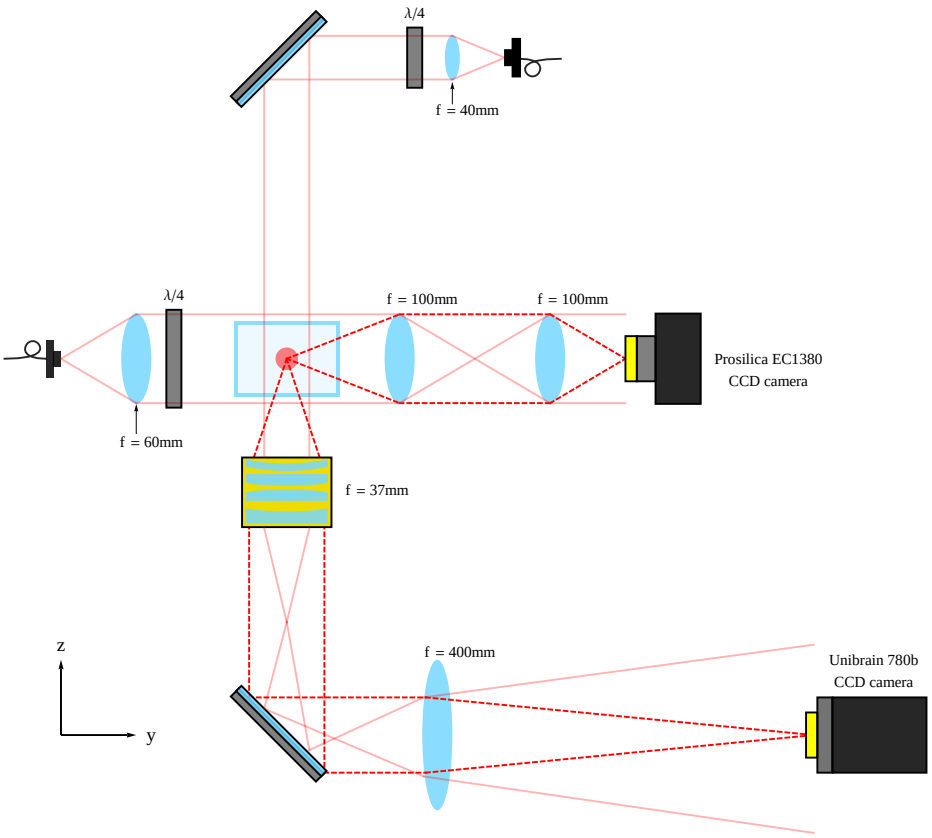


Figure 5.14: The horizontal and vertical imaging systems. The solid, light red lines show the beam paths, and the dashed, deep red lines demonstrate the propagation of the image of the atoms. The focal lengths of the lenses are labelled, but the figure is not drawn to scale. The $\lambda/4$ waveplates give circularly polarised light which optically pumps the atoms onto the closed cooling transition.

magnification which acts to distribute small features over a greater number of pixels. The 4-lens objective requires careful alignment due its shallow depth of field, and is therefore mounted on a 3 axis translation stage, where separate control over the pitch and yaw of the lens is also available.

The atoms are magnetically trapped in the $|F = 1, m_F = -1\rangle$ state, however the narrowband probing light is resonant with the cooling transition ($|F = 2, m_F = 2\rangle \rightarrow |F' = 3, m_{F'} = 3\rangle$) so the atoms require repumping prior to imaging. The repumper light is fiber coupled to the science cell area, where via a collimating lens and mirror, it is incident upon the atoms along the x axis.

5.6 Computer control

The timing precision and overall complexity of a cold atom experiment demands powerful computerised control solutions to manage the diverse range of apparatus involved. The computer control is a real asset to this experiment (in terms of reliability and versatility) and whilst a brief overview is presented below, an excellent discussion is presented in Marcus Gildemeister's DPhil thesis [131]. A field programmable gate array (FPGA) controls all the analogue and digital inputs and outputs that connect to the experiment. The front end interface is provided by National Instruments LabVIEW version 8.5 which reads in user defined parameters and prepares this data to be sent to the FPGA via a direct memory access channel. The experimental computer control hardware consists of a National Instruments PCI-7813R board with a Virtex-II 3M gate FPGA chip running a 40 MHz clock. Two NI 9151 expansion chassis connect to the board, each one hosting 4 input/output modules that can be selected from the range offered by National Instruments. In this experiment, 20 analogue outputs (5 × NI 9263), 32 digital outputs (1 × NI 9043), 32 analogue inputs (1 × NI 9205) and 4 thermocouple inputs (1 × NI 9211) are available to communicate with the apparatus.

The experimental control sequence is coded as entries in a 2D matrix within LabVIEW. Each column presents a timestep of a variable, user defined length. The row entries within each column represent the values of the analogue and digital outputs for that times step. Data is read in sequentially, column by column and then sent to the FPGA following the first in first out (FIFO) protocol. Several software solutions have been implemented in this control code, including the ability to ramp analogue outputs between values and add time delays to digital channels.

The DDS frequency source is not part of the FPGA construct and has its own control hardware and software. The DDS unit is not just used as a fixed or ramped frequency source, but it is programmed to allow real time adjustments to the amplitude and phase of each channel, allowing for instance a rotating, elliptical polarisation for the dressing radiation that is used to spin up the atoms. The DDS unit contains four channels, at the heart of each of which is the AD9852 Analog Devices digital synthesizer chip. The master clock for the unit runs at 300 MHz, limiting the chips (by the Nyquist-Shannon sampling theorem [157]) to a maximum output frequency of 150 MHz. Each channel is controlled and updated simultaneously, in real time using a separate digital board (NI 6534). DDS instructions written by the user into a LabVIEW VI (independent of the experimental control VI) are downloaded onto the onboard digital board memory. Following a TTL pulse, the board begins issuing commands to update the amplitude and phase of each DDS channel. The rate at which the amplitude and phase can be updated is a variable that can be set by the user. Typically updates are sent every 0.4 ms.

Chapter 6

BEC production

6.0.1 MOT loading and optimisation

The realisation and optimisation of a large, functioning MOT is critical to the effective operation of this experiment. A large number of atoms must be trapped in order to mitigate against the considerable atom loss incurred first under magnetic transport and second during evaporative cooling of a magnetically trapped cloud at an initially (relatively) high temperature ($\sim 500\,\mu$K). As a result of this, the principal figure of merit that was used to optimise the performance of the MOT was the number of trapped atoms. Where no negative impact on this key parameter was incurred, adjustments were made to decrease the cloud temperature or increase its density.

During a typical MOT loading time of 20 s, the MOT number saturates to $3 - 3.5 \times 10^9$ atoms. To achieve this number the detuning of the cooling light is set to the optimised value of 24 MHz below the atomic resonance. The *Transport* coils are symmetrically located above and below the MOT chamber and are used to produce a quadrupole field with a 13.9 G/cm gradient. In order minimise the potential energy gained by the atoms when being transferred from the MOT to a purely magnetic trap, the zero of the quadrupole field is approximately aligned with region of peak intensity of the MOT beams. This is achieved with the help of three bias coils that surround the MOT chamber and point in (approximately) orthogonal directions. By observing the size and density of the magnetically trapped cloud, the currents in each coil were empirically adjusted until optimal conditions were reached.

Before loading the atoms into a magnetic trap, a compressed MOT (cMOT) stage is employed. The purpose of the cMOT is to increase phase space density and improve the loading efficiency into the magnetic trap. The absence of outward light pressure in a quadrupole trap means the cloud is typically smaller than in a standard MOT. Correspondingly in a cMOT efforts are made to increase the confinement experienced

by the atoms.[1] By simultaneously increasing the detuning and decreasing the magnetic field gradient over a period of 50 ms enhanced confinement is to some degree achieved in this experiment. At higher detunings, the trapped atoms scatter fewer photons, reducing the outward light pressure and decreasing the size of the cloud. At lower field gradients, the region over which sub-Doppler processes may operate to cool the cloud increases, resulting in a higher density sample.[2] During the cMOT stage, the detuning is continuously increased to final value of 60 MHz below the transition resonance, and the quadrupole gradient is decreased over the same interval to 5 G/cm. The cMOT stage causes a dramatic improvement to the number and temperature of atoms loaded into the magnetic trap, however it is not a stable trap configuration for a large number of atoms and as a result is only used for the duration of the ramps discussed above.

6.0.2 Magnetic trap loading

A critical stage for the success of the whole experiment is the loading of the laser cooled atoms, from the MOT to the first purely magnetic trap formed by the *Transport* coil pair. The trapping potential must be established in a short time (< 1 ms) to capture the atomic cloud before it expands, however the inductance of the *Transport* coils (1.4 mH each) limits to the speed at which this can occur. A solution to this problem is to short a capacitor charged to a high voltage through the coils to first establish a current, then rapidly switch on a high current DC power supply to maintain it.

The circuit depicted in fig. 6.1 operates in the following way. The Xantrex power supply provides the stable DC current that flows through the *Transport* coils under normal usage. This current can be switched off rapidly using the MOSFET M_{os}. The gate voltage to this MOSFET is supplied by an analogue output from the computer control system, that is galvanically separated from the circuit using an optocoupler. The fast switching part of the circuit consists of a Kenwood PSU (0-110 V) used to charge a 1 mF capacitor to a voltage of 90 V, and a LabVIEW triggered thyristor used to rapidly switch the stored charge of the capacitor through the coils. The diodes D_1 and D_2 prevent current flowing back into the power supplies. The varistor V_{ar} and Zener diode D_z are included in order to protect components in the circuit against large transient voltages.

During the MOT loading stage, the Xantrex power supply drives a current of 5 A through the *Transport coils*. During the cMOT stage, the output power of the Xantrex is increased to its maximum at the same time as the MOSFET M_{os} is ramped to a partially non-conducting state. These seemingly conflicting actions allow the current in

[1] This occurs at the expense of the cooling power of the trap, hence it is not a suitable configuration to use until a large number of atoms have already been cooled down to the approximately Doppler temperature.

[2] It should be noted that a conventional cMOT involves an *increase* in the magnetic field gradient [158]. The improvements in the loading of the magnetic trap in this experiment were discovered by a purely empirical exploration of the relevant parameter space.

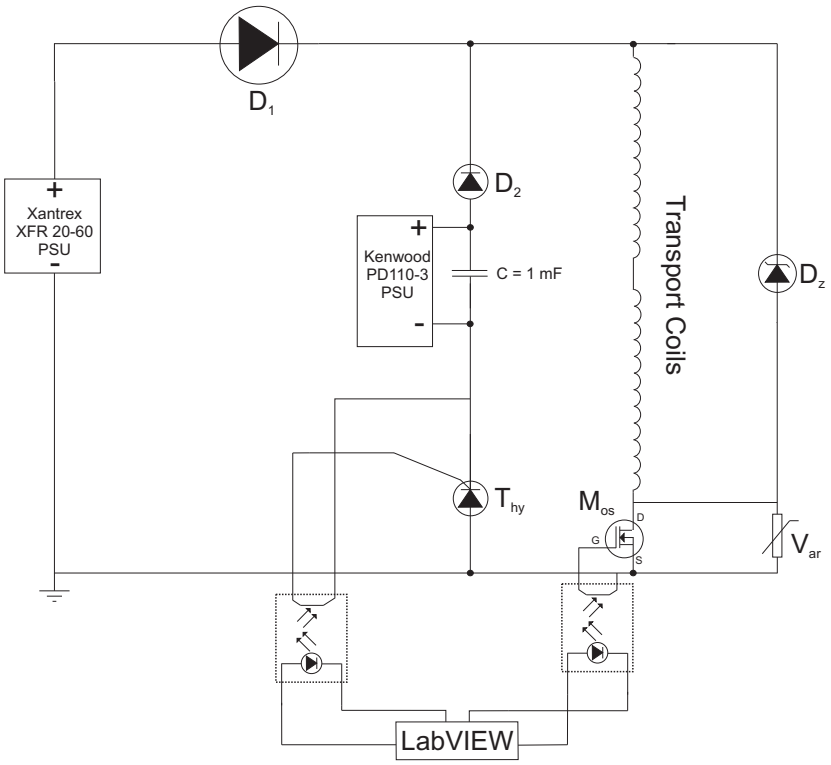


Figure 6.1: The 'quick start' circuit for rapidly changing the current in the *Transport* coils.

the coils to be smoothly ramped down as required for the cMOT stage, whilst energising the output circuitry of the Xantrex PSU.

The magnetic trap loading is initiated by rapidly shuttering off the MOT light. The repumper is shuttered 1 ms before the cooling light, allowing time for all the atoms in the MOT to fall into the $|F = 1\rangle$ hyperfine ground state. A scheme for optically pumping the atoms into the low-field-seeking m_F state has not yet been implemented, so only approximately 1/3 of the MOT number or 1×10^9 atoms are captured in the magnetic trap. When the MOT light is switched off, the MOSFET M_{os} is made fully conducting again, allowing the maximum current of 60 A from the Xantrex PSU to pass through the coils. However before the supply has had a chance to properly react to this change, a 100 μs LabVIEW TTL pulse triggers the thyristor to start conducting, allowing the capacitor to discharge into the coils in $\approx 900\,\mu$s. With a current already established in the coils, the Xantrex power supply is able to quickly reach its output value, sustaining the capacitor discharge current with just a small oscillation. The thyristor stops conducting when the current passing through it has dropped below a

threshold level, preventing the Kenwood supply from passing current directly into the coils. The result is a quadrupole field where $B'_{\mathrm{q}} = 76\,\mathrm{G/cm}$ that strongly confines the atoms is established in $< 1\,\mathrm{ms}$.

Unfortunately, there is a price to pay for this rapid switch on. Eddy currents in the circular MOT chamber mount, chamber itself or stainless steel pyramid mirror mounts appear to be induced by the rapidly changing magnetic flux. The cloud can be crudely observed to be violently displaced downwards, whereafter it subsequently returns to an equilibrium position as the eddy currents damp out. This suggests the fields produced by the eddy currents subtract from the lower *Transport* coil, a fact which correlates with it being closer to the potential sources for eddy currents. To go someway to mitigate against this, a single, shorted coil is placed above the upper *Transport* coil in an effort to induce a corresponding eddy current that will subtract from the upper coil and reduce the effect on the magnetic trap centre. Empirical observations suggested that the rapid vertical displacement is reduced and less heating of the atoms in incurred in the presence of the extra shorted coil.

6.1 Hybrid magnetic transport sequence

The total distance between the MOT and the centre of the *Quad* coils over which the atoms must move is 520 mm. The term *hybrid* magnetic transport refers to the two most commonly used ways to move magnetically trapped atoms that combine in this experiment. The majority of the distance is covered by physically translating the trapping coils, using the motorised translation stage [159]. The final 90 mm of the hybrid sequence utilises static coils, with carefully optimised current ramps that create overlapping quadrupole fields that shift the centre of the magnetic trap along the vacuum system [160]. The reason for this dichotomy of transport techniques is the presence of the 4-lens objective located under the cell. This imaging device (and is associated mounting components) blocks the otherwise free path through which the transport coils would pass if the atoms were to be translated the full distance using the transport rail.

Once a stable 60 A current in the *Transport* coils has been established, the poor lifetime for magnetically trapped atoms in the MOT chamber requires transportation of the atoms to start quickly. A 70 A current in the *Lateral steering* coil is ramped up over 200 ms producing a magnetic bias field that aligns the centre of the magnetic trap with the hole in the side of the MOT mirror (see fig. 6.2). A TTL pulse triggers the control box for the motorised transport rail to execute a user defined movement profile. The tight confinement of the atoms allows the transport rail to accelerate the coils at up to a speed of 1.2 m/s before any detrimental effects on the atoms become apparent.[3] The transport rail is carefully aligned with the x axis of the vacuum system to minimise losses

[3]Although not fully characterised in detail, the heating of the cloud at higher accelerations is thought to come from momentum transfer to the trapped atoms due changes in the trap velocity occurring over non-adiabatic timescales.

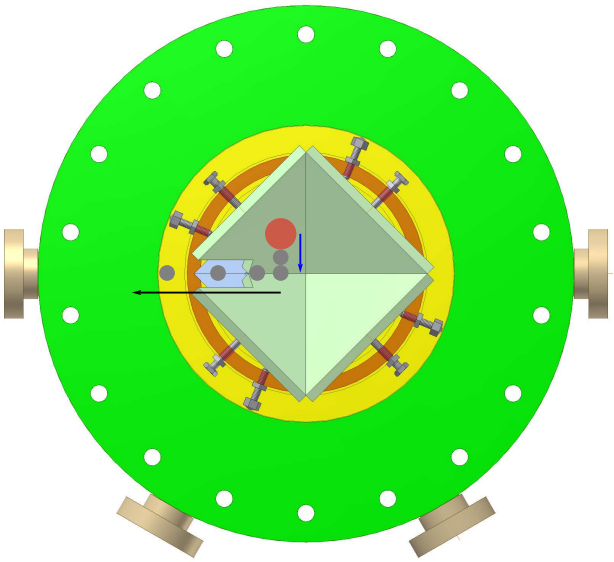


Figure 6.2: View from above of the pyramid mirror located inside the MOT chamber. The red disk illustrates the off-centre position of the MOT that avoids atom loss by unbalanced beams due to gaps between the pyramid mirrors. The grey disks (not to scale) represent the magnetically trapped atoms moving, first due to ramping current up in the *Lateral steering* coil (blue arrow) and second by moving the *Transport* and *Lateral steering* coils using the motorised translation stage (Black arrow).

from contact with the walls of the differential pumping tube during magnetic transport. The current in the *Lateral steering* coil is kept constant for the duration of the magnetic transport part of the sequence.

The second part of the hybrid magnetic transport (referred to as magnetic transfer) employs the current ramps depicted in fig. 6.3 to complete the sequence.[4] The current ramps are optimised to deliver the maximum number of atoms to centre of the *Quad* coils. The layout of the magnetic trap does not allow the 2:1 aspect ratio of the cloud to be maintained during magnetic transfer, however the 4 s allocated to the switching sequence ensures all changes occur adiabatically.

Following hybrid magnetic transport, approximately 4.5×10^8 atoms arrive in the glass cell at a temperature of a few hundred μK.

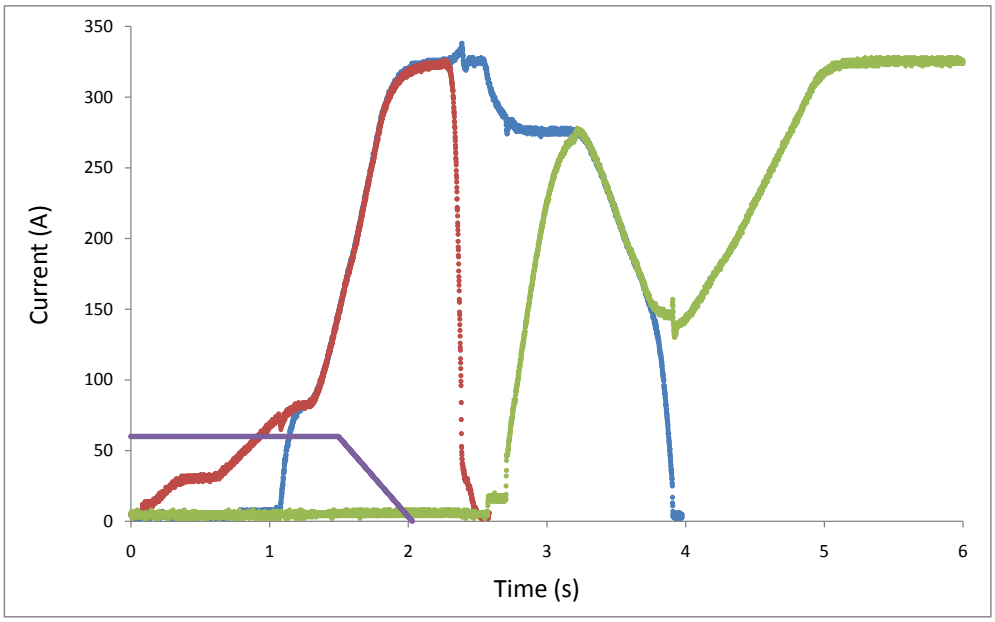


Figure 6.3: Magnetic transfer current ramps in the *Transport* (purple), *Push* (Red), *Auxiliary* (Blue) and *Quad* (Green) coils. Note the current spikes that are observed most noticeably on the *Auxiliary* (at $t = 2.5$ s) and *Quad* (at $t = 4$ s) coil traces result from back EMFs induced when a coil is switched off rapidly.

[4] All of magnetic transfer takes place outside of the differential pumping tube, where the internal diameter of the vacuum system is much larger and hence the *Lateral steering* coil is not required.

6.2 Evaporative cooling in the quadrupole trap

When the atoms arrive in the glass cell, the lack of sub-Doppler cooling and the heating incurred in loading the magnetic trap mean the cloud is too hot to efficiently load into the TOP trap. Therefore prior to TOP loading, with the atoms trapped in the quadrupole trap formed by the *Quad* coils a stage of rf induced evaporative cooling is performed. As shown in fig. 6.3, the current in the *Quad* coil pair is slowly ramped over 1 s to ensure an adiabatic compression of the cloud, until the gradient of the field reaches its maximum value of $B'_{\mathrm{q}} = 399\,\mathrm{G/cm}$. With the cloud maximally compressed (giving the highest possible elastic collision rate), a period of evaporation in this quadrupole trap is desirable for the following reasons: As mentioned, following magnetic transport the temperature of the atoms is comparable with the maximum achievable trap depth of 361 μK for the TOP trap (limited by the maximum amplitude of the rotating bias field of 43 G) so to minimise losses some pre-cooling is required. The linear potential of the quadrupole trap actually provides greater compression and thus higher elastic collision rates than the harmonic TOP trap [106]. Finally the temperature of the atoms means the rate of losses via Majorana spin flips at the field zero is relatively slow compared with colder samples.

The evaporation ramp in the quadrupole was empirically optimised to run from 120 MHz to 20 MHz in 10 s, with 1×10^8 atoms remaining at the end of the ramp. Based on a measurement taken in the TOP trap immediately following loading (when the quadrupole gradient is lowered to $B'_{\mathrm{q}} = 36.3\,\mathrm{G/cm}$) the temperature of the atoms at this stage is 20 μK.

6.3 Loading the TOP trap

Following the period of evaporation in the tight quadrupole trap, the gradient is adiabatically reduced to the low value of 36.3 G/cm in preparation for the application of the rotating bias field that gives rise the to the TOP trap. When loading the TOP trap, the magnitude of the bias field should be large enough to push the field zero of the quadrupole trap out beyond the radius of the cloud. However the bias field is established in approximately 100 μs, thus affecting (weakening) the geometry of the trap in a highly non-adiabatic fashion. To minimise the impact of this abrupt change, an initially low value of the TOP field (4.2 G) is used, which with the low gradient of the quadrupole trap produces a radius for the *circle of death* of $r_0 = 1.1\,\mathrm{mm}$.[5] A simple estimate for the radius of a 20 μK cloud in this TOP trap gives a value of 0.87 mm. This suggests that whilst the majority of the atoms are captured inside the radius of the *circle of death*, some losses are incurred during this stage, but the impact of such losses on the

[5] In principle, a mode matching condition of sorts could be applied if the quadrupole gradient could be changed as quickly as the TOP field in order to keep the trap stiffness approximately constant during the switch on stage. However, the timescales at which the SQA power supply responds to changes in the required output are typically 100 ms, or much too slow to match changes in the TOP circuitry.

ultimate condensate number is lower than the loss of phase space density resulting from non-adiabatic changes to the trap geometry.

6.4 Evaporation in the TOP trap

To evaporatively cool a sample to quantum degeneracy in the TOP trap takes of the order of 40 s. The total evaporative sequence is divided into ~ 5 s stages, where the phase space density of the cloud at the end of each stage used as a figure of merit for optimisation.[6] The sequence begins by slowly increasing both the quadrupole gradient and the TOP field, in an effort to increase the elastic collision rate by adiabatic trap compression, i.e. increasing the trapping frequencies without incurring atom loss via the *circle of death* impinging on the atoms. From this point forward the TOP field is gradually ramped downward, with its changes being roughly followed by the frequency of the evaporative rf radiation.

In the TOP trap the magnitude of the rotating bias field determines the Zeeman shift experienced by the atoms, the size of which represents the location in frequency space of the trap bottom. For ^{87}Rb in the $|F = 1\rangle$ manifold the Zeeman shift equals 0.7 MHz/G, and so the trap bottom is simply found from the product $B_T \times 0.7$ MHz/G. The plots in figs. 6.4 and 6.5 show the changes occurring during the TOP trap evaporation sequence to the quadrupole gradient, TOP field amplitude (and thus trap bottom) and evaporative field frequency. These plots also illustrate that despite several months of optimisation,[7] and a system that regularly produces condensates in the TOP trap of 4.5×10^5 atoms, clearly improvements remain to be made.

Considerable effort is made during the TOP trap evaporation sequence to ensure that atoms are removed via rf induced spin-flips rather than intrinsic evaporation by the rotating field zero. Although it is entirely possible to evaporate to BEC using only the latter technique, on this apparatus the resulting condensates tend be much smaller, and the sequence would have to be made somewhat longer. By adjusting the current in the *Evap rf* coils, a independent control is afforded over the 'sharpness' (i.e. width in frequency space) of the rf cutting surface, allowing greater selectivity of atoms which is particularly important in the final stages before the onset of condensation.[8]

[6] Phase space density naturally incorporates the changes to the trap stiffness that occur widely during the evaporative sequence, and so allows a consistent comparison between evaporation in different trap configurations.

[7] A detailed account of the early evaporation sequences is presented in [143].

[8] If the quadrupole gradient is held constant then evaporation using the *circle of death* has no analogous control over the sharpness of the cutting surface in frequency space. As a result, as the cloud temperature drops and the energy distribution narrows, it is increasingly difficult to select and remove atoms with above average thermal energy, therefore decreasing the overall efficiency of evaporation.

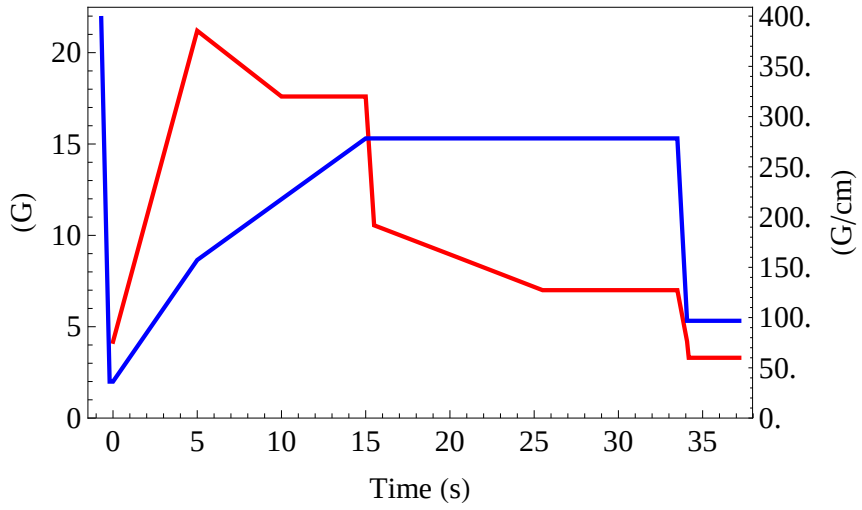


Figure 6.4: Quadrupole gradient (Blue) plotted in units of (G/cm) on the right hand y axis, and the TOP field amplitude (Red) plotted in (G) on the left hand y-axis, during the TOP trap evaporation sequence. Adiabatic compression occurs in the first 5 s of the sequence, whereafter the quadrupole gradient is increased further, and the ever decreasing temperature of the cloud allows the TOP field to be reduced. The dramatic decrease of both the TOP field and the gradient in the final stage is an artifact from the preparation for the loading of the TAAP trap, where bias fields of the order of 3 G are required.

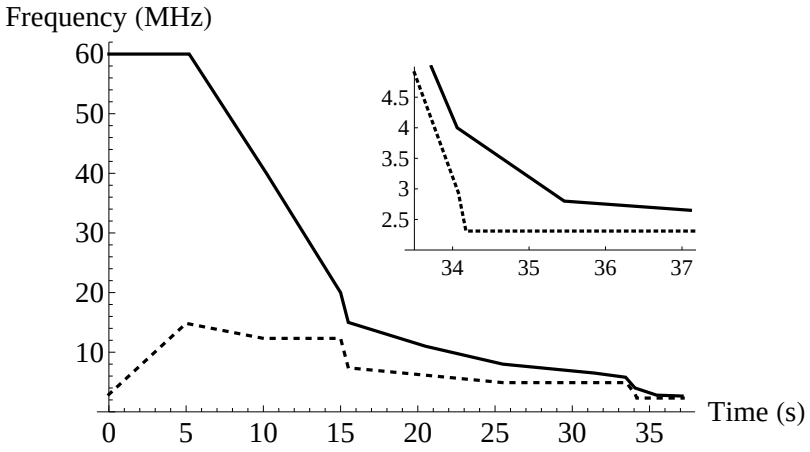


Figure 6.5: The evaporation frequency (solid line) and the trap bottom of the TOP trap (dashed line) during the TOP trap evaporation sequence. The inset magnifies the final 4 s of the sequence.

6.5 Imaging the atoms

The interaction of light with an atom is governed by three processes; absorption, emission and phase-shifting. Each process has been exploited by atomic physicists to provide information on the sample of atoms being investigated. The scattering of photons out of a laser beam underlies the technique of absorption imaging. Fluorescence imaging involves focussing some of the spontaneously emitted photons down on to a camera. Dispersive techniques such as phase-contrast [88] or dark-ground imaging [161] can take non-destructive images of a BEC by detuning the probe light sufficiently that the effects of dispersion dominate those of absorption.

In absorption imaging, three images are combined in software to extract quantitative information about the atom cloud. The first image contains the shadow left in the probe beam by a cloud of atoms after some time of flight (C_1). The second image is an identical probe pulse, but in the absence of the atoms (C_2) and the third is a dark image taken in the absence of any probe light, thus providing a measurement of the stray light and dark current of the detector (C_3).

The Beer-Lambert law relates the absorption of light to the properties of an optically thin sample of the material it propagates in. The probe beam, in the absence of an ultracold cloud of ^{87}Rb in the glass cell will register an intensity of $I_0^{i,j}$ in the pixel (i,j). Following a successful experimental sequence, the atoms will reduce this intensity at each pixel to

$$I^{i,j} = I_0^{i,j} e^{-\int n^{i,j} y \sigma dy}, \tag{6.1}$$

where $n^{i,j}$ is the number of atoms per unit length in the area A imaged onto a single pixel, and σ is the absorption cross-section for a two level transition [17],

$$\sigma = \frac{\Gamma}{2} \frac{2(I_0/I_{\rm sat})}{1 + 2(I_0/I_{\rm sat}) + 4\delta^2/\Gamma^2} \frac{\hbar\omega}{I_0}. \tag{6.2}$$

The number of counts C registered by the CCD per unit light intensity depends on the efficiency α of each pixel thus, $C^{i,j} = \alpha^{i,j} I^{i,j}$. Substituting for this expression for the intensity and rearranging eqn. 6.1, the number of atoms recorded on the (i,j) pixel is

$$N^{i,j} = -\frac{A}{\sigma} \ln \left(\frac{C_1^{i,j} - C_3^{i,j}}{C_2^{i,j} - C_3^{i,j}} \right). \tag{6.3}$$

The total atom number is simply found by summing over the contributions from each pixel. A limitation of absorption imaging is that for the above analysis to be valid, the cloud must be optically thin, i.e. optical depth ≤ 1. This means it is not possible under normal circumstances, to take *in situ* images of ultracold clouds, as even before condensation the optical depths are rather large. The rapid expansion that occurs under time of flight reduces the sample density sufficiently that (depending on the initial confinement) after 10-20 ms of free fall the optical depths are within suitable range for

absorption imaging. Further information such as size and temperature is extracted from the images by fitting a 2D bimodal distribution, that uses Gaussian and parabolic functions to fit the thermal and condensed parts of the cloud respectively.

In the horizontal imaging system, the images C_1, C_2, C_3 are taken approximately 1 s apart. However, the higher magnification of the vertical imaging system causes a problem during this process. The time interval between exposures gives the fringe pattern imprinted in the beam an opportunity to change due to oscillations in the imaging optics mounts. The cancellation of fringes that is performed in the imaging software becomes compromised, degrading the quality of the final image. To limit the impact of this effect, the Unibrain camera is programmed to take two consecutive exposures of the minimum exposure time (50 ms). By adjustment of the probe pulse timings, the situation may be engineered where the first pulse falls at the end of the first exposure and the second pulse at the beginning of the second exposure, achieving a total pulse interval of only 500 μs. One of the side-effects of this approach was that it required reversing the order of the C_1 and C_2 images as it was observed that after only 500 μs the atoms that had been imaged (during C_1) had not had time to exit the field of view (and were detected in C_2). The atoms begin in the $|F = 1, m_F = -1\rangle$ state and so require repumping before they can be effectively imaged using the cooling light. By delaying the repumper pulse until after C_2, the atoms only interact with a single probe pulse.

6.6 Observing the BEC phase transition

Evidence for the thermal cloud to BEC phase transition is manifest in two equally dramatic phenomena. The narrowing of the cloud density distribution as atoms that enter the condensed state take on the Thomas-Fermi distribution is complemented by the anisotropic expansion of the condensate under time of flight. In the condensed state, the interaction energy which is proportional to the trap frequency, dominates the atom's thermal energy, and thus powers the condensate to invert its in-trap aspect ratio under time of flight.

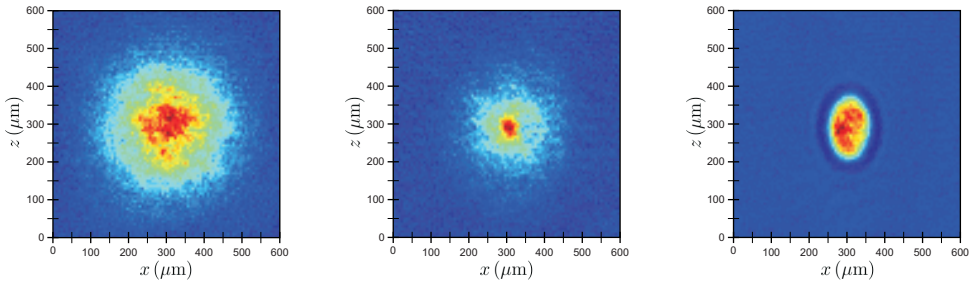


Figure 6.6: Images of a thermal cloud (left) as it is evaporatively cooled to the quantum phase transition (centre) and beyond to become a pure BEC (right). Each image is taken with the horizontal imaging system after the same 24 ms time of flight. The final atom number in the condensate is 4.5×10^5 atoms.

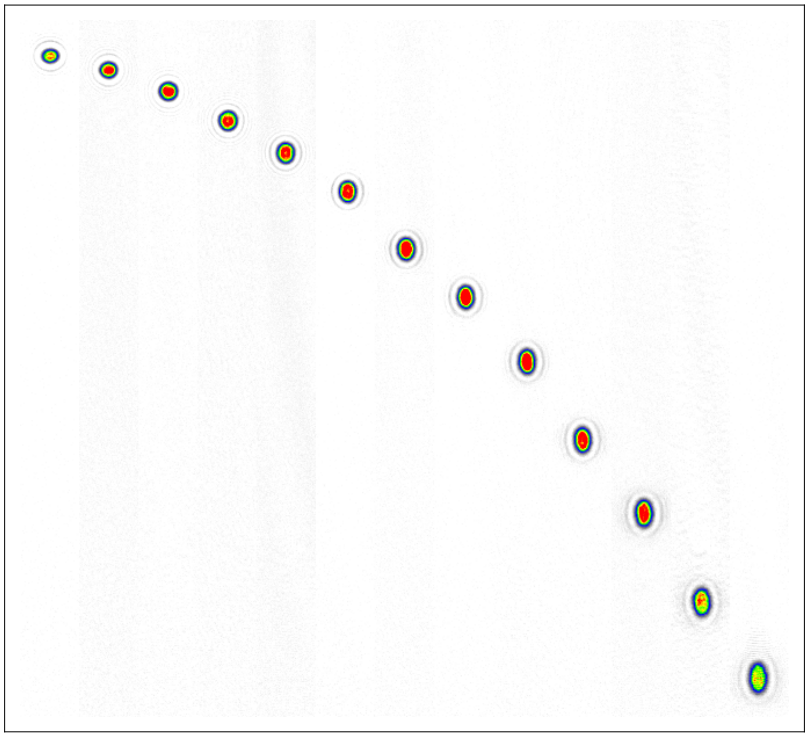


Figure 6.7: Images of the anisotropic expansion of a BEC released from the TOP trap as it falls under time of flight. The images were taken using the horizontal imaging system, at 2 ms intervals, starting at 3 ms and finishing at 27 ms. The TOP trap from which the condensates were released had trapping frequencies of $\omega_{x,y} = 2\pi \times 30$ Hz and $\omega_z = 2\pi \times 85$ Hz.

Chapter 7

The double-well TAAP trap

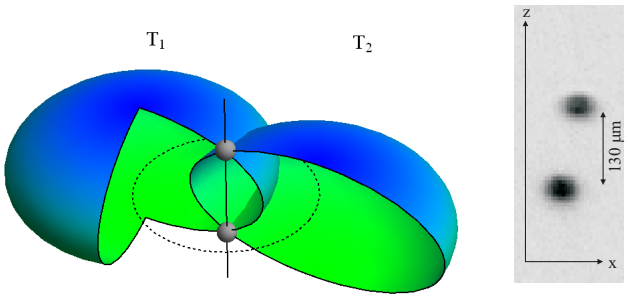


Figure 7.1: The vertically offset double-well TAAP trap. (Left) The resonant ellipsoid is illustrated at two times (T_1, T_2) during its rotation cycle. The atoms are trapped at the positions where the ellipsoid intersects with the rotation axis. The dashed line represents the orbital path of the quadrupole field zero. (Right) An *in situ* absorption image of the atoms trapped in the double-well potential. The tilt evident in this image is attributed to misalignments of the rotation axis with respect to the symmetry axis of the quadrupole field.

The realisation of a time-averaged adiabatic potential for ultracold atoms represents another milestone in the evolution of research into the quantum degenerate gases. A combination of static and time-dependent magnetic fields allows the TAAP to access a myriad of trapping geometries, many of which are beyond conventional magnetic traps, placing this potential in a leading position in the field of magnetic trapping technology. Dynamic optical dipole potentials that are formed by either rapidly scanning a focussed laser beam around a BEC [109] or using a spatial light modulator [162] have shown similarly promising results (particularly the former technique).

In the following chapter a hybrid scheme that combines a form of the TAAP with a time-averaged dipole trap is proposed as a method for accessing some highly demanding

regimes of confinement. In general, the term TAAP refers to a *class* of potentials that generate confinement using magnetic fields at three well separated frequencies, rather than a single, unique trap. In the interests of clarity, this chapter will focus on the double-well TAAP trap that arises from the combination of a rotating bias field and a rf-dressed quadrupole potential. This is the first TAAP trap that was loaded with ultracold atoms and a detailed account of its characterisation can be found in [131]. In this chapter a brief overview of the double-well TAAP trap is presented, including its role as a loading scheme for the bare rf-dressed shell potential. Some recent results are presented that show the inbuilt LZ loss mechanism can be used for evaporative cooling of a thermal cloud across the BEC phase transition. The chapter concludes with the proposal and realisation of a horizontal double-well TAAP trap, where the symmetry breaking effects of gravity can be negated allowing approximately equal numbers to loaded into each well.

7.0.1 Thesis nomenclature

In this and the following two chapters, repeated reference will be made to trap frequencies of the particular potentials under discussion. Presently no convention exists to label the directions which these frequencies refer to. In the interests of simplicity, in this thesis trap frequencies will be referred to as either radial or axial. Radial refers to the confinement experienced by the atoms in the horizontal (xy) plane. Axial frequencies are measured parallel to the vertical (z) axis. To see how these directions related to the experimental apparatus see fig. 5.3.

7.1 Overview

In the vertically offset double-well TAAP, a radial rotating bias field causes the resonant ellipsoid formed by the dressing of a cylindrically symmetric quadrupole trap to rotate in the xy plane. In the absence of gravity, this system has a pair of symmetric minima at the positions where the ellipsoid intersects with the rotation axis (see fig. 7.1).

7.1.1 Loading the TAAP trap

The loading stage for this TAAP begins with a cloud of 5×10^6 atoms in an axially (z) symmetric TOP trap where $B'_{\mathrm{q}} = 56\,\mathrm{G/cm}$ and $\mathrm{B_T} = 3.2\,\mathrm{G}$. For all the work performed in the double-well and shell potentials, the atoms remain (within the displacement caused by gravity) on the avoided crossing. Thus in the double-well TAAP trap the bias field acts to determine the atoms' position around the resonant ellipsoid. Prior to the application of the dressing radiation $\mathrm{B_T}$ must be adjusted such that it lies in the interval,

$$\frac{\omega_{\mathrm{rf}}}{0.7\,\mathrm{MHz/G}} < \mathrm{B_T} < \frac{2\omega_{\mathrm{rf}}}{0.7\,\mathrm{MHz/G}}. \tag{7.1}$$

Here the lower bound ensures that the atoms are loaded into the correct (i.e. $|+\rangle$) dressed state. The upper bound prevents the atoms from being trapped at higher order avoided crossings (see section 4.3.2) where due to power considerations the atoms are rapidly lost from the system. Provided the atoms are located close to the centre of this interval the dressing radiation does not significantly modify the trap geometry — in effect the atoms do not experience any difference from the TOP trap at this stage (see fig. 7.2).

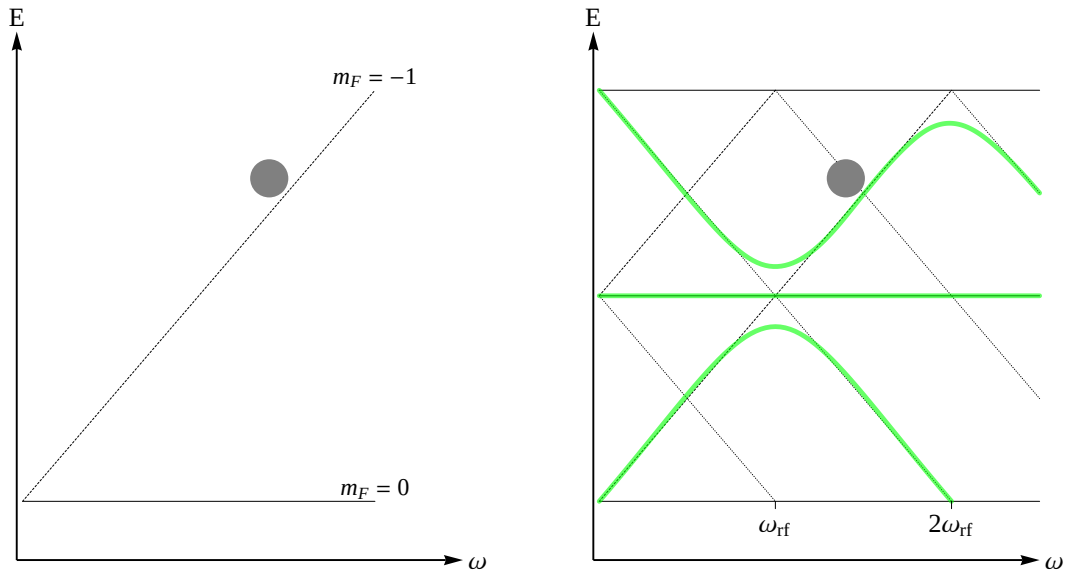


Figure 7.2: Energy levels in the TOP trap in the absence (left) and presence (right) of a rf-dressing field. The thick green lines show the dressed state manifold in which the atoms are trapped. In the figures the potential at the position of the atoms is (to a good approximation) the same. The effects of the dressing radiation on the system become apparent if the rotating bias field is either increased, typically causing rapid atom loss at the $2\omega_{rf}$ avoided crossing, or decreased resulting in the loading of the TAAP potential.

The dressing frequency in this experiment is fixed at $\omega_{rf} = 2\pi \times 1.4\,\mathrm{MHz}$[1] and so the TOP field amplitude of $B_T = 3.2\,\mathrm{G}$ is comfortably inside the interval defined above. Following the rapid switch on of the dressing radiation, B_T is ramped down. The TAAP is loaded when equality in the lower bound of relation 7.1 is satisfied, which for this experiment occurs at $B_T = 2\,\mathrm{G}$. Gravitational sag in the TOP trap results in the lower of the two wells to be preferentially populated by the atoms. Throughout this thesis, any reference to atoms trapped in the vertical double-well TAAP refers only the lower

[1]It is of pure coincidence that the frequency of the most convenient resonance found in the rf coil circuitry was an integer multiple of the Zeeman shift for atoms in the $|F = 1\rangle$ hyperfine state, giving values for the lower and upper bounds of the inequality 7.1 of 2 G and 4 G.

of the two wells.[2]

When TAAP loading is undertaken with xy circularly polarised dressing radiation the best results are achieved when the rotating bias field is quickly ramped over 100 ms to a value of 1 G. The reason for this relatively fast change in the potential is, under this polarisation the coupling strength $\Omega(\boldsymbol{r})$ at the equator is half its maximum value at the South pole. The sensitivity of the LZ loss to this quantity (see eqn. 4.59) means that the bias field must be changed quickly to shift the trapping position around the ellipsoid, towards the South pole where $\Omega(\boldsymbol{r})$ takes is maximum value.

Although efforts are made to ensure the changes in the trapping potential occur slowly during the TAAP loading, some heating and atom loss is observed particularly when the resonant ellipsoid first impinges on the atoms. For this reason, the evaporative ramps that produce a BEC in the TOP trap are truncated, to leave the sample at a temperature of 1 μK before TAAP loading. The final stage of evaporative cooling is performed in the TAAP, where condensates of a similar size (4.5×10^5 atoms) to those made in the TOP trap result. The topic of rf evaporation in the TAAP trap is revisited in the Appendix B.

7.1.2 Characterisation

The double-well TAAP trap has a variable aspect ratio that is parameterised by the amplitude of the rotating TOP field. Shortly after loading, the double-well takes on a spherical symmetry (i.e. $\omega_r = \omega_z$). As $\mathrm{B_T}$ is reduced the trap frequencies diverge from one another. For a typical TAAP trap configuration, i.e. $B'_\mathrm{q} = 84\,\mathrm{G/cm}$ and $\mathrm{B_T} = 1\,\mathrm{G}$, the trap frequencies are measured to be $\omega_r = 2\pi \times 48\,\mathrm{Hz}$ and $\omega_z = 2\pi \times 205\,\mathrm{Hz}$.

Landau-Zener spin-flip transitions are the dominant source of atom loss in the double-well TAAP trap and this mechanism is known to be strongly sensitive to $\Omega(\boldsymbol{r})$. As alluded to in the discussion about loading the TAAP trap, lifetimes in the TAAP trap are determined by the interplay between the rf polarisation and the position of the atoms around the resonant ellipsoid. This behaviour was investigated in detail by adjusting the value of $\mathrm{B_T}$, and the changes were observed to be consistent with the LZ model. The results of these investigations were reported in [140].

The TAAP as a loading scheme for the shell trap

The double well TAAP trap, in addition to being a useful potential in its own right, also marks the beginning of the loading scheme for the bare rf-dressed shell trap (see chapter 8). In other experiments with ultracold atoms trapped in shell type potentials, the loading scheme relied on either a frequency ramp of the dressing radiation over several MHz [111, 115] or the use an optical dipole potential to bias the atoms away from centre

[2] As shown in fig. 7.1, both wells can be loaded using careful adjustment of the quadrupole gradient. A full investigation of the feasibility splitting and separating a BEC in this potential is yet to be performed.

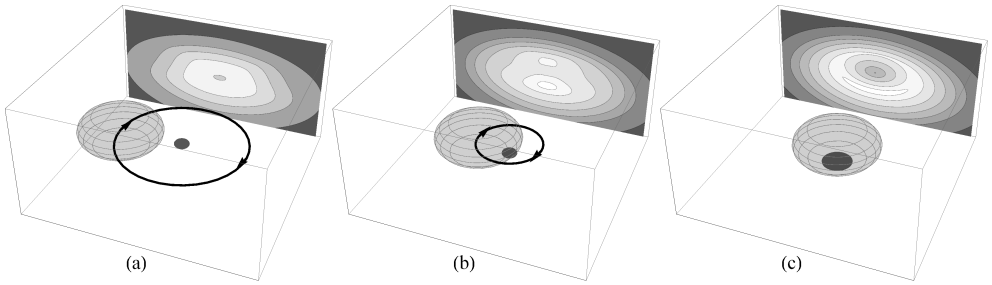


Figure 7.3: The TAAP-trap loading scheme. The bold line shows the locus of the center of the quadrupole field. Cross sections of the potential in the plane $x = 0$ are projected at the rear of each plot. (a) The conventional TOP trap. Switching on the rf does not significantly modify the potential experienced by the atoms (represented by the central darkened region) as the resonant ellipsoid orbits exterior to their position. (b) The vertically offset double-well TAAP trap. Lowering B_T causes the resonant ellipsoid to spiral inwards, trapping the atoms at the two positions where it intersects with the rotation axis. Note due to gravity, in this case only the lower well is loaded. (c) The shell trap. In the absence of a time-averaging field, the atoms are trapped on the resonant ellipsoid, their final position being determined by the balance between gravity and the variation in $\Omega(\mathbf{r})$.

of the quadrupole field [163]. Both methods have their intrinsic problems. Experiments employing the former method observed varying degrees of heating during the frequency ramp, whilst the latter method was very sensitive to thermally induced misalignments in the dipole beam path requiring repeated alignment every few hours. The improved magnetic trap found in this experiment allows the simultaneous application of time-averaging and rf-dressing fields,[3] therefore enabling the double-well TAAP trap (with all atoms in the lower well) to be used to smoothly load the shell trap by decreasing $B_T \to 0$.

7.2 Natural evaporation in the TAAP trap

Natural evaporation in the lower well of the double-well TAAP trap exploits the holes in the rf-dressed potential where $\Omega(\boldsymbol{r}) \to 0$. The potential is adjusted so that the energetic barrier separating the atoms' trapping position (in the lower well) from the region where LZ losses occur rapidly is of the order of the thermal energy of the cloud. By slowly decreasing the height of the barrier, forced evaporative cooling is effected in a manner analogous to evaporative cooling in optical dipole traps [164]. At this juncture is worth mentioning some results reported in [165] that show a similar natural evaporation across the quantum phase transition occurring in the rf-dressed shell potential. In this instance

[3]The previous apparatus in Oxford that worked with rf-dressed potentials had only a single set of coils to deliver the time-averaging and rf-dressing fields.

the shell potential is supplemented by a weak blue-detuned optical dipole potential that acts to prevent atoms from following all around the shell potential. The more energetic atoms that are able to climb over this potential barrier are lost via LZ transitions, thus the sample is evaporatively cooled with the weak repulsive dipole potential playing the same role as the time-averaging field in the current apparatus.

The barrier height is controlled using the amplitude of the rotating bias field. Efficient evaporation is assisted by a quadrupole gradient of $B'_{\rm q} = 176\,{\rm G/cm}$ which helps maintain a high elastic collision rate (even as the radial trap frequencies tend to low values). The experimental data in figs. 7.4, 7.5, 7.6 compares the process of rf forced evaporation[4] in a typical TAAP trap configuration where $B'_{\rm q} = 55\,{\rm G/cm}$ and $\mathrm{B_T} = 1\,{\rm G}$, with natural evaporation in a TAAP where $B'_{\rm q} = 176\,{\rm G/cm}$, and $\mathrm{B_T}$ is ramped $0.86\,{\rm G}$ to $\mathrm{B_T} = 0.75\,{\rm G}$ over $1.2\,{\rm s}$, resulting in a condensate of 2.5×10^5 atoms.

The apparent simplicity of this process immediately begged the question of why it had not been observed earlier on this experiment. The answer is believed to lie in the unusually high quadrupole gradients used during natural evaporation. In the double-well TAAP trap there is only a narrow window within which the atoms will remain trapped at gradients $> 150\,{\rm G/cm}$. During the loading process if the gradient is too high, the atoms will be pushed into the upper well straight away where they are lost due to the hole in the rf-dressed potential where $\Omega(\boldsymbol{r}) \to 0$. Similarly, a shell potential[5] with $\omega_{\rm rf} = 2\pi \times 1.4\,{\rm MHz}$ will invert if $B'_{\rm q}$ exceeds $80\,{\rm G/cm}$. However, as shown in fig. 7.7 for a narrow range of $\mathrm{B_T}$, where the gravitational potential between the two vertically offset wells is close to its maximum value and the gradient of the coupling strength is not as large as it is around the ellipsoid equator, a minimum in the trap potential persists even when $B'_{\rm q} = 176\,{\rm G/cm}$. In order to arrive at the appropriate TAAP configuration for natural evaporation, the standard TAAP loading sequence is employed, followed by a slow ramp of the quadrupole gradient over $1\,{\rm s}$ from $55\,{\rm G/cm}$ to $176\,{\rm G/cm}$. When the gradient has stabilised the $\mathrm{B_T}$ ramp is initiated. Note that if the ramp continues beyond the quoted final value to a lower value of $\mathrm{B_T} = 0.725\,{\rm G}$ complete atom loss is observed.

The numerical simulations contained in figs. 7.7, 7.8, 7.9 were made using an adapted version of a *Mathematica* code [166], where $\omega_{\rm rf} = 2\pi \times 1.4\,{\rm MHz}$, $B'_{\rm q} = 176\,{\rm G/cm}$, $\mathrm{B}^x_{\rm rf} = \mathrm{B}^y_{\rm rf} = 0.7\,{\rm G}$.

[4]For completeness, the rf ramp that gives rise to the evaporation takes place in $3\,{\rm s}$ over the frequency interval 2.0 - 1.95 MHz.

[5]Some cooling has been observed in the shell potential (see section 8.2.2), however a combination of significantly lower elastic collision rate and a poor lifetime prevented the observation of increases in phase space density.

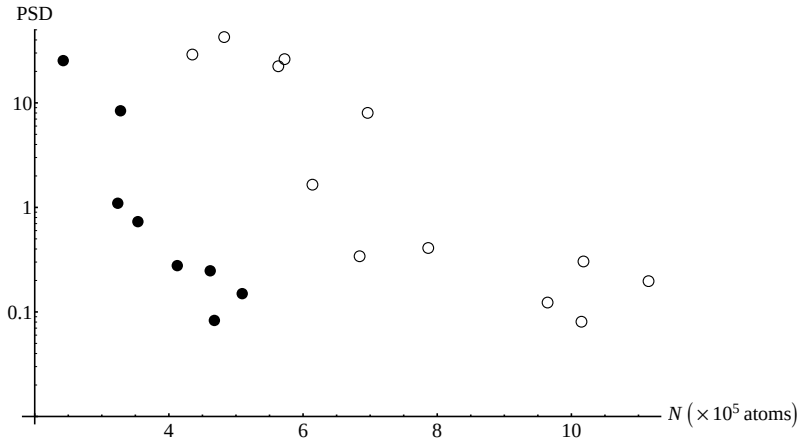


Figure 7.4: Changes in phase space density with atom number during the evaporation process. The natural evaporation data (closed circles) shows favourable increases in PSD for the number of lost atoms, compared with the rf evaporation (open circles).

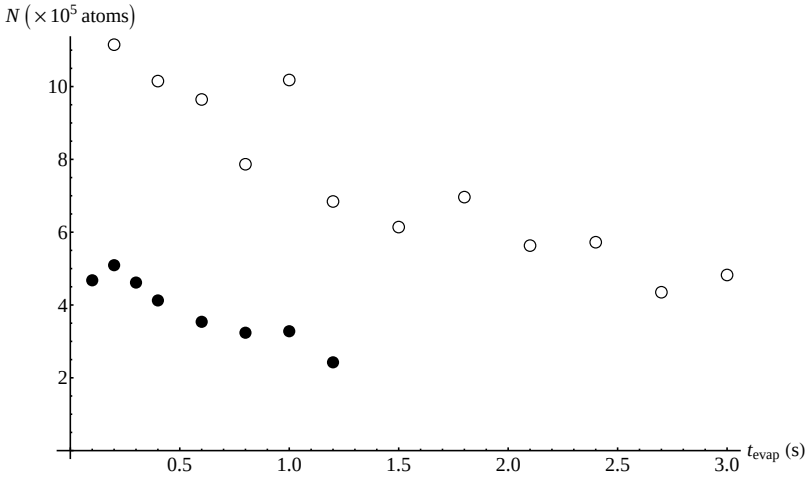


Figure 7.5: Atom number changes over the course of natural (closed circles) and rf (open circles) evaporation.

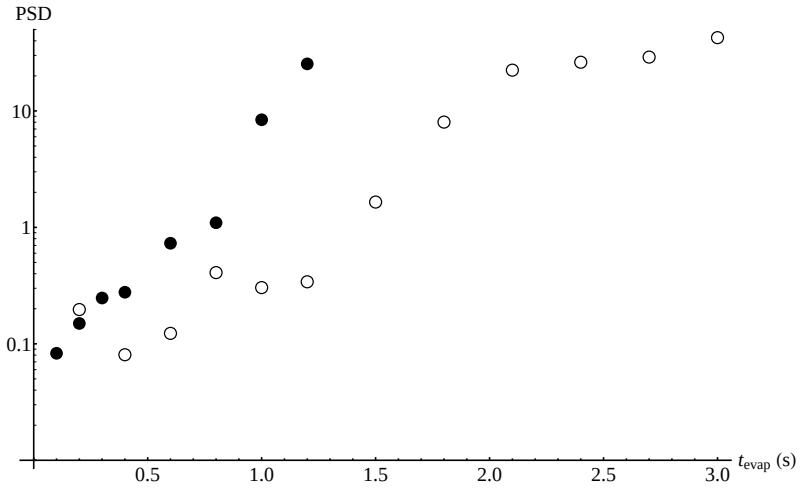


Figure 7.6: Phase space density changes over the course of natural (closed circles) and rf (open circles) evaporation.

7.3 The horizontal double-well potential

The versatility of the TAAP trap is conveniently demonstrated by the transition from a vertically offset to a horizontally offset double-well. In the double-well TAAP trap, the minima of the potential are always located along the rotation axis of the bias field, thus if this axis is located into the horizontal plane, then horizontally offset wells result (see fig. 7.10). In this experiment this is straightforward to achieve by, prior to switching on the dressing radiation, ramping up the field in the $zTOP$ coils over 100 ms to an amplitude approximately equal to the radial TOP field. The current in the $xTOP$ coil pair (this is in-phase with the z TOP field (see section 5.4.2)) is ramped down over 100 ms leaving a bias field that rotates in the $x = 0$ plane. TAAP loading proceeds as normal as the y and z TOP fields are simultaneously ramped down over 300 ms to the values that give the desired separation of the horizontal double-wells.

As with the vertical double-well TAAP trap, the separation of the wells can be smoothly varied by changing the amplitude of the bias field. In order to efficiently load this trap, the polarisation of the dressing rf must be altered from the configurations used for the vertical double-well TAAP. Where the TOP field rotation axis lies in the xy plane, the polar regions of the ellipsoids are the first to impinge on the atoms (as opposed to the equatorial regions in the vertical double-well). As a result the xy circular polarisation commonly used for the vertical double-well, shell and ring potentials will not work for this application. The best results in the horizontal double-well have been achieved using rf that is linearly polarised along the radial direction perpendicular to the bias field rotation axis, i.e. for the yz TOP trap, the rf is polarised along the x direction. This configuration allows the wells to be split to their maximum separation without exposing the atoms to the regions where $\Omega(\boldsymbol{r}) \to 0$.

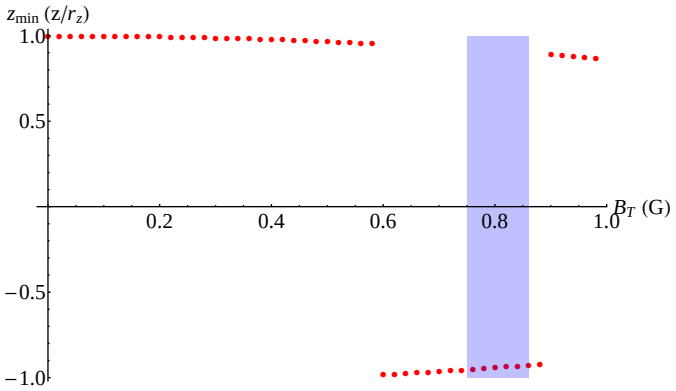


Figure 7.7: The location of the minimum trapping position in the double well TAAP trap. The high quadrupole gradient pushes the minimum position of the TAAP trap to the upper well for rotating bias fields around 1 G. At a range of lower values of B_T the minimum position shifts to the lower well before returning to the upper well as $B_T \to 0$. The blue rectangle shows the range of B_T over which natural evaporation in this potential is observed. The position data on the y axis is quoted in units of the semi-minor axis of the ellipsoid r_z.

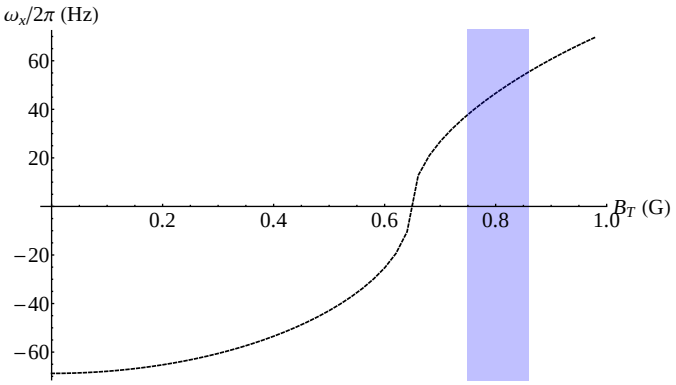


Figure 7.8: Simulated changes to the radial trapping frequency at the position of the lower well in the double-well TAAP trap. The negative frequencies represent a trap with negative (i.e. anti-trapping) curvature. The blue rectangle represents the range of B_T over which natural evaporation in this potential is observed.

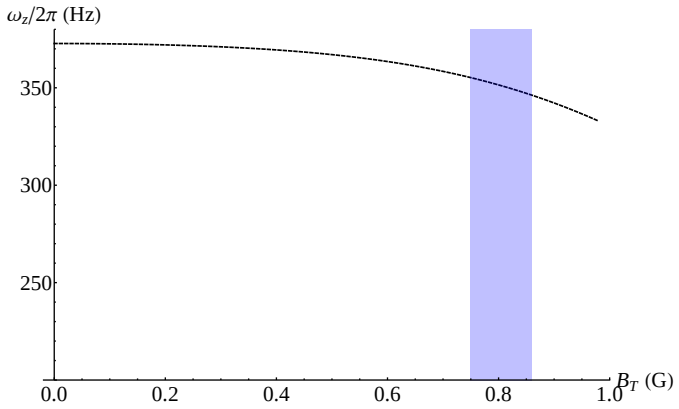


Figure 7.9: Simulated changes to the axial trapping frequency at the position of the lower well in the double-well TAAP during natural evaporation.

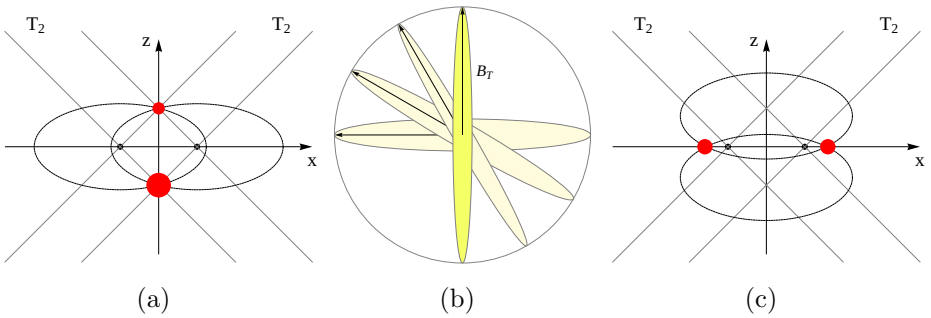


Figure 7.10: (a) The vertically offset double-well TAAP trap that arises from a conventional TOP trap. (b) Rotating the plane of the TOP trap from xy to yz by simultaneously ramping up an axial TOP field and ramping down one of the radial components. (c) The horizontal orientation of the rotation axis gives rise to a TAAP trap with horizontally offset double wells.

An advantage of the horizontal double-well is that gravitational anisotropies between the wells are much smaller than in the vertical case. The radial bias field not being used to form the horizontal wells of the TAAP can be used to introduce a controlled tilt to the potential. As shown in fig. 7.12, the gravitational potential difference[6] between the wells that results from imperfect alignment in the coils can be comfortably overcome using a tilting field of only 0.2 G.

[6] A non-ideal polarisation could also give a small asymmetry between the wells.

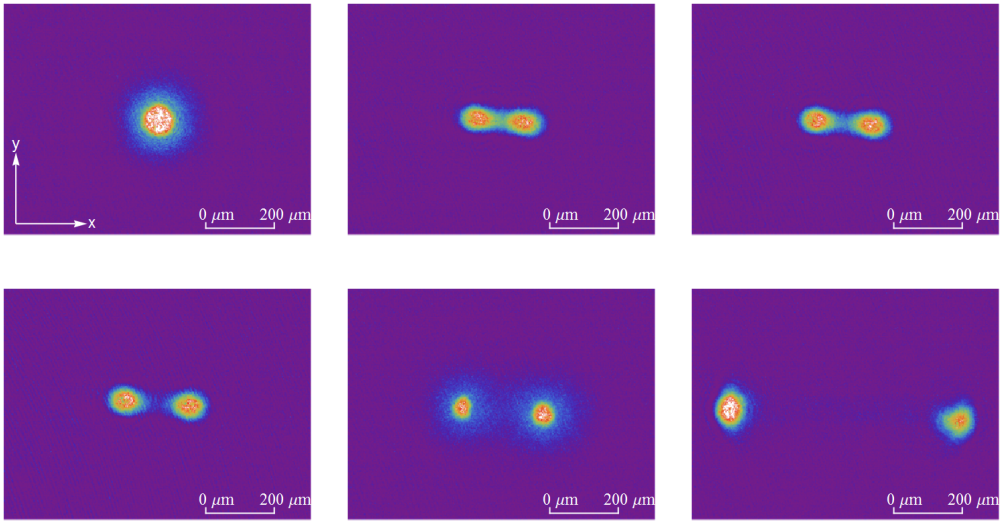


Figure 7.11: A BEC being split in the horizontal double-well potential.

7.4 Conclusion

The double-well TAAP trap is presented as the natural result of the combination of a rotating time-averaging field and a rf-dressed quadrupole field. The principal feature of TAAP traps, namely their versatility is demonstrated by the simple process of transforming a double-well potential with a vertical offset, into one where the wells are separated horizontally. In both cases the separation of the wells is determined by a single parameter, the amplitude of the rotating bias field. Note that although it is not performed on this experiment, the distance between the wells could be changed by adjusting the dressing frequency, or the quadrupole gradient, or to a lesser degree magnitude and spatial dependence of the coupling strength.

The value of a thorough investigation of a potential is demonstrated by the phenomenon of natural evaporation, which was not observed or considered during the initial experiments to characterise the properties of the double-well TAAP trap. Numerical analysis is used to estimate the changes in the potential as B_T is reduced. Although the simulations do not precisely match the experimental results, they do support the general trend of the observations. Small uncertainties in the size of the experimental parameters, combined with the known imperfections in the apparatus can reconcile these results, and thus provide a form of assurance that the mechanism responsible for natural evaporation is understood.

The utility of the natural evaporation process is a valid question since it has been demonstrated in earlier work (and mentioned in this chapter) that conventional evaporation techniques can operate well in these potentials. However, the observation of natural evaporation does show that the progress is being made in understanding the operation and the limitation of TAAPs, which possess powerful attributes that, if they

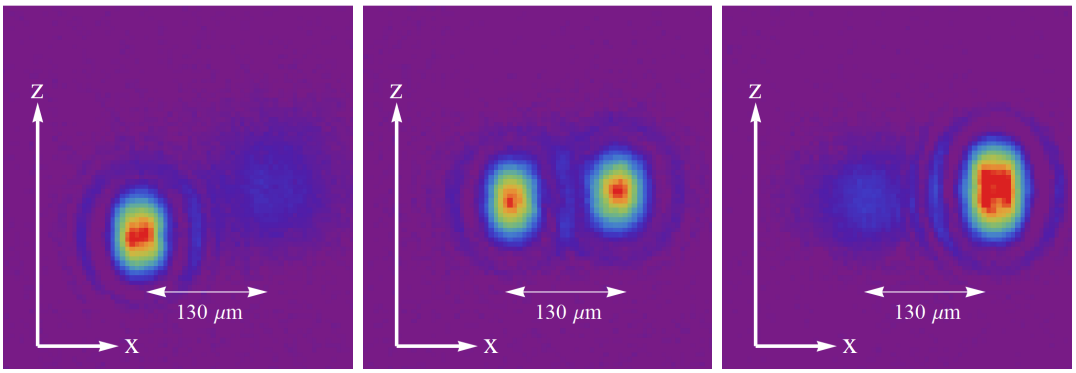
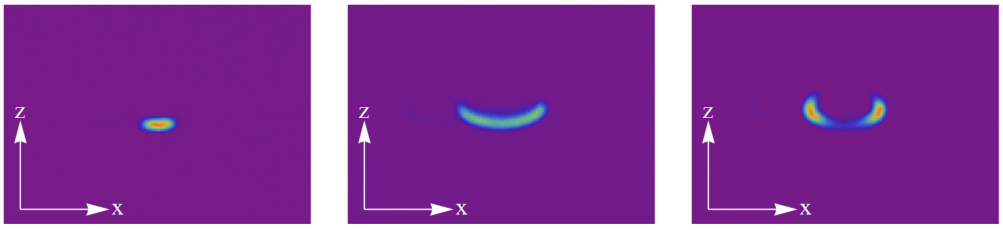


Figure 7.12: A BEC trapped in the horizontal double-well. Intrinsic anisotropies in the magnetic trap cause the majority of a BEC of 3×10^5 atoms to be loaded into a single well (left). The population of each well can be adjusted by tilting the potential using the *xTOP* coils. A field of 0.2 G approximately balances the wells (centre) and 0.4 G tilts the potential to favour the opposite well (right). The faint rings around the condensates are imaging artifacts.

can be correctly harnessed present attractive prospects for experiments with ultracold atoms.

Chapter 8

The rf-dressed shell trap



(a) (b) (c)

Figure 8.1: Atoms in the rf-dressed shell trap. (a) Atoms well localised at the bottom of a balanced shell trap. (b) Atoms spreading around the shell. (c) Splitting the cloud by adjusting the polarisation of the rf dressing field from circular to approximately linear.

The shell trap potential results from the dressing of atomic energy levels in a quadrupole trap with a uniform radio-frequency field, following the theoretical ideas developed in Chapter 4. This potential provides a smooth, flexible and anisotropic trap for ultracold atoms with low heating rates and long lifetimes. The category of rf-dressed potentials to which the shell trap belongs is often touted as a good candidate for studying the manifestation of certain physical phenomena in 2D systems. However, previous experiments were beset by technical problems with loading [115] or heating [111], meaning that the promise of this potential has yet to be realised. The following sections present an experimental characterisation of the shell trap, including evidence for a viable route to the 2D regime.

8.1 Two dimensional systems

Early theoretical investigations into the behaviour of systems experiencing lower dimensional confinement predicted previously unobserved physical processes. Predictions regarding the BKT phase transition in 2D systems, the behaviour of quasi-condensates with distinct regions of phase coherence [39] or the fermoinization of a 1D gas of bosons [167] formed the motivation for the experimental realisation of these systems. The first 2D systems studied in the laboratory were thin films of liquid helium [36] and spin-polarised hydrogen [168] that were made using cryogenic techniques. The first form of 2D confinement for ultracold atoms was achieved in MIT in 2001 using a single tightly focussed dipole trap [169]. Since then numerous experiments using optical or hybrid (magnetic and optical) schemes have achieved lower dimensional confinement for ultracold gases [170, 171, 172, 42, 43]. Despite pioneering work performed by researchers in Paris and NIST, open questions remain concerning the relationship between quasi-condensation and the presence of superfluid behaviour in 2D ultracold systems. Experimental investigation of this subject is part of the future goals for this experiment and will be discussed in the final section of this chapter.

Although 2D confinement in the shell trap is yet to be conclusively observed, the trap does possess some distinct advantages for working in this area of physics over the (currently more popular) optical approach. Evaporative cooling via rf induced spin-flips can be used to regulate the temperature and atom number in the shell trap. The trap is formed from the far-field pattern of macroscopic magnet coils making it very smooth and robust against misalignment. The shell confines atoms in a single plane which is important for achieving single atom imaging using a lens with a shallow depth of field. In some optical schemes where atoms are trapped at the nodes of standing wave, a significant effort is required to remove atoms loaded into the incorrect plane.[1]

8.2 Characterising the potential

The confinement of atoms in the rf-dressed shell trap results from the interplay of 3 factors; the detuning of the rf radiation from the atomic resonance frequency (eqn. 4.22), the spatial variation of the coupling strength (eqn. 4.24) and the force of gravity. Following on from the analysis of chapter 4, the shell potential including gravity, for xy circularly polarised rf dressing radiation can be written as

$$V_{\text{shell}} = mgz + \hbar\sqrt{\left(\omega_{\text{rf}} - \frac{g_F \mu_{\text{B}} B'_{\text{q}} f_{\text{q}}(x,y,z)}{\hbar}\right)^2 + \Omega_0^2 f_{\text{c}}(x,y,z)}, \tag{8.1}$$

[1] It is worth at this point noting that some experiments e.g. [42] benefit significantly from being able to trap atoms in more than one plane.

where

$$\begin{aligned} f_{\mathrm{q}}(x,y,z) &= \sqrt{x^2+y^2+4z^2}, \\ \Omega_0 &= \frac{g_F \mu_{\mathrm{B}} \mathrm{B}_{\mathrm{rf}}}{2\hbar}, \\ &\text{and} \\ f_{\mathrm{c}}(x,y,z) &= \left(1 - \frac{4z}{\sqrt{x^2+y^2+4z^2}} + \frac{4z^2}{x^2+y^2+4z^2}\right), \end{aligned} \tag{8.2}$$

describe the spatial variation of the static quadrupole field, the maximum coupling strength amplitude and the spatial dependence of the coupling strength respectively.

8.2.1 The lifetime of atoms in the shell trap

Atoms remain in a rf-dressed trap until either there is a inelastic background collision or they are lost by a non-adiabatic Landau-Zener spin-flip at the avoided crossing. The LZ losses themselves can be divided into two categories. The first type are crudely referred to as *in situ* LZ losses, where the atom remains in the same position in the trap, and via traversing the avoided crossing at a finite velocity, it fails to adiabatically follow the changes in the dressed state, resulting in a transition to another dressed state where it is lost.

The second type of LZ atom loss occurs when the balance between the gradient of the coupling strength and the gravitational force creates a trap minimum at a position on the ellipsoid where the coupling strength vanishes. In such regions LZ transitions occur rapidly, and the lifetime of the atom cloud is severely reduced.

A delicate balance must be struck between the spatial variation of the coupling strength and the gravitational energy across the shell. The reduction of the LZ transition rate for strong coupling strengths (eqn. 4.59) means a high power dressing field is desirable. However a careful analysis of eqn. 8.1 (see figs. 8.2 and 8.3) shows that when the magnitude of the coupling strength at the South pole exceeds the gravitational potential energy across the shell then the trapping potential inverts, pushing the atoms to the North pole of the ellipsoid where they will be rapidly lost via LZ transitions.

The results on the shell trap lifetime are shown in fig. 8.4. These results show long lifetimes for particular combinations of B_{rf} and B'_{q}. Although the 58 s lifetime that was measured is more than sufficient to use for the intended experiments, it is worth noting that moving to higher dressing frequencies would allow for longer lifetimes, or the use of stronger gradients (to increase trapping frequencies) without adversely affecting the lifetime. This is an important theme that will be revisited in the final chapter. The implication of the plot shown in fig. 8.3 is that at a dressing amplitude of the order of 1 G the coupling strength at the bottom of the shell, will exceed the gravitational potential energy across it, leading to anti-trapping in these regions and so rapid losses from the trap. The reduced lifetime evident in the final datum point in fig. 8.4 supports

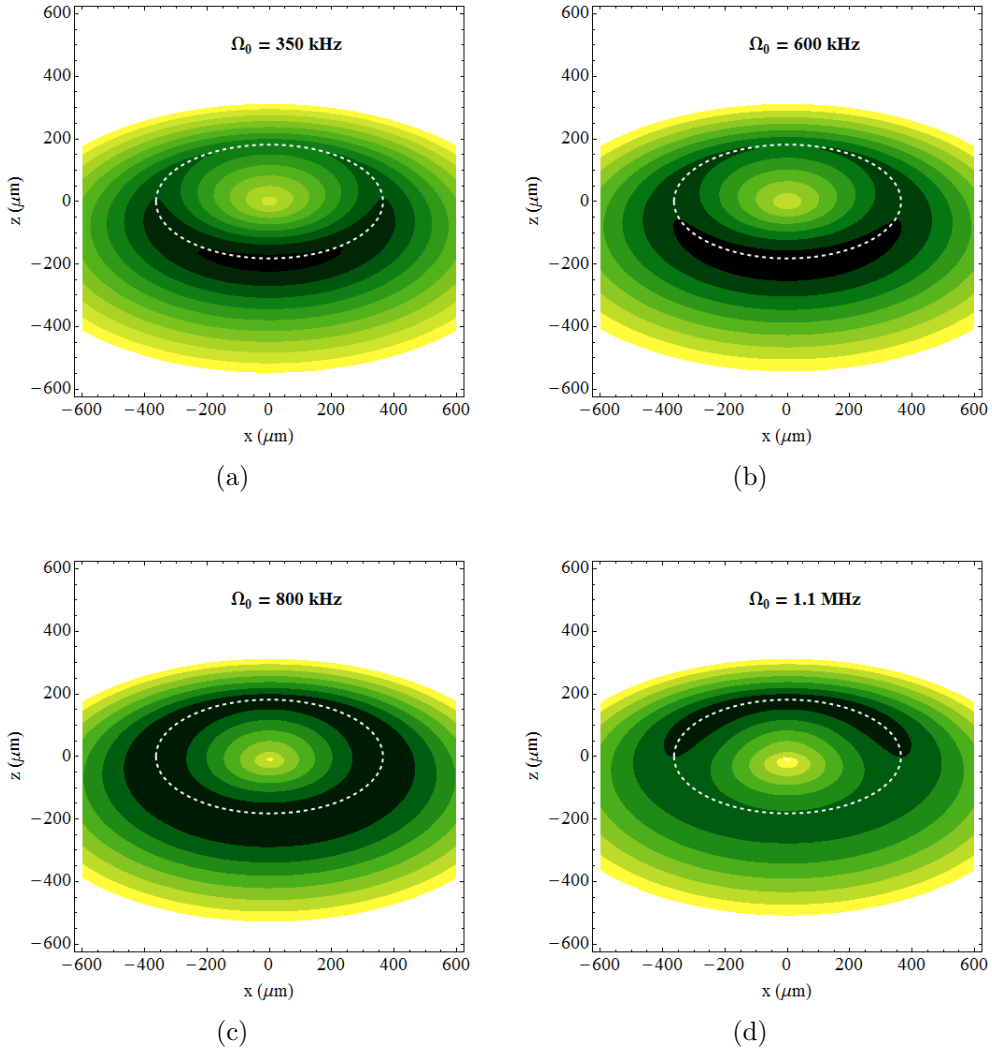


Figure 8.2: Simulations of the shell potential in the $y = 0$ plane for V_{Shell} plotted between $0\,\mu$K and $100\,\mu$K. The darker colours represent the regions of lower potential energy. Increasing the amplitude B_{rf} changes the shape and position of the potential minimum, until the trap inverts. For each plot the following dressing field amplitudes were used; $B_{rf} = 0.5\,G$ (a), $B_{rf} = 0.85\,G$ (b), $B_{rf} = 1.2\,G$ (c), $B_{rf} = 1.6\,G$ (d). The gradient and dressing frequency are held constant at $B'_q = 55\,G/cm$ and $\omega_{rf} = 2\pi \times 1.4\,MHz$. The dashed white line shows the locus of the avoided crossing in this plane. The magnitude of the coupling strength Ω_0 is shown in each plot.

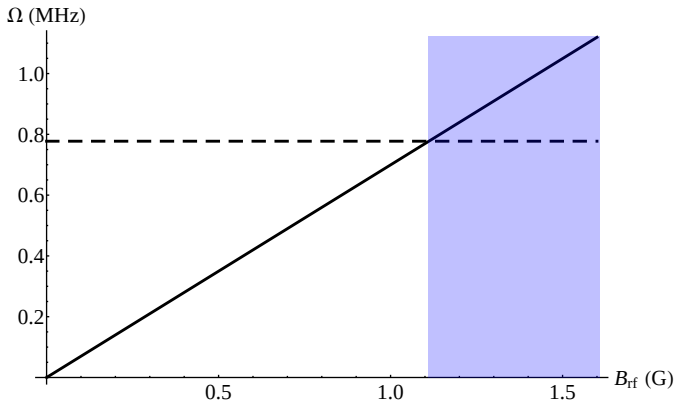


Figure 8.3: The variation of the coupling strength Ω at the South pole of the resonant ellipsoid with the amplitude of B_{rf} (solid line). The gravitational potential across the full height of the shell is also plotted (which is invariant with B_{rf}). Anti-trapping in the shell is indicated by the blue shaded region. In both cases a dressing frequency of $\omega_{rf} = 2\pi \times 1.4\,\mathrm{MHz}$ and a quadrupole gradient $B'_q = 55\,\mathrm{G/cm}$ is used.

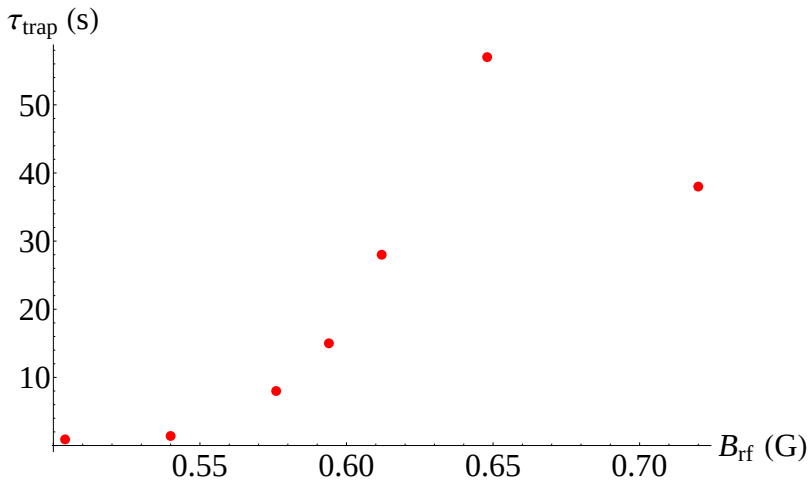


Figure 8.4: Lifetime of atoms trapped at the bottom of a shell trap formed by dressing a quadrupole field with $B'_q = 55\,\mathrm{G/cm}$ with xy circularly polarised rf at $\omega_{rf} = 2\pi \times 1.4\,\mathrm{MHz}$. Increasing the amplitude of the dressing field causes the *in situ* LZ loss rate to decrease exponentially. However when $B_{rf} = 0.72\,\mathrm{G}$ the lifetime has started to decrease suggesting the coupling strength is beginning to overcome gravity and allow the atoms to move further around the ellipsoid, into regions where $\Omega(\boldsymbol{r}) \to 0$ and the LZ loss rate grows rapidly.

B_{rf} (G)	$T_{Initial}$ (nK)	T_{Final} (nK)	t_{Hold} (s)	ΔT (nK)
0.72	435	408	9.9	-27
0.72	465	564	13.9	99
0.72	220	233	13.0	-13
0.65	526	554	13.0	28
0.61	480	455	13.0	-25
0.59	477	426	13.0	-51
0.57	509	407	13.5	-102

Table 8.1: Tabulated temperature changes in the shell trap. All measurements were taken in a shell with a dressing frequency of $\omega_{rf} = 2\pi \times 1.4\,\mathrm{MHz}$ and a quadrupole gradient $B'_q = 60\,\mathrm{G/cm}$. Note that $\Delta T = T_{Final} - T_{Initial}$.

this general trend.

8.2.2 Heating rate

Forced rf evaporative cooling of a thermal cloud across the BEC phase transition has been successfully implemented in the shell, suggesting that the residual heating rate in this potential is well suited to working with ultracold quantum gases. A more quantitative study was performed that measured the temperature of a thermal cloud 1 s after loading into the shell potential, and compared it with the temperature after a variable hold time. The temperature was extracted from fitting to the size of the cloud after time of flight. Unless stated the temperature is quoted as the average of the temperature along the x and z directions. The results are summarised in table 8.1, where the temperature of the cloud appears as likely to decrease as it is to increase. The fluctuating polarity of the difference between the initial and final temperatures is consistent with an approximately constant value for the temperature with a relatively large associated uncertainty.[2]

By careful adjustment of the shell parameters, natural evaporative cooling in the shell of the type also reported in [113] is observed. The data in fig. 8.5 implies it is possible to engineer a scenario where the atoms of above average energy are able to sample regions in the trap where there exists a high probability of the atom being lost via LZ spin-flip transition. To allow for the selectivity of the more energetic atoms the rf power had to be reduced to a value where the measured lifetime was 2.2 s, and the associated atom loss during cooling prevented any apparent increase in phase space density.

[2]The table also appears to show that cooling is more likely to be observed at lower values of B_{rf} suggesting that *in situ* LZ losses are perhaps responsible for cooling the sample. In order to demonstrate this conclusively a more comprehensive study must be undertaken.

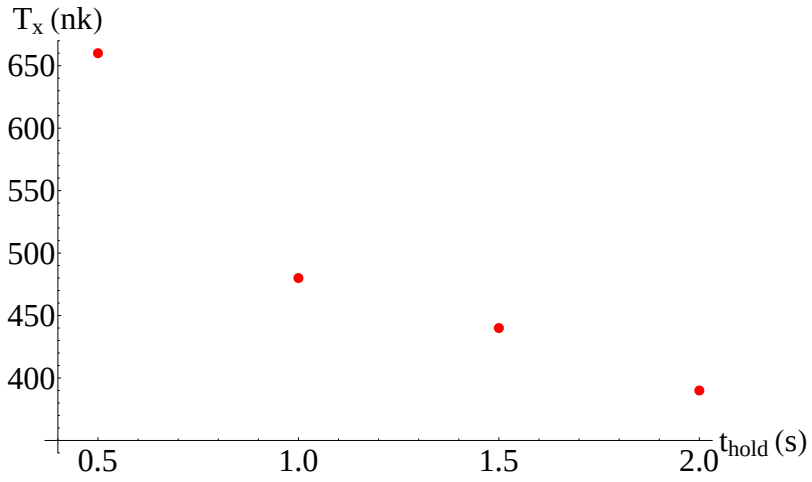


Figure 8.5: Evidence for natural cooling in the shell potential where $\omega_{\rm rf} = 2\pi \times 1.4\,\mathrm{MHz}$, $B'_{\rm q} = 77\,\mathrm{G/cm}$ and $\mathrm{B_{rf}} = 0.56\,\mathrm{G}$. The data is only for the temperature of the cloud along the x axis. The corresponding temperature along the z axis remained approximately constant.

8.2.3 Tilting the shell trap

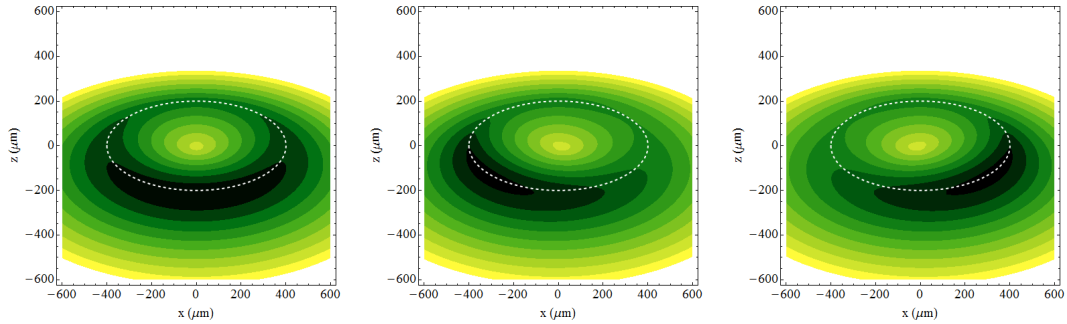
Inherent imperfections in the alignment of the symmetry axis of the quadrupole field with gravity acts to break the radial symmetry of the shell trap, causing atoms to localise in a single region of the trap. These undesirable tilts can be corrected for by modifying the polarisation of the dressing rf using a field from the z *rf* coils. The combination of xy circularly polarised rf and an axial (z axis) dressing field at the same frequency causes the general rf field of eqn. 4.5 to become,

$$\mathbf{B}(\boldsymbol{r},t) = \mathrm{B}^r_{\rm rf}\left(\cos(\omega_{\rm rf}t)\hat{\mathbf{e}}_x + \sin(\omega_{\rm rf}t)\hat{\mathbf{e}}_y\right) + \mathrm{B}^z_{\rm rf}\cos(\omega_{\rm rf}t + b)\hat{\mathbf{e}}_z. \tag{8.3}$$

The gravitational and detuning terms of the shell potential remain unchanged, however full expression for the coupling strength becomes

$$\Omega_0^2 f_c(x,y,z,b) = \left(\frac{g_F\mu_{\rm B}\mathrm{B}^r_{\rm rf}}{2\hbar}\right)^2\left[1 - \frac{4z}{\sqrt{x^2+y^2+4z^2}} + \frac{4z^2}{x^2+y^2+4z^2} + \frac{R^2(x^2+y^2)}{x^2+y^2+4z^2}\right.$$
$$\left. - \frac{2Rx\cos b}{\sqrt{x^2+y^2+4z^2}} + \frac{2Ry\sin b}{\sqrt{x^2+y^2+4z^2}} - \frac{4Rz(y\sin b + x\cos b)}{\sqrt{x^2+y^2+4z^2}\sqrt{x^2+y^2}}\right] \tag{8.4}$$

where $R = \mathrm{B}^z_{\mathrm{rf}}/\mathrm{B}^r_{\mathrm{rf}}$ is the ratio of the magnitude of the axial and radial rf fields.



(a) (b) (c)

Figure 8.6: Tilting the shell potential using an axial dressing field. The figures show the shell potential in the $y = 0$ plane, plotted between $0\,\mu$K and $100\,\mu$K. Using only idealised xy circularly polarised rf and assuming the quadrupole is precisely aligned with gravity, the shell has radial symmetry (a). A controlled tilt in the potential is brought about by the application of an axial rf field of equal magnitude, i.e. $\mathrm{B}^z_{\mathrm{rf}} = \mathrm{B}^r_{\mathrm{rf}} = 0.72\,\mathrm{G}$ and frequency $\omega_{\mathrm{rf}} = 2\pi \times 1.4\,\mathrm{MHz}$ with a relative phase of $b = \pi/2$ (b) and $b = -\pi/2$ (c).

The combination of the three rf fields results in a magnetic field vector that rotates in a plane tilted with respect to the radial plane by an angle given by

$$\theta_{\mathrm{tilt}} = \arctan\left(R\right). \tag{8.5}$$

The direction of the tilt is determined by the relative phase b of the axial dressing field. The tilted rf magnetic field vector changes the position around the resonant ellipsoid where the coupling strength $\Omega(\boldsymbol{r})$ takes its maximum value, which in turn affects the minimum energy position of the shell trap (see fig. 8.6). This adjustable tilting mechanism can be used to correct for intrinsic tilts in the trap to allow the potential to achieve its native anisotropy (the trap frequencies for the bare shell trap are derived in [165]) or to introduce a tilt to localise the atoms in one region of the trap. As will be discussed in section 9.6, adjusting the frequency of the axial dressing radiation relative to the radial fields causes the angle of the tilt to rotate at a rate equal to the frequency difference. Depending on the rotation rate, this technique can be used to instigate rotation of the trapped atoms,[3] or to change the potential landscape by time-averaging the position of the maximum coupling strength.

[3]This is the so called 'gold pan' rotation scheme, that has yet to be utilised in this experiment, but further details can be found in [165].

Stage	Ramp time (s)	Start Frequency (MHz)	End Frequency (MHz)
1	0.8	1.86	1.87
2	1.8	1.87	1.88
3	2.2	1.88	1.886

Table 8.2: The sequence of evaporative cooling ramps used to produce a pure BEC in the shell trap where $\mathrm{B_{rf}} = 0.72\,\mathrm{G}$, $B'_{\mathrm{q}} = 60\,\mathrm{G/cm}$, $\omega_{\mathrm{rf}} = 2\pi \times 1.4\,\mathrm{MHz}$.

8.2.4 RF evaporation in the shell trap

The pooling of atoms at the bottom of the shell increases the density and hence the elastic collision rate so improving the conditions for evaporative cooling. The transition selected for evaporation in the shell trap has a resonant frequency of $\omega_{\mathrm{rf}} + \Omega(\boldsymbol{r})$. The unconventional potential landscape of a shell trap formed with a circularly polarised rf field results in those atoms populating the low energy part of the Boltzmann distribution being generally found in the region where the trap bottom is largest. To efficiently cool by rf forced evaporation in this potential, in contrast to conventional rf evaporation in magnetostatic traps, the frequency of the evaporative field is *increased* over a relatively narrow frequency interval.[4]

The optimised 4.8 s evaporative sequence listed in table 8.2, reliably produces pure condensates of 3.5×10^5 atoms in the shell trap. The evaporative sequence is required to be 1.8 s longer than the corresponding sequence in the radial TAAP trap due to the lower elastic collision rate in the shell potential.

8.2.5 Shell trap frequencies

The frequencies in the shell trap can be found both theoretically and experimentally using conventional techniques. Theoretical values for the harmonic oscillation frequencies of the trapped atoms are extracted by expanding the potential of eqn. 8.1 about the equilibrium trapping position $(0, 0, -z_0)$, where $z_0 = \frac{\hbar\omega_{\mathrm{rf}}}{2g_F\mu_{\mathrm{B}}B'_{\mathrm{q}}}$. For xy circularly polarised

[4]When operated in a configuration that gives long trap lifetimes (i.e. when the maximum value of the coupling strength is significantly smaller than the gravitational potential energy from South to North pole), the potential has a minimum at the South pole of the resonant ellipsoid. Thus the position where the atoms with the lowest kinetic energy congregate is also the position where the term that describes the spatial dependence of the coupling strength (f_{c}) has a maximum (see fig. 4.5). As a result the frequency (found by substituting $x = y = 0$ and $z = 0$) $\omega_{\mathrm{rf}} + 2\Omega_0$ gives the value needed to spin-flip atoms out of the trap at this position. Atoms with larger values of kinetic energy sample the regions around the resonant ellipsoid away from the South pole where the coupling strength is lower. It therefore follows that the frequency required to evaporate these atoms will be lower, and so to evaporatively cool in the shell trap, evaporation must proceed *upwards*.

rf, the shell frequencies are,

$$\omega_x = \frac{1}{2}\sqrt{\frac{g}{z_0}\left(1-\frac{\hbar\Omega_0}{mgz_0}\right)}, \tag{8.6}$$

and

$$\omega_z = 2\frac{g_F\mu_B B'_q}{\hbar}\sqrt{\frac{\hbar}{2m\Omega_0}}. \tag{8.7}$$

Measurement of the trap frequency is performed by exciting dipole mode oscillations by giving the atoms a kick using a coil that is suddenly switched off[5] and measuring the periodic change in atom cloud position following time of flight. Some results of the shell trap frequency analysis are shown in fig. 8.7.

The radial frequencies are measured along the x axis as the horizontal imaging system is most commonly used for such measurements. In order to demonstrate the symmetry of the potential, f_y was measured using the vertical imaging system. At $B'_q = 44\,\mathrm{G/cm}$, $f_y = 11\,\mathrm{Hz}$ which matches f_x to within 1 %.

With the goal of accessing the 2D regime, a strength of the shell trap lies in the approximately independent control afforded over the radial and axial oscillation frequencies. As shown in the fig. 8.7, by simply increasing the quadrupole gradient it is possible to achieve large changes in the axial oscillation frequency, without a dramatic change in the radial values. However in the present shell configuration, increasing the quadrupole field gradient above $B'_q = 60\,\mathrm{G/cm}$ causes the minimum position in the shell to flip to the North Pole, resulting in rapid LZ atom loss. Decreasing the coupling strength mitigates against this, but at the cost of trap lifetime due to *in situ* LZ losses. The plot in fig. 8.8 indicates the number of atoms at which the 2D criterion (see section 2.3) is satisfied for the most anisotropic bare shell trap so far measured.

8.3 Increasing the shell trap anisotropy

In order to move deeply into the 2D regime the trap anisotropies must be increased. Fortunately, the unique flexibility of this potential presents three separate methods that may be employed to do this.

[5]The coil used to excite the dipole oscillations are installed on a temporary *ad hoc* basis, they do not form part of the magnetic trap. The coils are typically 50-100 turns of enamelled copper wire and have a radius of $\sim 100\,\mathrm{mm}$ to deliver an approximately uniform bias field in the direction of the trap frequency under investigation.

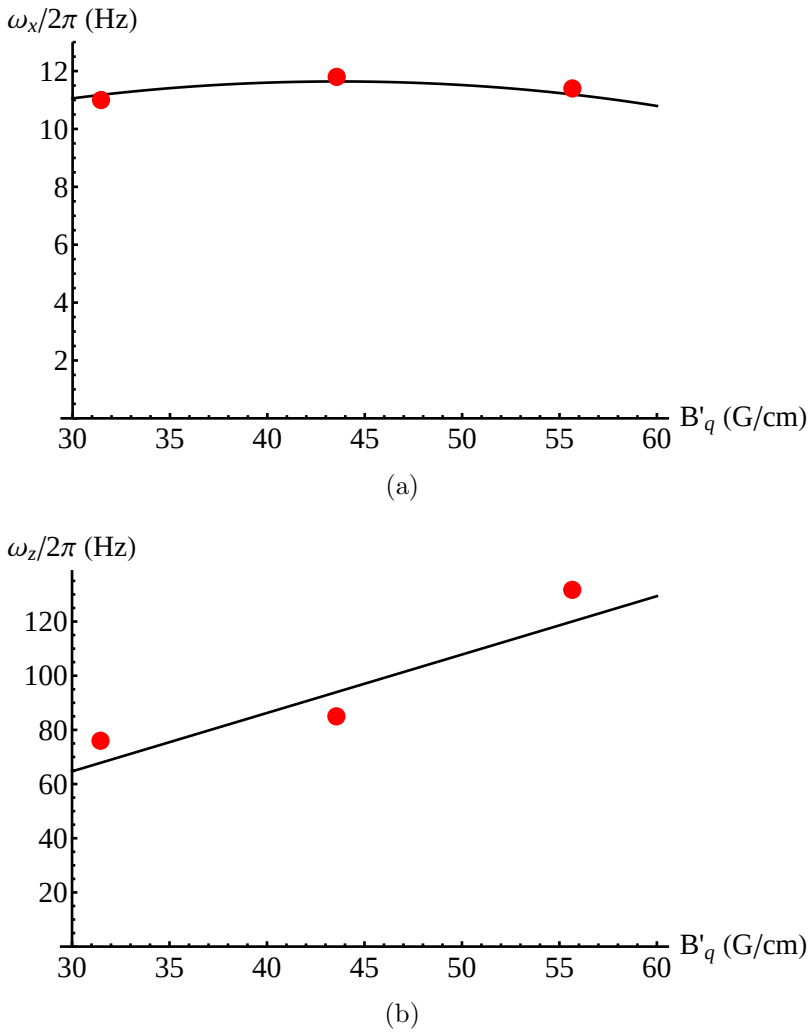


Figure 8.7: Radial (a) and axial (b) shell trap frequencies at the bottom of the shell trap where $\omega_{\rm rf} = 2\pi \times 1.4\,\mathrm{MHz}$, $\mathrm{B}'^{r}_{\rm rf} = 0.72\,\mathrm{G}$. The solid lines are plots made using eqns. 8.6 and 8.7.

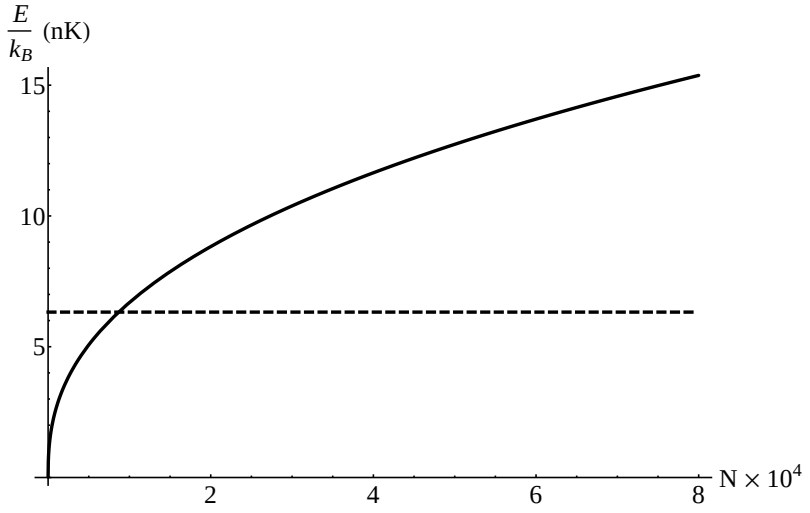


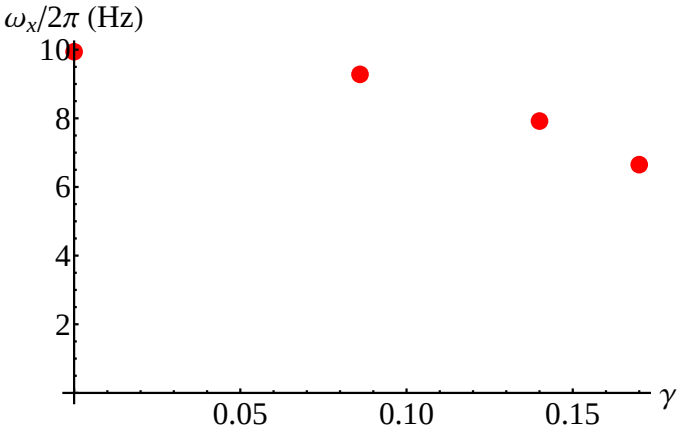
Figure 8.8: Energy scales in the shell trap where $\omega_x = 2\pi \times 11.4\,\mathrm{Hz}$, $\omega_z = 2\pi \times 131.7\,\mathrm{Hz}$. The dashed line marks the energy associated with the axial trap frequency. The 3D chemical potential μ and its dependence on the atom number is shown by the solid line. The intersection of this two lines shows the maximum number of atoms ($N_{\mathrm{max}} = 9000$ in this instance) for which the 2D criterion is fulfilled.

8.3.1 The zTOP modified shell trap

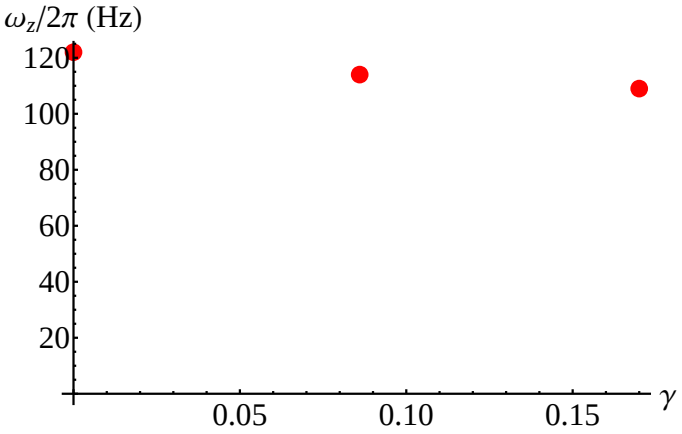
The use of a radially rotating bias field to time-average the dressed potential gives rise to the double-well TAAP. Time-averaging with an axial oscillating bias field forms a ring trap, the investigation of which is reported in the following chapter. Prior to the realisation of the ring trap, the axial bias field causes the potential at the bottom of the shell to flatten. This modified shell TAAP uses the amplitude of the axial time-averaging field to controllably reduce the radial trapping frequencies. At this juncture it is convenient to introduce the modulation depth γ which parameterises the magnitude of the axial time-averaging field $\mathrm{B}^z_{\mathrm{T}}$,

$$\gamma = \frac{m_F g_f \mu_{\mathrm{B}} \mathrm{B}^z_{\mathrm{T}}}{\hbar \omega_{\mathrm{rf}}}. \tag{8.8}$$

As shown in fig. 8.9 the radial frequencies are reduced by almost a factor of two, without significant modification of the axial trap frequency. In many ways, this technique is similar to increasing the quadrupole gradient in the shell trap until the potential minimum is on the brink of inverting. However, the modified shell TAAP has a distinct advantage over this technique. Although every effort is made to ensure the applied rf approximates closely to the desired polarisation, technical difficulties such as reactive coupling between the coils complicate this process. As a result, in the bare shell the potential is often slightly uneven, and as the quadrupole gradient is increased the atoms



(a)



(b)

Figure 8.9: Trap frequency measurements in the modified shell TAAP trap. The modulation depth γ which is proportional to B_T^z is defined in eqn. 8.8. The results were taken for a shell with $B'_q = 55\,\mathrm{G/cm}$, $\omega_{rf} = 2\pi \times 1.4\,\mathrm{MHz}$ and $B_{rf} = 0.7\,\mathrm{G}$. Larger values of γ can be used before realising the ring potential however it proved difficult to make reliable measurements of the long period oscillations using conventional techniques.

pool in the local minima,[6] instead of flowing outwards and forming a very flat system. Using the axial time-averaging this effect is not observed to the same degree. Despite the improved trap anisotropy, experience suggests that this technique alone will not be sufficient to enter the 2D regime with a large number of atoms. As the radial frequencies drop, performing adiabatic manipulations of the atoms becomes increasingly time consuming. The frequencies also become increasingly difficult to measure and the decreasing density means that controlling the cloud temperature using evaporative cooling also becomes difficult. To avoid these issues the following techniques adopt the alternative methodology of increasing the axial trap frequency whilst leaving the radial frequency approximately unaffected.

8.3.2 Increasing the dressing frequency

A simple change of the dressing frequency can have profound results for the operation of the experiment. An increase in ω_{rf} increases the shell size, allowing a proportional increase in B'_{q} to be applied before the shell inverts. No change in $\mathrm{B_{rf}}$ is required so the lifetime is unaffected. The plots in fig. 8.10 demonstrate the advantages of increasing the dressing frequency by approximately a factor of 3, for creating a 2D potential. However, various technical issues[7] have so far prevented any measurements from being made of atoms confined in rf-dressed potentials created at frequencies $> 1.4\,\mathrm{MHz}$. Solutions or workarounds to these problems are currently being sought and will be discussed in the final chapter of this thesis.

8.3.3 Time-averaging the rf polarisation

The spatial variation of the coupling strength creates a potential gradient that acts to push atoms away from the bottom of the shell trap, with only gravity preventing the atoms from flowing around the ellipsoid to the positions where $\Omega(\boldsymbol{r}) \to 0$. Perrin and Garraway [173] proposed a technique that has been implemented on this experiment, where the gradient of coupling strength is modified by adding a time dependence to the coupling strength, such that it may be time-averaged in such a way that the maximum coupling strength pushes the atoms away from the holes in the trap.

The rotation of the rf-dressing polarisation vector is achieved by combining a xy circularly polarised field with a signal from the zRF coils at a frequency $\omega_{\mathrm{rf}} + \delta_{\mathrm{rf}}$. The axial dressing field tilts the rf polarisation vector out of the radial plane, but the frequency difference causes the relative phase of this field (and so the direction of the tilt)

[6] In the extreme case of using linearly polarised rf, this effect can be used to split a cloud of thermal atoms as seen in fig. 8.1 (c).

[7] The main problem is achieving sufficient power in the dressing fields to ensure a good lifetime. The stray capacitance of the coils and leads has a significant impact on the circuit dynamics at the higher dressing frequencies, making it difficult to form a resonant circuit. The *skin* and *proximity* effects which increase with the AC frequency are also believed to add additional impedance that limits the amplifiers ability to drive large currents through the coils.

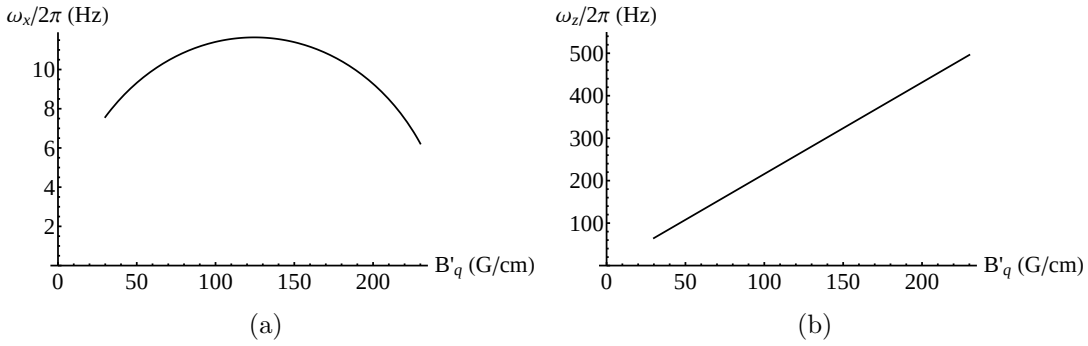


Figure 8.10: Axial (left) and radial (right) trap frequencies at the bottom of the shell trap formed using $\omega_{\rm rf} = 2\pi \times 4\,\mathrm{MHz}$. For quadrupole gradients in the regions of $230\,\mathrm{G/cm}$, trap anisotropies of 85:1 are achievable, allowing over 2×10^5 atoms to be confined in the 2D regime.

to change at $\delta_{\rm rf}$. When $\delta_{\rm rf}$ is chosen to fall in the time-averaging frequency interval (see section 4.1) the atoms do not follow the changing potential landscape but experience a modified shell trap where the variation in the coupling strength acts *with* gravity to confine the atoms at the bottom of the shell. As a result a minimum persists at the South pole of this shell trap for much higher values of the quadrupole gradient B'_q (see fig. 8.11) than in the static coupling case.

A BEC has been confined in the shell trap where the rf polarisation axis was rotated at $\delta_{\rm rf} = 15\,\mathrm{kHz}$. Despite a quadrupole gradient of $B'_{\rm q} = 165\,\mathrm{G/cm}$, the atoms were held for 0.5 s in a trap where $\omega_x = 2\pi \times 23.5\,\mathrm{Hz}$ and $\omega_z = 2\pi \times 350\,\mathrm{Hz}$. The increase in the radial trapping frequency is indicative of the fact that by time-averaging the rf polarisation, the confinement in the shell is actually enhanced. The large value of the radial trap frequency suggests that the quadrupole gradient may be increased further before the atoms are lost from the trap. The limitations of this promising technique are yet to be fully explored,[8] however the initial measurements suggest that it may be another useful tool for manipulating atoms in TAAP's.

8.4 Conclusion

In this chapter the rf-dressed shell trap has been presented as a viable candidate for working with ultracold atoms in the 2D regime. The trap is characterised by experimental results that measure very low heating rates, lifetimes of almost a minute and highly adjustable trap frequencies. On this last point an extended discussion focuses on continuing efforts to adjust the trap potential to make it better suited to access short term

[8] Although no quantitative data is available, the trap lifetime is reduced by time-averaging the rf polarisation. This is to be expected as the atoms no longer sit at the position where $\Omega(\boldsymbol{r})$ is a maximum.

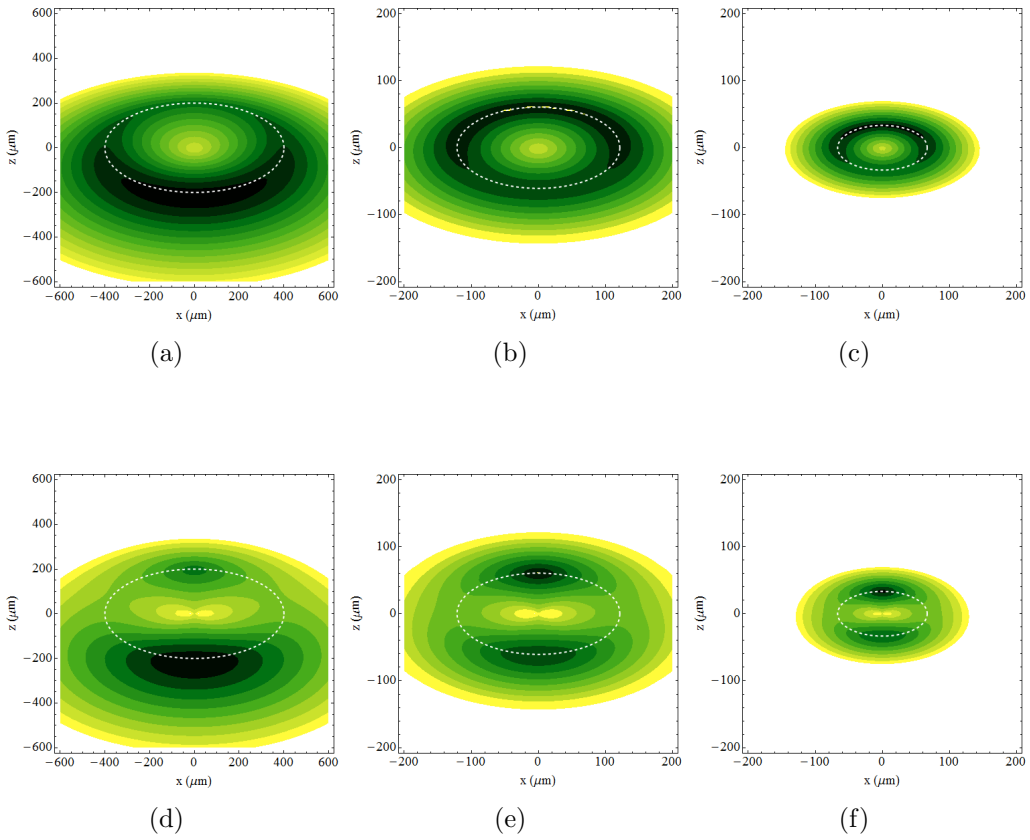


Figure 8.11: Simulations of z_{rf} time-averaging in the shell potential in the $y = 0$ plane. The top row shows the location of the minimum energy position around the bare shell for $B'_{\mathrm{q}} = 50\,\mathrm{G/cm}$ (a), $B'_{\mathrm{q}} = 165\,\mathrm{G/cm}$ (b) and $B'_{\mathrm{q}} = 300\,\mathrm{G/cm}$ (c). In the bottom row, by time-averaging the rf polarisation, the trapping is enhanced at the bottom of the shell at $B'_{\mathrm{q}} = 50\,\mathrm{G/cm}$ (d), and a local minimum still exists in this position even as the gradient is increased from $B'_{\mathrm{q}} = 165\,\mathrm{G/cm}$ (e) to $B'_{\mathrm{q}} = 300\,\mathrm{G/cm}$ (f). In these simulations, $\mathrm{B}^{r}_{\mathrm{rf}} = 0.72\,\mathrm{G}$ and $\mathrm{B}^{z}_{\mathrm{rf}} = 4\mathrm{B}^{r}_{\mathrm{rf}}$. A different scale is used in (b), (c), (e) and (f) for clarity.

(2D regime) and longer term (fractional quantum Hall regime) experimental targets. The most promising techniques appear to be increasing the dressing frequency above its current value (1.4 MHz) and simultaneously employing some form of time-averaging for the position of the coupling maximum.

The immediate outlook for the shell trap is to achieve 2D confinement and then pursue an investigation into the relationship between superfluidity and quasi-condensation in a 2D gas. To date there has been no systematic study of the growth of superfluidity across the BKT phase transition. A measurement of the frequency of scissors mode oscillations was used as one of the earliest demonstrations of the superfluid nature of a 3D BEC [114]. By performing a similar measurement on a 2D gas as it cooled through the BKT phase transition it is anticipated that a direct measure of the superfluid properties of this system will be achieved. The requisite manipulations to excite the scissors mode (elongation and then a small, sudden rotation) can be performed in the bottom of the shell by adjusting the polarisation of the dressing radiation.

A longer term research goal of the shell trap is to investigate the strongly correlated states that arise in the FQH regime. The shell trap possesses several positive attributes that make it an attractive prospect in the pursuit of a long term goal of the research community. The successful demonstration of evaporation in the shell means that the atom number and temperature can be controlled using this method.[9] The presence of a 'built in' rotation scheme that has already been successfully demonstrated with thermal atoms [131] reduces the need for an additional stirring dipole potential. The positive quartic contribution to the ellipsoidal potential has been discussed as assisting with accessing the FQH regime [174]. An elegant experimental demonstration of the effect of the addition of a weak quartic confinement to a harmonic potential is presented in [175]. Going beyond a simple additional quartic term, a recent pre-print by Jean Dalibard [176] suggested that the FQH regime maybe reached by initially rotating in a ring trap, and then adiabatically adjusting the geometry of the potential back to a simple harmonic trap, bringing the atoms into the strongly correlated regime. Such manipulations can be realised on this experiment.

A further advantage in the shell is manifest in the process of detecting these strongly correlated states. A discussion of the improvements to the imaging scheme is presented in chapter 10, however the shell trap can be used to control the preparation of the cloud prior to the imaging stage. The tight axial confinement of the shell will result in a rapid condensate expansion in this direction under standard time of flight. This causes a problem for imaging systems with a shallow depth of field as much of the cloud may be outside the region of sharp focus. To circumvent this problem a 'horizontal time of flight' scheme is proposed where the dressing frequency of the shell (or alternatively the quadrupole gradient) is increased (decreased) over a period of 5-10 ms, increasing the size of the resonant ellipsoid and allowing the atoms to expand radially whilst maintaining

[9]Provided the trap frequencies can maintain a sufficient elastic collision rate to allow evaporative cooling to function at very low atom numbers.

their axial size.[10] The technique of 'horizontal time of flight' will improve the prospects for resolving single atoms when imaging. At this stage it is legitimate to question whether the correlations in the atoms' positions in the trap are preserved following a period of free expansion. In a paper by Read and Cooper [177] a theoretical argument suggests that provided the atoms are in the LLL, these correlations do persist under time of flight, with the in-trap positions of the atoms being scaled by a factor of $\omega_r t$ (where t is the time of flight time) and globally rotated around the symmetry (z) axis of system by a factor of $\pi/2$.

A proposal to approach the FQH regime using the shell potential would likely begin with a mechanical spin-up of a thermal cloud in the standard shell potential. Following this, the shell potential could be adiabatically adjusted to move towards a tighter overall configuration. Note that the chemical potential which sets the temperature scale for these systems is linearly dependent on the radial trap frequency, hence it has been suggested that a time-averaged, rotating dipole trap could be employed to augment the radial trapping frequency at the South pole of the ellipsoid (see fig. 8.12).

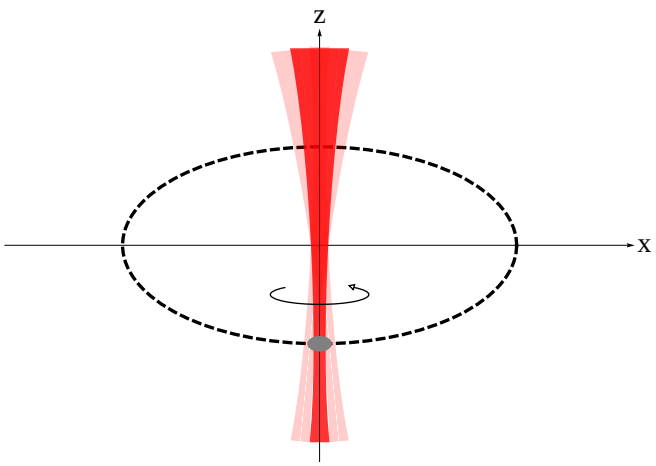


Figure 8.12: A red-detuned (830 nm) laser beam, focussed at the lower surface of the resonant ellipsoid could be used to enhance the radial trapping frequencies at the South pole of the shell. By rotating the angle of incidence of the beam at a time-averaged frequency, a very circular dipole potential can be created.

This system could be evaporatively cooled down to quantum degeneracy in this hybrid potential, and then by removing atoms into the FQH regime. Calculations performed in this group suggest that if both the axial and radial trap frequencies can be increased into the kHz regime then strongly correlated states such as those discussed in section 2.4 should appear when rotating at $\Omega_{\rm rot} = 0.995\omega_r$ for 50 atoms with a chemical

[10]Note that if the quadrupole gradient is decreased, the axial size will increase in proportion with this change.

potential of approximately 5 nK, a temperature accessible by conventional evaporative cooling.

Chapter 9

The TAAP ring trap

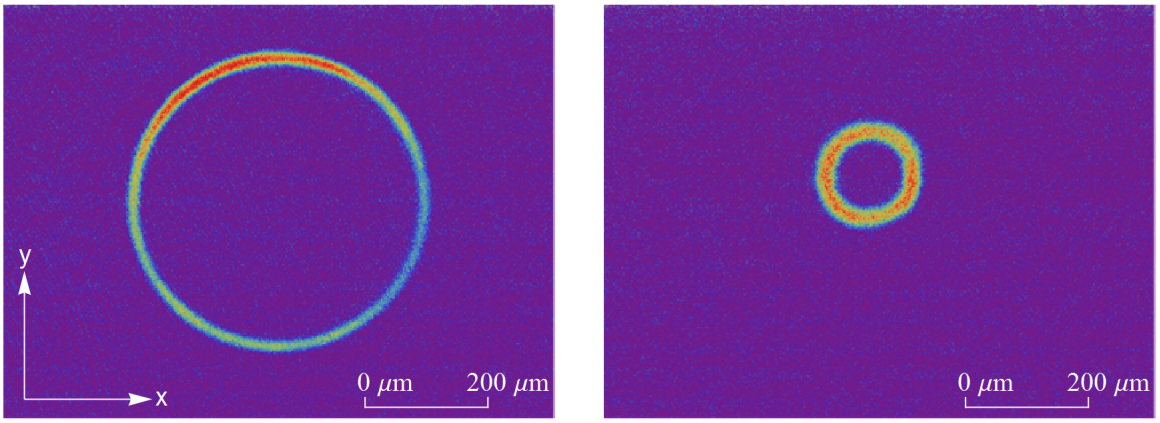


Figure 9.1: Absorption image of atoms confined in the TAAP ring trap. In (a) the cloud of atoms has a ring radius of 262 μm and in (b) the radius is 71 μm. This change is achieved by increasing the gradient of the quadrupole field from (a) 65.3 G/cm to (b) 277.1 G/cm. In both cases $\omega_{\mathrm{rf}} = 2\pi \times 1.4\,\mathrm{MHz}$, $\mathrm{B_{rf}} = 0.8\,\mathrm{G}$ and $\mathrm{B_T^z} = 0.9\,\mathrm{G}$.

9.1 Introduction

For any ring trap there are two regimes that can be distinguished. In the first the quantum coherence extends all around the ring. Under these conditions the superfluid nature of an interacting dilute ultracold quantum gas is manifested e.g. persistent flow. The angular momentum of a superfluid confined in annular geometry dissipates only if

the rotational velocity exceeds a critical value [29, 178]. Below the critical velocity the mass flow is dissipationless in analogy to electrical current in superconductors. Such a persistent flow was observed with ultracold atoms in an optically plugged magnetic trap [179]. Recently an all optical ring trap experiment demonstrated that superflow around a ring is suppressed by a barrier where the local flow velocity exceeds the critical value [180]. This may lead to an analogue of the superconducting quantum interference device (SQUID) using a BEC.

The second regime employs the ring trap as a wave guide for matter-wave interferometry. In combination with coherent beam-splitting, a circular waveguide forms a Sagnac interferometer [181] and acts as an inertial sensing device. Several experiments have been designed with this goal in mind [182, 183, 184], and further schemes have been proposed [185, 186, 187].

The two regimes can be loosely distinguished by the constraints placed on the chemical potential for a BEC in 3D ring trap [185]:

$$\mu_{\text{ring}} = \hbar\bar{\omega}\sqrt{\frac{2a_s N}{\pi r_0}}. \tag{9.1}$$

Here $\bar{\omega} = \sqrt{\omega_z \omega_r}$ is the geometric mean of the axial (ω_z) and radial (ω_r) trapping frequency, a_s the s-wave scattering length, N the atoms number and r_0 the ring radius. For the first regime, μ_{ring} must be large compared to the potential inhomogeneities around the ring, enabling the BEC to spread around the full ring circumference. In the second regime the condensate is localised at a minimum of the potential around the ring.

The ring trap described in this chapter aspires to both regimes. It is based on the proposal for a time-averaged adiabatic potential (TAAP) ring trap [139]. In this particular experiment a rf dressed quadrupole trap is time-averaged along its symmetry axis which results in a ring-shaped trap geometry (see fig. 9.1) with a range of radii suitable for exploring both of the above regimes.

In previous work a rf-dressed potential was combined with two blue frequency detuned light sheets to create a ring potential [114]. This arrangement was susceptible to thermally induced drifts in the position of the optical potential in which atoms had only moderate lifetimes ($\tau \sim 1\,\text{s}$). The new experimental design depends only on magnetic potentials which do not require repeated alignment. Increased power in the rf fields has resulted in lifetimes $> 11\,\text{s}$, whilst a custom designed DDS frequency source has led to improved dynamical control over the rf polarisation allowing the trap to be tilted and rotated.

In this chapter a description of the formation of the ring trap and its associated loading scheme is presented. A discussion on the ring trap radius, lifetime and frequencies is included along with the relevant data from the experiment. In order to observe superfluid behaviour such as the persistent flow it is generally necessary to impart angular momentum to the system and so this chapter concludes with a section detailing the ring trap rotation scheme and some preliminary experimental results.

The ring trap described here is a TAAP that results from the application of an axial time-averaging field to a dressed quadrupole trap, in an extension of the work detailed in section 8.3.1. When the shell trap is time-averaged along its symmetry (z) axis, the radial curvature at the bottom of the shell decreases as the amplitude of the time-averaging field grows. This process continues until zero curvature exists at the initial position of the atoms. A further increase in the amplitude of the axial time-averaging field results in a negative curvature at this position (the bottom of the ellipsoid) and an annular minimum develops, giving a ring trap in the radial (xy) plane.

The loading procedure for the ring trap starts with a condensate in the bare shell potential where $B'_{\mathrm{q}} = 55\,\mathrm{G/cm}$. The geometry of the shell is smoothly morphed into the ring potential by simultaneously ramping the axial time-averaging bias field ($\mathrm{B}^z_{\mathrm{T}}$) and the field gradient over 1 s. Typical values used to achieve the ring potential are $B'_{\mathrm{q}} = 84\,\mathrm{G/cm}$ and $\mathrm{B}^z_{\mathrm{T}} = 0.6\,\mathrm{G}$. The ramps are performed relatively slowly to minimise non-adiabatic heating which is inevitably incurred to some degree as the radial trapping frequencies pass through zero and the adiabaticity criterion diverges. Typically only a small amount of heating is observed during the loading process resulting in a BEC with a small thermal fraction being loaded into one side of the ring potential.

9.2 The ring radius

The ring radius r_0 is determined by B'_{q} and ω_{rf} which combine through the resonance condition to dictate the length of the semimajor axis of the resonant ellipsoid r_e (see eqn. 4.23). In the original TAAP ring proposal, the dressing frequency was modulated at the time-averaging frequency to ensure the atoms always remained on the avoided crossing. This technique has not yet been implemented on this experiment as it presents a significant technical challenge with regards to reprogramming the DDS frequency source, and also maintaining a constant dressing frequency circumvents technical problems relating to atom heating during frequency ramps observed in [188].[1]

Despite the constant dressing frequency, as illustrated in fig. 9.3 r_0 can be continuously varied by adjusting the value of the quadrupole gradient, with the upper limit set by the minimum value of B'_{q} required to support the atoms against gravity.[2] Operating the magnetic trap at the maximum value for $B'_{\mathrm{q}} = 398\,\mathrm{G/cm}$ gives a lower limit for r_0 of $50\,\mu\mathrm{m}$. Once the ring is established there is a weak dependence of r_0 with $\mathrm{B}^z_{\mathrm{T}}$, typically on the order of a few percent across the full range of oscillatory field amplitudes $0.4\,\mathrm{G} \leq \mathrm{B}^z_{\mathrm{T}} \leq 1.6\,\mathrm{G}$. The principal result of changing the magnitude of the

[1] Despite these issues it remains likely that some form of frequency modulation (fm) of the dressing radiation will be realised in the future as this is expected to make significant improvements in the lifetime of atoms in the ring.

[2] In principle this is true, however due to a technical problem with the SQA power supply the minimum output when operating it in current control mode is 26 A. This gives a field gradient in the *axial* direction of 62 G/cm which is approximately twice the minimum value required to support atoms against gravity.

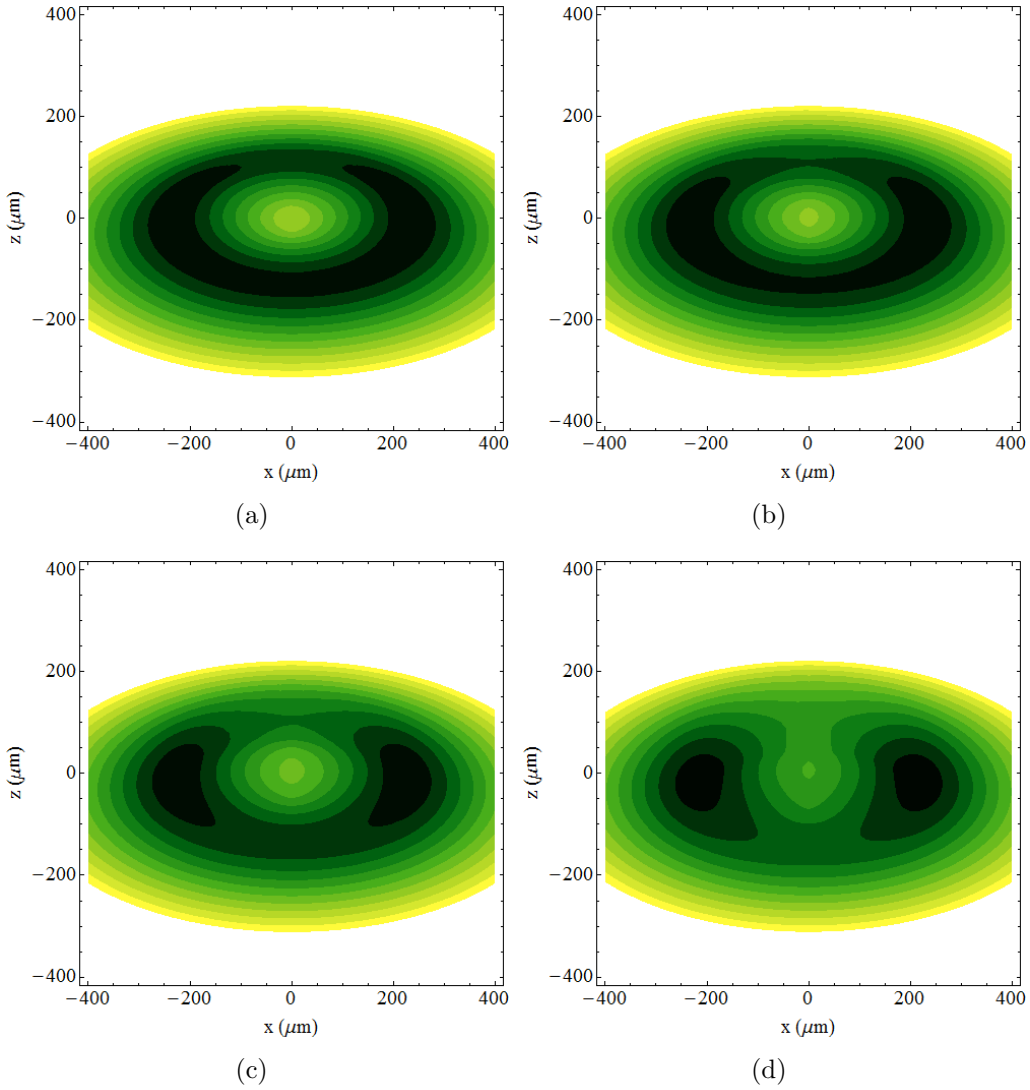


Figure 9.2: Simulations showing the formation of the ring potential in the $y = 0$ plane. For modulation depths (this quantity is defined in eqn. 8.8) $\gamma = 0.2$ (a) and $\gamma = 0.3$ (b) the field gradient $B'_{\mathrm{q}} = 84\,\mathrm{G/cm}$ allows atoms to flow almost all the way around the ellipsoid. Increasing the modulation parameter to $\gamma = 0.45$ (c) and $\gamma = 0.65$ (d) confines the atoms to the equatorial regions of the ellipsoid, giving well defined ring potentials that lie in the xy plane and thus are observed in cross-section in this figure. The other plot parameters are $\omega_{\mathrm{rf}} = 2\pi \times 1.4\,\mathrm{MHz}$ and $\mathrm{B_{rf}} = 0.8\,\mathrm{G}$.

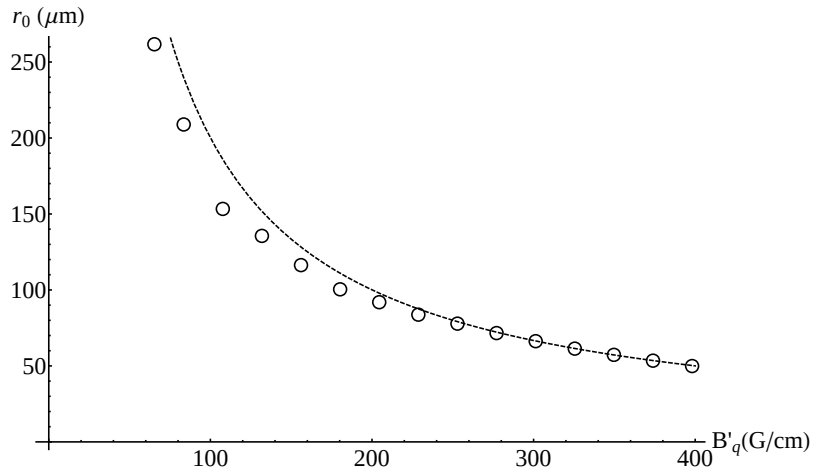


Figure 9.3: Variation of ring radius r_0 with $B'_{\rm q}$, for $\mathrm{B_{rf}} = 0.8\,\mathrm{G}$ and $\mathrm{B_T^z} = 0.9\,\mathrm{G}$ ($\gamma = 0.44$). The dashed line represents the theoretical value for semi-major axis of the resonant ellipsoid r_e using $\omega_{\rm rf} = 2\pi \times 1.4\,\mathrm{MHz}$.

time-averaging field is to adjust the trap frequencies.

9.3 Ring trap frequencies

The axial and radial ring trap frequencies were measured against B_T^z by fitting to dipole mode oscillations in the trapped cloud. Axial oscillations were excited by rapidly displacing the position of the potential minimum using a magnetic bias field. Radially, the height of the centrally repulsive region was reduced by sharply decreasing $\mathrm{B_T^z}$ by 50 % for a period of 5 ms causing the ring radius to oscillate harmonically. The values depicted in fig. 9.4 demonstrate how the aspect ratio in the ring can be adjusted. Results of a numerical analysis suggest that both ω_r and ω_z scale linearly with $B'_{\rm q}$ implying a factor of 9 increase in trap frequencies is readily attainable with the current apparatus.

9.4 Lifetime in the ring trap

Experiments on persistent flow in superfluid ultracold gases requires the lifetime in a multiply connected ring trap to be at least several seconds. The data in the fig. 9.6 demonstrates that under certain conditions these lifetimes are attainable in the ring trap. However, the utility of the trap in these cases is somewhat limited by anisotropies in the potential that prevent a BEC from spreading around the full ring circumference.[3]

[3]This issue is discussed in more detail in the following section.

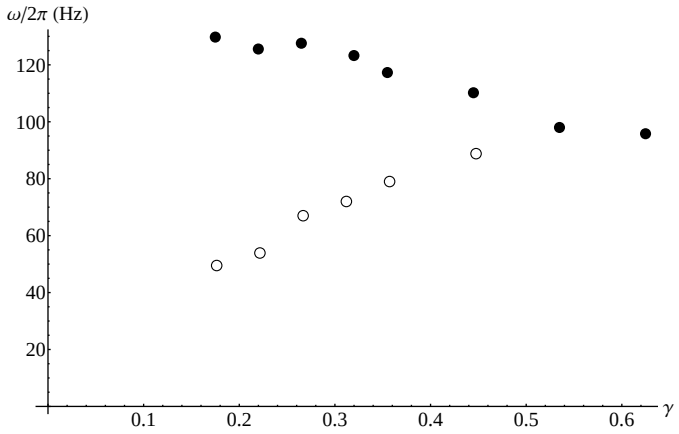


Figure 9.4: Ring trap frequency measurements in the axial (closed circles) and radial (open circles) directions as a function of the modulation depth γ with $B'_{\mathrm{q}} = 83.5\,\mathrm{G/cm}$ and $\mathrm{B_{rf}} = 0.8\,\mathrm{G}$. As the modulation depth decreases, the trap frequencies tend towards the values in the bare shell trap.

The data in fig. 9.5 show a correlation between decreasing lifetime and the smaller ring radii that result at higher quadrupole field gradients. Increased trap frequencies in the ring that naturally accompany increases in B'_{q} result in the atoms traversing the avoided crossing with a larger relative velocity, causing an increase in the *in situ* LZ loss rate. Also the smaller resonant ellipsoids may allow the atoms to sample a greater proportion of the ellipsoid including those regions where the coupling strength sharply decreases.

In fig. 9.6 the lifetime also appears correlated with the magnitude of the axial time-averaging field. Here the ring trap radius and frequencies remain approximately constant suggesting that a change in the motion of the avoided crossing is responsible for the increased loss rate. The velocity at which the axial bias field drags the avoided crossing through the atom cloud is proportional to the amplitude of this field. As discussed in the previous section, unlike the radial TAAP trap, the atoms in the ring do not remain on the avoided crossing. As a result even for the unphysical situation of a stationary (in the laboratory frame) atom, a finite relative velocity will exist between it and the avoided crossing therefore enabling the LZ loss mechanism.

Although explanations have been put forward to reconcile the data within figs. 9.5 and 9.6, much like the shell trap, currently no *ab initio* model has been constructed that accurately predicts this behaviour, suggesting that further theoretical work is required before a complete understanding of the atom's dynamics in these potentials is ascertained.

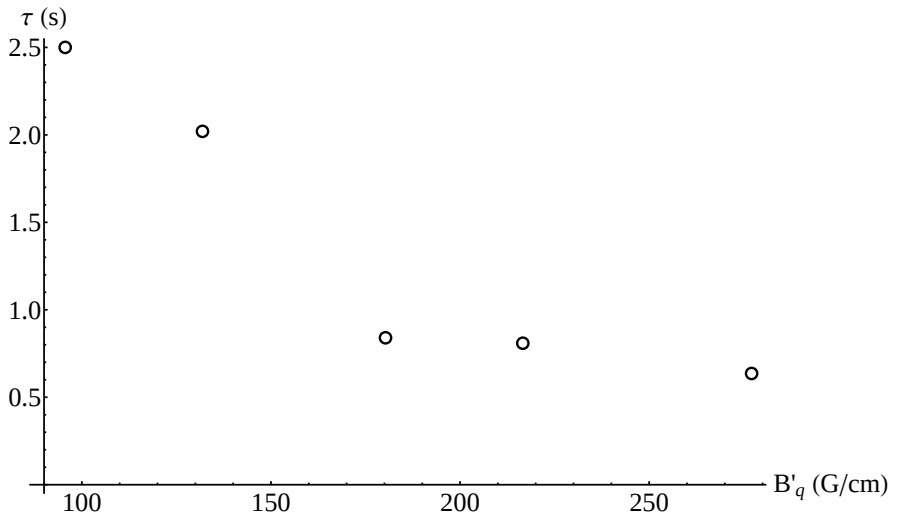


Figure 9.5: Ring trap lifetime for increasing values of the quadrupole field gradient. These data were taken with a constant modulation depth of $\gamma = 0.44$.

9.5 Tilting in the ring trap

Misalignments of the quadrupole field symmetry axis with gravity resulting from the construction and positioning of the magnetic coils led to the first ring traps being tilted by approximately 2°. Via the same mechanism that allowed for tilting in the shell trap (see section 8.2.3), the vectorial nature of $\Omega(\boldsymbol{r})$ can be exploited to adjust how the potential varies around the ring. In this experiment, the principle advantage of introducing an axially directed dressing field is to counter the effect of gravitational tilts in the ring potential. Using this technique the balancing of the ring in the radial plane has been significantly improved such that a cloud at $\sim 85\,\mathrm{nK}$ spreads fully around a ring of radius $r_0 = 238\,\mu\mathrm{m}$. In order for the quantum coherence to spread fully around the ring, the chemical potential must exceed the size of the inhomogeneities around the ring. Assuming the dressing rf is to a good approximation xy circularly polarised, then the condition for a multiply connected condensate is,

$$\mu_{\mathrm{ring}} > mg\Delta z, \tag{9.2}$$

where Δz is the vertical height difference around the ring. This condition is yet to be satisfied on the experiment.[4] The poor lifetime (at high values of B'_{q}) hampered initial attempts to push the condensate around the ring, however several promising approaches exist to tackle this problem:

[4]Much of the work performed with condensates in the ring has thus far been done in tilted rings where $\mu_{\mathrm{ring}} \sim 6\,\mathrm{nK}$ and $mg\Delta z = 170\,\mathrm{nK}$. This configuration was chosen to allow the presence of a condensate to be confirmed from time of flight observations of the aspect ratio inversion of the cloud.

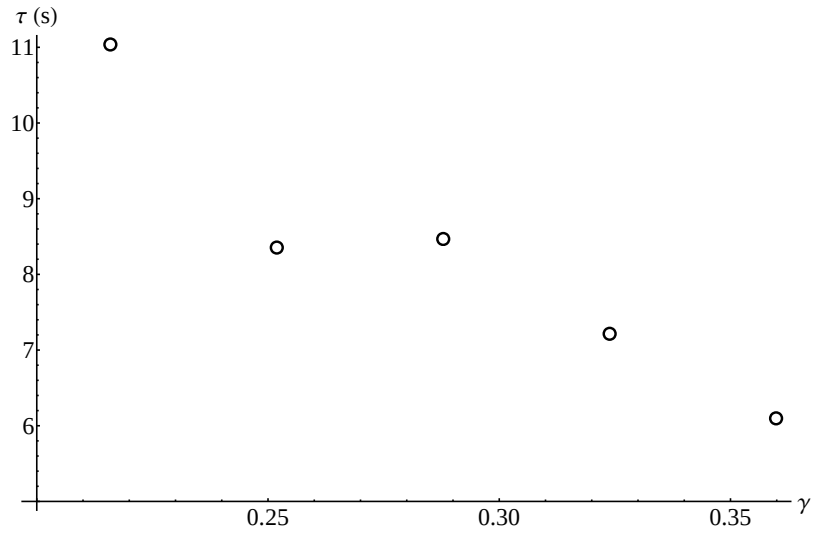


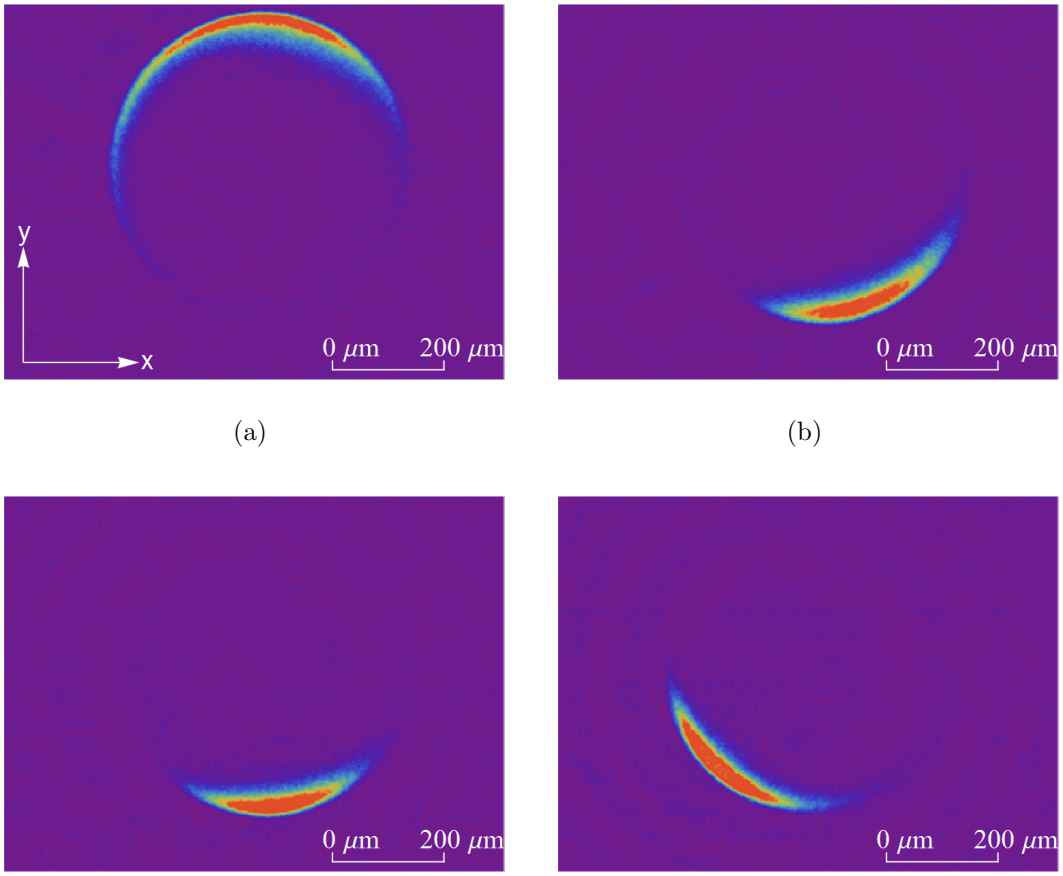
Figure 9.6: Ring trap lifetimes for increasing value of the modulation depth γ. These data were taken with a constant field gradient $B'_{\mathrm{q}} = 68\,\mathrm{G/cm}$.

- Decrease ω_{rf}: For the same value of B'_{q}, the new ring will be smaller, thus decreasing the impact of gravitational imbalances around the ring i.e. not having the ring precisely located in the plane perpendicular to gravity.
- Increase ω_{rf}: Conversely, by increasing the dressing frequency the ring radius can be maintained by using a higher value of B'_{q}. This dramatically increases the trapping frequencies and therefore μ_{ring}, helping squeeze the condensate all around the ring.
- Increase $\mathrm{B_{rf}}$: Small rings which reduce the impact of gravity on the ring trap can be produced, however they are always associated with low lifetimes. A larger dressing field could be used to militate against this.

9.6 Rotation in the ring trap

In order to study the dynamics of superflow in dilute atomic vapour BEC's trapped in ring potentials it is necessary to controllably introduce rotation into the system. In this experiment, as shown in fig. 9.9, a rotation scheme that utilises the vectorial nature of the coupling term $\Omega(\boldsymbol{r})$ has successfully been employed to rotate atoms in the ring trap.

By relative adjustment of the dressing field amplitudes (such that $\mathrm{B}^x_{\mathrm{rf}} \neq \mathrm{B}^y_{\mathrm{rf}}$) the circularly symmetric coupling term takes on an elliptical form, introducing a spatially periodic variation in the potential around the ring (see fig. 9.8). If the axis of this asymmetry is rotated, the atoms follow the variations in the potential and begin to



(a) (b)

(c) (d)

Figure 9.7: Images of a BEC in a tilted ring trap. The direction of the tilt is controlled by the relative phase b (see eqn. 4.5) of the axial dressing radiation B^z_{rf}. Here (a) $b = 0°$, (b) $b = 90°$, (c) $b = 180°$ and (d) $b = 270°$. A gravitational tilt in the ring trap prevents the atoms from responding linearly to changes in the rf polarisation. It is apparent that the adjustment is sufficient to offset the intrinsic tilt caused by imperfect alignment of the coils with respect to the vertical axis defined by gravity.

orbit in the radial plane. To observe the dynamics of a rotating cloud, the circular symmetry of the potential is restored. A full account of how the elliptical polarisation is rotated using amplitude and phase updates of the dressing fields from the DDS frequency source can be found in Appendix C in [131].

In order to characterise the smoothness of the rf-dressed potential the behaviour of a cloud that is first spun-up in the ring potential, then allowed to rotate freely in the bare shell potential is observed. The advantage of going to a potential where $\gamma \to 0$ is that as the cloud dissipates its rotational energy, its radius shrinks by the conservation of angular momentum. Therefore the radius decrease provides an indirect measure of the potential smoothness in the rf-dressed potential. The data in fig. 9.10 shows a slow decrease in the rotating cloud radius, suggesting the potential is smooth and well suited to rotation based experiments for those parameters. A simple way to further test this idea would be to change the polarisation away from its radially symmetric configuration in the shell potential and observe the effects on the spin down rate. The data appear to show an increase in the spin down rate for hotter clouds. This may just be the result of heating, which causes the larger cloud to expand around the resonant ellipsoid. From the vantage point of the vertical imaging system this would appear as if the radius of the cloud was shrinking.

9.7 Conclusion

The multiply connected systems that arise from the geometry of the ring traps mean that generating this mode of confinement has long been an important goal in ultracold atom research. The ring trap presented in this chapter has been demonstrated to possess several desirable characteristics such as a simple loading scheme, a highly degree of

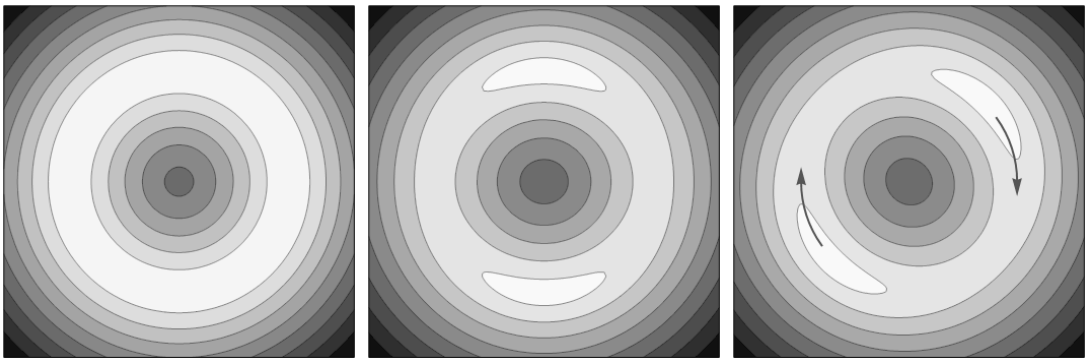


Figure 9.8: The ring trap rotation scheme in the $z = 0$ plane. Circular symmetry around the ring is broken by transforming to elliptically polarised rf. By rotating the axes of the elliptical polarisation the deformations around the ring act to stir the cloud into a rotating state.

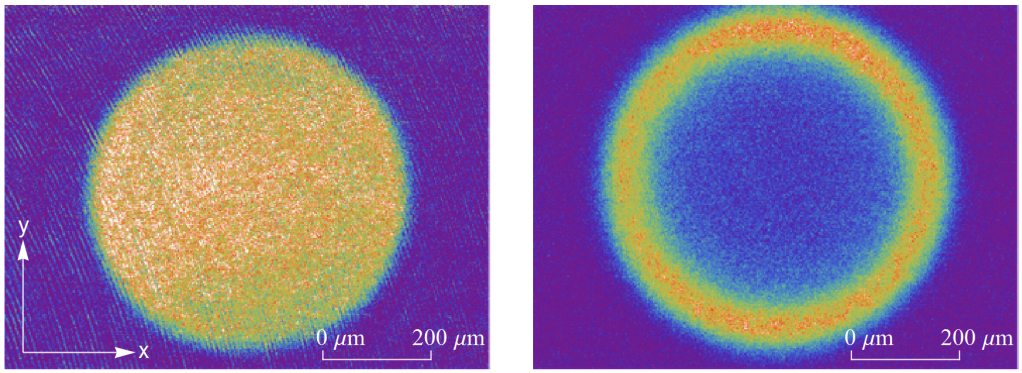


Figure 9.9: Evidence for rotation in the ring potential. (Left) In the absence of rotation, when B_T^z is ramped to zero the atoms return to the rf-dressed shell potential where they are approximately uniformly distributed around the lower half of the ellipsoid (for the parameters listed below). (Right) For a rotating cloud (potential rotated at 25 Hz for 800 ms), the ring shape persists after the removal of the time-averaging field, because the atoms' angular momentum holds them at the equatorial regions of the ellipsoid. Both images are of a thermal cloud, 100 μs after release from a shell trap where $B'_q = 71$ G/cm and $B_{rf} = 0.8$ G.

versatility and importantly access to a broad parameter space. The ring trap is directly loaded from the rf-dressed shell trap and although some heating is observed a condensate is routinely loaded into one side of this potential. The ring radius and trap frequencies can be smoothly adjusted over a range of values using conveniently accessible experimental parameters (B_T^z and B'_q). Finally with improvements to certain aspects of the ring trap, it will be possible to extend the quantum coherence all around the ring. Even where this is not possible, the ring in addition with a coherent beam splitter operation (this may be achievable by either tilting the ring or adjusting the elliptical polarisation of the rf) could act as a waveguide for an inertial sensing device. An increase of the dressing frequency to $\omega_{rf} = 2\pi \times 4$ MHz, would allow ring traps with a total internal area of $> 1.6\,\mathrm{mm}^2$ which would improve the sensitivity to small inertial rotation.

As discussed in the introduction to this chapter, experiments have begun to use barriers to investigate the dynamics of superflow in multiply connected condensates. While dissipation in superfluids has been measured, no observations have been made of the phase slip mechanism believed to underlie this process. Numerical simulations performed by Piazza *et al.* have shown that for increasing barrier heights, a vortex and then antivortex will enter the body of a ring condensate [189]. The vortex and antivortex may annihilate or orbit on the same loop, but in either case the global system loses a single unit of angular momentum. Direct imaging of these topological defects would augment the indirect evidence for this process being responsible for dissipation in

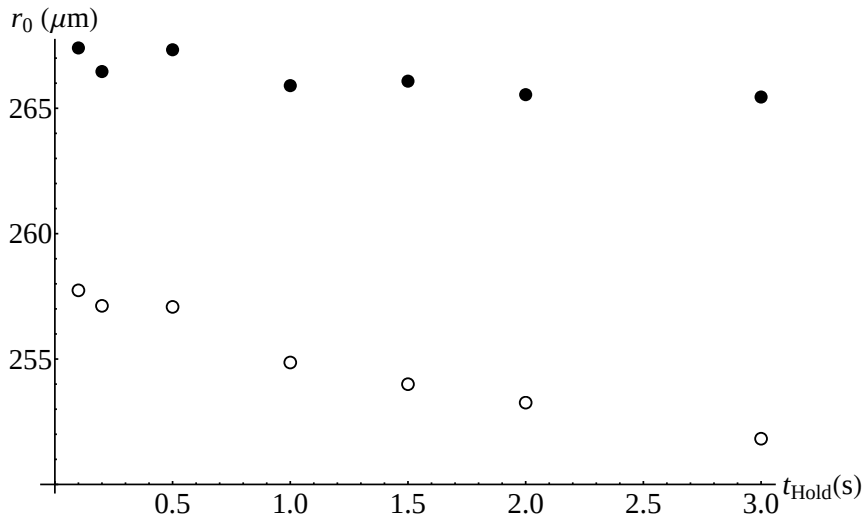


Figure 9.10: The persistence of rotation in the ring trap. In the absence of the static ring trap potential, a rotating cloud undergoes a spin down process that is slow compared to the trap lifetime in this potential. The closed circles show data taken with a cloud just above the BEC transition temperature, the open circles show data that was taken with a thermal cloud at $\sim 1\,\mu$K. The radius of the rotating cloud that is calculated directly from the image acquired using the vertical imaging system. The atoms were initially rotated at 20 Hz for a period of 400 ms in a ring trap where $B'_{\mathrm{q}} = 71\,\mathrm{G/cm}$, $\mathrm{B_{rf}} = 0.8\,\mathrm{G}$ and $\gamma = 0.2$.

superfluids.

The efficiency of evaporative cooling in the ring potential is yet to be tested, although the oscillatory nature of the trap bottom is likely to make forced rf evaporation challenging. Provided all difficulties can be overcome, the system presents an opportunity to perform a detailed study of the Kibble-Zurek mechanism (KZM) [190, 191] in ultracold cold gases trapped in ring shaped potentials. Experimental confirmation of the principle of spontaneous topological defect formation when quenching through the critical point of a phase transition have been observed using ultracold quantum gases [192]. However the theory also states that the density of topological defects should scale with the quench rate, and to date no direct evidence for this relationship has been observed [193]. In a ring trap, the defects predicted by the KZM would manifest as spontaneous rotation in the newly created condensate, with the geometry of the ring potential providing an energetic barrier to the decay of rotation. Rotation could be detected under time of flight using a similar technique used in [179].

An interesting extension of all work performed with adiabatic potentials, but particularly in the case of the ring is the idea of dressing magnetically trapped atoms at multiple frequencies [117]. Under a 'double dressing' scheme, two concentric ring traps

could be formed with a separation that could be adjusted by changing one or both of the dressing frequencies. In this system each ring trap could be controlled independently allowing manipulations to be performed on one BEC and its phase read out using the other. A pair of coupled 1D ring traps[5] has been proposed as a system where angular momentum Josephson oscillations are predicted to spontaneously occur [194].

[5]It should be noted that significant modification (along similar lines to the changes discussed in section 9.5) will be required before the ring trap is able to achieved 1D confinement of a multiply connected condensate.

Chapter 10

Conclusions and outlook

10.1 Conclusion

This thesis is an account of recent measurements made with ultracold gases trapped in time-averaged adiabatic potentials. The prospects for new physics in TAAPs goes beyond what is currently possible using the apparatus described herein, and it is anticipated that the investigations into the double-well, shell and ring traps will act to motivate further experiments in these and the more exotic geometries.

The first TAAP that was used to trap ultracold atoms was the vertically offset double-well potential that arises as a natural consequence of dressing energy levels in a TOP trap with a radio-frequency field. Initially the double-well potential acted as proof-of-principle demonstration of the feasibility of trapping atoms in a TAAP, and the associated early characterisation work for this potential is reported elsewhere [140, 131]. In this thesis, following a further in-depth investigation of the double-well potential, the results of the natural evaporation mechanism are presented and discussed. The success of this technique in cooling a thermal cloud down to the quantum degenerate regime confirms a long held belief that cooling using the LZ loss channel should be possible and also shows that the control and understanding of these potentials is continuously improving.

The shell trap can be regarded as a natural end point for all TAAP traps where the adiabatic potential derives from an rf-dressed quadrupole field. The confinement of ultracold atoms on a single, smooth surface has naturally led to the proposal that the shell trap is a good candidate for the study of physical processes in 2D systems. Evidence for a 2D BEC in the shell trap is yet to be observed however the data in chapter 8 suggests this goal is tantalisingly close. A variety of techniques have been implemented to increase the anisotropy of the confinement and improve the prospects for achieving a large 2D BEC. Perhaps the most promising of these is the time-averaging of the rf polarisation,

causing the coupling strength maximum to orbit between the position of the atoms at the bottom of the shell and the position where $\Omega(\boldsymbol{r}) \to 0$. The spatial variation of the coupling strength now acts to provide additional confinement at the bottom of the shell allowing considerable increases in the quadrupole gradient to be made before the shell potential inverts. Although some issues with lifetime remain to be addressed, the early results of this technique are positive.

In chapter 9 the experimental realisation of a versatile ring trap for ultracold atoms is reported. The ring geometry is created by the time-averaged adiabatic potential resulting from the application of an axially oscillating magnetic bias field to a rf-dressed quadrupole trap. Lifetimes for a Bose-Einstein condensate in the ring can exceed 11 s and the ring radius may be continuously varied from 50 μm to 262 μm. An efficient method of loading the ring from a conventional TOP trap is presented together with a rotation scheme which introduces angular momentum into the system. Time constraints have so far prevented the creation of a multiply connected condensate which would allow a number of new experiments to be performed. As with the shell, research is ongoing into how to improve the properties of the ring trap, with a change in the dressing frequency appearing to be the most promising candidate.

10.2 Outlook

In terms of improving the confinement of the atoms, both the ring and shell potentials are predicted to benefit from an increase in the dressing frequency ω_{rf}. This broadening of the parameter space would enable e.g. large numbers of atoms to be confined in a 2D BEC in the shell, or form a multiply connected condensate in the ring trap. The most recent activity on the experiment has involved attempts to change the dressing frequency, which at time of writing have presented only modest success. The rf coil circuitry has a strong frequency response which causes the impedance to grow significantly at driving frequencies above 2 MHz. In an attempt to solve the problem via brute force, the 1 W minicircuits rf amplifiers have been replaced by 25 W units (HDCOM 27413). Using the new amplifiers a BEC has been confined in a shell where $\omega_{\mathrm{rf}} = 2\pi \times 4\,\mathrm{MHz}$, however lifetimes of only a few seconds were observed. Further testing and optimisation of the circuitry is ongoing.

A topic that has yet to be addressed is the improvements to the imaging system on this experiment. There is a belief that the vortex anti-vortex pairs that bind as a 2D gases is cooled through the BKT phase transition will not survive under time of flight. Thus in order to image these structures directly, an imaging system with a resolution exceeding the 1.8 μm diffraction limited performance of the current imaging system is required. The proposals to probe the fractional quantum Hall regime make even more stringent demands of the imaging system. At the breakdown of the mean-field regime, the position of atoms in the trap becomes strongly anti-correlated. In order to detect these correlations an imaging system capable of single atom detection is required. The imaging of small clouds with single atom resolution or detection has undergone a rapid

development over the last decade. The atomic analog of the Hanbury Brown Twiss effect was demonstrated using a microchannel plate to detect single helium atoms in an ultracold sample [195]. A scanning electron microscope was used to ionize atoms at individual lattice sites of an optical lattice, the resulting ions being detected with single particle resolution [196]. A time of flight method has been developed that achieves single atom detection within a narrow slice of a free falling BEC [197]. Currently the state of the art technique is fluorescence imaging of atoms trapped in a deep, far-detuned optical lattice [198, 199].

The proposed imaging system for this experiment is based on the latter scheme, whilst also adopting some ideas previously developed in Oxford [200]. A diode laser locked $\sim 10\,\mathrm{GHz}$ from the 795 nm D1 line in ^{87}Rb (using a technique first demonstrated by [201]) is used to create a 3D optical lattice. The lattice will be rapidly switched on following a 'horizontal time of flight' expansion (see section 8.4) to lower the cloud density and ensure the mean occupation number of the lattice sites is considerably less than one. As a result the true number distribution of the cloud is measured rather than just the parity at each lattice site. The atoms are interrogated with near resonant light arranged in optical molasses configuration to allow long exposure times ($\sim 1\,\mathrm{s}$) without heating the atoms out of the lattice. The 2 mm thickness of the glass cell walls inhibits the use of extremely high NA objectives, which typically have working distances of less than this distance, to resolve the individual lattice sites but a combination of commercial microscope objective (NA = 0.6) and a technique developed by co-workers in Oxford [202] to dynamically expand the site separation of an optical lattice will allow the single atoms at individual lattice sites to be resolved.

A consistent theme throughout this thesis has been the versatility of the potentials used to confine and manipulate ultracold atoms. This is perhaps illustrated most clearly by summarising the diverse range of experimental goals that represent the future for an apparatus that is still relatively young.[1] In the shell trap, experiments on the growth of superfluidity as a 2D gas crosses the BKT phase transition, will precipitate a push towards rapid rotation of small numbers of atoms in an effort to reach the FQH regime. In the ring trap, whilst the potential is currently suited to interferometry based experiments, other possible avenues of investigation include rapid quenching through the BEC phase transition to observe topological phase defects as predicted by the Kibble-Zurek mechanism, the decay of superflow by barriers or constrictions placed around the ring, or multiple ring traps where the effects of tunneling in this geometry could be observed.

[1] The first BEC was observed in this experiment on 09/09/09.

Appendix A

Calibration

In the interests of completeness, this appendix is used to catalogue some calibration work undertaken during the building-up phase of the experiment.

A.1 The TOP field

The field in the *yTOP* coil is used to define the quantisation axis for the horizontal imaging system. As a result by changing the TOP field, the centre of the resonance is shifted by the differential Zeeman shift between the $|F = 2, m_F = 2\rangle$ state (where $g_F = 1/2$) $|F' = 3, m_{F'} = 3\rangle$ where $g_F = 2/3$. For a given TOP field amplitude the transition line centre will shift by the frequency interval,

$$\Delta f = |\left[m_F = 2 \times 0.7\,(\mathrm{MHz/G}) - m_{F'} = 3 \times 0.93\,(\mathrm{MHz/G})\right]|\mathrm{B_T} \tag{A.1}$$

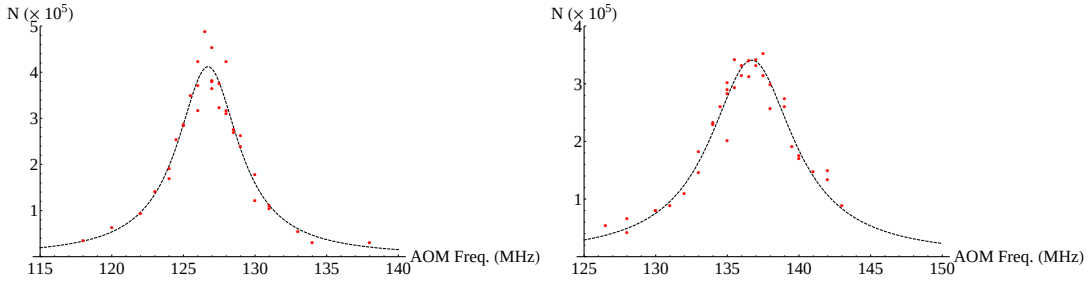
and thus,

$$\mathrm{B_T} = \frac{\Delta f}{1.4\,\mathrm{MHz}}. \tag{A.2}$$

To measure the transition line centre, the frequency detuning of the probe beam was scanned across the resonance with the number of atoms measured being used as the metric for the strength of absorption.

The calibration of $\mathrm{B_T}$ is calculated from the frequency difference of the two transition centers. This method is chosen as it avoids the assumption that under time of flight the atoms experience a zero field. The results in fig. A.1 give a calibration of

$$\mathrm{B_T} = 0.86\ I_\mathrm{T}\,(\mathrm{G/A}). \tag{A.3}$$



(a) (b)

Figure A.1: The TOP field calibration data. Each plot shows the data (red points) and corresponding Lorentzian fit (dashed line) for the variation of the atom number as the probe beam detuning is scanned across the cooling transition. (a) The fitted centre frequency is 126.7 MHz and the measured TOP field current amplitude is $I_{\mathrm{T}} = 24.6$ A. (b) The fitted centre frequency is 136.7 MHz and the measured TOP field current amplitude is $I_{\mathrm{T}} = 41.1$ A.

A.2 The quadrupole gradient

Once the calibration of the TOP field is complete, immediately the quadrupole gradient may be calibrated using the trap frequency measurements in the TOP trap and eqn. 3.18. Trap frequency measurements were made in a TOP trap with a constant bias field of $\mathrm{B_T} = 14.28$ G, and *Quad* coil currents of $I_{\mathrm{q}} = 99$ A and $I_{\mathrm{q}} = 230$ A. The mean value for the field gradient per amp given by the *Quad* coil pair was,[1]

$$B'_q = 2.42\ I_q\,(\mathrm{G/cm/A}) \tag{A.4}$$

A.3 The rf-dressing coils

The rf-dressing coils were calibrated prior to being mounted on the experiment using a DC current, and a gaussmeter located at the centre of each coil pair. As shown in figs. A.2 values for the size of the magnetic field were plotted against current and a fit was used to extract the G/A number for each coil. The utility of this calibration is that in the experiment the current is very easy to measure using clip-on AC current probes (Tektronix P6021), but measuring MHz frequency magnetic fields (in the centre of the glass cell) is very difficult. Hence with a G/A figure, a good estimate of the magnitude of the dressing field being experienced by the atoms can be made. An alternative

[1]Note that prior to this calibration process, the value of the quadrupole gradient had been numerically simulated at 2.45 G/cm/A, and also measured at low currents prior to the coils being installed in the magnetic trap at 2.38 G/cm/A. The fact that these values bound the calibrated value gives an increased degree of confidence in the result.

spectroscopic method has been used to directly measure the size of the coupling strength in the shell and TAAP potentials, the result for which approximately agree with the DC calibration of the rf-dressing coils.

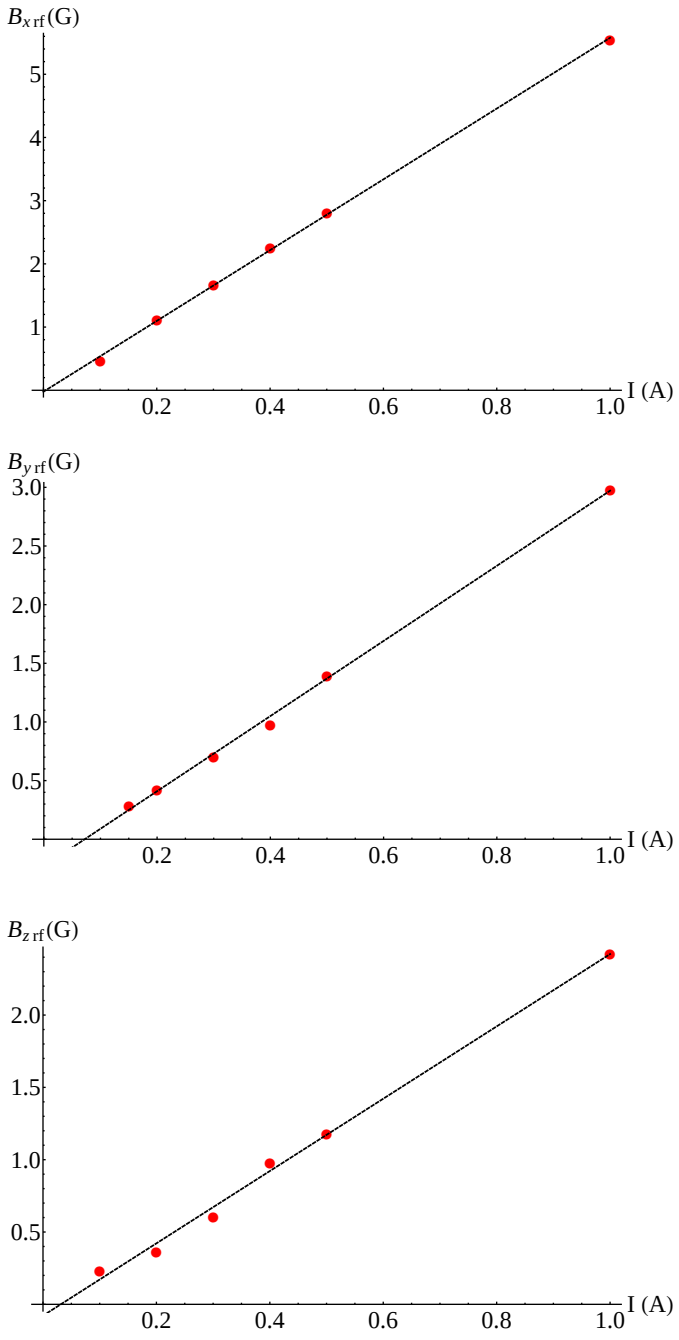


Figure A.2: Radio-frequency dressing coil calibration data. The size of the magnetic field is measured on axis at the centre of the coil pair against the current passing through the coils. A linear fit is used to extract the G/A value for each coil pair. This value was measured at 3.2 G/A for the x *rf* coils (top), 5.6 G/A for the y *rf* coils and 2.5 G/A for the z *rf* coils.

Appendix B

Evaporation in the shell and TAAP traps

A comparison between evaporation in the shell and vertically offset double-well TAAP trap can be used as the basis for an interesting discussion of the dressed atom picture. In section 4.3.3 the argument was presented that when pure, circularly polarised dressing radiation is used to form the shell trap, a single avoided crossing occurs between states from 3 neighbouring bare state manifolds. Under these circumstances the RWA is exact and only transitions allowed within the RWA can be excited using a weak evaporative rf field. In this instance, these transitions occur at the frequencies Ω, $\omega_{\rm rf}/(2\pi) \pm \Omega$ (see fig. 4.11). By contrast when dressing with elliptical or linearly polarised rf, coupling between higher order terms allows transitions to be excited at regular intervals given by,

$$\nu_{evap} = n\frac{\omega_{\rm rf}}{2\pi} \pm \Omega \tag{B.1}$$

for n a positive integer. In this experiment the sense of the rf polarisation is always defined relative to the $+z$ axis, which is most relevant for atoms trapped at the bottom of the shell. However, in the radial TAAP trap the atoms' magnetic dipole moments precess about a different quantisation axis due to the spatial variation of the quadrupole field. In the laboratory frame, the rf polarisation vector is constant in space, however in the atom's frame the orientation of this vector is dependent on their position around the resonant ellipsoid.[1] Following this line of reasoning, a double-well TAAP trap formed using xy circularly polarised dressing radiation should possess higher order transitions, that are absent for a bare shell trap under the same conditions.

To test this proposal, a weak evaporative field was applied at a constant frequency

[1]This interpretation can be used to understand the variation of the coupling strength around the ellipsoid. The σ^+ field that strongly couples the bare states at the South pole of the shell trap, becomes σ^- polarised when 'viewed' by the atoms from the North pole. This field is unable to excite transitions out of the $|F = 1, m_F = -1\rangle$ state, hence the vanishing coupling strength.

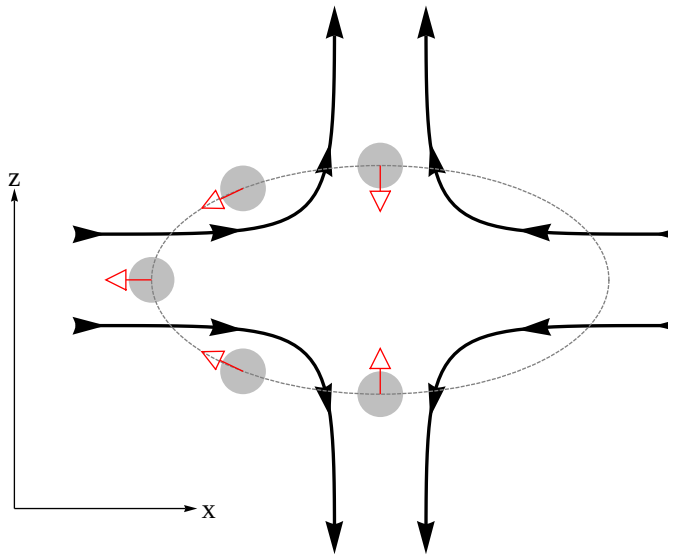


Figure B.1: Spatial variation of the atom's quantisation axis around the resonant ellipsoid in the $y = 0$ plane. The magnetic flux lines close to the centre of the quadrupole trap are depicted by solid black lines. The magnetic dipole of an atom instantaneously found in the $|F = 1, m_F = -1\rangle$ state (red arrows) will precesses about a direction antiparallel to the local magnetic field direction.

for a period of 200 ms to atoms trapped in both a bare shell and double-well TAAP trap. Between each experimental run, the evaporative field frequency was changed by a small interval, thereby probing the whole transition. The results in fig. B.2 support the ideas discussed above. The broadening of the transition in the TAAP trap in B.2(a) compared with the shell trap can be explained by a small asymmetry in the radial TOP fields which causes the trap bottom to be smeared out over 1 rotation cycle. In a manner analogous to Doppler broadening of spectral lines in room temperature vapours, this technical deficiency allows atoms in the trap to enter into resonance with the monochromatic evaporative field over a range of frequencies determined not by the natural linewidth of the transition, but by the amplitude of oscillation of the trap bottom. In the TAAP trap, the strength of the coupling to the evaporative field on the higher frequency transition decreases,[2] matching the observations of [203].

[2]Despite this issue, evaporation across the phase transition to BEC in the TAAP trap has been observed for all transition where $n = 0, 1, 2$.

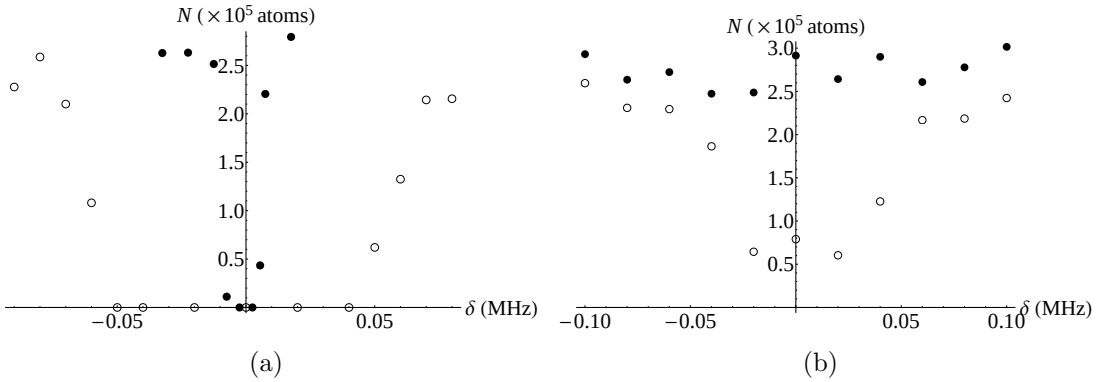


Figure B.2: Evaporation in the shell (closed circles) and vertical double-well TAAP (open circles) traps. Applying an evaporative field on the $\omega_{\rm rf}/(2\pi) + \Omega$ transition (a) removes atoms from both the shell and TAAP traps. In the same potentials, evaporating on the $2\omega_{\rm rf}/(2\pi)+\Omega$ transition (b) only causes atom loss from the TAAP potential. Note the x axis in both plots is scaled relative to the transition centre. The radial TOP field used for the TAAP trap was 1 G.

Bibliography

[1] H. K. Onnes. *Nobel lectures, Physics 1901-1921.* Elsevier (1967).

[2] T. Hänsch and A. Schawlow. Opt. Comm., **13**, 68 (1975).

[3] D. J. Wineland, R. E. Drullinger, and F. L. Walls. Phys. Rev. Lett., **40**, 1639 (1978).

[4] P. D. Lett, R. N. Watts, C. I. Westbrook, W. D. Phillips, P. L. Gould, and H. J. Metcalf. Phys. Rev. Lett., **61**, 169 (1988).

[5] M. H. Anderson, J. R. Ensher, M. R. Matthews, C. E. Wieman, and E. A. Cornell. Science, **269**, 5221 (1995).

[6] P. Medley, D. M. Weld, H. Miyake, D. E. Pritchard, and W. Ketterle. Phys. Rev. Lett., **106**, 195301 (2011).

[7] R. Feynman. Int. J. Phys., **21**, 467 (1982).

[8] J. Stenger, S. Inouye, D. M. Stamper-Kurn, H. J. Miesner, A. P. Chikkatur, and W. Ketterle. Nature, **396**, 345 (1998).

[9] M. Greiner, O. Mandel, T. Esslinger, T. Hänsch, and I. Bloch. Nature, **415**, 39 (2002).

[10] K. W. Madison, F. Chevy, W. Wohlleben, and J. Dalibard. Phys. Rev. Lett., **84**, 806 (2000).

[11] Y. J. Lin, R. L. Compton, K. Jimenez-Garcia, J. V. Porto, and I. B. Spielman. Nature, **462**, 628 (2009).

[12] R. Eisberg and R. Resnick. *Quantum Physics of Atoms, Molecules, Solids, Nuclei and Particles.* Wiley (1985).

[13] A. J. Legget. *Quantum Liquids.* Oxford University Press (2006).

[14] C. J. Pethick and H. Smith. *Bose-Einstein Condensation in Dilute Gases.* Cambridge University Press (2008).

[15] H. J. Weber and G. B. Arfken. *Essential Mathematical Methods for Physicists*. World Scientific (2004).

[16] F. Dalfovo, S. Giorgini, L. P. Pitaevskii, and S. Stringari. Rev. Mod. Phys., **71**, 463 (1999).

[17] C. Foot. *Atomic Physics*. Oxford University Press (2005).

[18] J. F. Allen and A. D. Misener. Proc. R. Soc., **172**, 467 (1939).

[19] R. P. J. F. Allen and M. Z. Uddin. Nature., **140**, 62 (1938).

[20] R. E. Packard and T. M. Sanders. Phys. Rev. A, **6**, 799 (1972).

[21] J. D. Reppy and D. Depatie. Phys. Rev. Lett., **12**, 187 (1964).

[22] G. B. Hess and W. M. Fairbank. Phys. Rev. Lett., **19**, 216 (1967).

[23] L. Tisza. Nature, **141**, 913 (1938).

[24] L. Landau. J. Phys. USSR, **5**, 71 (1941).

[25] J. F. Annett. *Superconductivity, Superfluids and Condensates*. Oxford University Press (2004).

[26] F. London. Nature, **141**, 643 (1938).

[27] M. R. Matthews, B. P. Anderson, P. C. Haljan, D. S. Hall, C. E. Wieman, and E. A. Cornell. Phys. Rev. Lett., **83**, 2498 (1999).

[28] D. M. Stamper-Kurn, H. J. Miesner, S. Inouye, M. R. Andrews, and W. Ketterle. Phys. Rev. Lett., **81**, 500 (1998).

[29] C. Raman, M. Köhl, R. Onofrio, D. S. Durfee, C. E. Kuklewicz, Z. Hadzibabic, and W. Ketterle. Phys. Rev. Lett., **83**, 2502 (1999).

[30] G. Hechenblaikner, E. Hodby, S. A. Hopkins, O. M. Maragò, and C. J. Foot. Phys. Rev. Lett., **88**, 070406 (2002).

[31] R. E. Peierls. *Surprises in Theoretical Physics*. Princeton University Press (1979).

[32] N. D. Mermin and H. Wagner. Phys. Rev. Lett., **17**, 1133 (1966).

[33] P. C. Hohenberg. Phys. Rev., **158**, 383 (1967).

[34] V. L. Berezinskii. JETP, **32**, 493 (1971).

[35] J. M. Kosterlitz and D. J. Thouless. J. Phys. C., **6**, 1181 (1973).

[36] D. J. Bishop and J. D. Reppy. Phys. Rev. Lett., **40**, 1727 (1978).

[37] D. J. Resnick, J. C. Garland, J. T. Boyd, S. Shoemaker, and R. S. Newrock. Phys. Rev. Lett., **47**, 1542 (1981).

[38] V. Bagnato and D. Kleppner. Phys. Rev. A, **44**, 7439 (1991).

[39] D. S. Petrov, M. Holzmann, and G. V. Shlyapnikov. Phys. Rev. Lett., **84**, 2551 (2000).

[40] T. P. Simula, M. J. Davis, and P. B. Blakie. Phys. Rev. A, **77**, 023618 (2008).

[41] C. J. Foster, P. B. Blakie, and M. J. Davis. Phys. Rev. A, **81**, 023623 (2010).

[42] Z. Hadzibabic, P. Krüger, M. Cheneau, B. Battelier, and J. Dalibard. Nature, **441**, 1118 (2006).

[43] P. Cladé, C. Ryu, A. Ramanathan, K. Helmerson, and W. D. Phillips. Phys. Rev. Lett., **102**, 170401 (2009).

[44] V. Schweikhard, S. Tung, and E. A. Cornell. Phys. Rev. Lett., **99**, 030401 (2007).

[45] S. Tung, G. Lamporesi, D. Lobser, L. Xia, and E. A. Cornell. Phys. Rev. Lett., **105**, 230408 (2010).

[46] S. Viefers. J. Phys. Condens. Matter, **20**, 123202 (2008).

[47] N. Cooper. In *Lecture Notes of the Les Houches Summer School*. Oxford University Press (2010).

[48] K. v. Klitzing, G. Dorda, and M. Pepper. Phys. Rev. Lett., **45**, 494 (1980).

[49] D. C. Tsui, H. L. Störmer, and A. C. Gossard. Phys. Rev. Lett., **48**, 1559 (1982).

[50] R. B. Laughlin. Phys. Rev. Lett., **50**, 1395 (1983).

[51] H. L. Störmer. Rev. Mod. Phys., **71**, 875 (1999).

[52] Z. F. Ezawa. *Quantum Hall Effects*. World Scientific (2000).

[53] V. J. Goldman and B. Su. Science, **267**, 1010 (1995).

[54] L. Saminadayar, D. C. Glattli, Y. Jin, and B. Etienne. Phys. Rev. Lett., **79**, 2526 (1997).

[55] R. de Picciotto, M. Reznikov, M. Heiblum, V. Umansky, G. Bunin, and D. Mahalu. Nature, **389**, 162 (1997).

[56] S. Das Sarma, M. Freedman, and C. Nayak. Phys. Rev. Lett., **94**, 166802 (2005).

[57] L. Hormozi, N. E. Bonesteel, and S. H. Simon. Phys. Rev. Lett., **103**, 160501 (2009).

[58] B. Paredes, P. Zoller, and J. I. Cirac. Phys. Rev. A, **66**, 033609 (2002).

[59] N. K. Wilkin, J. M. F. Gunn, and R. A. Smith. Phys. Rev. Lett., **80**, 2265 (1998).

[60] I. S. Grant and W. R. Phillips. *Electromagnetism*. Wiley (2003).

[61] S. Stock, B. Battelier, V. Bretin, Z. Hadzibabic, and J. Dalibard. Laser Phys. Lett., **2**, 275 (2005).

[62] N. R. Cooper and N. K. Wilkin. Phys. Rev. B, **60**, R16279 (1999).

[63] I. Bloch, J. Dalibard, and W. Zwerger. Rev. Mod. Phys., **80**, 885 (2008).

[64] P. Engels, I. Coddington, P. C. Haljan, V. Schweikhard, and E. A. Cornell. Phys. Rev. Lett., **90**, 170405 (2003).

[65] V. Schweikhard, I. Coddington, P. Engels, V. P. Mogendorff, and E. A. Cornell. Phys. Rev. Lett., **92**, 040404 (2004).

[66] N. Gemelke, E. Sarajilic, and S. Chu. arXiv:1007.2677 (2010).

[67] Y. J. Lin, R. L. Compton, K. Jimenez-Garcia, W. D. Phillips, J. V. Porto, and I. B. Spielman. Nat. Phys., **7**, 531 (2011).

[68] H. J. Metcalf and P. van der Straten. *Laser cooling and trapping*. Springer (1999).

[69] P. Lebedev. Ann. Phys., **6**, 433 (1901).

[70] E. F. Nichols and G. F. Hull. Phys. Rev., **13**, 307 (1901).

[71] E. F. Nichols and G. F. Hull. Phys. Rev., **17**, 26 (1903).

[72] R. Grimm, M. Weidemüller, and Y. B. Ovchinnikov. Adv. At., Mol., Opt. Phys., **42**, 95 (2000).

[73] S. Chu, L. Hollberg, J. E. Bjorkholm, A. Cable, and A. Ashkin. Phys. Rev. Lett., **55**, 48 (1985).

[74] J. Dalibard and C. Cohen-Tannoudji. J. Opt. Soc. Am. B, **6**, 2023 (1989).

[75] Y. Shevy, D. S. Weiss, P. J. Ungar, and S. Chu. Phys. Rev. Lett., **62**, 1118 (1989).

[76] D. A. Steck. Rubidium 87 d line data (2010). Http://steck.us/alkalidata/.

[77] P. D. Lett, W. D. Phillips, S. L. Rolston, C. E. Tanner, R. N. Watts, and C. I. Westbrook. J. Opt. Soc. Am. B, **6**, 2084 (1989).

[78] S. Q. Shang, B. Sheehy, P. van der Straten, and H. Metcalf. Phys. Rev. Lett., **65**, 317 (1990).

[79] C. Salomon, J. Dalibard, W. D. Phillips, A. Clairon, and S. Guellati. Europhys. Lett., **12**, 683 (1990).

[80] M. Kasevich and S. Chu. Phys. Rev. Lett., **69**, 1741 (1992).

[81] A. Aspect, E. Arimondo, R. Kaiser, N. Vansteenkiste, and C. Cohen-Tannoudji. Phys. Rev. Lett., **61**, 826 (1988).

[82] E. L. Raab, M. Prentiss, A. Cable, S. Chu, and D. E. Pritchard. Phys. Rev. Lett., **59**, 2631 (1987).

[83] J. V. Prodan and W. D. Phillips. Prog. Quant. Elect., **8**, 231 (1984).

[84] W. D. Phillips and H. Metcalf. Phys. Rev. Lett., **48**, 596 (1982).

[85] K. E. Gibble, S. Kasapi, and S. Chu. Opt. Lett., **17**, 526 (1992).

[86] C. Monroe, W. Swann, H. Robinson, and C. Wieman. Phys. Rev. Lett., **65**, 1571 (1990).

[87] K. I. Lee, J. A. Kim, H. R. Noh, and W. Jhe. Opt. Lett., **21**, 1177 (1996).

[88] E. Hecht. *Optics*. Addison Wesley (2002).

[89] W. Ketterle, K. B. Davis, M. A. Joffe, A. Martin, and D. E. Pritchard. Phys. Rev. Lett., **70**, 2253 (1993).

[90] A. L. Migdall, J. V. Prodan, W. D. Phillips, T. H. Bergeman, and H. J. Metcalf. Phys. Rev. Lett., **54**, 2596 (1985).

[91] W. H. Wing. Prog. Quant. Elect., **8**, 181 (1984).

[92] D. E. Pritchard. Phys. Rev. Lett., **51**, 1336 (1983).

[93] J. J. Tollett, C. C. Bradley, C. A. Sackett, and R. G. Hulet. Phys. Rev. A, **51**, R22 (1995).

[94] M. O. Mewes, M. R. Andrews, N. J. van Druten, D. M. Kurn, D. S. Durfee, and W. Ketterle. Phys. Rev. Lett., **77**, 416 (1996).

[95] C. J. Myatt, E. A. Burt, R. W. Ghrist, E. A. Cornell, and C. E. Wieman. Phys. Rev. Lett., **78**, 586 (1997).

[96] U. Ernst, A. Marte, F. Schreck, J. Schuster, and G. Rempe. Europhys. Lett., **41**, 1 (1998).

[97] T. Esslinger, I. Bloch, and T. W. Hänsch. Phys. Rev. A, **58**, R2664 (1998).

[98] K. B. Davis, M. O. Mewes, M. R. Andrews, N. J. van Druten, D. S. Durfee, D. M. Kurn, and W. Ketterle. Phys. Rev. Lett., **75**, 3969 (1995).

[99] W. Petrich, M. H. Anderson, J. R. Ensher, and E. A. Cornell. Phys. Rev. Lett., **74**, 3352 (1995).

[100] E. Hodby, G. Hechenblaikner, S. A. Hopkins, O. M. Maragò, and C. J. Foot. Phys. Rev. Lett., **88**, 010405 (2001).

[101] E. Hodby, S. A. Hopkins, G. Hechenblaikner, N. L. Smith, and C. J. Foot. Phys. Rev. Lett., **91**, 090403 (2003).

[102] N. L. Smith, W. H. Heathcote, J. M. Krueger, and C. J. Foot. Phys. Rev. Lett., **93**, 080406 (2004).

[103] J. Ensher. *The first experiments with Bose-Einstein condensation of* ^{87}*Rb.* Ph.D. thesis, University of Colorado (1998).

[104] N. Masuhara, J. M. Doyle, J. C. Sandberg, D. Kleppner, T. J. Greytak, H. F. Hess, and G. P. Kochanski. Phys. Rev. Lett., **61**, 935 (1988).

[105] A. J. Moerdijk and B. J. Verhaar. Phys. Rev. A, **53**, R19 (1996).

[106] W. Ketterle and N. V. Druten. Adv. At., Mol., Opt. Phys., **37**, 181 (1996).

[107] D. J. Han, R. H. Wynar, P. Courteille, and D. J. Heinzen. Phys. Rev. A, **57**, R4114 (1998).

[108] W. Paul and H. Steinwedel. Zeitschrift Naturforschung Teil A, **8**, 448 (1953).

[109] K. Henderson, C. Ryu, C. MacCormick, and M. G. Boshier. New J. Phys., **11**, 043030 (2009).

[110] O. Zobay and B. M. Garraway. Phys. Rev. Lett., **86**, 1195 (2001).

[111] Y. Colombe, E. Knyazchyan, O. Morizot, B. Mercier, V. Lorent, and H. Perrin. Europhys. Lett., **67**, 593 (2004).

[112] S. Hofferberth, I. Lesanovsky, B. Fischer, J. Verdu, and J. Schmiedmayer. Nat. Phys., **2**, 710 (2006).

[113] O. Morizot, C. L. G. Alzar, P. Pottie, V. Lorent, and H. Perrin. J. Phys. B, **40**, 4013 (2007).

[114] W. H. Heathcote, E. Nugent, B. T. Sheard, and C. J. Foot. N. J. Phys., **10**, 043012 (2008).

[115] M. White, H. Gao, M. Pasienski, and B. DeMarco. Phys. Rev. A, **74**, 023616 (2006).

[116] T. Fernholz, R. Gerritsma, P. Krüger, and R. J. C. Spreeuw. Phys. Rev. A, **75**, 063406 (2007).

[117] P. W. Courteille, B. Deh, J. Fortgh, A. Günther, S. Kraft, C. Marzok, S. Slama, and C. Zimmermann. J.Phys. B, **39**, 1055 (2006).

[118] T. Schumm, S. Hofferberth, L. M. Andersson, S. Wildermuth, S. Groth, I. Bar-Joseph, J. Schmiedmayer, and P. Krüger. Nat. Phys., **1**, 57 (2005).

[119] J. Fortágh, H. Ott, S. Kraft, A. Günther, and C. Zimmermann. Phys. Rev. A, **66**, 041604 (2002).

[120] G. B. Jo, Y. Shin, S. Will, T. A. Pasquini, M. Saba, W. Ketterle, D. E. Pritchard, M. Vengalattore, and M. Prentiss. Phys. Rev. Lett., **98**, 030407 (2007).

[121] F. S. Levin. *An introduction to Quantum Theory*. Cambridge University Press (2002).

[122] I. Lesanovsky, T. Schumm, S. Hofferberth, L. M. Andersson, P. Krüger, and J. Schmiedmayer. Phys. Rev. A, **73**, 033619 (2006).

[123] E. Kreysig. *Advanced Engineering Mathematics*. Wiley (1999).

[124] D. T. Pegg. J. Phys. B, **6**, 241 (1973).

[125] B. H. Bransden and C. J. Joachain. *Physics of Atoms and Molecules*. Prentice Hall (2003).

[126] V. E. Lembessis and D. Ellinas. J. Opt. B., **7**, 319 (2005).

[127] F. Bloch and A. Siegert. Phys. Rev., **57**, 522 (1940).

[128] S. M. Barnett and P. M. Radmore. *Methods in Theoretical Quantum Optics*. Oxford University Press (1997).

[129] M. Allegrini and E. Arimondo. J. Phys. B, **4**, 1008 (1971).

[130] C. Cohen-Tannoudji. *Atoms in Electromagnetic Fields*. World Scientific (1994).

[131] M. Gildemeister. *Trapping Ultracold Atoms in Time-Averaged Adiabatic Potentials*. Ph.D. thesis, University of Oxford (2010).

[132] S. Hofferberth, B. Fischer, T. Schumm, J. Schmiedmayer, and I. Lesanovsky. Phys. Rev. A, **76**, 013401 (2007).

[133] S. Haroche, C. Cohen-Tannoudji, C. Audoin, and J. P. Schermann. Phys. Rev. Lett., **24**, 861 (1970).

[134] C. Zener. Proc. R. Soc., **137**, 696 (1932).

[135] C. E. Carroll and F. T. Hioe. J. Phys. A., **19**, 1151 (1986).

[136] N. V. Vitanov and K. A. Suominen. Phys. Rev. A, **56**, R4377 (1997).

[137] R. A. Williams, S. Al-Assam, and C. J. Foot. Phys. Rev. Lett., **104**, 050404 (2010).

[138] Z. Hadzibabic, P. Krüger, M. Cheneau, S. P. Rath, and J. Dalibard. New J. Phys., **10**, 045006 (2008).

[139] I. Lesanovsky and W. von Klitzing. Phys. Rev. Lett., **99**, 083001 (2007).

[140] M. Gildemeister, E. Nugent, B. E. Sherlock, M. Kubasik, B. T. Sheard, and C. J. Foot. Phys. Rev. A, **81**, 031402 (2010).

[141] B. E. Sherlock, M. Gildemeister, E. Owen, E. Nugent, and C. J. Foot. Phys. Rev. A, **83**, 043408 (2011).

[142] M. Greiner, I. Bloch, T. W. Hänsch, and T. Esslinger. Phys. Rev. A, **63**, 031401 (2001).

[143] B. Sheard. *Magnetic Transport and Bose-Einstein Condensation of Rubidium Atoms*. Ph.D. thesis, University of Oxford (2010).

[144] C. E. Wieman and L. Hollberg. Rev. Sci. Instrum., **62**, 1 (1991).

[145] L. Ricci, M. Weidemüller, T. Esslinger, A. Hemmerich, C. Zimmermann, V. Vuletic, W. König, and T. W. Hänsch. Opt. Commun., **117**, 541 (1995).

[146] A. S. Arnold, J. S. Wilson, and M. G. Boshier. AIP, **69** (1998).

[147] S. D. Saliba and R. E. Scholten. Appl. Opt., **48**, 6961 (2009).

[148] R. Lang. J. Quant. Elect., **18**, 976 (1982).

[149] R. K. Raj, D. Bloch, J. J. Snyder, G. Camy, and M. Ducloy. Phys. Rev. Lett., **44**, 1251 (1980).

[150] J. H. Shirley. Opt. Lett., **7**, 537 (1982).

[151] F. Bertinetto, P. Cordiale, G. Galzerano, and E. Bava. IEEE Trans. Instrum. Meas., **50**, 490 (2001).

[152] D. J. McCarron, S. A. King, and S. L. Cornish. Meas. Sci. Technol., **19**, 105601 (2008).

[153] R. W. P. Drever, J. L. Hall, F. V. Kowalski, J. Hough, G. M. Ford, A. J. Munley, and H. Ward. Applied Physics B: Lasers and Optics, **31**, 97 (1983). 10.1007/BF00702605.

[154] T. W. Hänsch, I. S. Shahin, and A. L. Schawlow. Phys. Rev. Lett., **27**, 707 (1971).

[155] G. Zürn. High current control for magnetic transport of cold atoms (2008). University of Oxford.

[156] P. Baranowski, J. Zacks, G. Hechenblaikner, and C. J. Foot. arXiv:physics/0412126 (2004).

[157] C. Shannon. Proc. IEEE, **72**, 1192 (1984).

[158] W. Petrich, M. H. Anderson, J. R. Ensher, and E. A. Cornell. J. Opt. Soc. Am. B, **11**, 1332 (1994).

[159] H. Lewandowski, D. Whitaker, and E. Cornell. QELS Technical Digest, page 203 (2000).

[160] M. Greiner, I. Bloch, T. Hänsch, and T. Esslinger. Phys. Rev. A, **63**, 031401 (2001).

[161] M. R. Andrews, M. O. Mewes, N. J. van Druten, D. S. Durfee, D. M. Kurn, and W. Ketterle. Science, **273**, 84 (1996).

[162] V. Boyer, R. M. Godun, G. Smirne, D. Cassettari, C. M. Chandrashekar, A. B. Deb, Z. J. Laczik, and C. J. Foot. Phys. Rev. A, **73**, 031402 (2006).

[163] W. Heathcote. *A toroidal trap for ultracold atoms in a rf-dressed state.* Ph.D. thesis, Oxford University (2007).

[164] C. S. Adams, H. J. Lee, N. Davidson, M. Kasevich, and S. Chu. Phys. Rev. Lett., **74**, 3577 (1995).

[165] E. Nugent. *Novel Traps for Bose-Einstein Condensates.* Ph.D. thesis, University of Oxford (2009).

[166] M. Gildemeister (2011). Private communication.

[167] D. S. Petrov, G. V. Shlyapnikov, and J. T. M. Walraven. Phys. Rev. Lett., **85**, 3745 (2000).

[168] A. I. Safonov, S. A. Vasilyev, I. S. Yasnikov, I. I. Lukashevich, and S. Jaakkola. Phys. Rev. Lett., **81**, 4545 (1998).

[169] A. Görlitz, J. M. Vogels, A. E. Leanhardt, C. Raman, T. L. Gustavson, J. R. Abo-Shaeer, A. P. Chikkatur, S. Gupta, S. Inouye, T. Rosenband, and W. Ketterle. Phys. Rev. Lett., **87**, 130402 (2001).

[170] S. Burger, F. S. Cataliotti, C. Fort, P. Maddaloni, F. Minardi, and M. Inguscio. Europhys. Lett., **57**, 1 (2002).

[171] D. Rychtarik, B. Engeser, H. C. Nägerl, and R. Grimm. Phys. Rev. Lett., **92**, 173003 (2004).

[172] N. L. Smith, W. H. Heathcote, G. Hechenblaikner, E. Nugent, and C. J. Foot. J. Phys. B, **38**, 223 (2005).

[173] B. M. Garraway and H. Perrin. Physica Scripta, **2010**, 014006 (2010).

[174] A. G. Morris and D. L. Feder. Phys. Rev. Lett., **99**, 240401 (2007).

[175] V. Bretin, S. Stock, Y. Seurin, and J. Dalibard. Phys. Rev. Lett., **92**, 050403 (2004).

[176] M. Roncaglia, M. Rizzi, and J. Dalibard. arXiv:1101.5593 (2011).

[177] N. Read and N. R. Cooper. Phys. Rev. A, **68**, 035601 (2003).

[178] T. W. Neely, E. C. Samson, A. S. Bradley, M. J. Davis, and B. P. Anderson. Phys. Rev. Lett., **104**, 160401 (2010).

[179] C. Ryu, M. F. Andersen, P. Cladé, V. Natarajan, K. Helmerson, and W. D. Phillips. Phys. Rev. Lett., **99**, 260401 (2007).

[180] A. Ramanathan, K. C. Wright, S. R. Muniz, M. Zelan, W. T. Hill, C. J. Lobb, K. Helmerson, W. D. Phillips, and G. K. Campbell. Phys. Rev. Lett., **106**, 130401 (2011).

[181] M. G. Sagnac and C. R. Hebd. Acad. Sci., **157** (1913).

[182] J. A. Sauer, M. D. Barrett, and M. S. Chapman. Phys. Rev. Lett., **87**, 270401 (2001).

[183] S. Gupta, K. W. Murch, K. L. Moore, T. P. Purdy, and D. M. Stamper-Kurn. Phys. Rev. Lett., **95**, 143201 (2005).

[184] A. S. Arnold, C. S. Garvie, and E. Riis. Phys. Rev. A, **73**, 041606 (2006).

[185] O. Morizot, Y. Colombe, V. Lorent, H. Perrin, and B. M. Garraway. Phys. Rev. A, **74**, 023617 (2006).

[186] P. F. Griffin, E. Riis, and A. S. Arnold. Phys. Rev. A, **77**, 051402 (2008).

[187] P. M. Baker, J. A. Stickney, M. B. Squires, J. A. Scoville, E. J. Carlson, W. R. Buchwald, and S. M. Miller. Phys. Rev. A, **80**, 063615 (2009).

[188] O. Morizot, L. Longchambon, R. Kollengode Easwaran, R. Dubessy, E. Knyazchyan, P. E. Pottie, V. Lorent, and H. Perrin. Eur. Phys. J. D, **47**, 209 (2008).

[189] F. Piazza, L. A. Collins, and A. Smerzi. Phys. Rev. A, **80**, 021601 (2009).

[190] T. W. B. Kibble. J. Phys. A, **9**, 1387 (1976).

[191] W. H. Zurek. Physics Reports, **276**, 177 (1996).

[192] C. N. Weiler, T. W. Neely, D. R. Scherer, A. S. Bradley, M. J. Davis, and B. P. Anderson. Nature, **455**, 948 (2008).

[193] J. S. A. Das and W. H. Zurek. arXiv:1102.5474v1 (2011).

[194] I. Lesanovsky and W. von Klitzing. Phys. Rev. Lett., **98**, 050401 (2007).

[195] M. Schellekens, R. Hoppeler, A. Perrin, J. V. Gomes, D. Boiron, A. Aspect, and C. I. Westbrook. Science, **310**, 648 (2005).

[196] T. Gericke, P. Wurtz, D. Reitz, T. Langen, and H. Ott. Nat. Phys., **4**, 949 (2008).

[197] R. Bücker, A. Perrin, S. Manz, T. Betz, C. Koller, T. Plisson, J. Rottmann, T. Schumm, and J. Schmiedmayer. New J. Phys., **11**, 103039 (2009).

[198] W. S. Bakr, A. Peng, M. E. Tai, R. Ma, J. Simon, J. I. Gillen, S. Fölling, L. Pollet, and M. Greiner. Science, **329**, 547 (2010).

[199] J. F. Sherson, C. Weitenberg, M. Endres, M. Cheneau, I. Bloch, and S. Kuhr. Nature, **467**, 68 (2010).

[200] M. D. Shotter. Phys. Rev. A, **83**, 033617 (2011).

[201] A. L. Marchant, S. Händel, T. P. Wiles, S. A. Hopkins, C. S. Adams, and S. L. Cornish. Opt. Lett., **36**, 64 (2011).

[202] S. Al-Assam, R. A. Williams, and C. J. Foot. Phys. Rev. A, **82**, 021604 (2010).

[203] R. K. Easwaran, L. Longchambon, P.-E. Pottie, V. Lorent, H. Perrin, and B. M. Garraway. J. Phys. B, **43**, 065302 (2010).